VLÁKNA A TEXTIL

FIBRES AND TEXTILES

1

Volume 32
March
2025

TECHNICAL UNIVERSITY OF LIBEREC

STU FCHPT

Trenčianska univerzita Alexandra Dubčeka v Trenčíne
Fakulta priemyselných technológií v Púchove

VUTCH
RESEARCH INSTITUTE OF TEXTILE CHEMISTRY
VÝSKUMNÝ ÚSTAV TEXTILNEJ CHÉMIE

CHEMOSVIT FIBROCHEM

VÚCHV

ZVTS

Indexed in:
SCOPUS
Chemical Abstract
World Textile Abstracts
EBSCO Essentials

ISSN 1335-0617
print version

ISSN 2585-8890
online version

VLÁKNA A TEXTIL

http://www.vat.ft.tul.cz

PUBLISHED BY
Technical University of Liberec, Faculty of Textile Engineering
Slovak University of Technology in Bratislava, Faculty of Chemical and Food Technology
Alexander Dubček University of Trenčín, Faculty of Industrial Technologies
Slovak Society of Industrial Chemistry, Bratislava
Research Institute of Man-Made Fibres, JSC, Svit
Research Institute of Textile Chemistry (VUTCH) Ltd., Žilina
Chemosvit Fibrochem, JSC, Svit

PUBLISHER
Technical University of Liberec
Studentska 1402/2, 461 17 Liberec 1, CZ
Tel: +420 485 353615
e-mail: vat@tul.cz
IČO: 46747885

ORDER AND ADVERTISEMENT OF THE JOURNAL
Technical University of Liberec
Faculty of Textile Engineering
Studentska 1402/2, 461 17 Liberec 1, CZ
Tel: +420 485 353615
e-mail: vat@tul.cz

TYPESET AND PRINT
Polygrafie TUL, Voroněžská 1329/13, 460 01 Liberec 1, CZ

DATE OF ISSUE
March 2025

APPROVED BY
Rector's Office of Technical University of Liberec
Ref. no. RE 12/25, 15th January 2025

EDITION
First

PUBLICATION NUMBER
55-012-25

PUBLICATION
Quarterly

SUBSCRIPTION
60 EUR

REG. NO. MK ČR E 24338

VLÁKNA A TEXTIL

Volume 32, Issue 1, March 2025

Special issue dedicated to the 24th International Conference STRUTEX 2024
"Structure and Structural Mechanics of Textile"
held on December 2 – 4, 2024 in Liberec, Czech Republic

The presented publication from the 24th International Conference STRUTEX 2024 is a collection of professional works of leading textile experts from all over the world, the Faculty of Textiles and also students of doctoral study programmes. The papers are thematically divided into two chapters according to the conference sections.
The first chapter contains papers focused on the topic Structure and structural mechanics of textiles. It includes publications focused on the structure of fibres and yarns, flat and spatial textiles, composites and biomechanics.
The second chapter covers innovations and applications of textile research in clothing, technical and medical textiles.
All papers were selected by an editorial committee, which guaranteed their high professional standard.

PROF. ING. BOHUSLAV NECKÁŘ, DRSC.

VLÁKNA A TEXTIL

Volume 32, Issue 1, March 2025

CONTENT

GEOMETRIC AND MECHANICAL MODELING OF WEFT-KNITTED FABRICS USING HELICOID SCAFFOLDS

BREEN, DAVID[1*]; WADEKAR, PARAS[1]; AMANATIDES, CHELSEA[2]; DION, GENEVIEVE[2] AND KAMIEN, RANDALL[3]

[1] Department of Computer Science, Drexel University, 3675 Market Street, Philadelphia, PA 19119, USA
[2] Center for Functional Fabrics, Drexel University, 3675 Market Street, Philadelphia, PA 19119, USA
[3] Department of Physics and Astronomy, University of Pennsylvania, 209 South 33rd Street, Philadelphia, PA, USA

ABSTRACT

We present a bicontinuous, minimal surface (the helicoid) as a scaffold on which to define the topology and geometry of yarns in a weft-knitted fabric. Modeling with helicoids offers a geometric approach to simulating a physical manufacturing process, which should generate geometric models suitable for downstream analyses. The centerline of a yarn in a knitted fabric is specified as a geodesic path, with constrained boundary conditions, running along a helicoid at a fixed distance. The shape of the yarn's centerline is produced via an optimization process over a polyline. The distances between the vertices of the polyline are shortened and a repulsive potential keeps the vertices at a specified distance from the helicoid. These actions and constraints are formulated into a single "cost" function, which is then minimized. The yarn geometry is generated as a tube around the centerline. The optimized configuration, defined for a half loop, is duplicated, reflected, and shifted to produce the centerlines for the multiple stitches that make up a fabric. The approach provides a promising framework for estimating the mechanical behavior/properties of weft-knitted fabrics. Fabric-level deformation energy may be estimated by scaling the helicoid scaffold, computing new yarn paths, determining the amount of ensuing yarn stretch, and computing the total amount of yarn stretching energy. Computational results are calibrated and verified with measurements taken from actual yarns and fabrics.

KEYWORDS

Minimal surface; Computational modelling; Weft-knitted fabrics; Yarn geometry; Optimization.

INTRODUCTION

The calculus of variations is the cornerstone of classical mechanics, elasticity theory, and modern economics. When physical models are formulated as optimization problems, the equations governing motion, stretching or bending describe critical points of the objective function [8]. When the objective depends on geometric quantities, the minima, maxima, and other extrema are likewise geometric. Functionals of length lead to geodesic equations (shortest length), while functionals of area lead to minimal surfaces. Soap bubbles, for instance, minimize their area subject to a volume constraint leading to Plateau's classic rules for foams [14].

Since minimal surfaces are the solutions to many extremal problems in physics, we posit that they may be used to define the topology and shape of yarns in a weft-knitted fabric. In previous work, we demonstrated, with physical prototypes, how yarns of a weft-knitted fabric may lie on a scaffolding of alternating left- and right-hand helicoids, a type of minimal surface, with the form of the helicoids producing the characteristic spatial relationships between the yarns [7]. Here, we summarize the mathematics and algorithms that create geometric models of the yarns making up a weft-knitted fabric, which exploit the lattice-like structural features of bicontinuous helicoid surfaces. See Wadekar et al. [18,20] for more details. The centerline of the yarn is specified as a geodesic path, with constrained boundary conditions, running along a helicoid at a fixed distance. The yarn geometry is then generated as a tube around the centerline. The helicoid therefore acts as a scaffold on which to define the shape of the yarns and their intertwinings.

The shape of a yarn's centerline is produced via an optimization process over a polyline [21]. The polyline is initially placed over a helicoid in the approximate configuration that will define a half loop of a stitch. The distances between the vertices of the polyline are shortened and a repulsive potential keeps the vertices at a set distance from the helicoid. In addition, the locations of the polyline's endpoints are

* **Corresponding author:** Breen D., e-mail: *david@cs.drexel.edu*

constrained. This process effectively models the shrinking of the initial polyline, while performing collision detection/avoidance with the scaffold surface, producing a geodesic path along the helicoid. These actions and constraints are formulated into a single "cost" function, which is then minimized. The optimization process modifies the vertices to produce a minimum cost configuration that balances the inter-vertex stretching cost with the repulsive cost from the helicoid. This configuration, defined for a half loop, is then duplicated, reflected, and shifted to produce the centerlines for the multiple stitches that make up a fabric.

Surface scaffolds have been explored in the context of weft-knitting because they are able to produce physically plausible geometric models of yarns. Additionally, when keeping the yarn models on opposite sides of the scaffold surface, the form of the surface provides the critical function of maintaining the topology and spatial relationships between the yarns; thus removing the need to compute yarn-yarn intersections. An even more important feature of this approach is that it provides a framework for analyzing the mechanical properties of knitted fabrics. Deformations may be applied to the underlying scaffold, while the yarns stay in contact with the deformed surfaces. Energies of deformation are then computed at the yarn level to derive the mechanical properties of the fabric as a whole. Since these mechanical properties are computed via the geometric solutions furnished by the supporting surfaces, the scaffold-surface approach enables an efficient analysis technique that should support rapid exploration of the fabric's design space. This approach provides a potential alternative to compute-intensive FEM methods for estimating the mechanical behavior of knitted fabrics.

RELATED WORK

The first published system to model and visualize complete knitted fabrics was developed by Eberhardt et al. [4,13]. Their system (KnitSim) accepts Stoll knitting machine commands and simulates the knitting process to produce an explicit topological representation of a knitted fabric, which can then be used to generate a 2D geometric layout of the fabric. Two decades later, a system with similar capabilities was developed by Counts [3]. Lin et al. [9] developed a modeling approach/system that works on various scales to model the yarns in and predict the mechanical properties of textiles, including knitted fabrics.

In ground-breaking work Kaldor et al. [5,6] simulated complete swatches and articles of clothing consisting of knitted fabrics by modeling the geometry and physics of individual yarns in these items. This work was extended by Yuksel et al. [23] and Wu et al. [22] to produce Stitch Meshes, an approach to generating Kaldor-style, yarn-level geometric models of knitted clothing from polygonal models that represent the clothing's surface. Cirio et al. [2] define a topological representation of knits consisting of a limited set of stitches. They developed a mechanical model based on the representation for the simulation of knitted clothing, which has been incorporated into a hybrid yarn/triangle model [1]. Liu et al. [10,12] perform Finite Element Modeling simulations of knitted fabrics based on solid yarn-level geometric models [19]. Others [11,15,17] utilize a homogenized model to simulate the mechanical behavior of knits.

Our work is novel compared to previous efforts in that it utilizes a helicoid-like bicontinuous surface to define the geometry and topology of yarns in a weft-knitted fabric. More importantly, it provides a unique approach for estimating the stretching energy of the fabric.

YARN MODEL DEFINITION

Helicoid scaffold model

The bicontinuous surface formulation employed as a yarn model scaffold is defined over *u* and *v* as a surface *S* such that

$$S(\mathrm{u}, \mathrm{v}) = [x, y, z] \quad (1)$$

where *x* and *y* are independent variables, and *z* is the set of values that satisfy Equation 2.

$$\tan z = \sin x / \cos y \quad (2)$$

Equation 2 defines a trigonometric approximation to the triply-periodic Schwarz D (Diamond) minimal surface, which has been shown to model physical structures (e.g., liquid crystalline phases) [4]. Equation 2 can be solved for *z* to produce

$$z = \tan^{-1}(\sin x / \cos y) \quad (3)$$

which defines a single *z* value for every (*x*, *y*) pair. Scale factors can be added to Equation 3 in order to control the size and spacing of the helicoids, which in turn scale the yarn models lying on them.

$$z = \gamma \tan^{-1}(\sin \eta x / \cos \varphi y) \quad (4)$$

where η and ψ control the spacing between the central axes of the helicoid structures in the *x* and *y* directions. The distance between the axes is π when $\eta = \psi = 1$. γ controls the height of each helicoid cycle, with the height of one cycle being 2π when $\gamma = 1$.

Computing the yarn configuration

The total configuration cost of the yarn is the sum of the costs computed at N −1 of the N vertices of the polyline that approximate it.

$$\boldsymbol{E_{total}} = \sum_{i=1}^{N-1} \boldsymbol{E_{total}^{i}} \quad (5)$$

The total cost associated with vertex *i* is given by

$$E_{total}^{i} = \alpha E_{len}^{i} + \beta E_{dist}^{i} \quad (6)$$

The cost term used to shrink the yarn is

$$E_{len}^{i} = (Length^{i} - TargetLength)^{2} \quad (7)$$

where $Length^{i}$ is the distance between vertex *i* and vertex *i* +1 and *TargetLength* is parameter that is adjusted in order to shorten the polyline. $\boldsymbol{E_{dist}^{i}}$ maintains the distance constraint between the polyline and the helicoid scaffold and is defined as

$$E_{dist}^{i} = \left(d^{i} - R_{y}\right)\log(d^{i}/R_{y}) \quad (8)$$

d^{i} is the distance between vertex *i* and the helicoid scaffold and R_y is the yarn radius. The distance cost is only computed for di values less than R_y. The equation is defined in this form in order to go to infinity at $d = 0$ and to have a value and derivative of 0 at $d = R_y$.

GENERATING GEOMETRIC MODELS

Polylines were placed over a helicoid scaffold defined by Eq. 4. The cost of the polyline, as defined by Eqs. 5 through 8, was minimized to produce a geodesic path on the scaffold. Tube-like geometry, with radius Ry, was defined around the polyline to produce solid geometric models of yarns in swatches of single Jersey, rib and garter knitted fabrics. The surface of the helicoid scaffold is shown in Fig. 1 (Left). A model of single loop of yarn is shown in Fig. 1 (Right). The color-coding of the surface demonstrates that the yarn remains on one side of the scaffold.

Figure 2 (Left) presents the yarn geometric model of an 8 x 8 swatch of stitches in a rib pattern (alternating columns of Knit and Purl stitches), with and without the helicoid scaffold. Figure 2 (Right) presents the yarn geometric model of an 8 x 8 swatch of stitches in a garter pattern (alternating rows of Knit and Purl stitches), with and without the helicoid scaffold. These results can be produced in several (5 to 10) seconds on a standard PC.

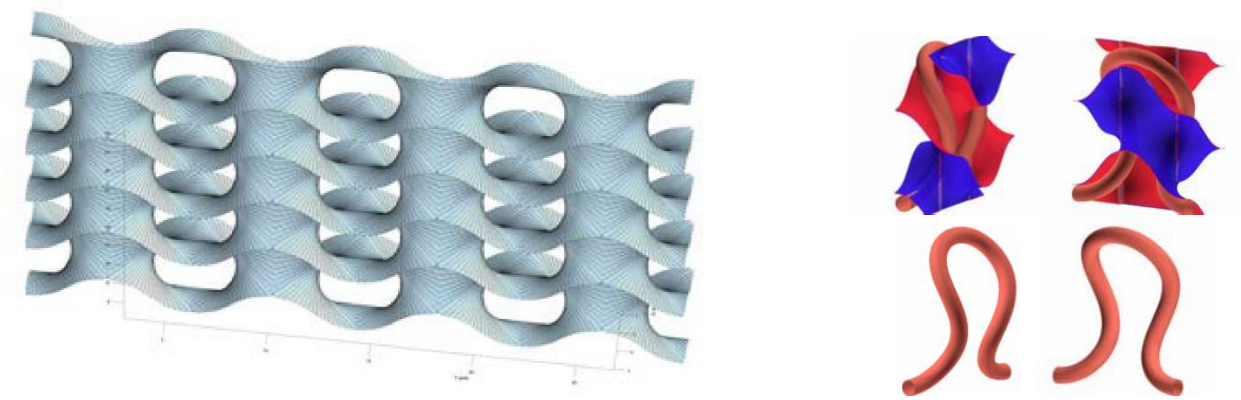

Figure 1. (Left) The helicoid scaffold surface. (Right) A model of a single loop of yarn is shown with and without the associated scaffold.

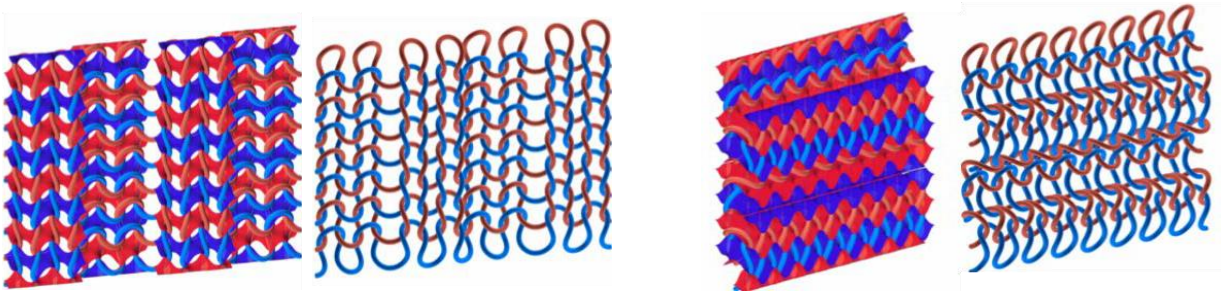

Figure 2. (Left) Geometric model of yarns on a rib pattern. (Right) Geometric models of yarns in a garter pattern.

ESTIMATING FABRIC STRETCHING ENERGY

The helicoid scaffold model for knitted fabrics provides a framework for estimating the mechanical properties of a weft-knitted fabric. Specifically, the model supports the computation of the stretching deformation energy of the fabric. The process is detailed in Figure 3. The general approach involves stretching the scaffold that defines the yarns in the fabric and computing the tensile strain energy of the yarns arising from the fabric stretching deformation.

The following outlines the steps in the process of computing knitted fabric stretching energy.

- Acquire force vs. displacement data for a yarn. Produce an all-Knit (single Jersey) fabric swatch from the yarn. Acquire force vs. displacement data for the knitted swatch.
- Convert the force vs. displacement data for the yarn into energy per unit length vs. strain by calculating the area under the curve.
- Convert the force vs. displacement data for the swatch into energy per unit swatch length vs. strain by calculating the area under the curve.
- Generate the yarn-level helicoid model using the size parameters of the fabric's stitches. The scale parameters for the loops are derived from the knitted swatch. (# stitches in a row/width of swatch; # rows/height of swatch).
- For a given amount of fabric stretching, generate the associated yarn-level helicoid models with stretched loops by increasing the scaffold width by the given swatch strain values.
- Decrease the scaffold thickness for these helicoid models and reoptimize the yarn path on the scaffold to adjust for the Poisson Effect.
- Compute the yarn strain for the stretched model compared to the original undeformed yarn model.
- Find the corresponding yarn energy per unit length for these yarn strain values using the yarn energy per unit length vs. strain data obtained earlier.
- Multiply the yarn energy per unit length by the loop length obtained from the undeformed yarn model to produce the energy per loop.
- Compute the final swatch energy prediction by multiplying the energy per loop by the total number of stitches in the swatch.
- Find the energy per unit length of the knitted swatch using the swatch energy per unit length vs. strain data obtained earlier.
- Multiply this swatch energy per unit length by the initial swatch length to obtain the measured swatch energy.
- Compare the model-based computed swatch energy with the measurement-based computed energy.

Acquiring force vs. displacement data

We measured the mechanical properties of a Merino wool yarn (Supra Merino, Silk City Fibers, New Jersey) with 3.5 twists per centimeter. Samples of the yarn were placed into a Shimadzu load frame, using capstan grips specifically suited for testing of yarns. The distance from grip to grip was 250 mm. The yarns were then pulled to breaking at a rate of 0.01 meters per second. This speed, which is close to the maximum speed for the Shimadzu load frame (max speed 0.016 m/s), was chosen to be as similar as possible to manufacturing speeds available on Shima Seiki weft knitting machines (minimum speed of 0.03 meters per second). Force and displacement data was recorded. See Figure 4 for the testing equipment and the results of measuring ten yarn samples.

The force vs. displacement data from four jersey fabric samples stretched in the wale direction is shown in Figure 5, with the displacement normalized to strain (mm/mm). It can be seen that each of the curves are well matched to the others, demonstrating consistent deformation behaviors.

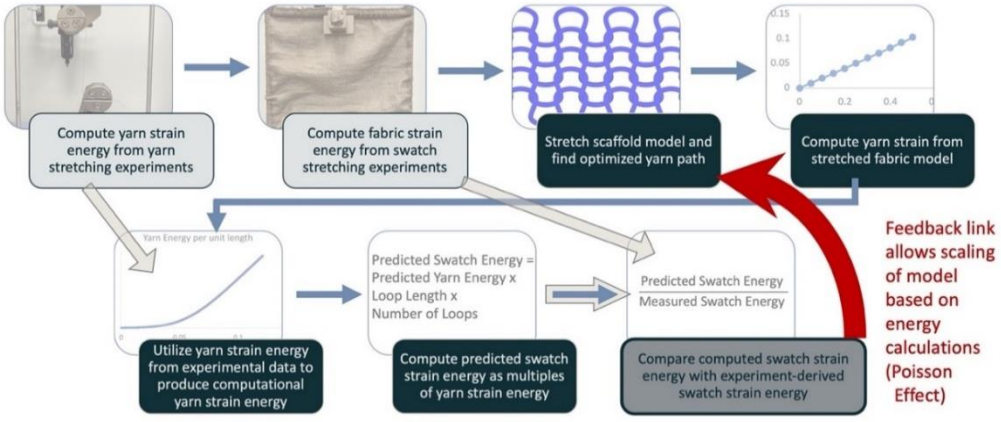

Figure 3. Process for computing fabric stretching energy using helicoid scaffolds.

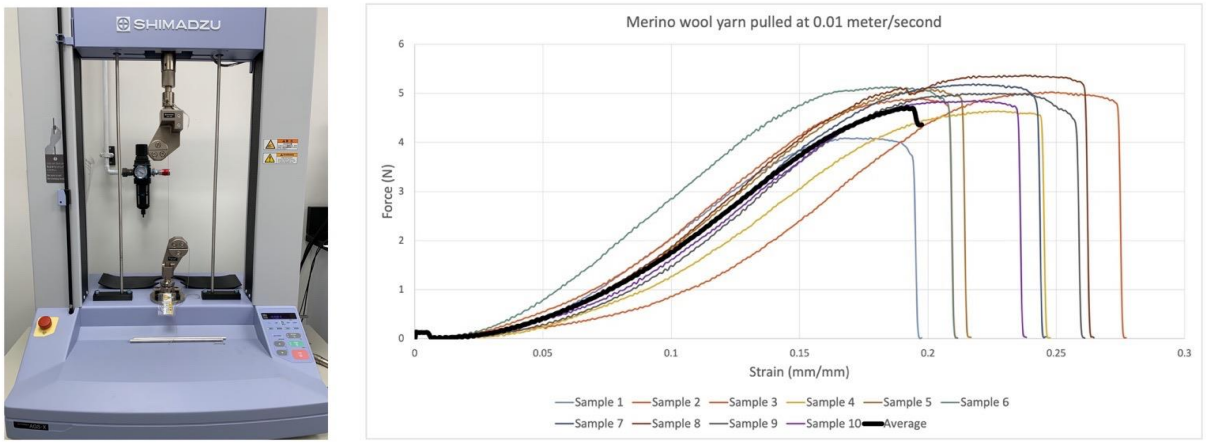

Figure 4. (Left) Merino wool yarn loaded in capstan grips on the Shimadzu load frame. (Right) Force vs. strain data for 10 samples of Merino wool yarn.

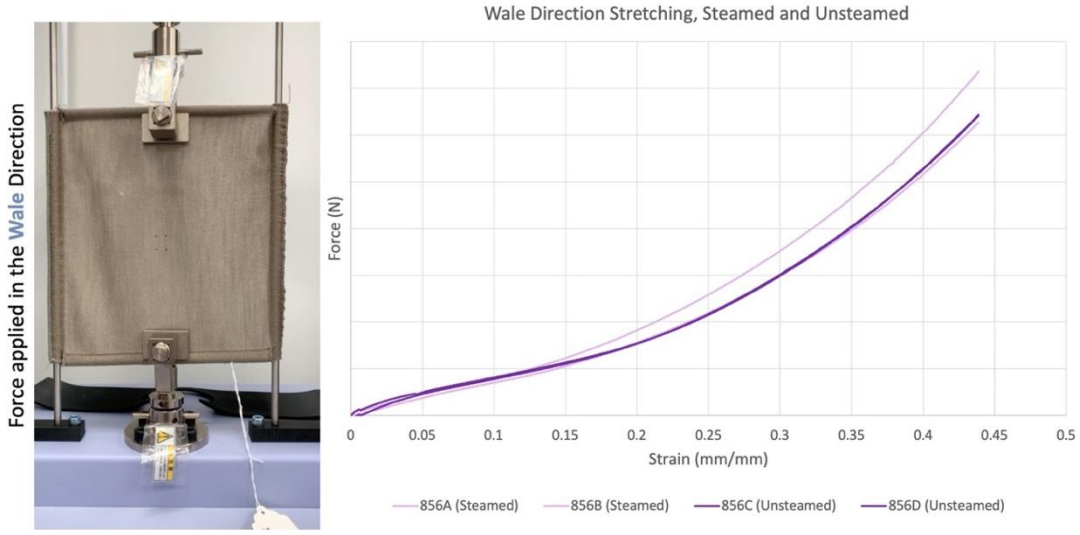

Figure 5. Stretching a single Jersey fabric with Merino wool yarn in the wale direction; (Left) experimental setup, (Right) force vs. strain data.

Computing yarn and swatch deformation energy

From the averaged force vs. displacement curves of the yarn, we can compute the force vs. strain values by dividing the displacement by the rest length of the yarn. Integrating force with respect to strain, which is effectively finding the area under the force vs. strain curve, gives us energy per unit length of the yarn.

This is then multiplied by the yarn length to obtain the energy in a stretched yarn. This approach allows us to now measure the stretching behavior of actual yarns and incorporate their measured behavior in our computational models.

The process of computing the measured swatch energy is similar to that of the yarn energy. We stretch the swatch in the wale direction and plot the force vs displacement curve for this stretching. This is then converted to a force vs. strain curve by dividing the displacement by the total wale length of the swatch at rest. The area under this curve gives us energy per unit wale length of the swatch for a given strain.

Generating and stretching the helicoid model

Given the loop scale parameters that are derived from the physical swatch, a yarn-level helicoid-based geometric model is computed using the methods described in previous sections and [5,6]. The shape of the yarn arises from its interaction with the helicoid scaffold. For a fixed set of strain values, the scaffold is stretched by the associated scale values in the wale direction, and the yarn model is updated. See Figure 6. In order to adjust the model for the Poisson Effect, the model should be scaled in the direction orthogonal to the plane of the fabric. The method utilized to compute this scale factor is described in Adjusting fabric thickness section.

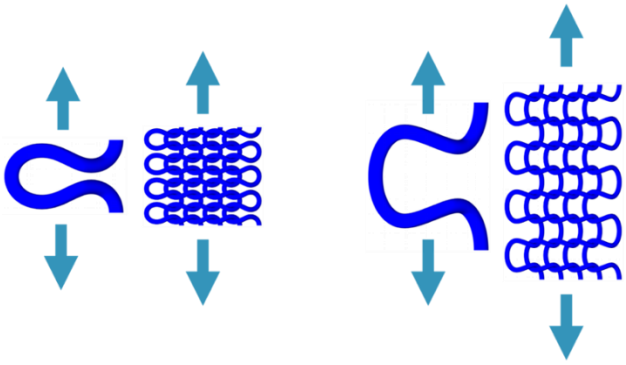

Figure 6. Stretching the helicoid yarn model in the wale direction.

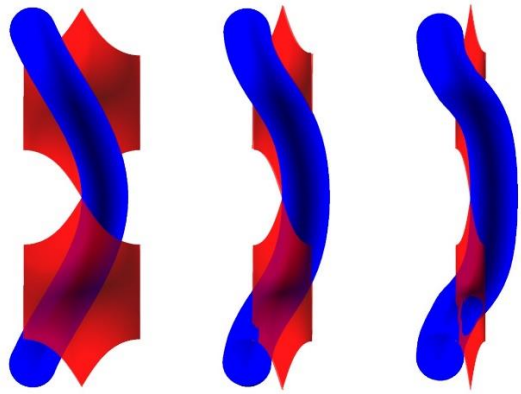

Figure 7. Effect of reducing scaffold thickness on loop shape and length.

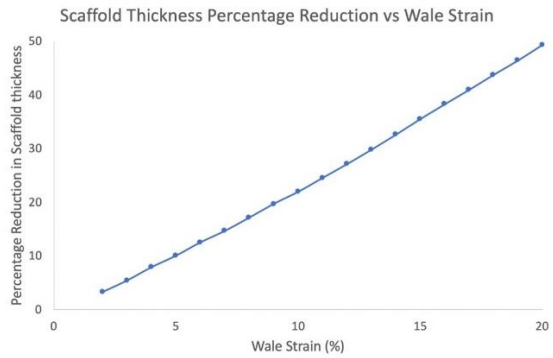

Figure 8. Scaffold thickness changes required to match the computed energy values to the measured values.

Computing swatch stretch energy from yarn stretch energy

The length of the yarn through the fabric model is calculated both before and after the model is stretched, providing yarn strain vs. fabric strain data, as seen in the upper right block of Figure 3. The helicoid scaffold model plays a critical role in this step, allowing us to determine how much the yarn deforms as the fabric is stretched.

In the bottom left block of Figure 3, the experimental yarn strain data is combined with the computational yarn strain data to produce a data-derived yarn strain energy curve. The computed scaffold geometric model tells us how much the yarn strains during fabric stretching, the experimental yarn strain data then allows us to compute the amount of energy needed to stretch the yarn. In the next step, the predicted swatch energy is computed by multiplying the length of a single loop, which is computed from the scaffold-based geometric model, by the predicted yarn strain energy, which gives us the energy needed to deform a single loop of yarn as the fabric is stretched. Multiplying this loop-level energy by the number of loops in the modeled swatch produces the predicted total energy needed to stretch the fabric sample.

In the final step the predicted swatch energy computed from the yarn-data-derived model is compared to the deformation energy that is based on the experimentally acquired swatch strain data. When this ratio is 1, the energy computed from our model exactly matches the energy that is acquired from measuring the associated fabric sample.

Adjusting fabric thickness

In our initial experiments, we produced computational swatch stretch energies that matched the measured swatch energies to within a factor of 2, except when the fabric strain exceeded 15%, where the ratio of computed and measured energy was over 6. We hypothesized that the main source of this high-strain anomaly was the absence of accounting for the Poisson Effect in the stretched computational model. To address this deficiency, we reran our computational pipeline and additionally adjusted the scaffold thickness to model the fabric thinning that occurs during stretching. See Figure 7. For each strain increment the scaffold thickness was decreased, with the yarn geometric model being accordingly modified. The scaffold thickness that produced an exact match between the computed and measured swatch energies was determined. This link, shown with the red arrow in Figure 3, forms a feedback loop that guides the adjustment of the thickness value.

Table 1 contains some of the derived data from this task, showing the percentage reduction in scaffold thickness needed for various strain increments to produce the desired exact energy matches. Figure 8 presents a plot of all our percentage reduction of scaffold thickness vs. wale strain data. The data is observed to be linear with a very high R^2 value of above 99.8% in all the cases that were tested. The equation of the least-squares line fit to the data in Figure 8 is

$$\%\ \text{thickness reduction} = 2.6 \times \text{wale strain} - 3.2. \quad (9)$$

Table 1. Scaffold thickness reduction required to match the measured energy for different swatch strain values.

Swatch Strain [%]	Percentage reduction in scaffold thickness	Ratio of computed swatch energy values to measured swatch energy values
5	10.05	1.00
10	21.97	1.00
15	35.50	1.00
20	49.36	1.00

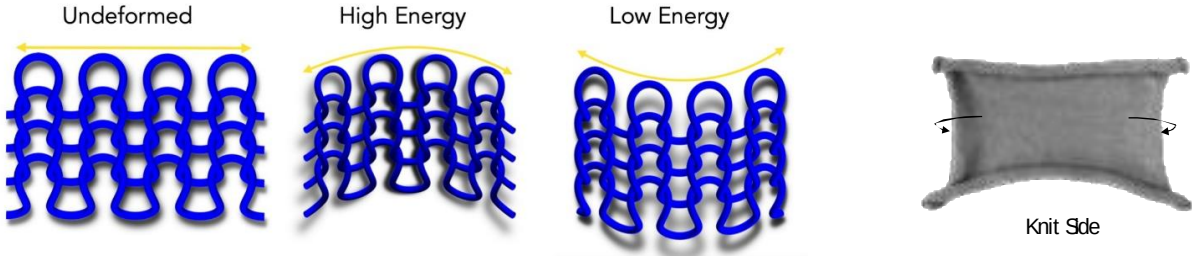

Figure 9. (Left) Generalized energy for two knit structure deformation modes. (Right) Natural curling of a single Jersey knitted fabric.

The relation between the change in thickness of the fabric with respect to its stretching is similar to the Poisson Effect in solid materials. The linear relationship between swatch thickness reduction and wale strain provides encouraging evidence that our approach may be utilized to predict fabric deformation energies.

DISCUSSION

The helicoid-based approach to estimating mechanical behavior demonstrates a number of advantages over more conventional methods. It shows promise for computing physical quantities of weft-knitted fabrics purely based on geometric calculations. Utilizing a helicoid, a type of minimal surface, as a scaffold for defining the topology and geometry of weft-knitted fabrics allows for the rapid calculation of yarn geometry, fabric deformation and deformation energy. These quickly produced results could support extensive exploration of the fabric's design space in a short amount of time. While the helicoid-based approach to estimating mechanical behavior of weft-knitted fabrics shows promise, it also clearly has several deficiencies. The swatch-level stretching energy calculations completely rely on the change in yarn length during fabric deformation, and do not include yarn bending energy and friction; two quantities that certainly affect knitted fabric mechanical behavior. It is notable though that experimental results can be computationally reproduced by just taking into account yarn stretching energies. It is also important to note that our results have been produced under low fabric strains, and it is anticipated that the relationship between yarn stretching energy and swatch stretching energy may change at higher strains, requiring additional model features and parameters for accurate prediction.

Finally, the helicoid-based approach provides a qualitative framework for analyzing and understanding the structural properties of knitted fabrics. For example, the approach readily explains, through an energy-based analysis, the curling behavior of knitted fabrics (Figure 9). Applying circular deformations to a single Jersey model and computing the total yarn stretching energy shows that bending backwards produces a lower energy configuration, compared to a flat and forward bent fabric; thus, explaining the natural curling behavior of the fabric, as seen in Figure 9 (Left). This conclusion can be reached purely through a geometric calculation and does not require a computationally intensive dynamic simulation.

CONCLUSIONS

We have presented the mathematics and algorithms needed to utilize the helicoid, a bicontinuous, minimal surface, as a scaffold for defining the topology and geometry of yarns in a weft-knitted fabric. The geometry of a half-loop of yarn is specified as a geodesic path along the surface with fixed boundary conditions. This optimized path may be duplicated, reflected, and shifted to produce the centerlines for the multiple stitches that make up a fabric. The approach provides a promising framework for estimating the mechanical behavior/properties of weft-knitted fabrics. For example, fabric stretching energy may be estimated by scaling the helicoid scaffold, computing new yarn paths, determining the amount of ensuing yarn stretch, and computing the total amount of yarn stretching energy based on measurements of actual yarns. The total computed swatch stretching energy has been calibrated with the energy needed to stretch an associated actual knitted

fabric. Additional research is required to advance the method towards a deployable design tool.

Acknowledgement: *This work was financially supported by the US Army Manufacturing Technology Program (US Army DEVCOM) under Agreement number W15QKN-16-3-0001. Additional support was provided by National Science Foundation grant CMMI #1537720 and Simons Foundation Investigator Grant #291825.*

REFERENCES

1. Casafranca J.J., Cirio G., Rodrıguez A., et al.: Mixing yarns and triangles in cloth simulation. Computer Graphics Forum (Proc. Eurographics), 39, 2020, pp. 101-110. https://doi.org/10.1111/cgf.13915
2. Cirio G., Lopez-Moreno J., Otaduy M.A.: Yarn-level cloth simulation with sliding persistent contacts. IEEE Transactions on Visualization and Computer Graphics, 23, 2017, pp. 1152-1162. https://doi.org/10.1109/TVCG.2016.2592908
3. Counts J.: Knitting with Directed Graphs. Master's thesis. Massachusetts Institute of Technology, 2018.
4. Eberhardt B., Meissner M., Strasser W.: Knit fabrics, in: House, D., Breen, D. (Eds.), Cloth Modeling and Animation. AK Peters. chapter 5, 2000, pp. 123-144. https://doi.org/10.1201/9781439863947
5. Kaldor J.M., James D.L., Marschner S.: Simulating knitted cloth at the yarn level. ACM Transactions on Graphics (Proc. SIGGRAPH), 27(65), 2008, pp.1-9. https://doi.org/10.1145/1399504.1360664
6. Kaldor J.M., James D.L., Marschner S.: Efficient yarn-based cloth with adaptive contact linearization. ACM Transactions on Graphics (Proc. SIGGRAPH), 29(105), 2010, pp. 1-10. https://doi.org/10.1145/1833351.1778842
7. Knittel C.E., Tanis M., Stoltzfus A.L., et al.: Modelling textile structures using bicontinuous surfaces. Journal of Mathematics and the Arts, 14, 2019, pp. 331-344. https://doi.org/10.1080/17513472.2019.1651891
8. Lagrange J.L.: Essai sur une nouvelle methode pour determiner les maxima et minima des formules integrales indefinies. In: Miscellanea Taurinensia II., 1772, pp. 173-195. https://doi.org/10.3931/e-rara-877
9. Lin H., Zeng X., Sherburn M., et al.: Automated geometric modelling of textile structures. Textile Research Journal, 82, 2012, pp. 1689-1702. https://doi.org/10.1016/j.ijsolstr.2017.01.019
10. Liu D., Christie D., Shakibajahromi B., et al.: On the role of material architecture in the mechanical behavior of knitted textiles. International Journal of Solids and Structures, 109, 2017, pp. 101-111. https://doi.org/10.1016/j.ijsolstr.2017.01.019
11. Liu D., Koric S., Kontsos A.: A multiscale homogenization approach for architectured knitted textiles. Journal of Applied Mechanics, 86, 2019, JAM–19–1125. https://doi.org/10.1115/1.4045309
12. Liu D., Koric S., Kontsos A.: Parallelized finite element analysis of knitted textile mechanical behavior. Journal of Engineering Materials and Technology, 141, 2019, MATS–18–1132. https://doi.org/10.1115/1.4043615
13. Meissner M., Eberhardt B.: The art of knitted fabrics, realistic & physically based modeling of knitted fabrics. Computer Graphics Forum (Proc. Eurographics), 17, 1998, pp. 355-362. https://doi.org/10.1111/1467-8659.00261
14. Plateau J.: Statique Expérimentale et Théorique des Liquides Soumis aux Seules Forces Moléculaires. Paris: Gauthier-Villiard, 1873. https://doi.org/10.3931/e-rara-10182
15. Poincloux S., Mokhtar A.B., Lechenault F.: Geometry and elasticity of a knitted fabric. Physical Review X, 8, 2018, 021075 p. https://doi.org/10.1103/PhysRevX.8.021075
16. Santangelo C., Kamien R.: Triply periodic smectic liquid crystals. Physical Review E, 75, 2007, 011702 p. https://doi.org/10.1103/PhysRevE.75.011702
17. Sperl G., Narain R., Wojtan C.: Homogenized yarn-level cloth. ACM Transactions on Graphics (Proc. SIGGRAPH), 39(48), 2020, pp. 1-16. https://doi.org/10.1145/3386569.3392412
18. Wadekar P., Goel P., Amanatides C., et al.: Geometric modeling of knitted fabrics using helicoid scaffolds. Journal of Engineered Fibers and Fabrics, 15, 2020, pp. 1-15. https://doi.org/10.1177/1558925020919350
19. Wadekar P., Perumal V., Dion G., et al.: An optimized yarn-level geometric model for finite element analysis of weft-knitted fabrics. Computer Aided Geometric Design, 80, 2020, 101883 p. https://doi.org/10.1016/j.cagd.2020.101883
20. Wadekar P., Amanatides C., Kapllani L., et al.: Geometric modeling of complex knitting stitches using a bicontinuous surface and its offsets. Computer Aided Geometric Design, 89, 2021, 102024 p. https://doi.org/10.1016/j.cagd.2021.102024
21. Witkin A, Fleischer K, Barr A. Energy constraints on parameterized models. In: Proc. ACM SIGGRAPH, July 1987, pp. 225-232. https://doi.org/10.1145/37401.37427
22. Wu K., Gao X., Ferguson Z., et al.: Stitch meshing. ACM Transactions on Graphics (Proc. SIGGRAPH), 37(130), 2018, pp.1-14. https://doi.org/10.1145/3197517.320136
23. Yuksel C., Kaldor J.M., James D.L., et al.: Stitch meshes for modeling knitted clothing with yarn-level detail. ACM Transactions on Graphics (Proc. SIGGRAPH), 31(37), 2012, pp.1-12. https://doi.org/10.1145/2185520.218553

PYTEXLIB – OPEN SOURCE PYTHON LIBRARY FOR SCRIPTING TEXTILE STRUCTURES

KYOSEV, YORDAN*; NAAKE, ANSELM AND SCHMIDT, ANN-MALIN

Institute of Textile Machinery and High Performance Material Technology, Faculty of Mechanical Science and Engineering, TU Dresden, Hohe Strasse 6, 01069 Dresden, Germany.

ABSTRACT

This work presents a small, minimalistic, pure Python based open source library, which was designed to simplify the parametric creation of textile structures. The library comes as result of long years of teaching modelling of textiles at master and PhD level, where the difficulties with all existing packages and the learning outcomes from such one course were considered. The idea of the library is that the students learn at the same time first steps of programming Python using small library, it is running on any operation system and from other point of view, the user is able to concentrate on the textile architecture, not getting lost in the coding style, data structures etc. PyTexLib is used since 4 years successful in the education at TU Dresden and in WE-TEAM program and is available as open source at GitHub.

KEYWORDS

Modelling; Textile structures; Library; Open source; 3D modelling; Python.

INTRODUCTION

There are many professional CAD packages for automatic creation of textile structures, which cover single type or groups of textiles. For weaving – there are more than 20 CAD packages [1], which creates photorealistic simulation of the fabrics and can export machine data, but only few of these can provide real 3D data for FEM simulation or other analysis of the structures (as pore size, CFD, etc.). Only WiseTex provides mechanical computations of the minimal potential energy of the yarns in order to provide mechanically correct geometry [2]. For knitted structures the CAD packages are very limited. Both leading machine producers Stoll and Shima Seiki have excellent photorealistic representations of the weft knitted structures, but 3D view can be generated only by the software of Shima Seiki, but until now is no reported any export option for more simulations. Several types of weft knitted structures and warp knitted structures and as well braided can be generated in 3D and exported to various format by the software of company TexMind (https://texmind.com/). These are convenient for work and export, but are as well limited to the programmed structures inside. Only the software TexGen [3] is open source, which allow scripting and creation of custom structures. Actually, there are few shortcomings working with TexGen which have prevented the authors of using it in the research and caused the creation of a new library. Once problem is, that TexGen works fine with unit cells, but is (or at least during the last year was) not capable to operate fast with large structures with more yarns and filaments (like knitted). The second problem is, that it is GPL Licensed and any advances of the software have to remain GPL License, which is potential problem in case of performing applied research together with industrial partners. Another, third problem is, that although TexGen can be compiled on MACOS and Linux, it does not provide direct installation files for such systems, which was causing troubles during the education of students in a classroom.

Based on this analysis and experience the authors decided in the past to develop small (minimalistic), open access, pure Python based library for scripting textile structures, which can be effiziently used in the education and for creation of complex or custom structures, which are not covered in the packages of TexMind or else. This was already successful applied in one PhD thesis [4] [5]. In the education of the WE-TEAM master students (https://we-team.education/) during the course of Computation Sciences and Engineering Principles for Textiles and during the lectures at TU Dresden.

LIBRARY STRUCTURE

Python was chosen as language, because it is currently wide used, free, open source and available on all systems. The library is hosted on GitHub

* **Corresponding author:** Kyosev Y., e-mail: *Yordan.kyosev@tu-dresden.de*

(https://github.com/virtualtextiles/pytexlib) and a MIT License was chosen, so that any person is free to use it and apply in any projects – public and commercial, without any limitations.

The goal is to have simple library for creating textile structures, where the develop concentrates on the textile and not on the programming structures in Python. For this several classes were developed:

The ***fibre*** class (file fiberlib.py) is the basic class in the library in the same way as the fibers are the basic elements of all fiber based structures. Each fiber is at the current state with circular cross section and has defined fibre diameter d, colour with the red, green and blue values and has list of coordinates of the fibre axis. The generation of fibre with two points of the axis is as simple as follows:

```
fi=fiber()
fi.diameter=0.2
fi.setcolour(123,23,230)
fi.append_point(1.0,2,3)
fi.append_point(12.0,2,3)
```

The first line constructs new fiber "*fi*". The second and third lines specify its diameter and color. After that the developer has to add points with their *x*, *y*, *z*, coordinates and can use not only numbers, but as well parameters with all possible options of the Python syntax.

Before one fibre is assigned to a yarn (or other structure), this has to be created by the constructor

```
ya=yarn()
```

In this case as yarn can be created as well non-woven structure, the meaning of one yarn is that it represents ***a group of fibers***.

Adding the fiber is then one simple line:

```
ya.add_fiber(fi)
```

Analogously, the yarn has to be assigned into textile structure

```
t=textile()
```

and added there

```
t.add_yarn(ya)
```

With these steps, the textile structure with one yarn and one fiber is ready and can be saved into CSV file

```
t.write_file("mysample.csv")
```

so that this can be visualized by the TexMind Textile Viewer (free software), used as wellin the book Warp Knitting Fabrics Construction [6] and can apply all types of exports (for instance LS-Dyna, Abaqus, Ansys, gltf, STL, x3d etc, Wisetex, Texgen script) in the standard TexMind packages.

The structure can be visualized by the simple command:

```
t.plot()
```

DISCUSSION POINTS WITH OPEN ISSUES

The current library does not contain class for "groups of yarns" which is the case for all ply yarns. Actually two- and three-ply yarns are used very often and even more than the single ply yarns. Additionally, contrary to the structures in the software and the data formats of TexMind for instance, there is no implemented class for groups of (ply) yarns. Such grouping helps significantly for selection and visualization of warp or weft yarns only at woven structures, or different systems of multilayer woven structures (upper layer, bottom layer, connecting warp etc.). Such grouping is efficient in the warp knitting, too, where each guide bar represents separated group of yarns. Both the ply yarns and group of yarns represents two levels of lists of existing objects. During the creation of the library the developers decided initially to skip these levels, in order to simplify the coding. Because in the case of structure with single yarn, it has to be added into ply yarn with one yarn, and this ply yarn has to b added to a group of yarns, which could contain only one yarn, too, if all levels have to be represented. One alternative option for sorting, which is less efficient but more convenient for beginners is the adding of attributes like "Ply Yarn ID" or "Yarn Group ID", which can be used internally for searching and sorting and visualization of the objects from one group without the need of implementation of two more levels of grouping.

Another aspect is the 3D visualization of the structures. At the current time one option is the export of the geometry as text file with specific format (CSV) and visualization with the free TexMind Viewer. This visualization is better than the using only the 3D axis. The integration of the 3D visualization of the library is possible but had some disadvantages during the teaching. One very powerful 3D library is vtk, actually used in TexMind Viewer. Vtk can be used in Python, too, but requires C++ compiler during the installation. This requires often administrative rights and was trouble for the installation in classroom environments. A very nice and simpler to use, compared to vtk library

Figure 1. Objects in PyTexLib. The red objects are not implemented for simplicity at the current time

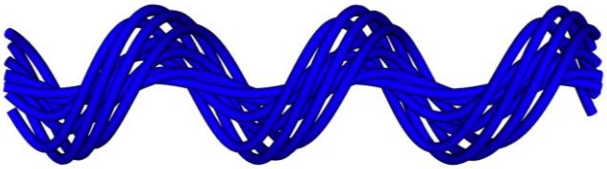

Figure 2. Created yarn with spiral effects within PyTexLib.

are pyVista, open3D, or Vedo. They actually all present python warping of vtk, and this brings the same troubles as vtk itself. The authors are looking at the current time for suitable, pure python based 3D library for visualization, which has as less dependencies as possible and works on multiple platform without needs of administrative rights at this point.

RESULTS

Figure 2 presents one example of a multifilament yarn created with PyTexLib. This is a yarn with spiral effects, where some core filaments are placed almost straight in the middle of the structure and the remaining filaments are around these. The generation is done within 14 lines of code for this structure, (not considering the PyTexLib and the visualization libraries itself).

CONCLUSIONS

The new open source python library PyTexLib allows quick start in creating 3D geometries of textile structures. It requires only basic understanding of programming and elementary syntax in order to implement parametric geometric models into 3D visualizations. It can be a good tool for quick start in the 3D modelling of textile structures, especially for such structures, which are not covered in the available CAD packages.

REFERENCES

1. Kyosev Y.: Simulation of wound packages, woven, braided and knitted structures. In Veit D., (Editor), Simulation in Textile Technology, Woodhead Publishing, 2012. https://doi.org/10.1533/9780857097088.266
2. Lomov S.: Modeling the geometry of textile composite reinforcements: WiseTex. In: Boisse Ph. (Editor): Composite Reinforcements for Optimum Performance (Second Edition), Woodhead Publishing, 2021. https://doi.org/10.1016/B978-0-12-819005-0.00007-1
3. Brown L.P.: TexGen, in Advanced Weaving Technology, Y. Kyosev and F. Boussu, Editors. Springer International Publishing, 2022, Cham. pp. 253-291. https://doi.org/10.1007/978-3-030-98160-9_8
4. Storck JL, Gerber D, Steenbock L, et al.: Topology based modelling of crochet structures. Journal of Industrial Textiles, 52, 2022. https://doi.org/10.1177/15280837211073429
5. Storck J. L., Feldmann B. A., Kyosev Y.: Design tool for automated crocheting of fabrics. Communications in Development and Assembling of Textile Products, 4(2), 2023, pp. 254–272. https://doi.org/10.25367/cdatp.2023.4.p254-272
6. Kyosev Y.: Warp knitting fabrics construction. CRC Press, 2019. https://doi.org/10.1201/9780429026864

THE RESISTANCE OF FIBER-REINFORCED 3D PRINTED STAB-PROOF ARMOR ELEMENTS: MATERIALS, GEOMETRIES, DIMENSION AND ORIENTATION

SITOTAW, DEREJE BERIHUN[1*]; MUENKS, DOMINIK[1] AND KYOSEV, YORDAN KOSTADINOV[2]

[1] Ethiopian Institute of Textile and Fashion Technology, Bahir Dar University, Bahir Dar, Ethiopia
[2] Chair of Development and Assembly of Textile Products, Institute of Textile Machinery and High Performance Material Technology, Faculty of Mechanical Science and Engineering, TU Dresden, 01069, Dresden, Germany

ABSTRACT

The majorities of stab protective armors limit several comfort parameters such as locomotion, movement, respiration, flexibility and weight which determine the efficient use by officers. Lightweight and effective protection with the necessary comfort parameters such as flexibility, respiration and free locomotion through the development of three dimensional printed (3DP) scales based on natural armors from fibers using continuous filament fabrication is the main objective of this research. In this study, stab protective armor scale-like elements with different materials, shapes, sizes and portions of a part investigated against stabbing force. Onyx, Aramid, carbon and different ratio Onyx/Kevlar by inserting fiber at different fiber filling angles $(0/45/90/135)_N$ were used in this investigation. The specimens were tested according to VPAM KDIW 2004. The result revealed that the scales with Onyx, Kevlar/Onyx and Kevlar fiber-reinforced protective scales failed while the carbon fiber resists the puncturing energy level K1 (25 J) with the penetration depth less than the maximum allowable penetration depth of the knife through the protectors. The large size protective elements and rectangular geometries withstand the impact energy relative to triangular geometries. The result revealed that the material type, its alignment, size and shapes of protection elements and portions of the scales where the weight dropped significantly influence the resistance against the impact energy to puncture with the intended energy level and sharp tipped knife.

KEYWORDS

Protection armor; 3D printed scales; Impact energy; Penetration depth; Fiber-reinforcement; Geometries and their sizes; 3D printing; Stab protection.

INTRODUCTION

Protective clothing is one of the most important pieces of safety equipment to save lives. A stab resistant vest is a reinforced piece of body armor designed to resist knife or needle attacks specifically to the upper part of the body (chest, back and sides) and it can be worn either as covert or overt.

Early humans used comparatively primitive armors which were manufactured out of metal, horn, wood or leather lamellae [1] [2] but as civilizations evolved and knowledge advanced, body armor introduced. Then in the last century, with its two world wars, various attempts were made to advance the technology of body armor [1]. It was reported that the first soft body armor was developed by the Japanese and in that instance, was made of silk and was most effective against low-velocity bullets [3]. Thus the first so-called bullet-proof vests were designed in America in the two decades following World War I [4] [5] while the modern police body armor was introduced into practice in the 1970s [6].

Security officers are stabbed everywhere during their duty shift and most of the stabbed officers are killed immediately after stabbing by the suspected assailants. As the news and reports showed that the number of stabbed officers increased from year to year in developed countries, for example, in United states of America, Germany, United Kingdom, but the stabbing frequency is more in developing, Saharan and sub Saharan countries [7-15]. The main reason for fatal injury is the officer's negligence to wear protective armor vest during their duty shift because most armor vests are heavy, non-permeable and reluctant mode of the officers. With all these limitations of most of the current armor vests police officers, military, transport and correction administrators should encourage their staffs to wear stab vests during the whole duty shift to save them from a fatal injury if stabbed in torso [16]. Armor vests

* **Corresponding author:** Sitotaw, D.B., e-mail: *dere96@yahoo.com*

might not be universal but has to be designed according to the level of protection, type of weapons and techniques of stabbing by assailants in the region with the desired comfort. The level of protection required in soft and sensitive bodily regions is determined by the type of attacks that are likely to be encountered [17]. The design of appropriate stab vests with the desired level of protection can be challenging for a wide range of weapons which are used for puncture and the stabbing techniques are different depending on assailants [18].

Though protection and comfort are conflicting, body armors for stab protection should also consider [19] flexibility and other ergonomic issues for acceptance along with coverage and duration [20-22].

The selection of advanced materials (both for performance and comfort) and appropriate armor design should ideally allow the flow of excessive metabolic heat away from the body (thermo-physiological property) which can be reflected by a combination of air permeability, thermal resistance, and moisture evaporation [23-25]. The garment should be able to transfer heat and moisture away from the skin to the atmosphere [25-27]. Tactile comfort, the feel or sensation on the skin when worn should be considered during design of protection gear [28] [29].

The use of body armor has always been an issue when ease of body movement and cognitive functions are considered [30, 31] and should not be drastically compromised by the design of the body armor [22]. Many biological systems possess hierarchical and fractal-like interfaces and joint structures that bear and transmit loads, absorb energy, resist puncture and accommodate growth, respiration and/or locomotion [32], which are determined by their geometry [33-35]. In the case of bio-inspired flexible protection, natural segmented armors from fish, alligator, snake, tonicella marmoreal, pangolin, scaly foot gastropods, arapaima or armadillos are attracting an increasing amount of attention because of their unique and highly efficient protective systems to resist mechanical threats from predation, while combining hardness, flexibility, breathability, thinness, puncture-resistance and lightweight [35-40]. These natural armors, which inspired researchers because of their diversity of geometrically structured interfaces and joints, are found in biology, for example in armored exoskeletons [41] [42], the cranium [33] [34], the turtle carapace [43] and algae [44].

Learning by imitation and further by linking all the data has probably been one of the most fruitful ways of development ever used. The extreme contrast of stiffness between hard scales and surrounding soft tissues gives rise to unusual and attractive mechanisms, which now serve as models for the design of bio-inspired armors. Despite this growing interest, there is little guideline for the choice of materials, optimum thickness, size, shape and arrangement for the protective scales [45].

The performance of 3D printed aramid FRP for stab resistance was studied for 2 mm, 4 mm and 6 mm thickness and the last two showed excellent performance for 25 J impact energy while 2 mm thick scales failed the puncturing test [46]. In this research, the scales are designed, developed and its performance is checked for energy level K1 (25 J) with a relatively low thickness, mass, production time and material usage as compared to the previous research result.

The aim of this research is to design and develop three dimensional (3D) printed stab resistant armor vest based on continuous filament fabrication (CFF) inspired by natural armors. The plan is to combine soft textile undergarment and hard stab protective elements in terms of fiber-reinforced plastic (FRP) of segmented scales. As a first step for the development of innovative stab protection clothing, the stab protection properties of 3D printed and fiber-reinforced functional elements are investigated based on material types, shape of the geometries of the scales and size of geometries, which are used for the development of a novel vest. The main novelty of this research is its comfort as studied and published in a reputable journal [47] by the same authors to this article. The comfort is found to be improved as compared to the current stab protective armor because the armor's protective elements in this research are segmented scales [47] without compromising the protection performance for the intended energy level, as investigated in this research in terms of material types and its alignment during 3D printing, geometry and size.

MATERIALS AND METHODS

Materials

3D printed stab protective elements in this research are produced as circular, quadrilateral and triangular scales with defined dimensions from thermoplastic composite filament (Onyx) and functional fibers such as Kevlar from aramid groups and carbon fibers with the mechanical properties shown in Table 1. Different blend layers ratio of fibers and plastics are used in Markforged Inc.'s Mark Two Desktop 3D printer [48] with its CFF process and two printing nozzles. One nozzle of the printer operates like a typical extrusion process to lay down a plastic filament that forms the outer shell and the internal matrix of the part. The second nozzle deposits a continuous strand of composite fibers such that carbon, Kevlar, glass and others on every defined layer [49] [50] inside a conventional fused filament fabrication (FFF) thermoplastic part [51].

The specimens were sliced at 0/45/90/-45 degrees of infill angles, with defined repetitions written as a subscript after the last bracket (see Table 2), using

Table 1. Mechanical properties of materials [48].

Properties	Onyx	Carbon	Kevlar
Tensile strength (MPa)	37	800	610
Tensile modulus (GPa)	2.4	60	27
Flexural strength (MPa)	71	540	240
Flexural Modulus (GPa)	3	51	26
Compressive strength (MPa)		420	130
Compressive modulus (GPa)		62	25
Density (g/cm^3)	1.2	1.4	1.2

(Association of Test Laboratories for Bullet Resistant Materials and Constructions, 2011)

Table 2. Materials arrangement inside the 3D printed scales.

No.	Material	Fiber angle (in degree-°) coding	Filling fiber layers over the total layer	Dimension	Shape
1	Onyx	No fiber		3 mm thickness and 50 mm diameter	Circular
2	50% Onyx/50%Aramid	$(0/+45/90/-45)_3/0/45/90$	15/30 = 50.00%		
3	27%Onyx/73Aramid	$(0/+45/90/-45)_5/0/45$	22/30 =73.33%		
4	Aramid	$(0/+45/90/-45)_7$	28/30 =93.33%		
5	Carbon	$(0/+45/90/-45)_5/0/45$	22/24 =91.67%		
6	Carbon	0/+45/90/-45	24/32 = 75%	100 mm x 100 mm x 4 mm	Quadrilateral plate
7			24/32 = 75%		Quadrilateral scales
8			24.59%		Triangular scales

Eiger.io online software by Markforged Inc. Table 2 displays the material arrangement, design, and setup of the printing process to determine the optimum protective scales with the minimum possible thickness for Energy Level 1, which is 25 joules and a 20mm allowable deformation depth [52] of the knife through the 3D printed protective element. The materials and their arrangement in the 3D printed scales are shown in Table 2. The material ratio, expressed in percent (%), is based on the number of layers of reinforcing fibers relative to the layers of the whole part, but not the material volume, because the material volume depends on the density of the materials per unit volume of the geometry. The remaining layers, not shown in some of the rows in Table 2, are made from Onyx.

Methods

The development of 3D printed scales begins with designing, followed by STL file generation in Autodesk Fusion 360 software. The generated STL file is then imported into Markforged Inc.'s online slicing software called "Eiger.io" to select the type of material, assign alignment composition for each layer of the final product, and arrange the materials accordingly before being transferred to the 3D printer. The samples used for this study are 3D printed from the materials listed in Table 1, with each sample having a specific ratio and filling alignment without symmetry.

The scales are designed to have a thickness of 3 mm and a diameter of 50 mm for material investigation. Additionally, various dimensions are explored, including quadrilateral scales with a thickness of 4 mm, triangular scales, and a square plate measuring 100 mm x 100 mm x 4 mm, for shape and size investigation. The designs of the target samples are illustrated in Figure 1A to Figure 1D, along with their corresponding standard triangle language (STL) files (Figure 1E) generated from Fusion 360.

Figure 2 illustrates the material arrangement of every layer in the 3D printed scales. The layers are arranged with different material filling angles to potentially enhance protection while reducing the overall weight of the armor element (scales). The fiber angle coding follows the standard lamination theory for composite part production. To clarify the arrangement, for example, (0/+45/90/-45)*N* signifies that a reinforcement fiber is printed *N* times sequentially in the 0, +45, 90, and -45 filling angles to complete the construction. The repetition (*N*) of the print layers angle is determined by the fiber diameter. For instance, a carbon fiber with a diameter of 0.125 mm is printed approximately *N* = 5.5 times for the mentioned reinforcement fiber angles, while a Kevlar fiber from the aramid group with a diameter of 0.1 mm is printed approximately *N* = 7 times for the mentioned fiber angles arrangement. The first and last layers default to thermoplastic materials, which in this study is Onyx.

Four specimens are produced, and three of them are tested for each sample following the test method of the Association of Test Centers for Anti-attack Materials and Constructions [52].

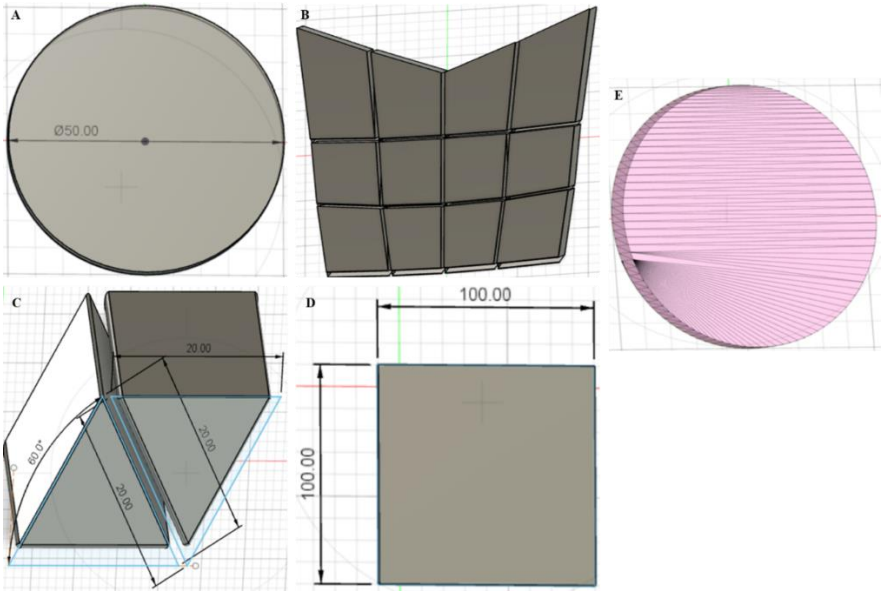

Figure 1. Designs generated from Fusion 360 A) Circular scale 3mm thick B) Quadrilateral scales 4mm thick C) Triangular scales 4mm thick D) Square plate 4mm thick E) STL file.

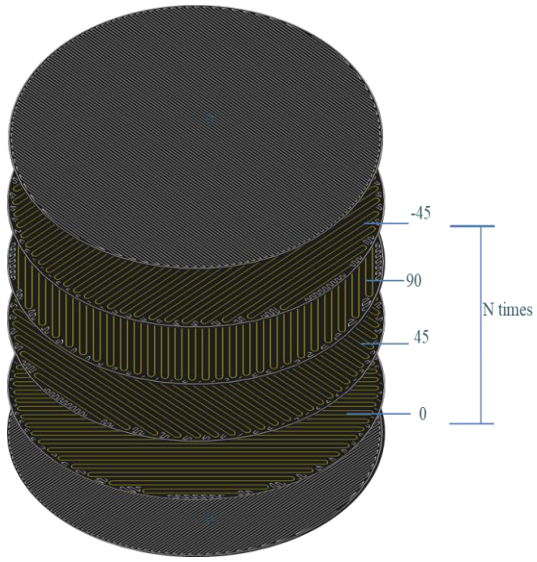

Figure 2. An example of material arrangement and printing order of polymers at filling angle $(0/+45/90/-45)_N$, generated from Eiger.io.

Experimental

The specimens are conditioned for a minimum duration of 24 hours at a temperature of 20 ± 2 °C and a relative humidity of 65 ± 5% [52]. The testing knife (blade), with specifications shown in Figure 3, is attached to the drop stand to test the resistance to puncture of the 3D printed scale-like armor elements. The dropping object, depicted in Figure 4a with the knife in Figure 4c, has a drop mass (*m*) of 2.51 kg, dropped from a height of 1.02 m at a speed (*v*) of 4.44 m/s, which is measured using an optical sensor to calculate the velocity right before impact. The kinetic energy (E_{kin}) applied to test the protection level of the specimens can therefore be calculated as follows:

$$E_{kin} = \frac{1}{2} m * v^2 = \frac{1}{2} 2.51\ kg * (4.47 \frac{m}{s})^{\ 2} = 25.07\ J$$

The kinetic energy used to test the specimens is 25.07 J, which is nearly identical to the specified energy in the corresponding inspection norm (K1=25 J) [52]. This energy level serves as an indicator of the specimen's protective performance, provided that the penetration depth does not exceed the standard allowable depth outlined in the norm.

The testing procedures in this study involve applying impact energy to the specimens to puncture and evaluate the performance of the armor scales against this energy. This process primarily consists of three steps: preparation of the testing setup (depicted in Figure 4, Figure 5A, and Figure 5B), puncture testing (Figure 5C), and measurement of the penetration depth (Figure 5E).

The dropping object is released from the suspension bar by pulling the rope with the holding hooked rod, causing the knife with the dropping weight to fall onto the 3D printed sample in a closed chamber (as shown in Figure 5C). Afterward, the dropped object, along with the impacted specimen, is removed from the plastiline box to measure the penetration depth of the testing knife through the scales (as illustrated in Figure 5E).

The relative alignment of the knife to the specimen with respect to the fiber filling angles $(0/+45/90/-45)N$ is random for all specimens, but the center of each scale of the specimens is aligned relative to the tip of the knife to avoid deflection of the specimen upon impact. Additionally, specimens with segmented scales and single plate protective elements are subjected to multiple drop tests at different parts of a sample made from carbon fiber reinforcement.

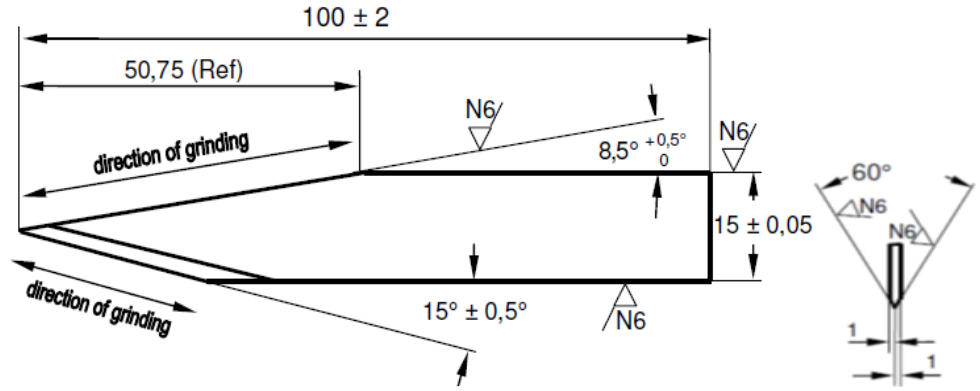

Figure 3. Geometry of the test blade P1/B (dimensions in mm) [52].

Figure 5. Test procedure of stab resistant scales using drop stand A) Leveling and center line of the plastiline B) Sample on the plastiline C) Dropped the knife with the weight D) Impacted object right after dropping E) dismantled the knife from the dropping object and measuring of the penetration depth of the knife.

Figure 4. Drop test stand with: a) Dropping weight b) Dropping weight fixing hook c) Knife d) Safety path e) Hook pulling rope f) Safety bar g) Specimen of plastiline h) Plastiline.

RESULTS AND DISCUSSION

As indicated in research results, the minimum organ distance from skin is pleura 22 mm, pericardium 31 mm, spleen 23 mm, kidney 37 mm, thoracic aorta 64 mm, abdominal aorta 87 mm [53] and liver 22 mm [54, 55]. The maximum penetration depth of the knife should be lower than the minimum distance of the organ from the skin. On the other side, the maximum penetration depth of the knife for energy level K1 (25 J) set by VPAM standard is 20 mm [52]. If the specimens allow the knife to penetrate deeper than the penetration depth set in the norm, then the samples are considered as failed to resist the specified impact energy level K1. As seen from Figure 6A - Figure 6E, the scales have shown different depths of the knife penetrated through the 3DP protective armor elements because of the type of reinforcement fibers, the fiber contents in the plates, the size of the scales and the shape of the scales.

As shown in Table 3, the influence of materials on the stab resistance at the intended energy level is investigated using various compositions: Onyx/Aramid (50% each), Onyx-27%/Aramid-73%, Kevlar-100%, Carbon-100%, and Onyx-100%. According to the test results, 50 mm diameter 3D printed carbon scales showed potential resistance against stabbing with a knife dropped at 25 joules of energy level 1. However, other materials investigated in this research demonstrated the worst potential against the same intended impact energy, resulting in fatal injury if used to develop protective armor with a 3 mm thickness and without symmetry of material

alignment during the 3D printing process. Carbon 3D printed scales do not allow the sharp tip of the knife to pass through, even for fractions of millimeters after the last layer of the 3DP protective scale, but the knife tip is deformed at every test.

The knife with the impact weight dropped on the 3D printed Kevlar scales fully passed through the plastiline with no resistance from the scale when it went through each of the aramid fiber layers. The main reason for this is the physical and mechanical properties of the materials, where the impact energy has a compression effect at first, then tensile and flexural effects. This means when an impact load is dropped on a specimen, it compresses the area, stretches it, and then deforms it. The material with the highest values for these parameters can relatively have high resistance against the intended impact energy. Carbon, with its 0.125 mm diameter, has the highest density, tensile, compression, and flexural strength and modulus (see Table 1), thus achieving the highest resistance against the intended impact energy.

The percentage of Onyx in the protective scales has no positive influence on resistance to the intended impact energy. Therefore, specimens with 3 mm thickness made from 100% Onyx and Kevlar from aramid fibers filled in the $(0/45/90/-45)_7$ degrees throughout the specimen have little to no resistance to puncturing because the penetration distance (>40 mm) is deeper than allowable within the testing standard [52]. Therefore, the analysis mainly focuses on the carbon and the Kevlar aramid fibers. Therefore, the analysis mainly focuses on carbon and Kevlar aramid fibers. The carbon fiber (Figure 6A) does not allow the tip of the knife to be seen behind the scale, even with fractions of a millimeter, while 100% Kevlar allows the knife to penetrate through the specimen without resistance to the impact energy (Figure 6B).

However, Kevlar with symmetry of material alignment (Figure 7) during printing showed potential resistance to the intended impact energy [56]. As the researchers reported in their paper, the symmetry of material alignment has a significant influence on the resistance to impact energy for stab protective armor. With this, Kevlar can withstand the intended impact energy when a 3 mm thickness of the scale is 3D printed with mirroring the other half thickness of the scale because half of the directions of the fiber alignment are totally opposite to the alignment of the other half fiber layers so that the running speed of the knife is disturbed during stabbing, resulting in low penetration depth.

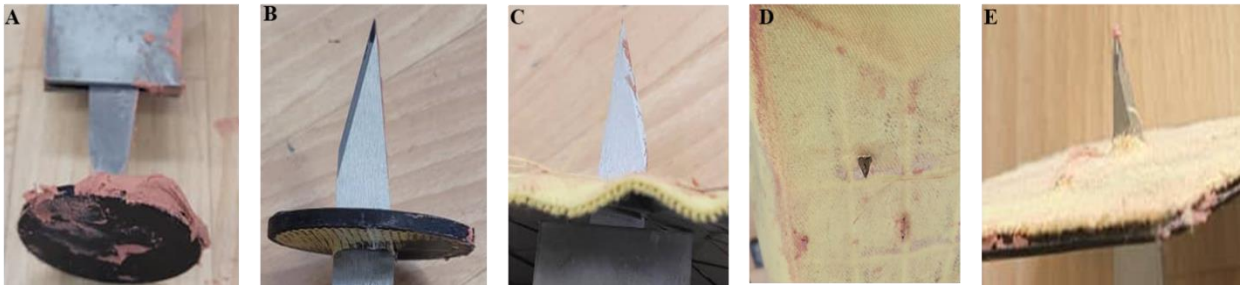

Figure 6. Appearance of scales right after impact; A) Carbon circular scale; B) Kevlar circular; C) Triangular plates; D) Quadrilateral scales on textiles E) Rectangular Plate.

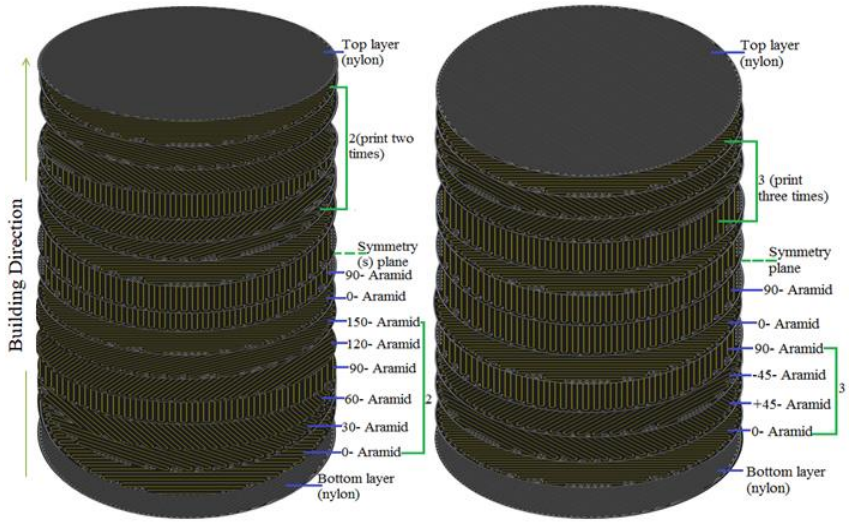

Figure 7. Example of material arrangement and printing order of aramid layers- at filling angles $[(0/30/60/90/120/150)2/0/90]_s$ and [(0/+45/90/-45)3/0/90]s, generated by Eiger.io o[56].

Table 3. Results of stab testing of FRP elements.

	Test runs	Penetration of knife in mm	Depth of plastiline deformation	Thickness	Plastic volume	Fiber Volume
Onyx/Aramid (50%)	1	44.86	16.61	3	3.9	2.12
	2	45.7	17.5	3	3.9	2.12
	3	46.21	20.45	3	3.9	2.12
	Average	45.59				
Onyx-27%/Aramid-73%	1	45.68	14.3	3	2.05	3.89
	2	46.22	18.37			
	3	43.18	15.07			
	Average	45.03				
Kevlar-100%	1	45.6	37.54	3	1.39	4.8
	2	42.25	41.12			
	3	39.45	53.43			
	Average	42.43				
Carbon-100%	1	0	64	3	1.46	4.53
	2	0	63.09			
	3	0	64.48			
	Average	0				
Onyx-100%	1	>48,5		3	5.81	
	2	>48,5				
	3	>48,5				
	Average	>48.50				
100x100mm Square Onyx-Carbon	1	20.65		4	11.92	26.79
	2	9.24				
	3	18.62				
	Average	16.17				
Quadrilateral Segments attached on textiles	1	30.63	No significant	4	17.83	24.46
	2	13.47				
	3	23.88				
	4	41.53				
	Average	27.38				
Triangular segments attached on textiles	1	41.93	No significant	4	38.24	12.47
	2	42.17				
	3	40.14				
	Average	41.41				

Figure 8 presents the 3D printed protective scales immediately after being impacted by the knife with the drop weight. The carbon fiber 3D printed protective armor element demonstrates extreme resistance to the intended stabbing energy from the drop weight. As seen from left to right in Figure 8A, the protection is perfect due to the carbon fiber's resistive reaction to the impact energy. The tips of the knives are bent, broken, and damaged in every cycle of the drop test on carbon fiber 3D printed scales (See Figure 11A to Figure 11C).

In contrast to this, the Kevlar 3D printed protective armor elements totally failed to save the wearer from fatal injury. As one views from left to right in Figure 8B, the viewer is shocked by the penetration depth of the knife through the scales because the Kevlar filaments are not able to resist the intended impact energy to puncture with the current infill angle alignment unless produced with symmetrical alignment for half of the thickness of a scale at $[(0/+45/90/-45)3/0/90]_s$ so that the penetration depth is reduced because each layer crosses over the other layer either diagonally or at a right angle to disturb the downward running of the stabbing knife with the impact load [56].

In addition to the materials, the shapes of the protective elements also have a significant influence on the penetration depth of the knife from the impact energy. The content of the reinforcement carbon fiber in triangular scales is lower than the content in the quadrilateral scales. Figure 9 presents the running distance and turning edges because the shapes of the geometries have a significant influence on the content of the fibers (blue lines in Figure 9A and Figure 9B) to be accumulated during printing. As viewed from Figure 9A, the impact load with the knife is not able to fully penetrate after puncture and saved the wearer from fatal injury with reduced penetration

Figure 8. Physical appearance of the 3D printed scales right after impacting drop weight on A) Carbon fiber B) Kevlar fiber from aramid group.

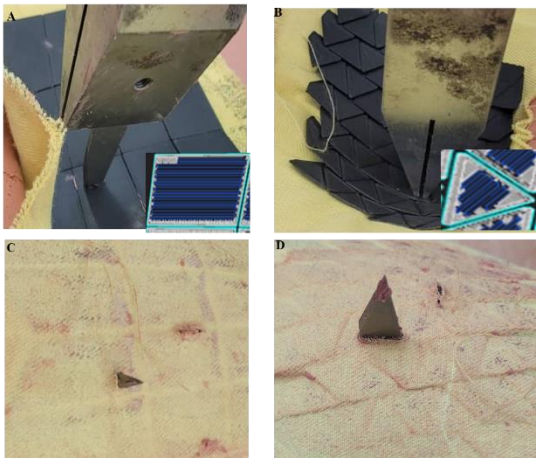

Figure 9. Appearance of the impact of drop knife on A) Quadrilateral scales B) Triangular scales and the penetration depth of knife through C) Quadrilateral D) Triangular scales.

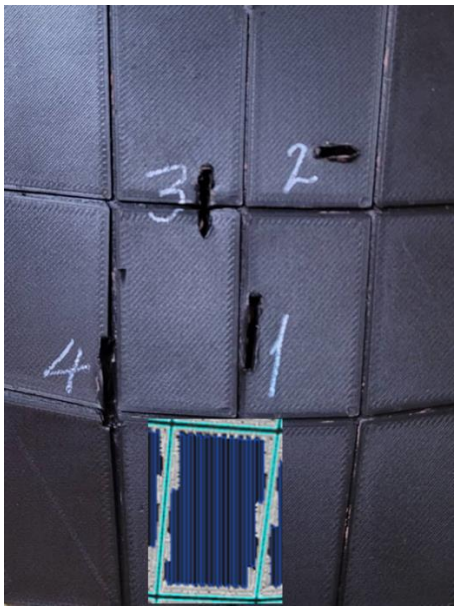

Figure 10. Appearance of the different parts of the scale right after puncture on the body (2), on the edges and joints (1, 3 and 4) of the protective elements.

depth (see Figure 9C). In contrast to quadrilateral geometries, triangular geometries allow the stabbing force with the knife to fully pass through the scales (Figure 9B) and result in fatal injury due to the shocking penetration depth of the knife (Figure 9D).

Another parameter investigated in this research is the size of the protective scales and its impact on resistance performance to stab impact energy. The size of the protective element refers to its surface area, classified as large (10,000 mm^2), medium (950-1,280 mm^2), and small size (640-750 mm^2) in this study. The large scale exhibited a penetration depth of 9.24 mm - 19.08 mm, the medium scale showed a penetration depth of 13.47 mm - 23.88 mm, and the small scales had a penetration depth greater than 30.63 mm observed during the experiment. The results showed that the sizes of the protective elements significantly influence the performance against puncture to penetrate through the scales (see Figure 6C and Figure 6E) due to the impact energy. The protection performance decreased as the dimensions of the scale became smaller. The difference in protection performance between the large scale and the small scale is akin to a saved life from fatal injury and life lost with fatal injury from the intended impact energy, according to standards and the minimum distance of sensitive organs from the skin [52-55]. The large size protective element bent the testing knife during the experiment, but the other sizes did not create physical damage to the testing knife. Previous research has revealed that the size of the protective element has an inverse relationship with comfort but is directly proportional to protection performance [56] [57] so optimization of comfort must be made without influencing protection performance.

The protection performance of the 3D printed scales also varies at different portions such as edges, joints, and the body of the protective element. As shown in Figure 10, a narrow puncture width is observed on the body (2), while a wider puncture hole is seen on the

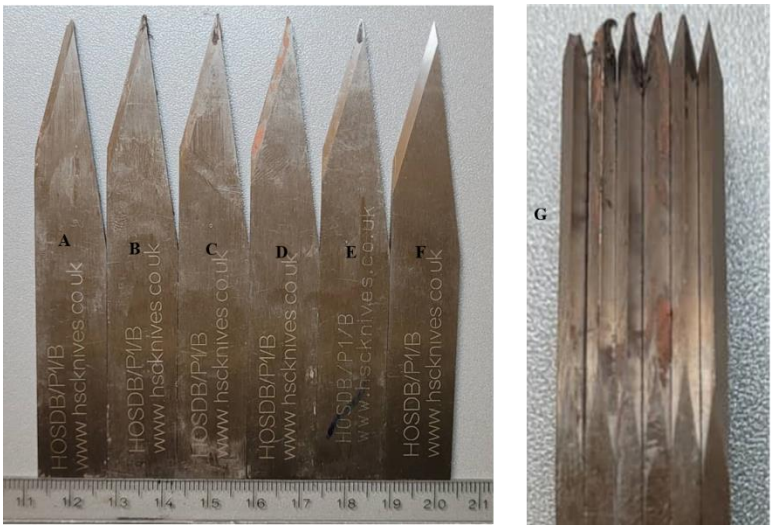

Figure 11. Damaged tip of the testing knife after impact.

edges and joints (1, 3, and 4) of the protective elements due to less fiber accumulation of the scales in edges and joint lines. The puncture width on the edges of the scales could lead to fatal injury unless improvements are made to the chamfered line in the joints of the protective elements for uniform distribution of the fibers in all parts of the scales, including the edges.

In summary, the knives are bent (Figure 10A – Figure 10E) after puncture testing and are not used to puncture repeatedly due to the high strength of the scales printed from carbon fiber in circular scales, quadrilateral scales on its body, and a 100 x 100 mm2 plate. The tips of the knives are broken, bent, or partially damaged during the drop test, according to the content of the carbon fiber in the scales. The knives in Figure 10A – Figure 10C are bent, damaged, and broken during the testing of circular scales made of carbon fiber. A knife in Figure 10D is bent during the testing of the 100 mm x 100 mm square plate, the tip of the knife in Figure 10E is bent during the testing of the body of the quadrilateral scales, while the physical appearance of the knife in Figure 10F remains unchanged during testing of the scales made from Kevlar fiber. The appearance of the tips of the knives in decreasing damage order from left to right is clearly shown in Figure 10G, with the first three knives impacted during testing carbon 3D printed scales, the fourth knife during testing of the 100 mm x 100 mm square plate, the fifth knife during the testing of the quadrilateral scales, and the last (on the right side) knife used during the testing of the circular scale made from Kevlar.

CONCLUSION

Stab protective armor is safety equipment designed to safeguard the lives of law enforcement workers for security assurance. This equipment should be capable of withstanding the intended stabbing impact energy level. This research primarily addresses the performance of continuous filament fabrication (CFF) 3D printed stab protective gear elements, considering various important factors such as the type of materials, shape of geometries, sizes of the protective elements, and related aspects. The results reveal that these considered factors significantly influence the ability to withstand stabbing impact energy from a knife with a drop weight.

The mechanical properties of materials, such as tensile strength (MPa), flexural strength (MPa), compressive strength (MPa), and their modulus (GPa), result in significantly different resistance to puncture force. Similarly, the density of the materials also plays a significant role in reducing the impact energy from the stabbing weight.

The types of geometries, described as shapes of protective scales in this study, were found to affect the penetration distance of the knife through the 3D printed protective elements because the turning point of the printer nozzle after running to print depends on the width of the printing line. The narrower the angle of the turning points of the nozzle, the lower the fiber accumulation. The sizes of the geometries influence the fiber content and affect the protection performance. The larger the geometry, the higher the fiber content, resulting in improved resistance to knife penetration through the protective element.

In general, the 3 mm thicker carbon fiber 3D printed protective scales fully resist the impact energy from the 25 joules drop weight. The tip of the knife was not measurable behind the last layer during all impact tests on carbon scales; instead, the tip of the knife is bent, broken, or damaged. Therefore, the investigators of this research suggest developing stab protective armor through 3D printing of quadrilateral scales from carbon fiber with optimal dimensions for reduced weight, flexibility, permeability, and breathability. The novelty of this study can be

explained in terms of materials mechanics as the fibers adhered to each other with crossing alignment when printing a layer over the layer. This creates an entangling path on the knife while running from layer to layer so as the impact energy is reduced by disturbing the falling speeding of the knife with its impact mass. These stab protective elements are designed for segmented arrangement for the possible flexibility with light weight from the thickness and material mechanics.

Future research activities will include the attachment method and adhesion between scales and fabrics, as well as the design and development of 3D printed scales for the full vest, and checking its performance both to protection and comfort.

Acknowledgement: *Authors would like to thank the Institute of Textile Machinery and High Performance Materials, TU Dresden and the staff for the valuable contribution to make this research effective.*

REFERENCES

1. Reiners P.: Investigation about the stab resistance of textile structures, methods for their testing and improvements. Université de Haute Alsace: HAL. 2016, pp. 195.
2. Fenne P.: Protection against knives and other weapons. Textiles for protection, ed. R.A. Scott. 2005, Cambridge: Woodhead Publishing, CRC.
3. Alil L.-C., et al.: Aspects regarding the use of polyethylene fibers for personal armor. Eastern Michigan University, 2004.
4. Cavallaro P.V.: Soft Body Armor: An Overview of Materials, Manufacturing, Testing, and Ballistic Impact Dynamics, N.U.W.C. Division, Editor. 2011, NUWCD-NPT-TR.
5. Laible R.: Ballistic Materials and Penetration Mechanics (Methods and phenomena, their applications in science and technology), 2012, Elsevier.
6. National Institute of Justice, O.o.J.P., U.S. Department of Justice, Stab Resistance of Personal Body Armor NIJ Standard–0115.00. 2000, US National Institute of Justice: Washington.
7. EMS1, Man accused of stabbing 2 police officers after killing 4 relatives. 2023.
8. VOA, Stabbing Attack in Tunisia, Suspect Detained 2022.
9. Staff T.: Police officer stabbed, 10 arrested at Tel Aviv protest over hit-and-run case, in The Times of Israel, 2023.
10. Jessup S., Kelly J.W.: Met Police officer speaks of ordeal as knife attacker is sentenced, in BBC News, 2023, BBC.
11. Amara T.: Tunisia national guard officer stabbed, police arrest attacker, R. Chang, Editor, 2023, Reuters.
12. Police1, N.M. officer killed in stabbing before suspect is shot and killed by witness. 2024, Associate Press.
13. Grieshaber K.: Stabbing attack at German gym leaves 4 severely injured, in Associate Press, 2023, AP.
14. zdfheute, Angriffe auf Bahn-Mitarbeiter 2022 gestiegen. 2023, Panorama.
15. Bundeskriminalamt(BKA), Bundeslagebild Gewalt gegen Polizeivollzugsbeamtinnen und Polizeivollzugsbeamte 2020. 2021, Bundeslagebild.
16. LaTourrette T.: The life-saving effectiveness of body armor for police officers. J Occup Environ Hyg, 7(10), 2010, pp. 557-562. https://doi.org/10.1080/15459624.2010.489798
17. Peleg K., Rivkind A., Aharonson-Daniel L.: Does body armor protect from firearm injuries? J Am Coll Surg, 202(4), 2006, pp. 643-648. https://doi.org/10.1016/j.jamcollsurg.2005.12.019
18. Jaslow C.R.: Mechanical properties pf cranal sutures. Journal of Biomechanical, 23(4), 1990, pp. 313-321. https://doi.org/10.1016/10.1016/0021-9290(90)90059-c
19. Larsen B., et al.: Body armor, performance, and physiology during repeated high-intensity work tasks. Mil Med, 177(11), 2012, pp. 1308-1315. https://doi.org/10.7205/milmed-d-11-00435
20. Greaves I.: Military Medicine in Iraq and Afghanistan: A Comprehensive Review. 2018, Taylor & Francis Group, CRC Press.
21. Ricciardi R., Deuster P.A., Talbot L.A.: Metabolic Demands of Body Armor on Physical Performance in Simulated Conditions. MILITARY MEDICINE, 173(9), 2008, 817 p. https://doi.org/10.7205/milmed.173.9.817
22. Park H., et al.: Impact of ballistic body armour and load carriage on walking patterns and perceived comfort. Ergonomics, 56(7), 2013, pp. 1167-1179. https://doi.org/10.1080/00140139.2013.791377
23. Chinevere T.D., et al.: Efficacy of body ventilation system for reducing strain in warm and hot climates. Eur J Appl Physiol, 103(3), 2008, pp. 307-314. https://doi.org/10.1177/0040517517690623
24. Nayak R., et al.: Body armor for stab and spike protection, Part 1: Scientific literature review. Textile Research Journal, 88(7), 2017, pp. 812-832. https://doi.org/10.1177/0040517517690623
25. Nayak R., et al.: Stab resistance and thermophysiological comfort properties of boron carbide coated aramid and ballistic nylon fabrics. The Journal of The Textile Institute, 110(8), 2018, pp. 1159-1168. https://doi.org/10.1080/00405000.2018.1548800
26. Matusiak M.: Thermal Comfort Index as a Method of Assessing the Thermal Comfort of Textile Materials FIBRES & TEXTILES in Eastern Europe, 18(2), 2010, pp. 45-50.
27. Djongyang N., Tchinda R., Njomo D.: Thermal comfort: A review paper. Renewable and Sustainable Energy Reviews, 14(9), 2010, pp. 2626-2640. https://doi.org/10.1016/j.rser.2010.07.040
28. Nayak R., et al.: Comfort properties of suiting fabrics. Indian Journal of Fibre and Textile, 34, 2009, pp. 122-128.
29. Philippe F., et al.: Tactile Feeling: Sensory Analysis Applied to Textile Goods. Textile Research Journal, 74(12), 2004, pp. 1066-1072. https://doi.org/10.1177/004051750407401207
30. Dempsey P.C., Handcock P.J., Rehrer N.J.: Impact of police body armour and equipment on mobility. Appl Ergon, 44(6), 2013, pp. 957-961. https://doi.org/10.1016/j.apergo.2013.02.011
31. Legg S.J.: Influence of body armour on pulmonary function. Ergonomics, 31(3), 1988, pp. 349-353. https://doi.org/10.1080/00140138808966679
32. Li Y., Ortiz C., Boyce M.C.: Bioinspired, mechanical, deterministic fractal model for hierarchical suture joints. Phys Rev E Stat Nonlin Soft Matter Phys, 85(3 Pt 1), 2012, 031901 p. https://doi.org/10.1103/PhysRevE.85.031901
33. Pritchard J., Scott J., Girgis G.: The structure and development of cranial and facial sutures. Journal of Anatomy, 90(1), 1956, pp. 73-86.
34. Herring S.W.: Mechanical influences on suture development and patency. Front Oral Biol, 12, 2008, pp. 41-56. https://doi.org/10.1159/000115031
35. Dunlop J.W.C., Weinkamer R., Fratzl P.: Artful interfaces within biological materials. Materials Today, 14(3), 2011, pp. 70-78. https://doi.org/10.1016/S1369-7021(11)70056-6
36. Vernerey F.J., Barthelat F.: On the mechanics of fishscale structures. International Journal of Solids and Structures, 47(17), 2010, pp. 2268-2275. https://doi.org/10.1016/j.ijsolstr.2010.04.018
37. Dastjerdi A.K., Barthelat F.: Teleost fish scales amongst the toughest collagenous materials. J Mech Behav Biomed Mater, 52, 2015, pp. 95-107. https://doi.org/10.1016/j.jmbbm.2014.09.025
38. Zhu D., et al.: Puncture resistance of the scaled skin from striped bass: collective mechanisms and inspiration for new flexible armor designs. J Mech Behav Biomed Mater, 24, 2013, pp. 30-40.

https://doi.org/10.1016/j.jmbbm.2013.04.011
39. Lin Y.S., et al.: Mechanical properties and the laminate structure of Arapaima gigas scales. J Mech Behav Biomed Mater, 4(7), 2011, pp. 1145-1156. https://doi.org/10.1016/j.jmbbm.2011.03.024
40. Connors M.J., et al.: Three-dimensional structure of the shell plate assembly of the chiton Tonicella marmorea and its biomechanical consequences. J Struct Biol, 177(2), 2012, pp. 314-328. https://doi.org/10.1016/j.jsb.2011.12.019
41. Ji B., Gao H.: Mechanical properties of nanostructure of biological materials. Journal of the Mechanics and Physics of Solids, 52(9), 2004. https://doi.org/10.1016/j.jmps.2004.03.006
42. Barthelat F., et al.: On the mechanics of mother-of-pearl: A key feature in the material hierarchical structure. Journal of the Mechanics and Physics of Solids, 55(2), 2007, pp. 306-337. https://doi.org/10.1016/j.jmps.2006.07.007
43. Krauss S., et al.: Mechanical Function of a Complex Three-Dimensional Suture Joining the Bony Elements in the Shell of the Red-Eared Slider Turtle. Advanced Materials, 21(4), 2009, pp. 407-412. https://doi.org/10.1002/adma.200801256
44. Garcia A.P., Pugno N., Buehler M.J.: Superductile, Wavy Silica Nanostructures Inspired by Diatom Algae. Advanced Engineering Materials, 13(10), 2011, pp. B405-B414. https://doi.org/10.1002/adem.201080113
45. Martini R., Balit Y., Barthelat F.: A comparative study of bio-inspired protective scales using 3D printing and mechanical testing. Acta Biomater, 55, 2017, pp. 360-372. https://doi.org/10.1016/j.actbio.2017.03.025
46. Ahrendt D., et al.: Hybrid material designs by the example of additive manufacturing for novel customized stab protective clothing, in Light Weight Armour Group for Defense and Security. Roubaix, France, 2019, pp. 286-294.
47. Sitotaw D.B., Muenks D., Kebash A.K.: 3D printing applications on textiles: Measurement of air permeability for potential use in stab-proof vests. Journal of Engineered Fibers and Fabrics, 19, 2024, 15589250241232152 p. https://doi.org/10.1177/15589250241232152
48. Markforged. Markforged the Mark Two Desktop 3D Printer. 2019, online: https://markforged.com/mark-two/ [cited 05.04.2020]
49. Langau L.: What is Continuous Fiber Fabrication (CFF)?, in Make Parts Fast, A Design World Resource, 2017.
50. Dean A.: A Review on Markforged Mark Two: the basics of how it works, in DEVELOP3D, 2016, DEVELOP3D: UK, London.
51. Crease A.: 3D Printer Types & Technologies 2019, Markforged.
52. Association of test laboratories for bullet resistant materials and constructions, Test Standard “Stab and Impact Resistance” - Requirements, classifications and test procedures (VPAM KDIW 2004), 2011.
53. Connor S.E.J., Bleetman A., Duddy M.J.: Safety standards for stab-resistant body armour: a computer tomographic assessment of organ to skin distances. International Journal of the Care of the Injured, 29(4), 1998, pp. 297-299. https://doi.org/10.1016/s0020-1383(97)00205-2
54. Su S., et al.: Skin-Liver Distance and Interquartile Range-Median Ratio as Determinants of Interoperator Concordance in Acoustic Radiation Force Impulse Imaging. Journal of Medical Ultrasound, 27(4), 2019, 4 p. https://doi.org/10.4103/JMU.JMU_124_18
55. Shen F., et al.: Impact of skin capsular distance on the performance of controlled attenuation parameter in patients with chronic liver disease. Liver International, 2015, 9 p. https://doi.org/10.1111/liv.12809
56. Sitotaw D.B., et al.: Investigation of Stab Protection Properties of Aramid Fibre-Reinforced 3D Printed Elements. Fibres and Textiles in Eastern Europe, 29(3(147)), 2021, pp. 67-73.
57. Sitotaw D.B., et al.: A Review on the Performance and Comfort of Stab Protection Armor. 22(1), 2022, pp. 96-107. https://doi.org/10.2478/aut-2021-0013

ELECTROSPUN BIO-NANOCOMPOSITE WEBS BY CELLULOSE NANOCRYSTAL (CNC)-LOADED POLYLACTIDE AND ITS BLENDS

HANDAN, PALAK* AND BURÇAK, KARAGÜZEL KAYAOĞLU

Department of Textile Engineering, Faculty of Textile Technologies and Design, Istanbul Technical University, Istanbul, Turkey

ABSTRACT

In this study, effects of polylactide (PLA) melt flow rate, and dichloromethane (DCM)/dimethyl sulfoxide (DMSO) solvent blend ratio on cellulose nanocrystal (CNC) dispersion quality in PLA/CNC bio-nanocomposites, prepared via solution casting, were studied. Besides, the electrospinning behaviour of CNC-loaded PLAs and its blends with poly(butylene adipate-co-terephthalate) (PBAT) was explored. The rheological analysis confirmed good CNC dispersion ability in PLAs with high melt flow rate specifically in solvents comprising DMSO. Besides, it was observed that CNC loading directly affected the morphological structure of the obtained nanofibrous webs. Thermal analysis indicated that CNCs acted as a nucleation agent and promoting the crystallization process by lowering cold crystallization temperatures and increasing the degree of crystallinity. The outcomes provide a groundwork for future studies on the fabrication of bio-nanocomposite webs from PLA/PBAT blends for a variety of applications.

KEYWORDS

Polylactide; Polybutylene adipate-co-terephthalate; Cellulose nanocrystals; Bio-nanocomposite; Nanofiber.

INTRODUCTION

Cellulose nanocrystals (CNCs) are highly regarded as a leading nano-reinforcement for bio-nanocomposites (BNCs) due to their distinctive attributes, including nano-scale size, outstanding mechanical strength, ease of chemical modification, high aspect ratio, low density, renewability, biodegradability, and biocompatibility [1]. BNCs are composed of bioplastics combined with either organic or inorganic nanofillers. Although inorganic nanofillers may hinder biodegradability, organic nanofillers are more compatible with bioplastics and minimize phase separation due to improved interfacial adhesion and affinity. CNCs are produced through acid hydrolysis, which selectively targets and hydrolyzes the amorphous regions within cellulose microfibrils. Besides, sulfuric acid is commonly used in this method to generate more stable CNC suspensions [2]. On the other hand, the interacting hydroxyl groups on the surface of CNCs and the sulphate half-esters formed during the sulfuric acid hydrolysis process may cause CNCs to agglomerate in hydrophobic polymers, such as PLA. The characteristics of the matrix, including the polymer's molecular weight and crystallizability, can influence the dispersion of CNCs and the resulting properties of nanocomposites [3]. Besides, the characteristic of organic solvent, i.e., polar-nonpolar nature and dielectric constant, directly affect the dispersion of CNCs in a polymer matrix [4]. In addition, a significant breakthrough in processing CNC-reinforced BNCs is the use of electrospinning to create continuous one-dimensional fibers with diameters ranging from microscale to nanoscale. This technique enables the alignment of CNCs under strong electrostatic fields, orienting them along the fiber axis and greatly enhancing the axial strength of the electrospun nanocomposite fibers. Accordingly, in this study, polar/nonpolar binary solvent systems, and PLAs with different molecular weights were utilized to develop PLA-based nanocomposites via solution casting method, and CNC dispersion quality was investigated. Afterwards, the electrospinnability of PLA-based systems with various solvents was controlled, and key properties of BNC nanofibers were investigated.

Table 1. Properties of different PLA grades [5].

PLA Code	Melt flow rate (MFR: g/10 min, 210°C)
HPLA	6-10
MPLA	15-30
LPLA	70-85

* **Corresponding author:** Handan P., e-mail: palakh@itu.edu.tr

Table 2. Properties of the solvents [6].

Solvent	Polarity	Solubility Parameter, δ [Cal/cm^3]$^{1/2}$	Dielectric constant, ε	Boiling Point [°C]
DCM	Non-polar	9.7	9.10	40
DMSO	Polar	12.9	48.9	189

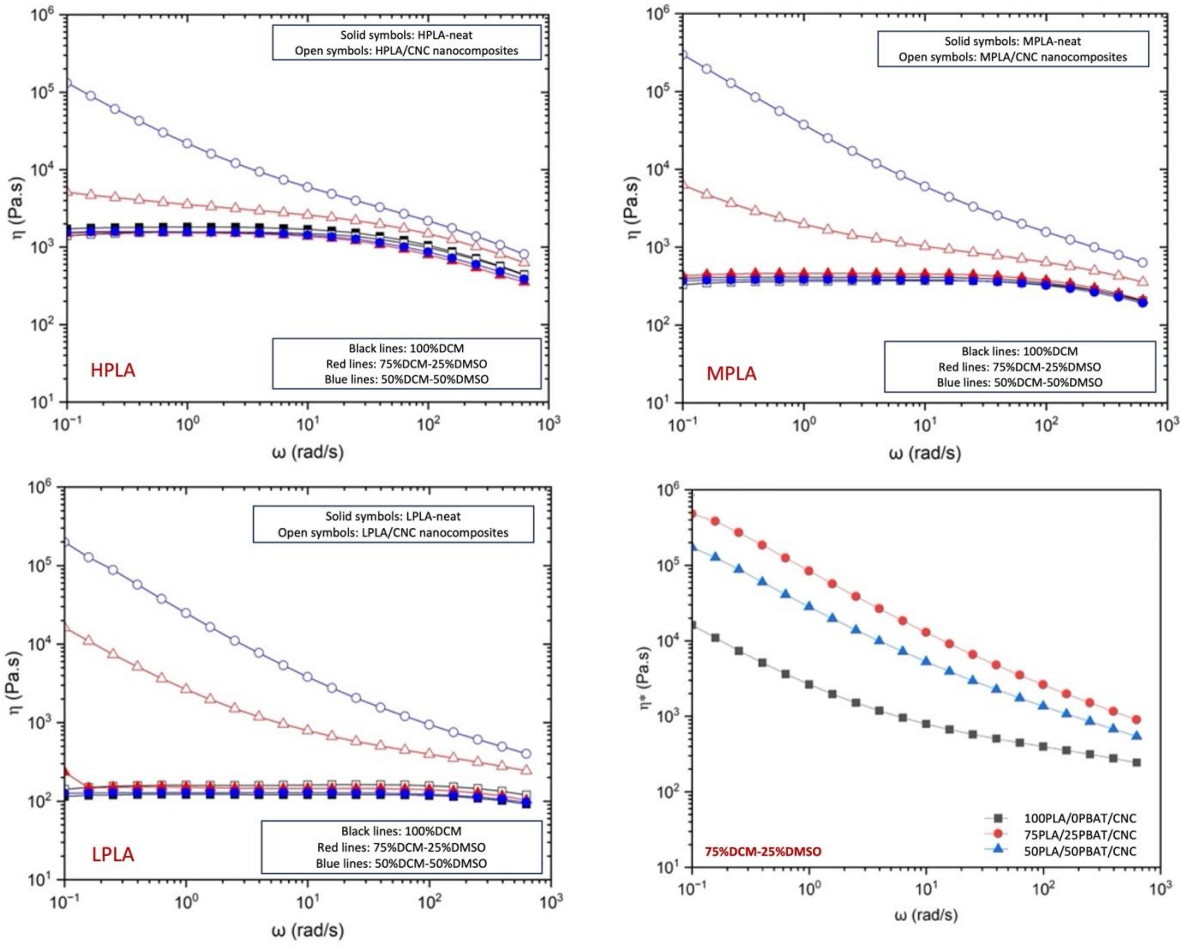

Figure 1. Complex viscosity versus angular frequency of bio-nanocomposites of (a) HPLA, (b)MPLA, and (c) LPLA (d) LPLA/PBAT blends with 3 wt.% CNC.

EXPERIMENTAL

Materials

Commercial semicrystalline PLAs with different melt flow rates (MFR) were kindly supplied by NatureWorks LLC, USA. PBAT, Ecoflex® F Blend C1200, having a polydispersity of 2.0 and an average molecular weight of 1.05×10^5 g/mol, was donated by BASF, Ludwigshafen, Germany. Spray-dried CNC in powder form was provided by CelluForce (Montreal, Canada). Organic solvents of dichloromethane (DCM) and dimethyl sulfoxide (DMSO) were purchased from Merck and Isolab Chemicals, respectively (Table 2).

Methods

CNCs were dispersed within the solvents in a water bath sonicator for 2.5 h at room temperature. Then, PLAs and PLA/PBAT granules were added to the CNC-solvent mixture and stirred on a magnetic stirrer for 3 h. Different solvent blends, i.e., 100%DCM (100DCM), 75%DCM/25% DMSO (75DCM/25DMSO), and 50%DCM/50%DMSO (50DCM/50DMSO) were employed. The CNC content in PLA based bio-nanocomposites was constant at 3 wt.%. When polymer granules were fully dissolved, polymer solutions were poured into glass petri dishes, and they were dried at 85°C in a vacuum oven.

The selected polymer solutions were individually loaded to a 1 mL syringe, with a metallic needle of 27 G, and delivered to the syringe pump in a horizontal electrospinning system. The electrospinning parameters of feed rate, voltage, and tip-to-collector distance were kept constant at 1.0 mL/h, 18-20 kV, and 15 cm, respectively. An MCR-301 rotational rheometer with a parallel plate geometry was utilized to conduct the small amplitude oscillatory shear rheological analysis. A scanning electron

microscope, Tescan Vega3, was used to conduct morphological analysis at 20.00 kV. A Perkin Elmer DSC400 differential scanning calorimetry was utilized to investigate the crystallization and melting behaviors.

RESULTS AND DISCUSSION

Rheological properties of BNCs

Figure 1 shows the complex viscosity versus angular frequency of bio-nanocomposites of HPLA, MPLA, LPLA, and LPLA/PBAT samples with 3 wt.% CNC. The low frequency upturns in complex viscosity indicate CNC networking formation. Accordingly, the use of DCM solely allowed the lowest degree of CNC dispersion within all PLA matrices, while solvent blends with higher DMSO contents enabled the most homogenous dispersion of CNCs. Among three types of PLAs, LPLA bio-nanocomposites had the highest relative increase in their complex viscosity with the DCM50/DMSO50 solvent blend, and with DCM75/DMSO25 also having a significant effect. On the other hand, CNC dispersion quality was suppressed in bio-nanocomposites with PLAs having higher molecular weights. Besides, when PBAT was blended with LPLA at different weight ratios, i.e., 25 wt.% and 50 wt.%, major upturns at the low frequencies were observed, indicating CNC networking formation, as well.

Crystallization behavior of BNCs

1st heating cycles showed that neither the solution-casted films of neat PLAs nor PLA/CNC bio-nanocomposites showed cold crystallization, indicating all PLAs were almost fully crystallized during the drying step of solution casted film production. At DMSO concentrations of 25% v/v, neat PLA samples exhibited a double melting peak, which could be due to imperfect crystallinity in the PLA, attributing to the plasticizing effect of residual DMSO within the polymer matrix. During 2nd heating scans, cold crystallization temperatures of neat PLAs were always higher than those of PLA/CNC bio-nanocomposites, indicating CNC acted as a nucleation agent and promoting the crystallization process by lowering T_{cc} and increasing the degree of crystallinity.

Morphological structure of BNC-nanofibers

Based on the rheological analysis, low molecular weight PLA was chosen as the optimum PLA grade and used in electrospinning method (Figure 3). Moreover, as the obtained results showed that the blend ratio of 75DCM/25DMSO provided a good CNC dispersion for LPLA grade, this blend ratio was selected to fabricate PLA/CNC bio-nanocomposite webs as well. The average fiber diameter of neat LPLA decreased from 1510 ± 200 nm to 1218 ± 205 nm with an addition of 1 wt.% CNC; then a dramatic drop to 342 ± 97 nm was observed when the CNC ratio was 3 wt.%. The results showed that 3 wt.% CNC-loaded LPLA/PBAT bio-nanocomposite webs were successfully produced; however, bead formation was observed in 100PLA/0PBAT. The addition of PBAT, i.e., 25 w/v% and 50 w/v%, to the structure resulted in more homogenous fibers with a higher mean fiber diameter (Figure 4).

Table 3. Thermal properties of BNCs.

	1st heating			2nd heating		
Sample	**T_{cc} [°C]**	**T_m[°C]**	**X_c[%]**	**T_{cc}[°C]**	**T_m[°C]**	**X_c[%]**
HPLA	-	162-166	56	-	167	5
HPLA/CNC	-	165	48	113	167	8
MPLA	-	158-162	53	-	162	5
MPLA/CNC	-	162	51	111	164	4
LPLA	-	158-169	35	105	169	23
LPLA/CNC	-	168	60	103	169	36

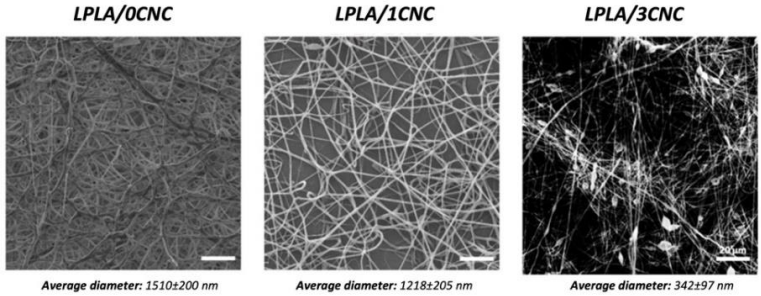

Figure 3. Electrospun bio-nanocomposite webs of LPLA having different CNC content levels.

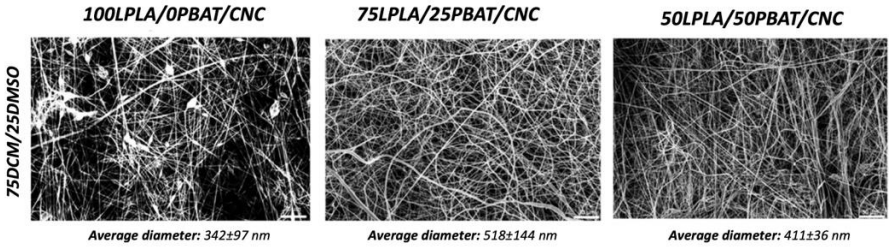

Figure 4. Electrospun bio-nanocomposite webs of LPLA/PBAT blends having 3 wt.% CNC.

CONCLUSIONS

In this study, the effects of utilizing binary solvent system of DCM/DMSO at different weight ratios, PLAs with various melt flow rates, and PLA/PBAT blends, on CNC dispersion quality through rheological analysis were revealed. The effect of CNC addition on the thermal characteristic of solution cast films were also investigated; besides, the electrospinnability of the bio-nanocomposites were studied as well. The findings provide valuable insights for optimizing the preparation of PLA/CNC bio-nanocomposites, highlighting the importance of selecting appropriate solvent blends, molecular weight of PLA and PLA/PBAT blend ratios to achieve good dispersion quality via solution solution-casting and electrospinning.

Acknowledgement: *The authors acknowledge the financial support provided by Istanbul Technical University Scientific Research Projects Fund under grant number 44582. Handan Palak thanks the Scientific and Technological Research Council of Turkey (TUBITAK) for the financial support under the TUBITAK-BIDEB 2214A Fellowship program.*

REFERENCES

1. Mali P., Sherje A.P.: Cellulose nanocrystals: fundamentals and biomedical applications. Carbohydrate Polymers, 275, 2022, 118668 p. https://doi.org/10.1016/j.carbpol.2021.118668
2. Moon R.J., Martini A., Nairn J., et al.: Cellulose nanomaterials review: structure, properties and nanocomposites, Chem. Soc. Rev., 40, 2011, pp. 3941–3994.
3. Vatansever E., Arslan D., Sarul D.S., et al.: Effects of molecular weight and crystallizability of polylactide on the cellulose nanocrystal dispersion quality in their nanocomposites. International Journal of Biological Macromolecules, 154, 2020, pp. 276–290. https://doi.org/10.1016/j.ijbiomac.2020.03.115
4. Ozdemir B., Nofar M.: Effect of solvent type on the dispersion quality of spray-and freeze-dried CNCs in PLA through rheological analysis, Carbohydrate Polymers, 268, 2021, 118243 p. https://doi.org/10.1016/j.carbpol.2021.118243
5. Natureworks. (n.d.). Online: https://www.natureworksllc.com/technology-and-products/products [cit. 15.01.2024]
6. Casasola R., Thomas N. L., Trybala A., et al.: Electrospun poly lactic acid (PLA) fibres: Effect of different solvent systems on fibre morphology and diameter. Polymer, 55(18), 2014, pp. 4728–4737. https://doi.org/10.1016/j.polymer.2014.06.032

MODAL ANALYSIS OF A LAMINATE PLATE WITH 10 MM NOTCH FOCUSED ON THE EFFECT OF A FUNCTIONALLY ORIENTED FABRIC LAYUP WITH 20 MM WIDE CARBON STRIPS

ZBONČÁK, RADEK*

VÚTS, a. s., Virtual and applied mechanics, Svárovská 619, Liberec, Czech Republic

ABSTRACT

Functionally oriented fabric (FOF) is a woven textile featuring irregularly distributed secondary material strips in both warp and weft directions, designed to locally improve the mechanical properties of laminates, particularly around openings. This study investigates the impact of different FOF laminate layups on the natural frequencies of laminates with a 10 mm notch. The analyzed layup configurations include [0/90]s, [0/45]s, and [0/30/60]s, with 20 mm wide carbon strips incorporated into the glass fiber structure. The research demonstrates that the FOF structure significantly increases the natural frequencies about 20 % for bending modes of 0/90 layup. About 5 % and almost 30 % for twisting and bending modes respectively in the 0/30/60 layup, and over 20 % and about 40 % for twisting and bending modes respectively in the 0/45 layup. These enhancements help to prevent resonance in standard operating frequencies of mechanisms and machines, thus extending their operational lifespan. Additionally, the strategic placement of functional material strips around structural openings provides increased stiffness without the need for extra layers, effectively reducing the laminate's overall mass. This study highlights the potential of FOF to improve the dynamic performance and lifespan of laminated composite structures used in various engineering applications.

KEYWORDS

Functionally oriented fabrics; Composite material; Modal analysis; Natural frequency; FEA; Circular notch.

INTRODUCTION

Non-woven and woven fabrics are two basic types of fabrics used in composites. They differ in fiber processing. While non-woven fabric has fibers bonded together non-mechanically, woven fabrics are constructed by weaving yarns together. The vertical fibers are called ‘warp’ yarns, while so-called ‘weft’ yarns are weaved through the warp yarns along the horizontal width of the textile. Woven fabrics are called textiles. In the weaving process of composite textiles, a yarn is called a roving. The roving consists of straight fibers which are not spun or twisted [1].

Woven fabrics are generally sorted into two groups based on the roving material. In the first case, warp and weft roving is made of the same material. The second type of fabric is so-called ‘hybrid fabric’, where roving in warp direction consist of different fibers than roving in weft direction, typically carbon-aramid combination. Such a regular alternation of materials in the hybrid fabric leads to homogenization of the properties of the laminate layer. In contrast to these common types of fabrics, the functionally oriented fabric structure (FOF) has irregularly distributed fibers of different materials in the warp and weft (Fig. 1). The base material (BM) predominates in the fabric. Such material is usually cheaper and has worse mechanical properties than the functional one. The functional material (FM) has a minority in the fabric and has better mechanical properties and therefor it is in principle more expensive than the base material. The advantage of a FOF is the efficient use of expensive material with high mechanical performance quality.

The production of a functionally oriented fabric structure allows lamination without cutting the continuous fibers in the layer and so having better mechanical properties at the same time. FOF is intended for using in the layup to locally improve mechanical properties to increase strength or stiffness in required area. The suitable applications are laminates with holes for fasteners, or with openings such as windows or mounting openings providing access to machine parts under the laminate part [2]. Other application is a large format laminate in which the strip of functional material weaved in the fabric acts like a ‘shell rib’.

* **Corresponding author:** Zbončák R., e-mail: radek.zboncak@vuts.cz

Figure 1. Example of functionally oriented fabric (FOF).

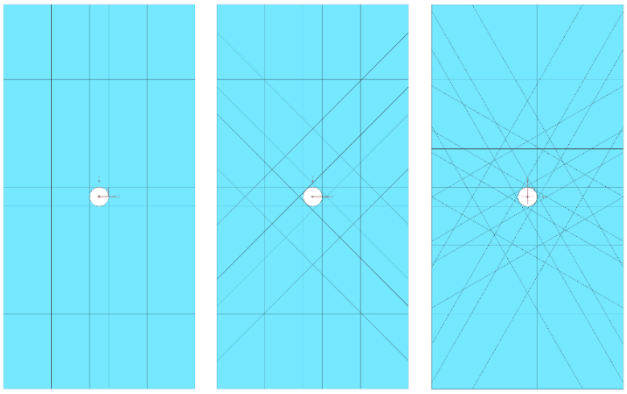

Figure 2. CAD model of FOF laminate layups: [0/90], [0/45] and [0/30/60].

The aim of this work is to determine first four modes of selected layups of FOF laminate. To evaluate natural frequencies of analyzed laminates and compare the obtained results. Finally, the conclusion of the effect of FOF layup on the natural frequency of a laminate with a notch will be made. The work is a continuation of the FOF parameter analysis. The presented results serve to the performance description of a FOF laminate.

LAMINATE

There are three regions of material type in sense of warp and weft roving combination in FOF laminate: glass-glass, glass-carbon (or carbon-glass) and carbon-carbon. The base material E-glass EC13 272 Z20 T63C roving is combined with the functional material carbon Tenax E HTA 40 E13 6K roving. Both are present in warp and weft directions in the way they form locally stiffened areas, as shown in Fig. 1. Both materials belong to the standard modulus materials. Glass fiber modulus is 71 GPa and carbon fiber modulus is 220 GPa. Mechanical properties of a laminate are estimated by theoretical elastic models [3] with use of an epoxy resin system with a modulus of cured system of 3 GPa.

A dimension of an analyzed plate is 100×200 mm (width×length). The size of a notch in the center of the plate is 10 mm. Thickness of the plate is given by its layup. The layups are [0°/90°]s, [0°/45°]s and [0°/30°/60°]s, see Fig. 2. A CAD model of the simulated specimen includes pads areas, as it would be in a real test setting. The purpose of the pads is to prevent a damage in the testing machine jaws. It clearly defines the area of load and constraints application in the simulation. The width of the carbon strips is 20 mm. FOF laminate simulation results are compared to results of base material only (glass) laminate with the same layup orientations and the notch size.

MODAL ANALYSIS

The parametric finite-element model of a functionally oriented fabric laminate is created by the ply-based modelling method. The woven fabric lamina is defined by software as three layers of unidirectional fibers (UD). Two outer layers of UD (warp) and one intermediate layer of UD rotated by 90° (weft). Material orientation plays an essential role in proper composite material definition. Each material region must have a correctly defined system of coordinates to respect an orthotropic character of composite material.

In general, the first step in solving the dynamic properties of a structure is the determination of natural frequencies and mode shapes by performing a modal analysis of a free body without external load and any constraints. If damping is neglected, the results of such a simulation are real eigenvalues and normal modes. The first six modes have zero frequency, which corresponds to the six degrees of freedom of freely constrained (unconstrained) body. For typical material damping values of laminates, the damping does not significantly influence the natural frequencies and mode shapes. The damping reduces the vibration level near resonance.

DISCUSSION

A plate laminated by standard process has layers of glass fabric and strips of carbon fibers in extra layers. That makes laminate thicker, which means heavier. The thickness in notch area is almost doubled. The mass of laminate plate with extra carbon strips is 0.08098 kg. The same size plate made of FOF with 10 mm notch has mass of 0.0488 kg. The difference is 40 % of total mass. The bigger size the plate is, the higher the absolute value of mass saving is. Another issue is the laminate symmetry and its A-surface quality. Laminate made of FOF has uniform thickness and can be made in a closed mold to get A-surface on both sides of the part.

The shapes of first four non-zero modes are shown in Fig. 4. First two are twist and bending of the laminate plate. The shapes of modes for glass only laminates and for FOF laminates are the same. The results differ only in displacement and frequency values.

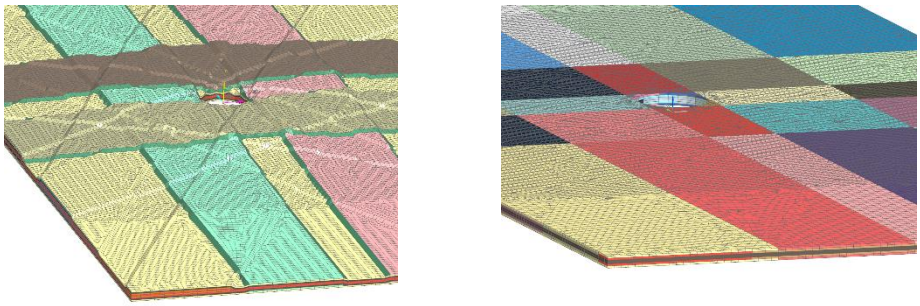

Figure 3. A FE model of laminate with carbon strips in extra layers (left) and a laminate made of FOF (right).

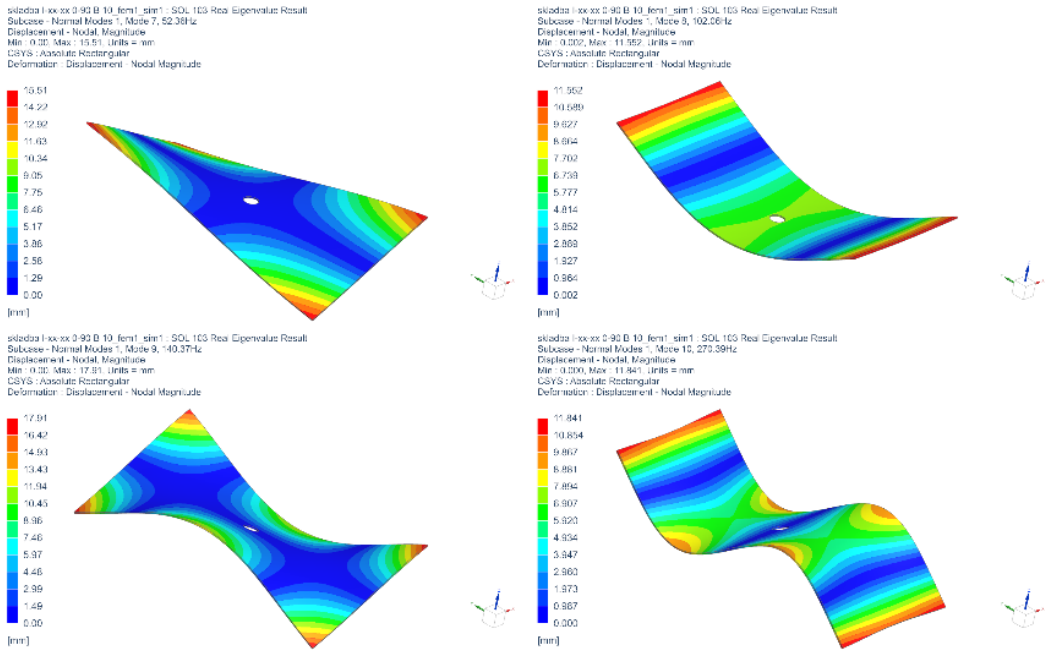

Figure 4. A FE model of laminate with carbon strips in extra layers (left) and a laminate made of FOF (right).

Table 1. Natural frequencies (Hz) of a plate with a 10 mm notch.

	[0/90]s			[0/45]s			[0/30/60]s		
	Glass	**FOF**	**Δ %**	**Glass**	**FOF**	**Δ %**	**Glass**	**FOF**	**Δ %**
1st mode	54.24	52.36	-3.5	63.60	79.32	24.7	103.6	116.8	12.7
2nd mode	80.33	102.1	27.1	78.16	111.6	42.8	114.1	148.0	29.7
3rd mode	137.6	140.4	2.0	152.6	187.4	22.8	241.9	268.0	10.8
4th mode	223.0	270.4	21.3	217.0	299.8	38.2	316.6	393.8	24.4

Natural frequencies of the mentioned four modes are summarized in Table 1. A glass-only and a FOF laminate plate are in the form of three layups. Significant benefit of carbon fiber strips in 0/90 layup is in second and fourth mode, which are the bending modes. Carbon strips make the plate frequency to increase about 27 % and 21 % in second and fourth mode respectively. The strips oriented in longitudinal and transverse direction increase the bending stiffness in 0/90 layup more than in twisting. That is consistent with the theoretical assumption. According to increase of natural frequency in 0/45 layup with carbon fiber strips, that layup is most efficient in the increase in stiffness of all three analyzed layups. The growth is over 20 % for first and third mode (twisting), and about 40 % for second and fourth mode (bending). 0/30/60 layup has higher frequencies than 0/90 layup, but lower than 0/45 layup. That corresponds with the theory, as it respects the dependency of mechanical properties on fiber orientation.

The frequency growth for 0/30/60 FOF layup is more than 25 % in bending modes and about 10 % in twisting modes compared to glass-only laminate. Frequency growth in bending modes is almost the

same as for 0/90 laminate layup. Higher frequencies are in comparison of twisting modes.

CONCLUSION

The functionally oriented textile structure (FOT) or functionally oriented fabric (FOF) is a 2D woven fabric material for manufacturing of continuous fiber laminates. It is a type of fabric with non-randomly irregularly distributed threads of fibers of functional material. The benefit of such a woven structure are effectively distributed material properties in the specific areas where the best material performance is needed. Predominant material are low-cost fibers with average mechanical properties. Such a material is called a based material (BM). BM is combined with a functional material (FM), which has very good mechanical properties. FOF allows to reduce the number of layers in layup as there is no need to puzzle cuts of different materials. That can help to reduce waste in mass production. The carbon fiber placement in warp and weft direction, strip width and span of strips can be modified during weaving process of FOF according the application requirements.

FOF structure helps to increase natural frequency of a laminate, which prevents standard operating frequency mechanisms and machines to reach the resonance. The functional material strips within the structure and especially around a structural opening (hole) helps to stiffen the laminate and the opening edge respectively. Speaking about resonance and stiffening the opening edge, the FOF has a potential to prevent the resonance of a mechanical joins, which can extend the joins' lifespan.

The results of simulations are consistent with the theory and show the potential of functionally oriented fabrics usage. The laminate layup customization allows tuning of laminate properties according to mode shape. Strips of functional material oriented in a longitudinal material direction have high effect on the bending modes. Strips angled from a longitudinal direction effect the twisting modes.

Analysis of FOF laminates with modified parameters are planned in the future to describe material performance and particular applications. After the evaluation of model with experimental data, simulations of FOF material in specific applications are going to be performed.

Acknowledgement: *This publication was supported by the Ministry of Industry and Trade (MPO) within the framework of institutional support for long-term strategic development of the research organization - provider MPO, recipient VÚTS, a. s.*

REFERENCES

1. Woven vs. non-woven. JPS Composite materials, 2021, online: https://jpscm.com/blog/woven-vs-non-woven-fabrics/ [cit. 25.04.2024]
2. Zbončák R.: Finite element model of a laminate made of functionally-oriented fabrics. In: Doubrava, Karel, Kristýna Kubášová, Zdeněk Padovec, Milan Růžička a Radek Sedláček. Experimental stress analysis 2022. Book of extended abstracts. Prague: Czech Technical University in Prague, 2022, pp. 144-145. ISBN 978-80-01-07010-9.
3. Zbončák R.: Elastic properties prediction models of continuous fibers composites: composite materials. Liberec: VÚTS, 2018. ISBN 978-80-87184-81-3.

PROPERTIES OF WOOL FIBERS REINFORCED COMPOSITES

BARBURSKI, MARCIN*; LEMMI, TSEGAYE AND PONIECKA, AGATA

Institute of Architecture of Textiles, Faculty of Material Technologies and Textile Design, Lodz University of Technology, 116 Żeromskiego str. 90-924, Lodz, Poland.

ABSTRACT

Natural fiber-reinforced composites (NFRCs) have gained significant attention for their array of advantages, including biodegradability, low density, and cost-effectiveness compared to synthetic fiber-reinforced composites. The surge in interest is driven by a global shift towards sustainability and eco-conscious practices across various industries. Consequently, there has been a significant increase in exploration and innovation within the realm of natural fiber composites, reflecting a collective effort towards more environmentally friendly material solutions. Industries such as automotive, construction, aviation, and aerospace are increasingly exploring the use of natural fiber composites. However, the flammability of natural fiber-reinforced composites is a major challenge that needs to be addressed. Wool fiber, known for its natural flame-retardant and self-extinguishing properties, has been widely used in the textile industry to produce apparel, but its use in composite production has been limited. This study explores the feasibility of using wool fibers for composite reinforcement, primarily for applications where fire resistance is required. In this work, wool woven fabric and unidirectional (UD) wool roving were used as preforms, and a bio-based resin was applied through resin infusion techniques to produce the composites. The prepared composite samples were subjected to tensile, three-point bending, thermal insulation, and fire-resistance experimental investigations. The results obtained from the experimental investigations indicate that wool fiber has promising potential as a reinforcement material in composite applications mostly where fire resistance is critical.

KEYWORDS

Wool fiber; Composite; Fire resistance; Mechanical properties; Sustainability; Natural fibers.

INTRODUCTION

Nowadays, most fiber-reinforced composites available on the market for various applications are made from glass or carbon fibers. However, due to the urgent environmental issues related to climate change and pollution, there is a growing need to focus on sustainable solutions and valuable alternatives. In light of these environmental challenges, there has been considerable interest in utilizing sustainable materials and processes [1] [2]. Natural fibers have become particularly prominent among the various options explored, especially as reinforcement materials or fillers in composite manufacturing. In the last decade, Industries such as automotive, construction, aviation, and aerospace are increasingly exploring the use of natural fiber-reinforced composites. Various research has been carried out in recent years on flax and other natural fiber-based composites [3–5].

Despite multiple benefits, such as environmental sustainability, ease of disposal at end-of-life, recyclability, and low cost, the commercial use of natural fiber-reinforced composites (NFRCs) remains limited in engineering applications. Their adoption in commercial domains is hindered by challenges like high moisture absorption, low thermal stability, and poor fire resistance. Fortunately, the issue of moisture absorption has been successfully addressed through alkali treatment or acetylation. Recently, the challenges of low thermal stability and poor fire resistance have also received attention. However, the main approaches used to address these challenges is the use of flame-retardant chemicals, but this have raised concerns about preserving the eco-friendly characteristics of NFRCs [6–8].

Therefore, in this work, the potential of using fibers with an inherent fire resistance property as a reinforcement material was explored. Wool fiber, primarily made of keratin, stands out as a noteworthy choice because of its renewable nature, biodegradability, flame resistance, and thermal insulation properties. Because of these qualities, wool fiber-reinforced composites are attractive options for use in a variety of industries where material performance and sustainability are crucial.

* **Corresponding author:** Barburski M., e-mail: *Marcin.barburski@p.lodz.pl*

EXPERIMENTAL

Materials

The study utilized a wool fiber-based woven fabric with a plain structure and a unidirectional (UD) wool roving as the reinforcing phase, along with a bio-based resin as the matrix phase. The wool fiber was chosen primarily for its inherent thermal insulation, flame resistance, and biodegradability, making it advantageous for applications that require environmental sustainability and safety in temperature-sensitive environments. The wool fiber preforms utilized are shown in Figure 1. The matrix phase comprises a bio-based, low-viscosity green epoxy resin selected specifically for its compatibility with natural fibers and low environmental impact. Derived from renewable resources, this resin exhibits favorable mechanical strength, adhesion to natural fibers, and a reduced carbon footprint compared to petroleum-based alternatives. Additionally, it provides a stable polymer network upon curing, ensuring effective load transfer between the wool fiber reinforcement and the matrix.

Methods

The composite samples were prepared using a resin infusion technique, shown in Figure 2a. Two variants of composites, wool-woven fabric and UD wool roving reinforced composites, were prepared using the resin infusion technique. For the woven fabric-based composites, four layers of the fabric were used, while for the unidirectional (UD) composite, the equivalent density of yarn was overlaid based on the density of the yarns per centimeter of the four layers of woven fabric. The resin infusion process began by arranging the preform layers in the desired orientation on a glass plate treated to prevent adhesion. A peel ply and flow mesh were placed over the preform stack to aid resin flow, and the setup was sealed with a vacuum bag. After leak testing, a vacuum pump created a pressure differential to draw the resin, pre-mixed with hardener and degassed, through an inlet port and into the fiber layers. Once infused, the composite was cured under vacuum at room temperature and then post-cured at 50 °C for 24 hours in an autoclave to enhance mechanical properties. The final composite was inspected for uniformity and structural integrity before being subjected to experimental investigations.

Experimental investigations of the composite samples

The prepared composite samples were subjected to mechanical and thermal property investigations in order to evaluate the potential of using wool fiber-based preforms as a composite reinforcement. On the Instron testing machine, the tensile and three-point bending tests were conducted according to IS0 527-4: 1997(E) and ISO 14125:1998(E). The flammability experimental investigations were conducted according to ISO 4589-2. In addition to these experiments, the thermal property of the composite samples was also investigated. The number of specimens used for each test was based on the specimen size and amount described in each standard mentioned above for those specific experimental investigations.

RESULTS AND DISCUSSION

The results obtained from each experimental investigation carried out for both variants of composites produced are presented and discussed in this section.

The result of tensile and flexural bending investigation of both types of composite samples, as presented in Figures 3 & 4, indicates that the UD_wool fiber reinforced composite sample exhibited a 105.97% and 26.89% higher flexural bending and tensile strength, respectively, compared to the woven fabric-reinforced composite sample. However, in the perpendicular direction, the woven fabric-reinforced composite sample demonstrated relatively higher bending and tensile strength. This difference evolves around the orientation of fiber reinforcement; the UD alignment of fibers provides enhanced flexural resistance and tensile strength along the fiber direction, while woven composites contribute to higher resistance in orientations where unidirectional fibers are less effective.

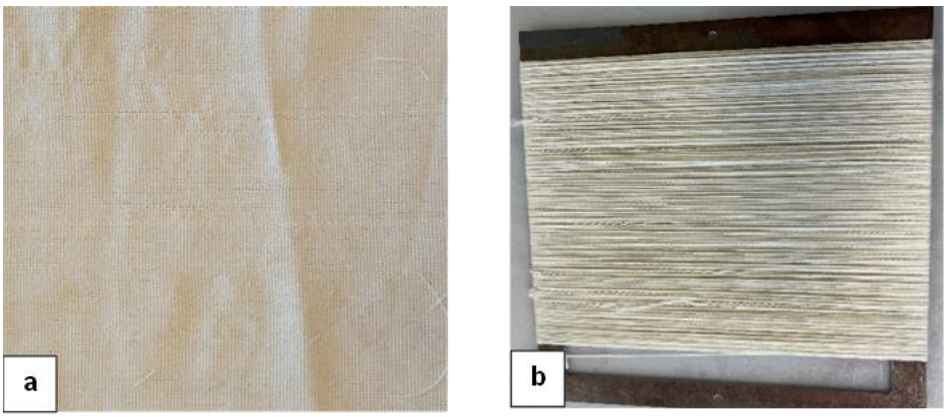

Figure 1. Wool fiber-based composite preforms. (a) Woven fabric, (b) Unidirectional wool roving.

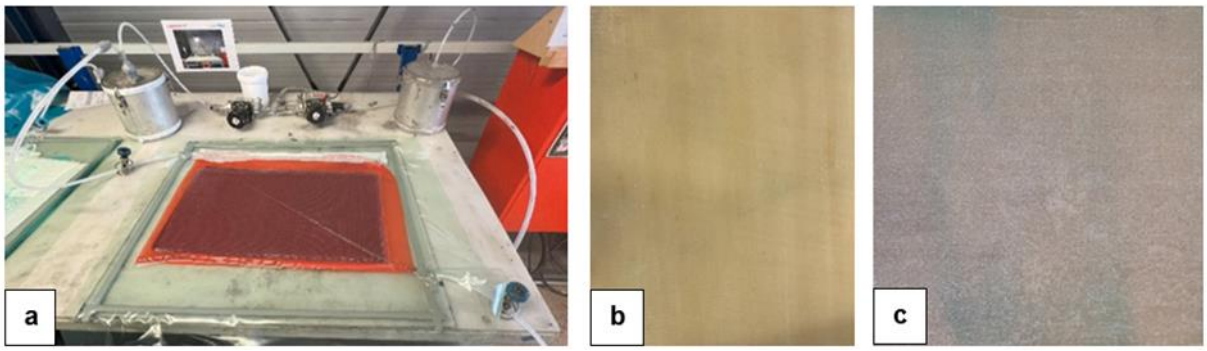

Figure 2. (a) Resin infusion technique, (b) UD wool roving reinforced composite, (c) Woven fabric reinforced composite.

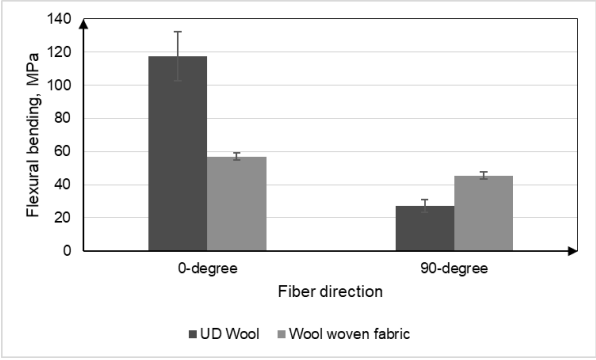

Figure 3. Flexural bending strength of the wool fiber reinforced composites.

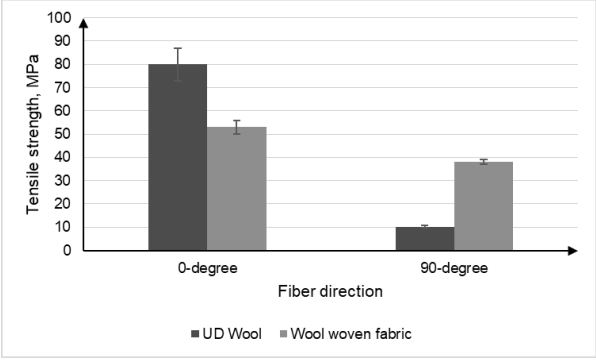

Figure 4. Tensile strength of the wool fiber reinforced composites.

The Limiting Oxygen Index (LOI) is defined as the minimum amount of oxygen required to sustain the flaming combustion of a material. The degree of flammability is ranked based on the LOI percentage of each material, where a material with an LOI of less than 20.95% is considered flammable, 20.95% < LOI < 28% is classified as slow-burning, 28% < LOI < 100% is considered self-extinguishing, and an LOI greater than 100% indicates a nonflammable material. To assess the flammability of the materials, an average LOI percentage of 24.55% and thermal resistance of 19.57K/W was obtained for both composite variants, with almost similar values for each variant. The LOI value obtained signifies that the use of wool fiber as a composite reinforcement can enhance the flammability of the composite.

CONCLUSIONS

This work investigated the possibility of using wool fiber-based preforms as a reinforcement material. The experimental investigation of UD and wool woven fabric reinforced composites has yielded several significant findings regarding their mechanical and flammability properties.

- It was observed that the mechanical properties of the wool woven fabric reinforced composites are notably lower compared to those of unidirectional (UD) wool roving reinforced composites in the fiber direction. This indicates that the reinforcement architecture significantly influences the composite's overall performance.
- The limited oxygen index (LOI) values obtained for the composite samples produced in this study demonstrate that wool fiber can effectively mitigate the flammability concerns associated with natural fiber-based composites. This finding highlights the potential of wool as a viable reinforcement material to enhance fire resistance.
- When examining the tensile and flexural bending strength properties obtained with the literature, the UD variant of the wool fiber-based composites exhibited commendable performance relative to other natural fiber-reinforced composites, such as flax and hemp. This suggests that wool fiber possesses reasonable mechanical characteristics within this sector.

In summary, the results of this research indicate that wool fiber has considerable potential as a reinforcement material when compared to more established natural fibers like flax and hemp. Although the mechanical properties of the wool-based composites developed in this study are promising, they remain lower than some alternative natural fibers available in the sector. Future research will focus on the incorporation of wool fibers with other reinforcement materials to further enhance the mechanical properties and to continue addressing the flammability issues inherent in natural fiber composites.

Acknowledgement: *The authors acknowledge the project "Sustainable Industrial Design of Textile Structures for Composites," which is funded by the European Union. Grant Agreement no. 101079009 Call: HORIZON-WIDERA-2021-ACCESS-03/Twinning. Acronym: SustDesignTex. The authors are also thankful to Rebecca Emmerich at Institut für Textiltechnik of RWTH Aachen University for the support provided during the preparation of the composites.*

REFERENCES

1. Rajak D.K., Pagar D.D., Menezes P.L., et al.: Fiber-reinforced polymer composites: Manufacturing, properties, and applications. Polymers, 11, 2019. https://doi.org/10.3390/polym11101667
2. Kumar S., Balachander S.: Studying the effect of reinforcement parameters on the mechanical properties of natural fibre-woven composites by Taguchi method. Journal of Industrial Textiles, 50, 2020, pp. 133–148. https://doi.org/10.1177/1528083718823292
3. Lemmi T., Barburski M., Samuel B.: Analysis of mechanical properties of unidirectional flax roving and sateen weave woven fabric-reinforced composites. Autex Research Journal, 21, 2021, pp. 2–7. https://doi.org/10.2478/aut-2020-0001
4. Poniecka A., Barburski M., Ranz D., et al.: Comparison of mechanical properties of composites reinforced with technical embroidery, UD and woven fabric made of flax fibers. Materials, 15, 2022. https://doi.org/10.3390/ma15217469
5. Baley C., Gomina M., Breard J., et al.: Variability of mechanical properties of flax fibres for composite reinforcement: A review. Industrial Crops and Products, 145, 2020, 111984 p. https://doi.org/10.1016/j.indcrop.2019.111984
6. Islam T., Chaion M.H., Jalil M.A., et al.: Advancements and challenges in natural fiber-reinforced hybrid composites: A comprehensive review. SPE Polymers, 2024, pp. 481–506. https://doi.org/10.1002/pls2.10145
7. Rashid M., Chetehouna K., Cablé A., et al.: Analysing flammability characteristics of green biocomposites. Fire Technology, 2021. https://doi.org/10.1007/s10694-020-01001-0
8. Khatkar V., Vijayalakshmi A.G.S., Manjunath R.N., et al.: Experimental investigation into the mechanical behavior of textile composites with various fiber reinforcement architectures. Mechanics of Composite Materials, 56, 2020, pp. 367–378. https://doi.org/10.1007/s11029-020-09888-0

HYDROPHOBIC AND ANTIBACTERIAL TREATMENT OF JUTE FIBERS AND STUDY THEIR APPLICATION IN BIO COMPOSITES DEVELOPMENT

MAHVISH, FATIMA[1] AND WASEEM, IJAZ[2*]

[1] Department of Physics, College of Science, Qassim University, Buraydah 51452, Qassim, Saudiarabia.
[2] Department of Chemistry, Riphah International University, Faisalabad, Pakistan.

ABSTRACT

Bio-composites refers to composite materials made from sustainable materials. Jute fiber reinforced composites have inherent problem due to moisture and bacterial attack. The developed green composites are having resistance against environmental factors. At first, waste of jute fibres was pre-treated. Then two different approaches were adopted to enhance ageing factors of developed green composites. This research was proposed to go through methyltrimethoxysilane (MTMS), hydrophobic treatments, and for antipathogenic effect with ZnO nanoparticles were used. Morphological effects of chemical treatments on the jute fibers was analysed by scanning electron microscope. A significant decrease in moisture regain, increase in antibacterial zone of treated and untreated reinforcement samples was observed, when the concentration of chemical finish (methyltrimethoxysilane (MTMS) was 30 g/L and ZnO NPs also 30g/L was used. Subsequently the effects on the both mechanical properties and regain of moisture of composites reinforced with jute fiber was observed. At the concentration of 30 g/L a notable difference was spotted in moisture regain values of both treated and control (untreated) samples of reinforcement. Treated based composites regain less content of moisture and presents better mechanical properties (tensile strength and flexibility).

KEYWORDS

Antibacterial; Bio-composites; Chemical treatment; Moisture regain; ZnO nanoparticles; Degradation.

INTRODUCTION

The word "bio-composites" refers to composite materials that use biopolymers as the embedding matrix or natural reinforcing fibers [1]. Jute, flax, hemp, kenaf, and sisal are among the natural fibers that are most frequently utilized as reinforcement in bio-composites [2]. Because of its many unique qualities, affordability, ease of access, and environmental friendliness, jute is a highly valued degradable natural fiber in composites. The jute fiber has drawn the consideration as support for composite materials due to its biodegradability, quality to weight proportion and great insulation properties. In any case, higher dampness assimilation of these strands prevents the utilize of this fiber in composites. The dampness retention may cause the swelling and maceration of the strands, hence essentially diminishing its mechanical properties. So, the jute fiber got to be altered either physically or chemically to make strides the compatibility between the fiber and the polymer matrix. The surface of common filaments is ordinarily chemically altered to minimize the wetting of strands as well as to move forward the interface between the matrix and the reinforcement. A few chemical surface adjustment methods incorporate treatment with sodium chlorite[3], methaacrylate [4], isocyanate [5], silane treatment [6], acetylation [7], , mercerization [9] [10] etherification [11], enzymatic treatment [12] , peroxide medications [10], benzoylation [9], dicumyl peroxide treatment [5], plasma treatment [13], ozone medications [14] [15] and joining [16] [17]. The oxidation of polyolefins [18], [19] has moreover been detailed to move forward the contradiction between the surfaces of characteristic fiber and polymer network. All these medications are pointed to decrease the dampness recapture of the characteristic strands and their resulting composites. It is well-documented that materials with lower surface free energy exhibit reduced moisture regain [20]. Methyltrimethoxysilane (MTMS) surface free energy compared to most compounds used in previous studies. Despite their lower surface tension, methyltrimethoxysilane (MTMS are not commonly utilized in treating jute fibers for composite applications. Jute fibers are less immune towards microorganisms, like synthetic fibers which give an excellent environment to microorganisms for growth due to their moisture-retaining property Different

* **Corresponding author:** Waseem I., e-mail: *ijazw4357@gmail.com*

types of bioactive nanoparticles and materials have been used to enhance the antipathogenic effect in reinforcements and composites [20].

Therefore, this study aimed to decrease the moisture absorption of composite materials made from jute reinforcement treated with methyltrimethoxysilane (MTMS) (silane finshes) to investigate the properties of these composite materials, and to validate our assumptions regarding MTMS. Moreover, second objective was to eliminate the ageing effect that comes due to the bacterial attack. The jute fiber reinforcements were further treated with ZnO NPs to gain the antipathogenic properties. Subsequently, Composites were fabricated by hand layup technique. The composites can be used in a number of application fields such as door panels, auto structure building materials, and furniture etc.

MATERIALS AND METHOD

Plain woven fabric with a density of 194 ± 2 g/m^2 was used to reinforce the bio expoxy resin matrix were purchased from resin research, and 1% cobalt naphthenate and methyl ethyl ketone were used as an accelerator and hardener. The chemical used in this study, methyltrimethoxysilane (MTMS), and ZnO nanoparticles were purchased from HUNTSMAN (Pvt).

Pre-treatment of Jute fibres

Initially, jute fibers were pre-treated (scourged) before performing various chemical treatments. For scrubbing, jute cloth was dipped in a pot of water and boiled. 10 g/L of NaOH, 2 g/L of detergent (Teepol), 2 g/L of wetting agent, and 2 g/L of Teepol detergent, two grams per liter of wetting agent, and two grams per liter of sequestering agent had been added to the pot. In order to ensure proper fabric penetration, the wetting agent has been applied. Sequestering agents have been used to extract minerals and heavy particles. At 70 °C, the jute cloth was stirred periodically for 60 minutes.

Hydrophobic treatment of Jute fibers

Jute fibers were hydrophobically treated with methyltrimethoxysilane (MTMS). The critical surface tension of methyltrimethoxysilane (MTMS) is 20–25 mN/m, which is extremely low [21]. Distilled water was used to dissolve methyltrimethoxysilane (MTMS) at three distinct concentrations (10, 20, and 30 g/L). With the aid of acetic acid, the pH of the solution was kept at 6. After dipping jute fabric in the prepared solution for half an hour at room temperature, the surplus liquid was squeezed out using a padder. Fibers were then dried for five minutes at 100 °C.

Antibacterial treatment of Jute fibers

Jute fibers were treated antibacterially using ZnO nanoparticles. ZnO nanoparticles dissolve in distilled water at three different concentrations (10, 20, and 30 g/L). After that, 2 g/L of the binder MTEX was added to the solution. The fabric was submerged in these solutions for 30 min. The cloth was crushed with a padder to remove any leftover moisture, and it was then dried at 100 °C for 5 minutes. Table 1 illustrates the reinforcement experiment design.

Composite fabrication

The hand lay-up approach was used to produce the composites. With a composite plate size of 200×200 mm^2 and a fiber volume proportion of 33%, they utilized eight layers of woven jute cloth as reinforcement. After an hour of initial treating at ambient temperature, three hours of post-curing were conducted at 120°C. Untreated jute reinforcement and jute reinforcement treated with methyltrimethoxysilane (MTMS) hydrophobic compound was used to produce composites. Table 2 provides specifics about the composite samples developed for the investigation.

Table 1. The design of experiments for reinforcements treated with different chemicals.

Sr. #	Reinforcement samples	Chemicals	Concentrations [g/L]
1	R1	No treated	-
2	R2	Hydrophobic agent (methyltrimethoxysilane (MTMS)	10
3	R3	Hydrophobic agent (methyltrimethoxysilane (MTMS)	20
4	R4	Hydrophobic agent (methyltrimethoxysilane (MTMS)	30
5	R5	ZnO nanoparticles	10
6	R6	ZnO nanoparticles	20
7	R7	ZnO nanoparticles	30

Table 2. Experimental design for composites samples.

Sr. #	Samples ID	Reinforcement ID	Chemicals
1	S1	R1	No
2	S2	R4	methyltrimethoxysilane (MTMS)
3	S3	R7	ZnO particles
4	S4	Simple resin	No

Surface Characterization

The morphological characteristics of treated reinforcements and ZnO nanoparticles have been evaluated by particle size analysis (Malvern Zetasizer) and scanning electron microscopy (Zeiss). SEM was used to study each variation in the shape of the ZnO particles. This can be achieved by using the 15K accelerated voltage.

Moisture regain of reinforcement

The moisture recovery test of a chosen jute cloth was examined using the standard test method known as ASTM D2495. Both treated and untreated jute fabrics were utilized in the tests. A well-known oven dry method was used to determine how much moisture the material had absorbed in a controlled environment. Additionally, composite samples were tested according to the standard test procedure known as ASTPMD5229 in order to examine the amount of moisture exchange.

Mechanical properties

Universal tensile strength tester measured the ultimate tensile strength using the standard testing approach [22]. Moreover, a standardized testing method named ASTM D7264 was applied to explore flexural properties via three-point bending test.

Antibacterial assessment

The standard AATCC-147disc diffusion method was followed to provide a qualitative assessment of all reinforcement and composite samples.

RESULTS AND DISCUSSION

Surface morphology

The surface morphologies of jute fiber, both treated and untreated, were examined using a scanning electron microscope. Figure 1 displays images of the untreated and nanoparticles treated (ZnO particle) fibers. In fact, a network of smaller particles can develop. The constant connection and impact coating between the tiny ZnO nanoparticles were noted. The deposition of ZnO nanoparticles were combined and evenly distributed throughout the whole surface of fiber substrate. It was discovered that the coated surface of fibers was entirely covered. It was found that particles deposition was more consistent and dense. The prepared coating sample was found to have the potential to produce a thicker layer over the fiber surface.

Moisture regain of reinforcement

The moisture regains %age of untreated fabric sample and those samples treated with methyltrimethoxysilane (MTMS) (silane finishes) as function of their concentrations is shown in Figure 2. The percentage of humidity regain of fibers treated with methyltrimethoxysilane (MTMS) of R4 (30g/L) is the lowest when compared to all other samples. The supplier of the chemicals states that they include hydrophobic reactive groups as required by the technical applications for which they are desired. In fact, the mechanism involved the cross-linking during curing, their interaction with the -OH groups in cellulose, and the development of films on fiber. Regarding methyltrimethoxysilane (MTMS), films formed on fibers primarily display hydrophobic chains, whereas films formed using methyltrimethoxysilane (MTMS) show both hydrophobic and hydrophilic chains. Figure 2 further, indicates clearly that the treated sample has a moisture regain of 3.83–7.38%, while the untreated sample has a moisture regain of roughly 12%. Furthermore, at a concentration of 30g/l, treated R4 reinforcement shows a lower moisture recovery value of 2.71%. In contrast, at a concentration of 30g/l, the moisture regain values of R2 and R3 are roughly 3.10% and 3.05%, respectively.

Moisture regain of composite

In the equilibrium condition, Figure 3 displays the moisture regain %age of composite samples made from both untreated and treated jute cloth. The plain resin sample had a moisture regain %age of 0.29%. In contrast to the 12% moisture regain of jute cloth, the untreated jute composite sample absorbed 4% moisture.

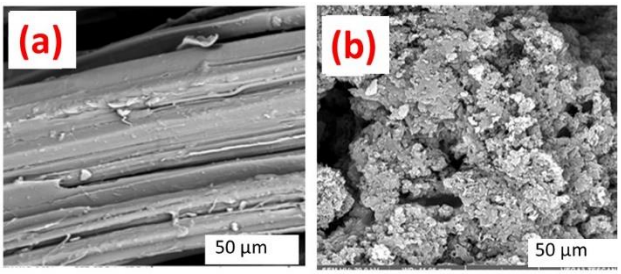

Figure 1. The Surface morphologies of (a) Untreated jute, (b) ZnO nanoparticles deposited.

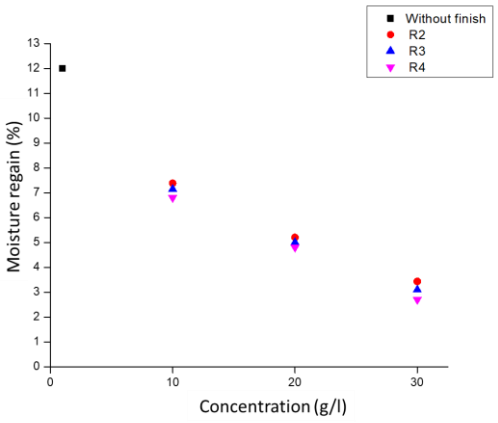

Figure 2. Moisture regain of untreated and treated fabric as function of chemical concentration.

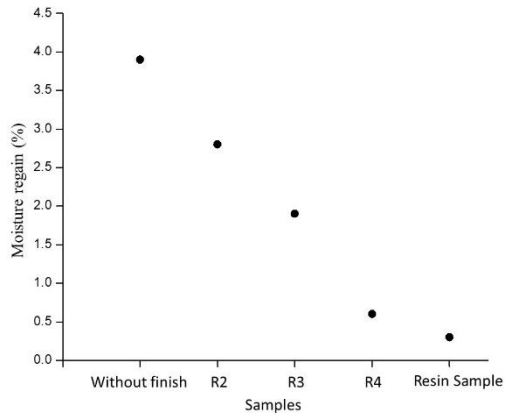

Figure 3. Moisture regain of resin and composite samples in equilibrium state.

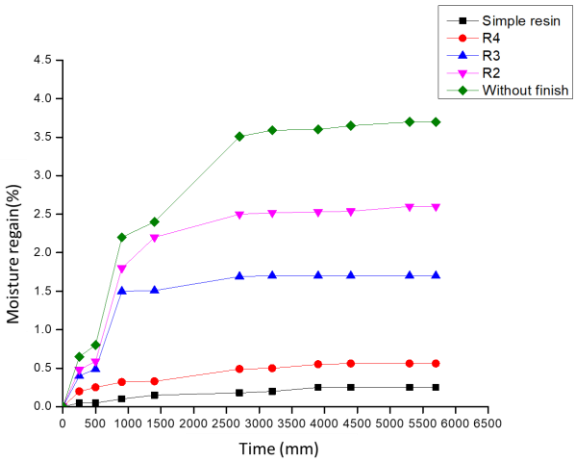

Figure 4. Moisture regains of composite samples.

The regain of moisture in composites and samples of clear resins verses the square root of time is shown in figure 4. All of the composite samples showed a consistent increase in moisture intake from the start to the 1000-minute mark. This makes sense because all test specimens were completely dried. Generally, figure 4 depicts the moist after 1000 minutes, the saturation of specimen began, and the rate of moisture recovery slowed. Almost every sample got saturated after 3000 minutes. To ensure that samples recovered the maximum amount of moisture and reached equilibrium, the test duration was extended.

Mechanical Properties

Analysis of the mechanical properties was performed on each composite sample. Following the ASTM D3039 standard, the tensile strength tester calculated the strength at break. The largest load that composites can withstand before failing was used to determine the maximum tensile strength of the manufactured composites. The tensile strength of every composite sample generated is shown in Figure 5. The tensile and flexural characteristics of composite materials were shown in table 3. S2 and S3 are composite sample created with treated reinforcement and S1, untreated reinforcement, While S4 only resin sample (having no reinforcement. Each sample is different in strength, because the strength of reinforcement has a significant impact on the strength of composite. The tensile strength of composites made with R7 (S3), reinforcement is greater than that of composites made with R1 and R7 reinforcement. Composites with treated reinforcing have varying tensile strengths. It is due to that R7 has

Table 3. Mechanical properties of composite materials.

Sr. #	Samples ID	Reinforcement ID	Chemicals	Tensile Strength [MPa]	Flexural Strength [MPa]
1	S1	R1	No	32.34	38.71
2	S2	R4	methyltrimethoxysilane (MTMS)	42.56	67.11
3	S3	R7	ZnO particles	48.72	81.73
4	S4	Simple resin	No	43.23	56.39

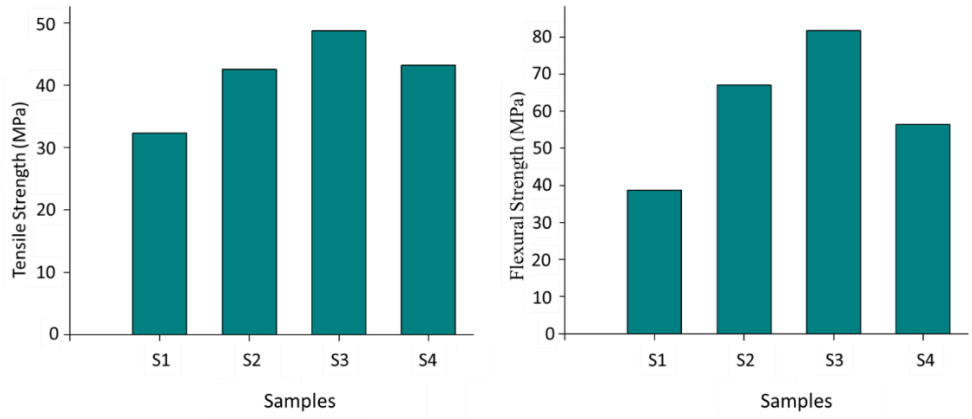

Figure 5. Mechanical properties of composite samples, (a) Tensile strength and (b) Flexural Flexural strength.

Table 4. Antibacterial properties of composite material.

Sr. #	Samples ID	Reinforcement ID	Chemicals	S. Aureus ZOI [mm]	E. Coli ZOI [mm]
1	S1	R1	No	0	0
2	S2	R4	methyltrimethoxysilane (MTMS)	0	0
3	S3	R7	ZnO particles	4	3
4	S4	Simple resin	No	0	0

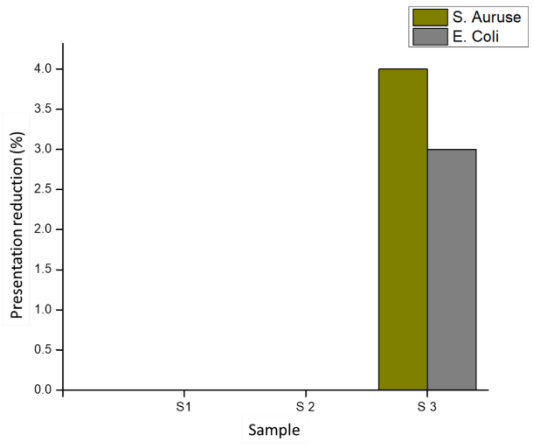

Figure 6. Antibacterial properties of composite samples against *E. coli* and *S. Aureus*.

higher concentration of ZnONPs. The provided data makes it evident that the treated reinforcement flexural strength of composite is greater than that of the sample of untreated reinforcement composites. This can be explained by the fact that the treated reinforcement is more powerful than the untreated one. Because of its improved resin-matrix interaction, the R2 treatment produced the biggest deflection.

Antibacterial Properties

The antibacterial properties of composite materials are shown in table 4. The antibacterial activity was tested against Gram-negative *Escherichia coli* (*E. coli*) and Gram-positive *Staphylococcus aureus* (*S. aureus*). S1 sample, which was not treated with any chemical showed no zone of inhibition against both bacteria (*E. coli* and *S. aureus*). Sample S2, treated with methyltrimethoxysilane (MTMS), also showed no antibacterial activity as MTMS is not an antibacterial agent. Sample S3 is treated with ZnO nanoparticles (antibacterial agent) displayed significant antibacterial properties. These results suggest that the sample S3 has moderate antibacterial properties, whereas S1 and S2 lack efficacy against the tested bacteria. Two nano ZnO composite films, ZnO/PC and ZnO/LLDPE, were made with a low doping of 0.2%. Compared to the ZnO/PC film, the ZnO/LLDPE film had a greater antibacterial rate (99.3% vs. 55.4%). ZnO/PC and ZnO/LLDPE had a 99.9% antibacterial rate when the nano ZnO concentration was quadrupled to 0.2%. Both composites can therefore attain a high degree of antibacterial activity [24].

CONCLUSIONS

This study concludes that there is a notable difference in the moisture regain between untreated and treated reinforcements. The reinforcement treated with methyltrimethoxysilane (MTMS) exhibited the lowest moisture regain value of 2.71% at a concentration of 30 g/L, in contrast to the other treatments. Reinforcement in the composite absorbs more moisture, as the moisture regain % for the pure resin sample was only 0. undefined Untreated jute composite sample has a moisture regain of 4% whereas for the composites prepared by using the methyltrimethoxysilane (MTMS) treated reinforcement has the lowest moisture regain of 0. 79% thus conforming the moisture regain of the corresponding reinforcement. Mechanical result comparison between the composite sample with untreated reinforcement and treated reinforcement showed the difference exists. ZnO nanoparticle-treated composites showed the greatest tensile strength (48.72 MPa) and flexural strength (81.73 MPa) because of improved resin-fiber bonding and consistent nanoparticle deposition. Zones of inhibition (ZOI) for *S. aureus* and *E. coli* were 4 mm and 3 mm, respectively, indicating considerable antibacterial efficacy in ZnO nanoparticle-treated composites, but MTMS-treated composites showed no antibacterial activity. When bio-epoxy resin is combined with hydrophobic and antibacterial treatments, it may find use in settings that need bacterial protection, mechanical endurance, and moisture resistance.

REFERENCES

1. Campbell F.C.: Structural Composite Materials. Ohio: ASM International, 2010, pp. 29–43.
2. Gay D., Hoa S.V., Tsai S.W.: Composite Materials: Design and Applications, 1st ed. Florida: CRC Press, 2003, 552 P.
3. Khan G.M.A., Alam S.: Surface chemical treatments of jute fiber for high value composite uses. Journal of Material Sciences, 1(2), 2013, pp. 39–44.
4. I. Cantero G., Arbelaiz A., Llano-Ponte R., et al.: Effects of fiber treatment on wettability and mechanical behaviour of flax/polypropylene composites. Composites Science and Technology, 63(9), 2003, pp. 1247–1254. https://doi.org/10.1016/S0266-3538(03)00094-0
5. Joseph K., Thomast S.: Effect of chemical treatment on the tensile properties of short sisal fibre-reinforced polyethylene composites. 37(23), 1996, pp. 5139–5149. https://doi.org/10.1016/0032-3861(96)00144-9
6. S. Alix S., Lebrun L., Morvan C., et al.: Study of water behaviour of chemically treated flax fibers-based composites: A way to approach the hydric interface. Composites Science and Technology, 71(6), 2011, pp. 893–899.

https://doi.org/10.1016/j.compscitech.2011.02.004
7. John M.J., Anandjiwala R.D.: Recent developments in chemical modification and characterization of natural fiber-reinforced composites. Polymer Composites, 29(2), 2008, pp. 187–207. https://doi.org/10.1002/pc.20461
8. V. de Velde, Kathleen, Kiekens P.: Thermoplastic polymers: overview of several properties and their consequences in flax fibre reinforced composites. Polymer Testing, 20(8), 2001, pp. 885–893. https://doi.org/10.1016/S0142-9418(01)00017-4
9. Joseph K. et al.: Natural fiber reinforced thermoplastic composites. Natural Polymers and Agrofibers Composites, 159, 2000, pp. 159–201. https://doi.org/10.1016/B978-0-12- 821090-1.00015-6
10. Sreekala M., Kumaran M., Joseph S., et al.: Oil palm fibre reinforced phenol formaldehyde composites: influence of fibre surface modifications on the mechanical performance. Applied Composite Materials, 7(6), 2000, pp. 295–329. https://doi.org/10.1023/A:1026534006291
11. Matsuda H.: Chemical Modification of Solid Wood, 1st ed. New York: Marcel Dekker Inc., 1996, 159 p.
12. Grönqvist S., Buchert J., Rantanen K., et al.: Activity of laccase on unbleached and bleached thermomechanical pulp. Enzyme and Microbial Technology, 32(3), 2003, pp. 439–445. https://doi.org/10.1016/S0141-0229(02)00319-8
13. Uehara T., Sakata I.: Effect of corona discharge treatment on cellulose prepared from beech wood. Journal of Applied Polymer Science, 41(7-8), 1990, pp. 1695–1706. https://doi.org/10.1002/app.1990.070410728
14. Hedenberg P., Gatenholm P.: Conversion of plastic/cellulose waste into composites. II. Improving adhesion between polyethylene and cellulose using ozone. Journal of Applied Polymer Science, 60(13), 1996, pp. 2377–2385. https://doi.org/10.1002/(SICI)1097-4628(19960627)60:13<2377::AID-APP9>3.0.CO;2-B
15. Shiffman D.: Chapter 7: Cellular automata. Nature of Code, 2012. Chtourou H., Riedl B., Kokta B.V.: Strength properties of wood-PE composites: Influence of pulp ratio and pretreatment of PE fibers. TAPPI Journal, 80(4), 1997, pp. 141–151.
16. Hon D.N.-S.: Graft copolymerization of lignocellulosic fibers. Washington D.C: American Chemical Society, 1982, pp. 3–19.
17. Meyer J.: Wood-polymer composites and their industrial applications. in Wood Technology: Chemical Aspects. Washington D.C: American Chemical Society, 1977, pp. 301–325. https://doi.org/10.1021/bk-1977-0043.ch020
18. Gugumus F.: Thermooxidative degradation of polyolefins in the solid state-6. Kinetics of thermal oxidation of polypropylene. Polymer Degradation and Stability, 62(2), 1998, pp. 235–243. https://doi.org/10.1016/S0141-3910(98)00004-4
19. Kotoyori T.: Activation energy for the oxidative thermal degradation of plastics. Thermochimica Acta, 5(1), 1972, pp. 51–58. https://doi.org/10.1016/0040-6031(72)80018-2
20. Arkles B., Pan Y., Kim Y.M.: The Role of Polarity in the Structure of Silanes Employed in Surface Modification. Silanes and Other Coupling Agents, 5, 2009, pp. 51–64.
21. Okada Y.S., Okada Y.H.M., Shibata T.: Surface Tension of HFC Refrigerant Mixtures. International Journal of Thermophysics, 1, 1999, 20 p.
22. Ali A., et al.: Fabrication of Conductive, High Strength and Electromagnetic Interference (EMI) Shielded Green Composites Based on Waste Materials. Polymers, 14(7), 2022, 1289 p. https://doi.org/10.3390/polym14071289
23. Sever K., Sarikanat M., Seki Y., et al.: Surface treatments of jute fabric: The influence of surface characteristics on jute fabrics and mechanical properties of jute/polyester composites. Industrial Crops and Products, 35(1), 2012, pp. 22–30. https://doi.org/10.1016/j.indcrop.2011.05.020
24. Wang Y., et al.: Antibacterial properties and mechanism of nanometer zinc oxide composites. Online: https://ssrn.com/abstract=4400851

INVESTIGATION OF THE EFFECT OF SOFTENERS ON COTTON KNITTED FABRIC STIFFNESS

GÜLER, BUKET[1*]; KALKAN, ISMET EGE[2]; ÇELEBI, ŞAMIL[1] AND ŞAHIN, UMUT KIVANÇ[2]

[1] TYH Textile Research and Development Center, Istanbul, Turkey.
[2] Department of Textile Engineering, Istanbul Technical University, Istanbul, Turkey.

ABSTRACT

Textile comfort of the fabrics is becoming very popular and soft touch is one of the prominent features. The main desired properties of cellulosic knits are their pleasant appearance, softness, absorbency, breathability, texture and comfort, which make them ideal for use in casual wear, sportswear, underwear, etc. Improving the performance and properties of cellulosic knits such as dimensional stability, smoothness, drapability, etc. through functional finishes is becoming necessary to cope with the demands of consumers and garment manufacturers. In this novel study 2 types of knitted structures (single jersey and pique) made of 100% cotton were used. Three different softening chemicals (macro silicone, micro silicone and seam facilitator) were used and acetic acid were used as a binding agent. According to the results, it was determined that macro silicone softener in single jersey knitted fabric and seam facilitator softener in pique knitted fabric gave more effective results in terms of hand feeling properties.

KEYWORDS

Comfort; Finishing; Hand feeling; Softener; Cotton.

INTRODUCTION

Comfort is a fundamental characteristic in the evaluation of clothing products, making it a key focus for textile manufacturers [1]. The literature reveals that softeners are the most commonly used method to enhance fabric comfort, as they play an essential role in improving the hand feel, smoothness, appearance, and usability of textiles. Softening treatments are typically applied after dye finishing as part of the finishing processes to ensure a soft touch and appealing look [2-4].

Textile materials are composed of various polymers, including natural cotton, cellulosic fibers, synthetic polyesters, and blends of these fibers. The combination of fibers directly influences the final quality and tactile feel of the fabric, which drives manufacturers to continuously improve fabric quality, smooth its surface, and enhance performance. In this regard, softeners are indispensable in textile production, with silicone-based softeners being especially common in enhancing fabric softness and tactile appeal [5].

There are studies about softener effects in the literature. Süpüren Mengüç, Dalbaşı, Özgüney & Özdil (2019), investigated the effects of various softeners on the hand-feeling properties and washing durability of cotton and bamboo knitted fabrics. They determined that the softening process did not have a successful performance in bamboo fabrics as in cotton fabrics. Hossain, Siddika & Islam (2019), examined the hand feel properties of single jersey fabric treated with three different types of cationic softener. They determined that aliphatic condensation softener gave the best results in terms of color fastness and hand feel properties of the fabric [6]. In another study; Illeez, Dalbaşı & Kayseri (2015), investigated the effects of parameters such as knitting structure, softener type and chemical concentration on sewability and seam shrinkage in ready-made clothing in cotton knitted fabrics. They found that softening treatments significantly improved sewability and seam shrinkage [7]. Silicone softeners are one of the most commonly used types of softeners in the textile industry. The use of silicone softeners is especially common in premium textile products and in areas that require high performance, such as sportswear and outerwear. These softeners are generally applied by the pad-dry-cure method and extend the life of textile products thanks to their long-term effects. These versatile advantages of silicone softeners make them a popular choice among textile manufacturers and consumers.

The aim of the study is to apply different types of softeners to fabrics with different knitted structures containing cotton and evaluate their findings. It is

[*] **Corresponding author:** Güler B., e-mail: *buketguler@tyh.com.tr*

believed that the study will provide new data aimed at optimizing parameters such as overall user comfort. This study aims to provide scientific and practical information to textile manufacturers and researchers on the selection of softeners by examining in detail the effects of softeners on the hand feeling properties of fabrics.

EXPERIMENTAL

In the scope of the study, macro silicone, hydrophilic silicone and seam facilitating softeners were applied on cotton fabrics with different knitting type. Cotton was preferred in the study because it is one of the most widely used textile fibers in the world. For this purpose, single jersey and double pique fabrics were chosen for this study and treated with three types of softeners. Softener types were applied to the fabrics by pad-dry method. The concentration level applied was determined to be average, consistent with commercial practice. After the chemicals were applied, they were left to dry at 100 °C for half an hour. Then, stiffness test was performed and comparative analysis was carried out to evaluate the effect of different knitted structure. The bending strengths of the fabrics were determined with a digital pneumatic softness tester according to the ASTM (American Society for Testing and Materials) D 4032-08 circular bending test method. Details of the applied softeners are given in Table 1.

RESULTS AND DISCUSSION

Bending strength tests were carried out on test specimens of knitted fabrics of different structures before and after softening treatment. The fabric stiffness tester measures the force applied to a fabric under a standard pressure and the results are expressed in kgf. The results of the test specimens are given in Table 2.

It was observed that macro silicone softener decreased the stiffness (hardness) value by 5% in single jersey fabric, while hydrophilic softener increased the hardness by 63% and seam facilitator softener increased the hardness by 72%. It was determined that macro silicone softened the pique fabric by 11.5%, hydrophilic silicone by 43% and sewing facilitator softener by 60%.

According to the tests, it was found that all softeners applied gave effective results on pique fabric. It was observed that hydrophilic silicone and seam facilitator finish had a negative effect on single jersey knitted fabric at the applied concentration. While it was observed that seam facilitator softener was more effective in pique fabric, it was determined that macro silicone was more effective in single jersey fabric.

In the literature, it is known that softeners cause a decrease in bending properties due to the decrease in friction forces between yarns caused by the lubrication effect. However, fabric structure plays a decisive role on the effectiveness of the finish [8]. It has been determined that the knitting structure and surface characteristics of the fabric can affect the way softeners penetrate the fabric and show their effects.

Single jersey fabrics have a fine and dense knitting structure. This structure makes the fabric more flexible and lighter. Therefore, it can be easier for softeners to penetrate the fabric. However, softeners that provide a thinner and homogenous spread to increase the feeling of softness will be more effective in jersey. Pique fabric, which has a thicker and bulkier structure, is usually heavier and stiffer than single jersey. In this fabric, the effect of softeners should be able to penetrate deeper. The softeners used in pique fabric may need to have a more intense effect due to the volume and textural differences in the knitting structure. In addition, softeners work on the fabric by different mechanisms. Macro silicone-based softeners provide lubricity by adhering to the fiber surface and it is thought that such softeners can create a more pronounced effect on thinner fabrics (such as single jersey). Hydrophilic silicone softeners increase the water absorbency of the fabric and give softness to the fabric. This type of softener is considered to be more effective on thicker fabrics with high moisture retention capacity, such as pique. The seam facilitating finish has a hydrophobic structure and is thought to facilitate sewing operations by reducing friction between the fibers and making the fabric smoother.

As a result, even though they are produced from the same raw material, the fact that single jersey and pique fabrics have different structure and surface properties causes the effects of softeners on the fabric to vary. The thickness and texture of the fabric and the chemical structure of the softeners are the main factors determining which softener is more effective. It is thought that the hardening effect of hydrophilic and seam facilitating softeners on single jersey fabrics is related to the applied concentration. For this reason, it has been observed that optimum concentration settings of softeners are important. Determining the ideal concentrations for different fabric structures is critical to achieve the desired results.

Table 1. Details of softener application process.

Softener	pH	Concentration (g/L)	Pick up (%)
Macro silicone (polysiloxane)	5	40	80
Hydrophilic silicone	5	40	80
Seam facilitator (polyethylene emulsion)	5	40	80

Table 2. Test results.

Fabric	Stiffness [kgf]			
	Non-treated	Softener 1 (macro silicone)	Softener 2 (hydrophilic silicone)	Softener 3 (seam facilitator)
Single jersey	0.024	0.022	0.039	0.041
Pique	0.072	0.064	0.041	0.028

CONCLUSIONS

Within the scope of the study, the stiffness properties were analyzed by applying equal concentrations of macro silicone, hydrophilic silicone and seam facilitator (polyethylene emulsion) softening finishes to single jersey and pique fabrics containing 100% cotton. As a result, it was determined that macro silicone finish provided a low amount of softening in single jersey fabrics at the applied concentration, while other silicones made the fabric even stiffer. In pique fabrics, it was found that all softening chemicals provided softening, but the maximum softening was provided by the seam facilitator finish.

In conclusion, the investigation provides valuable insights into the role of softeners in modifying the stiffness of cotton knitted fabrics. The findings highlight that careful selection and application of softeners can significantly enhance the tactile properties of fabrics. Additionally, it contributes to the development of softer and more comfortable cotton garments. It is thought that by understanding the specific effects of different fabric softeners on fabric stiffness, manufacturers can make informed decisions about the types and concentrations of softeners to be used, and tailor their products to meet specific consumer preferences for softness and comfort. In the continuation of the study, it is aimed to apply softeners to fabrics at different concentrations and to perform tests and analyses.

Acknowledgement: *The authors would like to thank TYH Textile Research and Development Center and Perge Tekstil İşletmeleri A.Ş. for their contributions.*

REFERENCES

1. Cimilli Duru S., Şahin U.K.: Effects of yarn type, process history, softener type and concentration on wicking and drying properties of cotton plain knitted fabrics. The Journal of The Textile Institute, 2019, pp. 1–10. https://doi.org/10.1080/00405000.2019.1689773
2. Hossain Md. S., Siddika A., Islam T.: Investigation of different cationic softener effects on shade appearance, colour fastness and hand feel properties of 100% cotton circular weft knitted single jersey fabric. Journal of Engineering Science, 10(1), 2019, pp. 85-92.
3. Illeez A.A., Dalbaşı E.S., Kayseri G.Ö. : Improving of sewability properties of various knitted fabrics with the softeners. Procedia - Social and Behavioral Sciences, 195, 2015, pp. 2786 – 2795.
4. Islam Md. S., Sazal Md. M.R., Ripon Md. M.I.: Variation of knit dyed fabric quality on different percentage of silicon softener. International Journal of Scientific & Engineering Research, 8(2), 2017.
5. Malwade S.R., Kulkarni R.R., Sayyed A.J.: Effect of block copolymer silicone softener on textile fabric hydrophilicity, softness, and durability. Journal of the Indian Chemical Society,101(8), 2024. https://doi.org/10.1016/j.jics.2024.101197
6. Orhan M., Tiritoğlu M., Ozbarutcu B.: Silikon yumuşatıcıların pamuk ve viskon örme kumaşlar üzerinde etkileri. Uludağ Üniversitesi Mühendislik Fakültesi Dergisi, 25(2), 2020, pp. 941-960. https://doi.org/10.17482/uumfd.660283
7. Süpüren Mengüç G., Özgüney A.T., Dalbaşı E.S., et al.: A comparative study on handle properties of bamboo and cotton fabrics. Industria Textila.70(3), 2019, pp. 278-284.
8. Gong R.H., Bhatia A.: Effects of Softeners on Mechanical Properties of Cotton Fabric. Research Journal of Textile and Apparel, 13(4), 2009, pp. 45–50. https://doi.org/10.1108/rjta-13-04-2009-b006

ANALYZING THE EFFECT OF BLENDING RATIO AND SPINNING SYSTEM ON THE PROPERTIES OF BAMBOO/COTTON FABRICS DYED WITH ACORN DYESTUFF

ÜZÜMCÜ, MEMIK BÜNYAMIN[1*]; SARIOĞLU, ESIN[1]; NACARKAHYA,TÜLIN[2]; SATIL, ŞEYMA[2] AND SARI, BURAK[3]

[1] Gaziantep University, Fine Arts Faculty, Department of Textile and Fashion Design, Gaziantep, Turkey
[2] Karafiber Tekstil San. ve Tic. A.Ş.R&D Center, Gaziantep, Turkey
[3] Bitlis Eren University, Fine Arts Faculty, Department of Traditional Turkish Arts, Bitlis, Turkey

ABSTRACT

In the context of sustainable development goals, a diverse array of contributing studies has emerged within the textile sector. It is evident that the majority of these studies encompass both legal and customer obligations. The objective of contemporary businesses is to manufacture products that demonstrate a high level of environmental sensitivity. For instance, the objective is to reduce the quantity of waste products, to achieve energy-efficient production, to minimize the amount of chemicals employed, to reduce water consumption, to utilize energy derived from renewable sources, and thus to diminish the carbon footprint. From an environmental standpoint, the chemicals utilized in textile product manufacturing have emerged as a significant consideration. It is preferable that the chemicals employed in the dyeing process (dyestuffs, bleaching agents, softeners, etc.) are environmentally sensitive. Furthermore, the use of organic dyes in the dyeing process is also employed as a means of obtaining a more sustainable product. In the context of this study, the production of bamboo/cotton yarn was conducted at varying blend ratios (67/33%, 50/50%, and 33/67%) through the use of three distinct production methods (open end, vortex, and ring systems). Single jersey knitted fabrics were produced using these yarns with the same production parameters. Subsequently, the fabrics were dyed using acorn natural dyestuff. Pilling, fastness and CIELab analyses were performed on the fabric samples, and the results were subjected to statistical analysis.

KEYWORDS

Sustainability; Organic dye; Acorn dye; Color fastness.

INTRODUCTION

The production of textiles is a highly intricate process, encompassing various mechanical, chemical, and physicochemical steps. These processes often involve the use of hazardous substances, including heavy metals and pesticides. However, they are subject to extensive monitoring and regulation by standards such as ZDHC (Zero Discharge of Hazardous Chemicals), OEKO-TEX (International Association for Research and Testing in the Field of Textile and Leather Ecology), and GOTS (Global Organic Textile Standard), with the aim of ensuring safety and reducing environmental impact [1].

In the present era, environmental sustainability represents a pivotal concern for the textile industry. The rapid changing fashion industry and the intensive use of chemicals present a significant challenge to achieving a sustainable future, with adverse effects on both the environment and human health. The textile industry is seeking novel and creative solutions that will enable it to become environmentally sustainable, with a view to reducing its reliance on natural resources, minimizing its carbon footprint and eliminating the generation of harmful chemical waste. In this context, dyeing with natural sources are attracting attention as an alternative to dyeing with synthetic dyestuff, offering a promising potential for sustainability.

Dyeing with natural sources is generally defined as the process of imparting color to textile products through the use of pigments derived from plants, minerals and other organic materials. The extraction of natural dye process typically begins with the collection of plant materials like roots, leaves, flowers, or bark. The dyes are then extracted using methods such as boiling, soaking, or fermentation [2-4]. The production of natural colorants promotes plantation, contributing to the reduction of atmospheric CO_2 and increasing oxygen levels. It can be asserted that there

* **Corresponding author:**Üzümcü M.B., e-mail: buzumcu@gantep.edu.tr

are certain disadvantages associated with the use of natural colors. Despite the necessity for a certain amount of time to obtain natural colorants, the yields are typically very low. The commercial production of natural colorant sources is not feasible on a large scale. Consequently, the low yield of natural colorants results in correspondingly high production costs [5].

The literature includes studies that examine the properties of textile products obtained from a variety of natural dyes. These studies investigate the application of different natural dyes on diverse raw materials and the associated quality analyses [6-16].

This study examined the use of acorn natural dyestuff in the production of single jersey fabrics produced nine different yarns with varying blend ratio and spinning systems.

EXPERIMENTAL

Materials

In this study, bamboo and cotton fibers were used in order to produce yarn samples at three different blend ratios (67/33%, 50/50%, and 33/67%). Yarns and knitted fabrics were produced with these blends. Fabrics were dyed with natural acorn dyestuff. In these dyeing processes $KAl(SO_4)_2$ was used as mordant.

Methods

To examine and compare the spinning systems, open end rotor, ring and vortex systems were chosen for yarn spinning in this study. Ne 30/1 nine different yarn samples with α_e 3.6 twist coefficient were obtained, then these yarns were knitted at the same production parameters. Single jersey knitted fabrics were dyed with acorn natural dyestuff. Tenacity and elongation, hairiness, imperfections and unevenness properties were carried out in accordance with related standards. In addition, weight, thickness, pilling, color fastness to water and rubbing (dry and wet) properties were also determined with related standards. Results were analyzed statistically using SPSS package program.

RESULTS AND DISCUSSION

Fiber Properties

In this study, 2 types of fibres were used. The properties of these fibres are presented in Table 1. These fibres were blended at different blend ratios and used to produce yarns in 3 different systems (ring, open end rotor and vortex).

Yarn properties

In this study, bamboo and cotton fibers with known fiber properties were blended in 3 different blend ratios and these blends were used in the production of ring, rotor and vortex yarns. Various yarn tests were carried out to determine the properties of the yarns produced. The measurements were taken in accordance with the following standards:

- TS EN ISO 2062 for strength and elongation tests,
- ISO 16549 for unevenness and yarn faults, and
- TS 12863 for unevenness determination.

In order to evaluate the results and ascertain the effects of the blend ratios of the fibers and the spinning system in which the yarn is produced, ANOVA tests were performed (Table 2). According to the results of this test, the spinning system has a statistically significant effect on all measured properties of the yarn. When the effect of blend ratio was analyzed, the effects of this parameter on yarn faults, strength and elongation were found to be significant.

When the yarn characteristics were analyzed (see Fig. 1), it was seen that ring-spun yarns have higher strength and elongation, lower yarn faults and unevenness values, and also the highest hairiness values. The lowest hairiness values were observed in vortex yarns for all blend ratios. Additionally, the tensile strength and elongation values of the yarns produced with the Vortex system are inferior to those of ring yarns. Rotor yarns were found to have the highest yarn faults, the highest unevenness values and the lowest strength and elongation. The data obtained in this study are similar to the literature [17] [18].

Table 1. Fiber Properties.

Fiber	Fineness [dtex]	Staple Length [mm]	Density [g/cm^3]	Strength [cN/tex]
Cotton	1.2	32	1,52	31,2
Bamboo	1.33	38	1.32	34

Table 2. Analysis of Variance Results of Yarn Properties.

Independent Variables	Dependent Variables				
	Unevenness [U%]	IPI	Hairiness [Uster H]	Elongation [%]	Tenacity [kgf*Nm]
Spinning system	**0.022***	**0.000***	**0.000***	**0.003***	**0.008***
Blend Ratio	0.086	**0.006***	0.262	**0.002***	**0.037***

*Statistically significant at 0.05 confidence level

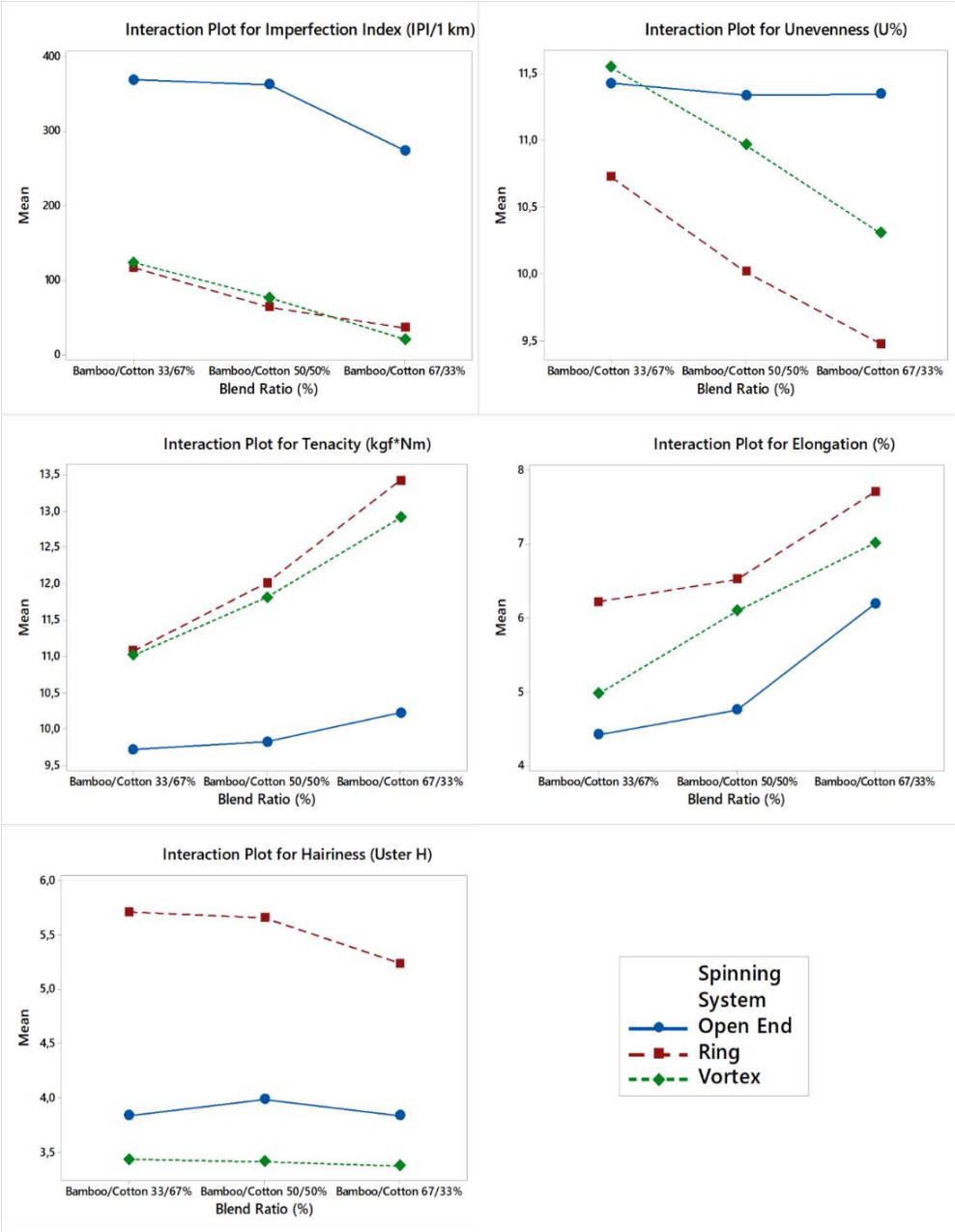

Figure 1. Interaction plots for different yarn characteristics.

When the yarn properties were evaluated within the framework of the blend ratio, it was found that an increase in the proportion of cotton in the blend caused higher unevenness values and more yarn faults. However, higher strength and elongation values were obtained in yarns with high bamboo content. It was an expected result that the increase in the ratio of bamboo fiber, which has higher strength, in the yarn positively affected the yarn strength. Hairiness was not much affected by the blend ratio. It was evident that hairiness was more influenced by the spinning system than by the raw material.

Fabric properties

As mentioned in the methods, single jersey fabrics were knitted using the same parameters. After fabric production all of these fabrics were dyed using acorn natural dyestuff. A number of tests were carried out to determine the properties of these dyed fabrics. The test results of these fabrics are given in Table 3.

When the results given in Table 3 are analyzed, it is seen that the highest air permeability is found in open end fabrics. This is an expected result in view of the low hairiness of rotor yarns. The difference in terms of blend ratio and spinning system as independent variables, is statistically significant according to ANOVA tests ($p=0.001<0.05$ for spinning system and $p=0.031$ for blend ratio). When pill grade values were analyzed, it was determined that the highest pilling resistance was achieved in fabrics produced with vortex yarns.

Table 3. Fabric properies.

Blend Ratio (B/C%)	Yarn Type	Thickness	Air Permeability	Pilling resistance
67/33	Ring	0.62	1358.68	2/3
50/50	Ring	0.59	1268.16	2/3
33/67	Ring	0.63	1415.42	2/3
67/33	Open End	0.53	1725.35	3/4
50/50	Open End	0.54	1866.49	3/4
33/67	Open End	0.57	1526.9	3/4
67/33	Vortex	0.62	1263.84	4/5
50/50	Vortex	0.62	1269.29	4/5
33/67	Vortex	0.65	1766.55	4/5

Table 4. Color Properties of acorn dyed fabrics.

Blend Ratio (B/C%)	Spinning System	Illuminant (D65 10 Deg)				
		L*	a*	b*	C*	h*
67/33	Ring	77.97	3.27	18.87	19.15	80.16
50/50	Ring	77.94	3.39	19.62	19.91	80.19
33/67	Ring	74.86	3.88	20.34	20.71	79.79
67/33	Open End	86.87	3.28	19.08	19.36	80.24
50/50	Open End	72.89	5.57	19.67	20.45	74.2
33/67	Open End	75.7	3.75	19.37	19.73	79.03
67/33	Vortex	77.06	3.61	19.37	19.7	79.43
50/50	Vortex	75.25	4.37	19.09	19.59	77.11
33/67	Vortex	75.15	4.29	19.66	20.12	77.69

Table 5. Color fastness to washing results.

Blend Ratio (B/C%)	Spinning System	Staining					
		Acetate	Cotton	Nylon	Polyester	Acrylic	Wool
67/33	Ring	4/5	4	4	4/5	4/5	4/5
50/50	Ring	4/5	4	4	4/5	4/5	4/5
33/67	Ring	4/5	4	4	4/5	4/5	4/5
67/33	Open End	4/5	4	4	4/5	4/5	4/5
50/50	Open End	4/5	4	4	4/5	4/5	4/5
33/67	Open End	4/5	4	4	4/5	4/5	4/5
67/33	Vortex	4/5	4	4	4/5	4/5	4/5
50/50	Vortex	4/5	4	4	4/5	4/5	4/5
33/67	Vortex	4/5	4	4	4/5	4/5	4/5

Table 6. Color fastness to rubbing results.

Blend Ratio (B/C%)	Spinning System	Rubbing	
		Dry	Wet
67/33	Ring	4	3/4
50/50	Ring	4	3/4
33/67	Ring	4	3/4
67/33	Open End	4	3/4
50/50	Open End	4	3/4
33/67	Open End	4	3/4
67/33	Vortex	4	3/4
50/50	Vortex	4	3/4
33/67	Vortex	4	3/4

Fabrics were dyed with acorn dyestuff as mentioned before. The color properties of these fabrics are given in Table 4. L value results indicate that the lightness of the fabrics increased with higher bamboo content. According to the other parameters in Table 4, it can be said that although there are some variations in the color of these fabrics, similar dyeing results were obtained.

Color fastness of these fabrics to water and rubbing (wet and dry) were also tested. Results of the staining on multifiber fabric after water treatment are given in Table 5. It can be seen from the results that the change in the spinning systems used for yarn production and the change in blend ratio for bamboo and cotton fibers did not affect these values.

Results of the staining on multifiber fabric after water treatment are given in Table 6. These results also indicate that there is no difference between the color fastness to rubbing results in terms of blend ratio and spinning system as independent variables.

CONCLUSIONS

In this study, acorn natural dyestuff was used in order to dye nine different types of single jersey bamboo-cotton blended knitted fabrics. Initially, yarns were produced with 3 different spinning systems (ring, rotor and vortex) with 3 different blend ratios (67%Bamboo-33%cotton, 50%bamboo-50%cotton and 33%bamboo-67%cotton). All these yarns were produced using the same αe 3.6 twist coefficient. After yarn productions single jersey fabrics were knitted using the same knitting parameters. In the end, fabrics were dyed, again, using the same dyeing parameters.

All the tests carried out during this study were done according to standards. These results were obtained at the end:

· Spinning system and blend ratio significantly affected yarn properties.

· Higher bamboo content in the blend resulted with lighter shades in fabrics.

· As both fibers are cellulosic and have similar structures, fastness results we investigated were similar (because of their interactions with the dye).

REFERENCES

1. Karadag R.: Establishing a new international standard for natural dyed textile goods [Natural Organic Dye Standard (NODS)]. Journal of Natural Fibers, 20(1), 2023, 2162187 p. https://doi.org/10.1080/15440478.2022.2162187
2. Pranta A.D., Rahaman M.T.: Extraction of eco-friendly natural dyes and biomordants for textile coloration: A critical review. Nano-Structures & Nano-Objects, 39, 2024, 101243 p. https://doi.org/10.1016/j.nanoso.2024.101243
3. Bishal A., Ali K.A., Ghosh S., et al.: Natural Dyes: Its Origin, Categories and Application on Textile Fabrics in Brief. European Chemical Bulletin, 12(8), 2023, pp. 9780-9802. https://doi.org/10.48047/ecb/2023.12.8.804
4. Singh K.A.R.U.N.A., Kumar P.A.N.K.A.J., Singh N.V.: Natural dyes: an emerging ecofriendly solution for textile industries. Poll Res, 39(2), 2020, pp. 87-94.
5. Uddin M.A., Rahman M.M., Haque A.N.M.A., et al.: Textile colouration with natural colourants: a review. Journal of Cleaner Production, 349, 2022, 131489 p. https://doi.org/10.1016/j.jclepro.2022.131489
6. Iqbal M., Panhwar A., Ahmed K., et al.: Textile dyeing of cotton and wool textile material with natural dyes extracted from bluish purple grapes. Bulgarian Chemical Communications, 54(1), 2022, pp. 14-18. https://doi.org/10.34049/bcc.54.1.5413
7. Benli H., Aydınlıoğlu Ö., Yılmaz F., et al.: Topping of naturally dyed wool fabrics with different natural dye sources. Coloration Technology, 139(2), 2023, pp. 171-181. https://doi.org/10.1111/cote.12648
8. Benli H., Bahtiyari M.İ.: Testing acorn and oak leaves for the UV protection of wool fabrics by dyeing. Journal of Natural Fibers, 19(14), 2022, pp. 7925-7938. https://doi.org/10.1080/15440478.2021.1958423
9. Pars A., Karadag R.: Sustainable Bio-Dyeing of Cellulosic-Based Fabrics with Anthocyanins from Black Carrot (L.). Fibres & Textiles in Eastern Europe, 32(3), pp. 50-56.
10. Chen J., Suo Q., Ni Y., et al.: Dyeing performance of wool fabric with natural pigment from Cordyceps militaris. The Journal of The Textile Institute, 115(9), 2024, pp. 1672-1682. https://doi.org/10.1080/00405000.2023.2261814
11. Ghosh J., Khan F., Noor T., et al.: Union dyeing of cotton-silk blended woven fabric using Tanin bio-mordant and thyme as a Colourant. Text Leather Rev, 7, 2024, pp.303-326.
12. Sankaralingam B., Balan L., Chandrasekaran S., et al.: Anthocyanin: a natural dye extracted from Hibiscus sabdariffa (L.) for textile and dye industries. Applied Biochemistry and Biotechnology, 195(4), 2023, pp. 2648-2663. https://doi.org/10.1007/s12010-022-03815-w
13. Nitayaphat W., Jintakosol T.: Dyeing of Pineapple Leaf Fibers Using Various Natural Dye Extracts and Mordants. Journal of Natural Fibers, 21(1), 2024, 2313867 p. https://doi.org/10.1080/15440478.2024.2313867
14. Melaku A., Demeke G., Aschale M., et al.: Extraction and Characterization of Natural Dye Stuff from Spent Coffee Ground and Bio-Mordant from Mango Bark. Journal of Natural Fibers, 20(2), 2023, 2276725 p. https://doi.org/10.1080/15440478.2023.2276725
15. Melaku A., Demeke G., Aschale M., et al.: Extraction and Characterization of Natural Dye Stuff from Spent Coffee Ground and Bio-Mordant from Mango Bark. Journal of Natural Fibers, 20(2), 2023, 2276725 p. https://doi.org/10.1080/15440478.2023.2276725
16. Rasool W., Adeel S., Batool F., et al.: Environmental friendly silk and cotton dyeing using natural colorant of Bougainvillea (Bougainvillea glabra) flowers: the sustainable approach towards textile industry. Environmental Science and Pollution Research, 30(8), 2023, pp. 21863-21871. https://doi.org/10.1007/s11356-022-23417-7
17. Anbumani N., Rameshkumar C., Anandkumar P., et al.: Comparitive studies on ring rotor and vortex yarn knitted fabrics. Autex Research Journal, 8(4), 2008, pp. 100-105. https://doi.org/10.1515/aut-2008-080402
18. Erdumlu N., Ozipek B., Oztuna A.S., et al.: Investigation of vortex spun yarn properties in comparison with conventional ring and open-end rotor spun yarns. Textile Research Journal, 79(7), 2009, pp. 585-595. https://doi.org/10.1177/0040517508093590

DEVELOPING CNN-AUGMENTED MODELS TO PREDICT CIELAB OUTCOMES POST-BLEACHING OF DENIM GARMENTS

KALKAN, İBRAHIM ERDEM[1*]; ÇALIŞKAN, EBRU[2]; ŞAHIN, CENK[1]; BALCI, ONUR[3] AND KUVVETLI, YUSUF[1]

[1] Çukurova University Department of Industrial Engineering Sarıçam, Adana, Turkey
[2] Baykan Denim R&D Center 2nd Organized Industrial Zone Yeşilyurt, Malatya, Turkey
[3] The University of Kahramanmaraş Sütçü İmam Textile Engineering Dep. 12 Şubat, K.Maraş, Turkey

ABSTRACT

Denim garment production demands efficient design processes to minimize waste, costs, and production delays. Bleaching, among other finishing processes, holds paramount importance due to its numerous variables and substantial impact on product value. Artificial neural networks have great potential to achieve superior performance in anticipating various process outcomes. Their parameterized structure effectively captures non-linear relationships between input features. This study aims to effectively predict fabric outcomes by developing an artificial neural network (ANN) model supported by convolutional neural networks (CNN) to provide additional features derived from raw and semi-processed fabric images. The study represents a comparison of CNN powered models with a common predictive ANN as base model. Competing models incorporate various process variables and fabric properties, such as dying number and elasticity to predict changes in denim CIELab properties after bleaching. The process features of the model are the number of bleaching cycles, total process time, and concentration of sodium hypochlorite (representing the total amount of chemical used). The mean absolute percentage error is used as the performance measure between predictions and desired outputs. This research plays a significant role in enhancing agility in denim production by providing businesses with more efficient approaches to digitized denim bleaching and Research and Development processes in the textile industry.

KEYWORDS

Denim; Bleaching; Effect; Artificial neural networks.

INTRODUCTION

Denim goes through various manufacturing processes that involve many variables, from fabric production to garment creation. The traditional denim processing begins with cotton fiber selection and dyeing the threads with indigo. Then, the denim fabric is woven using specific techniques [5]. After the garment is made, finishing processes are applied to achieve the desired aesthetic and comfort. These processes include techniques such as enzymatic washing, which can be optimized for fading color, comfort, and durability [6].

The bleaching effect is the process of removing or lightening the indigo from the surface of denim fabric. Typically, a strong oxidative bleach, such as sodium hypochlorite (NaOCl), potassium permanganate ($KMnO_4$), or hydrogen peroxide (H_2O_2), is used, and the bleaching process can be done with or without the addition of stones [7]. This process is labor-intensive, reliant on skilled workers, and considered as costly. Given the significance of bleaching, the importance of digitizing both bleaching-oriented production and related processes becomes apparent. By implementing decision support systems and associated predictive models, digitizing these processes will offer businesses a more agile and efficient approach. Efficiency improvements are crucially needed in the denim garment industry, particularly for businesses where labor, waste, and energy are significant costs.

The use of artificial neural networks (ANNs) in predicting the effects of processes applied to fabrics is encountered in studies. Farooq et al. employ an ANN system to predict the phenomenon of color change for different colors and shade percentages [8]. Mandal et al. model the relationships between measured fabric properties (such as thickness, weight, fabric count) and thermal protective performance and thermo-physiological comfort performance using an ANN to analyze garment performance [9]. Elkateb includes a study on

* **Corresponding author:** Kalkan İ.E., e-mail: iekalkan@cu.edu.tr

predicting output properties of woven fabrics with ANNs across different characteristics [10].

Anomaly detection on textile textures using "Variational Autoencoders" can be cited as an example of the use of images in textiles. In this application, the reconstructed images are compared with the original images, and the calculated reconstruction error is directly used to compute the anomaly score [11]. Another study used deep learning methods to approximately determine input parameters in laser texturing. Different combinations of laser parameters were selected to perform laser fading experiments on denim fabrics using laser technology in data generation, and denim image datasets with various laser fading effects were obtained. The trained convolutional neural network-based (CNN) prediction model produced an approximate parameter group based on the fading image and showed good performance with low prediction error according to the validation dataset [12].

In this study, the proposed CNN prediction models will equip businesses with an agile and thus more efficient approach to digitized denim bleaching in the denim garment industry. Proposed models have been developed to forecast the color properties of denim garments. To the best knowledge, this is the first study to predict color values using fabric images on deep learning models.

EXPERIMENTAL SETUP

This study aims to predict the possible changes in the physical properties of the denim garment after the sodium hypochlorite bleaching process, depending on the process variables and fabric properties to prevent production-related fabric defects. The basic steps of this effort are outlined in the following subsections: first, the material and its structure are described. Second, the data collection process and modeling details are presented, including explanations of the methods employed and the evaluation techniques use.

Materials

Prediction models have been developed based on collected data to forecast the "CIELab" color properties of denim garments. The CIELab color space, also known as L*a*b represents color using three parameters: L* for perceived lightness, and a* and b* for the four primary colors perceived by human vision: red, green, blue, and yellow. The models are built using 1,200 data points gathered from a full factorial design involving 1,200 experiments. The experiments focused on denim fabric type, process time, sodium hypochlorite concentration, and the replicate cycle of bleaching. The sodium hypochlorite bleaching process was conducted with two replicates. Three levels of process time were tested: 3, 5, and 7 minutes. Additionally, four concentration levels of bleach were selected: 2,000, 3,000, 4,000, and 5,000 ml. The bleaching cycle indicates how many times the same bleaching process is replicated to reach the desired visual effect.

50 different types of denim fabric are selected and four variables that can affect the color in the bleaching process have been included in the controlled experimental design. In addition, the constructional fabric properties as yarn count, weaving pattern and density, the CIELab values of raw and semi-processed fabric are accepted as inputs of the models. The semi-processing stage refers to intermediate steps in the bleaching process that prepare the denim for a final, controlled whitening or fading effect. In that stage a controlled amount of hydrogen peroxide is applied to the denim fabric and acts as a mild bleaching agent.

Methods

ANNs, ranging from simple computational units to complex architectures, are a heavily researched area in deep learning. Known for their versatility, strength, and scalability, ANNs excel at handling large-scale, highly intricate machine learning challenges. Their applications span from classifying billions of images to enabling advanced speech recognition systems [1]. ANNs also serve as powerful tools for predicting the outcomes of the processes handled in this research.

With techniques like stochastic gradient descent, ANNs can converge, although the solution may not necessarily reach the global optimum due to the presence of multiple local minima [2]. Additionally, while other machine learning methods require manually engineered features to be fed into the model as input, ANNs can extract useful features from the data without requiring an additional effort, thanks to the mechanism of weight updates [3]. However, when dealing with non-structural data types like image data, fully connected layers struggle to represent important features effectively. For example, even a small 100x100-sized image contains 10,000 inputs, and even if the first hidden layer has a high number of neurons, like 1,000, it may not capture a significant portion of the information [1]. As a result, a specialized structure known as a convolutional layer, commonly referred to as convolutional neural networks (CNNs), is necessary and has consistently delivered successful outcomes.

The convolution is the process of sliding filters of certain sizes, such as 3x3 or 5x5, over the 3-dimensional input data, stopping at every possible position to extract the 3-dimensional patch of environmental features. This patch corresponds to the region covered by the filter at that position. The process starts from the top-left corner of the data and continues towards the bottom-right corner. The weights of the filter are element-wise multiplied with the values in the patch, and the results are summed

Table 1. Input-Output configuration of models.

Attributes			ANN	CNN1	CNN2
INPUTS	Fabric Properties	Type of Dyeing	✓	✓	✓
		Elasticity	✓	✓	✓
		Onz/yd^2	✓	✓	✓
		Yarn Count	✓	✓	✓
		Density	✓	✓	✓
		Type of Weaving	✓	✓	✓
		CIELab (Raw Fabric)	✓	✓	✓
		CIELab (Semi-processed Fabric)	✓	✓	✓
	Process Features	The Number of Bleaching	✓	✓	✓
		The Bleaching Process Time	✓	✓	✓
		Sodium Hypochlorite Concentration	✓	✓	✓
	Image Features	Raw Fabric Images		✓	
		Semi-processed Fabric Images			✓
OUTPUTS	Color Properties of Processed Product	CIELab L*	✓	✓	✓
		CIELab a*	✓	✓	✓
		CIELab b*	✓	✓	✓

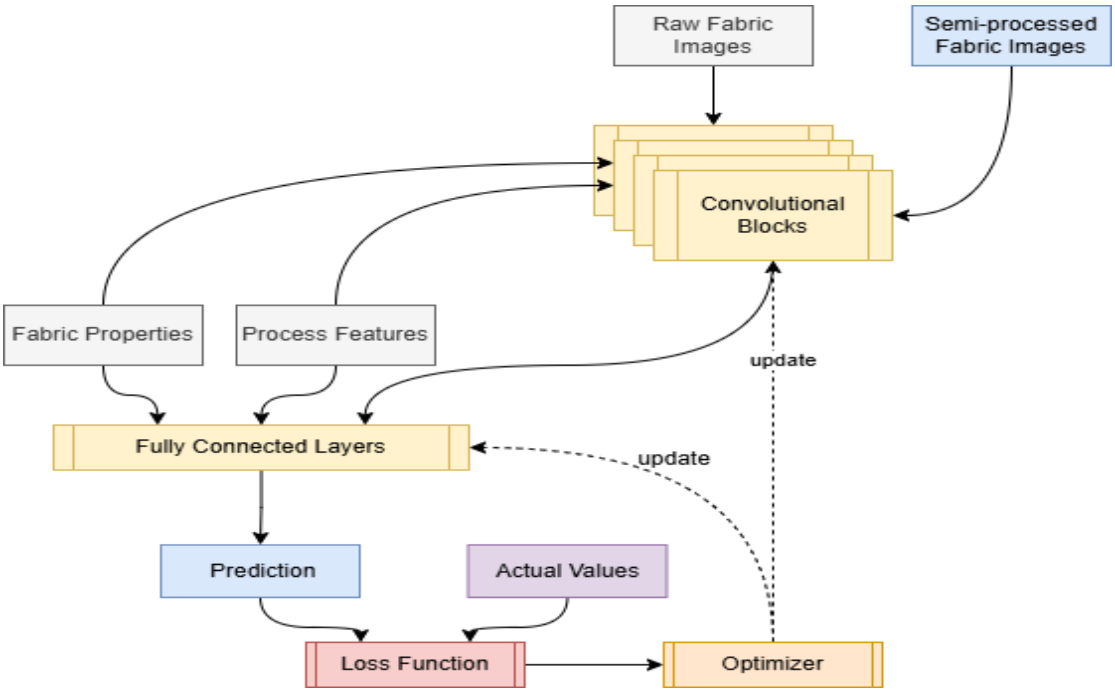

Figure 1. Proposed modeling schema.

to produce a single value. This operation is applied to all positions where the filter is placed [4].

The architectural design of models used in this study is illustrated in Figure 1. Convolutional blocks represent convolution operation over image data. Other types of data are diffused multiple times in following layers. An algorithm called backpropagation will be used to update the weights backward based on the values calculated forward for each neuron [3]. The backpropagation algorithm will search for the parameter set that minimizes errors in this way.

Data diffusion in Figure 1 involves propagating image data across convolutional layers to capture visual features, while feature data (fabric features and process features) are directly concatenated with features extracted from images before passing through fully connected layers. This integration allows the model to leverage both types of information (visual and non-visual) simultaneously for better predictions.

The loss function measures the difference between the predicted values and the actual values. This helps

in quantifying how well the model is performing. The optimizer updates the parameters of the model to minimize the loss, iterating through the network to improve predictions over time. It receives feedback from the loss function and adjusts the weights in both the convolutional and fully connected layers accordingly.

RESULTS AND DISCUSSION

A straightforward cross-validation method was employed to evaluate the approach. For each model, the dataset was randomly split five times into a 90/10 ratio. In each split, the first portion (90%) was used for training, while the second portion (10%) was used for prediction. Models' performance was assessed using the mean absolute percentage error (MAPE) as the evaluation metric. MAPE measures the average of absolute percentage errors between actual values and predicted values. It's especially useful for understanding how far predictions deviate from actual results on average, in terms of percentage.

The models were initially trained for 500 epochs. Throughout the training, the loss values were monitored to determine when the models reached a relative plateau. Since the training loss of the ANN model was observed to still be decreasing, it was trained for an additional 500 epochs to allow for a fairer comparison. At the end of each epoch, a performance metric was calculated on the validation dataset, which was kept separate from the training process. Figure 2-4 shows the progression of training and validation values over the first 500 epochs.show a rapid decrease in training loss early on, which then stabilizes, indicating effective initial learning.

Validation MAPE fluctuates more than training MAPE in all models, which is typical due to validation data variability. CNN2 seems to achieve the relatively stable and consistent performance for prediction of three properties.

Table 2 represents the average validation performance of three model types.

CNN2 performs best overall, achieving the lowest prediction values for all three color parameters (L*, a*, and b*), suggesting it provides the most accurate predictions. CNN1 is the second-best model, with relatively low prediction values, though slightly higher than CNN2, indicating it still performs well across parameters.

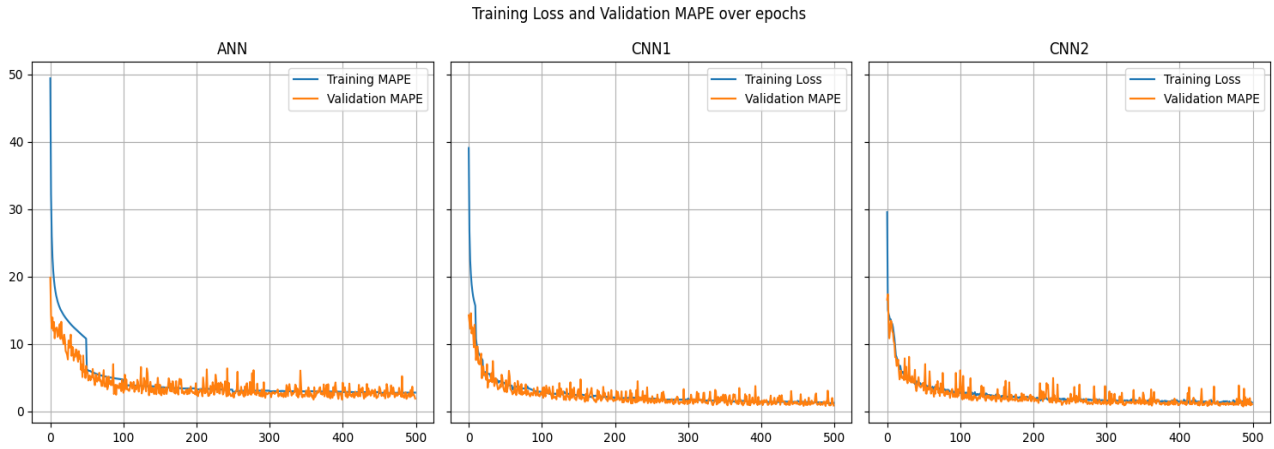

Figure 2. Tracking epochs for L* values.

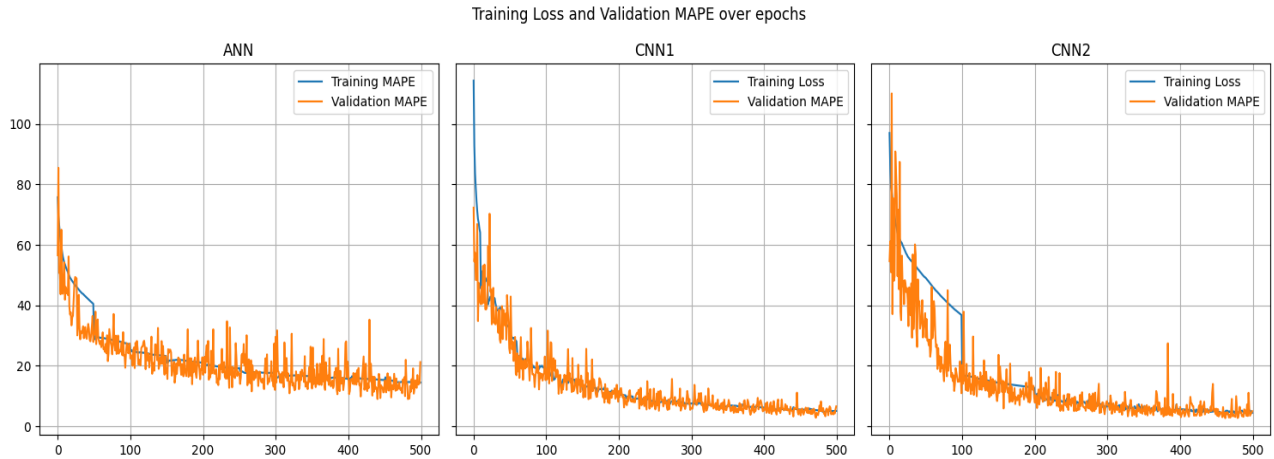

Figure 3. Tracking epochs for a* values.

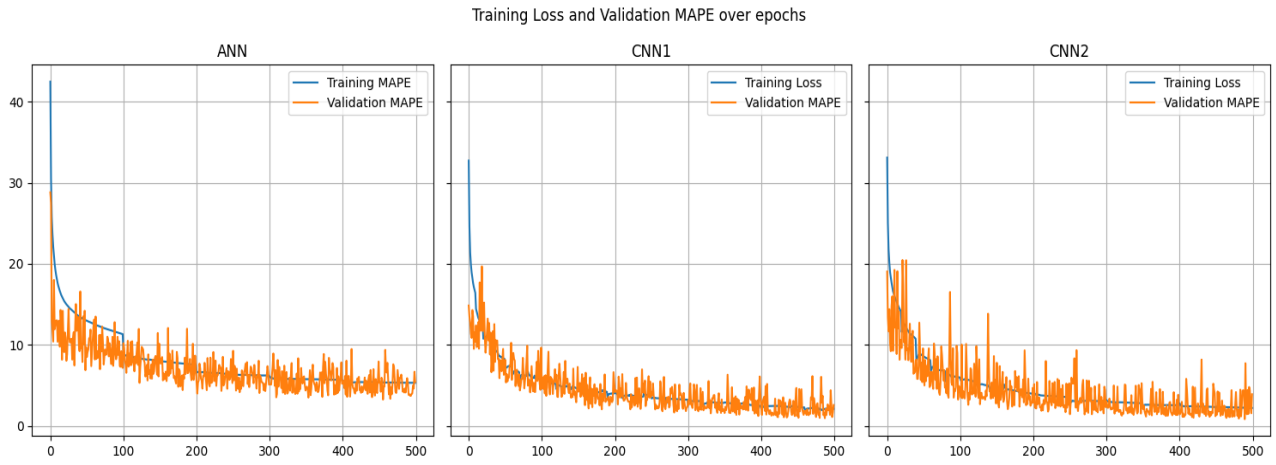

Figure 4. Tracking epochs for b* values.

Table 2. Average prediction error for color parameters (Lower values indicate better performance).

Predicted Value	ANN	CNN1	CNN2
L*	2.04	1.04	1.05
a*	7.56	6.55	4.97
b*	2.78	2.60	2.26

CONCLUSIONS

In this research study, the prediction of outcomes of bleaching process used in ground effecting of denim garments was examined. It has been established that both the dataset utilized and the augmented models employed for predictions have a significant impact on the accuracy of the forecasts. It is concluded that a factory employing these models will be able to forecast process outcomes effectively, minimizing the risk of any losses.

The fact that images of semi-processed fabrics perform better due to being closer to the final product is an expected situation. The results have shown this trend as well. Furthermore, it is an important finding that including images in similar prediction models in denim manufacturing could enhance prediction performance.

Acknowledgement: *This study includes the outputs of the research project supported by TÜBİTAK TEYDEB 1505 programme.*

REFERENCES

1. Géron A.: Hands-on Machine Learning with Scikit-Learn and TensorFlow: Concepts, Tools, and Techniques to Build Intelligent Systems. O'Reilly, 2017.
2. Goodfellow I., Bengio Y., Courville A.: Deep Learning. MIT Press, 2016.
3. Mitchell T.M.: Machine Learning. McGraw-Hill Education (Germany), 1997.
4. Chollet F.: Deep Learning with Python. Manning, 2018.
5. Paul R.: Denim: manufacture, finishing and applications, 2015.
6. Mondal M.I.H., Khan M.M.R.: Characterization and process optimization of indigo dyed cotton denim garments by enzymatic wash. Fashion and Textiles, 1(19), 2014. https://doi.org/10.1186/s40691-014-0019-0
7. Periyasamy A.P., Periyasami S.: Critical Review on Sustainability in Denim: A Step toward Sustainable Production and Consumption of Denim. ACS Omega, 8(5), 2023, pp. 4472-4490. https://doi.org/10.1021/acsomega.2c06374
8. Farooq A., Irshad F., Azeemi R., et al.: Prognosticating the shade change after softener application using artificial neural networks, Autex Research Journal, 21(1), 2020, pp. 79-84. https://doi.org/10.2478/aut-2020-0019
9. Mandal S., Mazumder N.U.S., Agnew R., et al.: Using Artificial Neural Network Modeling to Analyze the Thermal Protective and Thermo-Physiological Comfort Performance of Textile Fabrics Used in Oilfield Workers' Clothing. Int. J. Environ. Res. Public Health, 18, 2021, 6991 p. https://doi.org/10.3390/ijerph18136991
10. Elkateb N.: Prediction of Mechanical Properties of Woven Fabrics by ANN, Fibres & Textiles in Eastern Europe, 30(4), 2022, pp. 54-59.
11. Chu W.L., Chang Q.W., Jian B.L.: Unsupervised anomaly detection in the textile texture database. Microsyst Technol, 2024. https://doi.org/10.1007/s00542-024-05711-1
12. Tong Y., et al.: Prediction of parameters in the laser fading process of denim using convolutional neural networks. Textile Research Journal, 93, 2023, pp. 3790 - 3801. https://doi.org/10.1177/00405175231162643

THE DEVELOPMENT OF STONE WASHING PROCESS FOR DENIM WITH ALTERNATIVE MATERIALS USING FOAM APPLICATION TECHNIQUE

USLU, ONUR[1*]; YILMAZ, SERKAN[2] AND PEKTAŞ, ELIF AYLIN[3]

[1] Tayeks Textile Head Office, Design Centre, Cumhuriyet St. Old Hadimkoy Way, Inler Cihan Industrial Area, Apt C, Zip Code 34500, Büyükçekme, Istanbul, Turkey
[2] Tayeks Textile Laundry, R&D Centre, Ulas Organized Industrial Zone, 117 St, No:8, Ergene 2 OIZ, Zip Code 59930, Ergene Tekirdag, Turkey
[3] Inovaktif R&D, KSU Avsar Campus Technopark, Onikişubat Kahramanmaras, Turkey

ABSTRACT

Denim fabrics are fabrics dyed with indigo dye. As the garments produced from denim fabrics are washed, the indigo dye is easily removed from the product. The color of the product is bleached by the transfer of the dye in the product to the washing environment, the solution. Since indigo dye is a dye that can be easily eroded, especially by physical and chemical methods; it is also known as 'living dye'. In the conventional washing processes of denim products, the solution is first contaminated when the indigo dye passes into the solution. The return of this unbound dye found in the solution to the product is called 'back dyeing'. The most contaminated parts in back dyed products are the white pockets, labels and potassium permanganate ($KMnO_4$) applied parts of the product. Back dyeing occurs in the process called 'stone washing', where pumice stone is mostly used in wet processes. Pumice stone is a round and oval shaped stone with a rough surface collected from volcanoes. In order to obtain the desired appearance, the products are rotated in a wet environment in denim industrial washing machines with stones. Stones scrape off the dye particles from the surface of the dyed yarn and give the desired result. Stones can damage the garment and washing machine due to their high abrasion. They leave stone dust and residues on the garments and inside the pockets. This causes the addition of extra rinsing and manual pocket cleaning processes. The stone used as a physical abrasive melts after the abrasion effect and passes from the drain to the channel after a certain number of washes and becomes solid waste. By extending the abrasion feature of the stone, the physical waste rate left in the solution can be reduced. The dirt containing paint and stone waste coming out of the products after abrasion is carried to other products in the machine with the water in the solution. It causes the dirt to contaminate other products. For this purpose, physical abrasives that are not easy to melt and foam are combined in a water-free environment in the machine.

KEYWORDS

Denim; Foam; Stone; Back staining; Abrasion; Effecting.

INTRODUCTION

The most important element that adds value to denim garments is the mechanical and chemical washing processes performed after garment production. Some of these processes are stone, enzyme, ozone, softening, laser, sandpaper, laser, etc. washing. Stone washing is the most common of these and includes both mechanical and chemical interactions. Denim stone washing is a technique applied to give denim fabric a more worn and natural appearance. In this process, denim fabric is washed with stones in large drum machines. Rough stones such as pumice stones are usually used. The fabric is worn by rubbing with the stones, thus obtaining a more faded and worn appearance. Stone washing creates a change in both the color and texture of the fabric, providing a more comfortable and soft denim experience. As a result, denim stone washing process adds a vintage air to jeans, which is preferred in the fashion world, while also providing comfort. However, this process has negative aspects for both the fabric and the environment due to both water consumption, its effects on the fabric, and the pumice waste that is formed. Denim stone washing literature includes many academic studies and research related to textile industry and fashion technology [1-8].

The basic titles and topics covered in the literature regarding denim stone washing can be listed as stone washing process, combinations with chemical methods, environmental effects, effects on physical

* **Corresponding author:** Uslu O., e-mail: onur.uslu@tayeks.com.tr

and chemical properties of the fabric, fashion and consumer trends, alternative washing techniques.

Another topic to be examined in the study is foam application technique. Foam application is a technique generally used in the application of finishing processes in the textile industry. Foam finishing application has been developed as an alternative to the traditional impregnation method and offers advantages such as lower chemical consumption, water saving and energy efficiency. Foam finishing application is increasingly preferred in the textile industry as a sustainable technology that provides water and energy saving while also improving the performance of fabrics.

In this study, it is aimed to reduce back-dyeing, reduce the amount of water used in the cleaning processes of the products, save energy, shorten the production process, improve the physical strength tests of the product and the service life of the washing machine by eliminating the solid waste in the process with the alternative washing agent and method developed. The study includes innovations in terms of the effecting agent and washing method.

EXPERIMENTAL

The project implementation consists of two stages. The first of these is the development of an alternative synthetic stone material to pumice, and the second is related to the application of this stone to clothing. In the study, a synthetic stone was developed and examined in order to extend the wear life compared to conventional pumice stone. In this context, material development was carried out with 3 different recipes. The stone washing process was carried out without using water by injecting foam into the machine simultaneously. As it is known, in the conventional method, the washing process is carried out with water using auxiliary chemicals in industrial drum washing machines. Therefore, both water and chemicals are used in the application. In the scope of the project, the foam application technique was preferred instead of this process. In the scope of the study, Yılmak brand foam generator and Yılmak RF-60 brand drum washing machine were used. The foam generator and drum washing machine are seen in Figure 1.

Materials

The pumice stone is a natural, porous rock formed by the rapid cooling and solidification of lava as a result of volcanic eruptions. This stone creates many air spaces (pores) because of the rapid escape of gases in the lava, which creates the light and spongy structure of pumice. Its density is very low, and it can float on water. The use of pumice stone in the textile industry has an important place, especially in the processing of denim products. The main use of pumice stone in textiles is to create an abrasive effect on the surface of denim fabrics, giving them an old appearance. It is known that this process is carried out with a technique called "stone wash". During the grinding of denim fabrics, the fabrics are washed with pumice stone in large industrial washing machines. In this process, the pumice stone rubs on the surface of the denim fabric, abrading the fibers of the fabric and giving the fabric a soft, aged appearance.

Within the scope of the study, firstly a synthesis of polypropylene (PP), calcite ($CaCO_3$) mixture was made, and it was named Recipe 1. Recipe 2 was obtained by mixing glass fiber, broken stone, polypropylene and calcite. Thus, it was tried to create the advantage of increasing the impact resistance, reusing the waste stone and increasing the abrasion effect. Recipe 3 was obtained by mixing polyethylene, polypropylene, glass fiber, broken stone, silicate and calcite. Thus, it was tried to create the advantage of increasing the impact resistance, reusing the waste stone and increasing the abrasion effect. The photographs of these materials pumice stone are seen in Figure 2.

Within the scope of the study, clothes made from 3 different denim fabrics (Fabric A-B-C) were used. The same amount of stone was used in the trials carried out in conventional washings and newly developed washings. A total of 4 washes were made, 1 reference (pumice stone) and 3 new.

Methods

The foam generator used is given in Figure 1. RUCO FO 4010 was used as a foaming agent in the foam recipe and liquid cellulase enzyme was used to increase the effect. The stone materials obtained with Recipe 1-2-3 were used as abrasives. The washing process was carried out in a Yılmak RF-60 machine with 10 kg capacity, with 10 kg trousers. Foaming process was carried out using 9,6 liters of water each time. The process lasted at cold temperature and 30 minutes. After foam application, drying was carried out in the Yılmak HMS 600 dryer machine, at 70 °C temperature and for 40 minutes. Liquor ratio 1:1 at the rate 1 kg/trousers were used in the processes from the stones obtained with the newly developed recipes.

Figure 1. Foam generator and washing machine used in the study.

After the trials, photographs of the samples were taken and their performances were compared with the tensile and tear strength tests. The tests were carried out according to Tensile Test; EN ISO 13934-2-EQV method, Tear Test; EN ISO 13937-1-EQV, Stretch and Growth ASTM D3107, Color Fastness to Water EN ISO 105 E01, Color Fastness to Perspiration EN ISO 105 E04, Color Fastness to Crocking AATCC 8 and Color Fastness to Rubbing EN ISO 105X12 standards.

Figure 2. The photograph of stone obtained by Recipe 1-2-3 and pumice stone.

Figure 3. Recipe 1-2-3 and conventional washing effect of Fabric A.

Figure 4. Recipe 1-2-3 and conventional washing effect of Fabric B.

Figure 5. Recipe 1-2-3 and conventional washing effect of Fabric C.

Table 1. The physical performance of specimens from Fabric 1.

Test Methods	Fabric Direct	Conventional	Recipe 1	Recipe 2	Recipe 3
Tensile Strength [kg]	**Warp**	35	69.3	67.9	65.0
	Weft	29,7	43.9	42.5	39.7
Tearing Strength [g]	**Warp**	3937	5486	5207	4952
	Weft	2472	3909	3725	3480
Elasticity [%]	**-**	31,4	35,7	33,1	38,4
Growth	**-**	6,9	6,5	6,7	6,6
Color Fastness to Crocking	**Dry**	3/4	4/5	4	3/4
	Wet	1/2	1	1/2	1/2
Color Fastness to Rubbing	**Dry**	4	4	3/4	3/4

Table 2. The color fastness to perspiration of specimens from Fabric 1.

Fabric Type	Type	Color Change	Staining					
			Wool	Acrylic	Polyester	Nylon	Cotton	Acetate
Conventional	**Acid**	4/5	4/5	4	4/5	4/5	4/5	4
	Alkaline	4/5	4/5	4	4/5	4/5	4/5	4
Recipe 1	**Acid**	4/5	4/5	4	4/5	4/5	4/5	4
	Alkaline	4/5	4/5	4	4/5	4/5	4/5	4
Recipe 2	**Acid**	4/5	4	4/5	4/5	4/5	4/5	4/5
	Alkaline	4/5	4	4/5	4/5	4/5	4/5	4/5
Recipe 3	**Acid**	4/5	4/5	4	4/5	4/5	4/5	4
	Alkaline	4/5	4/5	4	4/5	4/5	4/5	4

Table 3. The color fastness to water of specimens from Fabric 1.

Fabric Type	Color Change	Staining					
		Wool	Acrylic	Polyester	Nylon	Cotton	Acetate
Conventional	4/5	4/5	4/5	4/5	4/5	4/5	4/5
Recipe 1	4/5	4/5	4	4/5	4/5	4	4/5
Recipe 2	4/5	4/5	4/5	4	4/5	4	4
Recipe 3	4/5	4/5	4/5	4/5	4/5	4/5	4/5

RESULTS AND DISCUSSION

Figure 3-4-5 shows the visual results of foam washing done with Recipe 1-2-3 with Fabric A-B-C.

What is expected from this washing trial is that the new recipes will give a similar bleaching effect with the application of pumice stone. When Figure 3-4-5 is examined, it can be seen that the effects are similar. This similarity showed that the newly developed synthetic stones (Recipe 1-2-3) worked successfully.

Table 1 shows the performance values of the Fabric 1 obtained from 3 recipes and conventional applications.

The pumice stone is a material that affects the physical properties of fabric. Because the pumice stone and similar materials are based on friction, abrasion and snatching of the fiber from the fabric surface.

Thus, the part in the center of the yarn that does not absorb indigo dye is revealed and the effect occurs.

When Table 1 is examined, it has been determined that the stones and prescriptions that provide friction cause positive difference in the physical properties. When the strength results were examined, it was determined that the samples made with Recipe 1-2-3 gave similar results among themselves, but the results were higher compared to conventional applications. While a similar effect is achieved with Recipe 1-2-3 (Figure 3-4-5), this results in a lower strength reduction. When the fabric elasticity and growth results were examined, no significant differences were detected.

When the fastness results in Table 1-Table 2 and Table 3 are examined, it was determined that the applications made with pumice stone and new polymer mixtures showed similar performance, and the type of the stone did not significantly affect the fastness results.

CONCLUSIONS

At the end of the study, an alternative material and washing method were developed. When compared to the conventional method, a total of 3 baths and 600 liters of water were saved. The processes were carried out at room temperature and energy savings were achieved in this respect. Accordingly, 20% energy savings were achieved. Not using pumice stone and repeated use of new materials reduced waste generation. Since stone reduces the strength of the fabric, clothes washed with the traditional method carry the risk of wear. On the other hand, with the proposed method, only half as much stone was used compared to the traditional method and a positive development was determined in terms of fabric strength. Since the new method requires 15 minutes less machine operation time compared to the traditional method and the foam process is applied at room temperature, less energy will be consumed. When the process is examined in terms of chemical consumption, a 20% cost gain can be predicted. In the proposed washing method, less back staining risk was observed. No back staining was observed in the proposed washing method.

REFERENCES

1. Cheriaa R., Baffoun A.: Effects of cross linkers combination, for three dimensional effects, on denim garment properties. Fibers and polymers, 16, 2015, pp. 1150-1155. https://doi.org/10.1007/s12221-015-1150-2
2. Choudhury A.K.R.: Environmental impacts of denim washing. In Sustainability in Denim, Woodhead Publishing, 2017, pp. 49-81. https://doi.org/10.1016/B978-0-08-102043-2.00003-4
3. Hoque S., Rashid M.A., Chowdhury S., et al.: Alternative washing of cotton denim fabrics by natural agents. American Journal of Environmental Protection, 7(6), 2018, pp. 79-83. https://doi.org/10.11648/j.ajep.20180706.12
4. Hoque M.S., Hossain M.J., Imtiaz M.A., et al.: Scope of dry wood & wood composite alternate to stone in case of acid wash on denim fabric. International Journal of Current Engineering and Technology, 8(2), 2018, pp. 382-388. https://doi.org/10.14741/ijcet/v.8.2.32
5. https://www.cottonworks.com/en/topics/sourcing-manufacturing/denim/sustainable-denim-finishing/
6. https://www.cottonworks.com/wp-content/uploads/2018/09/Denim-Webinar_Final.pdf
7. https://denimdudes.co/future-of-wash-sustainable-solutions-for-stone-and-acid-wash-in-the-denim-industry/
8. https://www.abiteks.com.tr/blog/sustainable-solutions-for-denim-processing

DESIGN OF ELECTRICALLY CONDUCTIVE, HIGHLY STRETCHABLE, HYGIENIC ELECTRODES FOR ELECTROTHERAPY

ALI, AZAM*; MILITKY, JIRI; TOMKOVA, BLANKA AND WIENER, JAKUB

Department of Material Engineering, Faculty of Textile Engineering, Technical University of Liberec, Czech Republic

ABSTRACT

The main objective of this study was to create versatile and wearable electrically conductive electrodes for Transcutaneous Electrical Nerve Stimulation (TENS) application, ensuring they are comfortable by depositing silver particles directly onto the carbon particles imparted rubber electrodes. Scanning Electron Microscopy (SEM) was used to analyze the shape of the deposited silver particles. To enhance the electrode's performance during body movements, the conductive fabrics were stretched repeatedly, and changes in resistivity were observed. The electrical resistance showed minimal variation with small extensions, remaining relatively constant between 0–75% stretch. Resistance increased significantly after 80% stretch, but the fabric's resistivity remained stable even after over 100 stretching cycles. Additionally, there was no significant change in resistivity over time at a constant current. The study also investigated the antibacterial properties of the deposited particles against bacteria like Staphylococcus aureus and Escherichia coli. The antifungal activity assessment using Aspergillus fumigatus further underscores the benefits of the silver-plated elastomers in combating fungal growth. Finally, the durability of the coated fabrics concerning comfort and electrical properties was evaluated through multiple pressure applied, showing good particle retention and only a slight decrease in conductivity.

KEYWORDS

Silver electroplating; Carbon particles; Multifunctional electrodes; Electrostimulation and Antibacterial.

INTRODUCTION

The design of electrically conductive, highly stretchable, and hygienic electrodes for electrotherapy is crucial in advancing therapeutic effectiveness and patient comfort. Electrotherapy relies on the precise delivery of electrical currents to stimulate muscles, manage pain, and promote healing, making the quality and functionality of electrodes a key factor in treatment outcomes [1]. Traditional electrodes often face challenges in maintaining conductivity and comfort during dynamic movements, as they may lack flexibility or introduce hygiene concerns with prolonged use. The use of electrotherapy, specifically Transcutaneous Electrical Nerve Stimulation (TENS), in physiotherapy and rehabilitation to manage pain and improve mobility. TENS therapy involves applying electric current to stimulate body nerves, typically using conductive hydrogel electrodes. While self-adhesive hydrogel electrodes are commonly used for TENS, they have drawbacks like discomfort, skin irritations, and hygiene issues [2]. Other types of electrodes, such as carbon rubber electrodes or metal plates covered with nonconductive fabric, have also been utilized but can pose challenges. Despite these challenges, the use of electrodes remains prevalent in TENS applications [3]. To address these limitations, modern electrode designs focus on creating materials that are both electrically conductive and capable of enduring high levels of stretch without compromising performance. Additionally, incorporating antimicrobial and biocompatible properties supports hygiene and skin safety, especially in extended or repeated therapy sessions. In this research, a unique substrate made of cotton, nylon, and lycra was chosen, and a special method for depositing silver nanoparticles onto fibers and within fabric structures was developed. This approach resulted in the creation of conductive fabric-based electrodes with excellent conductivity, flexibility, and stretchability to ensure comfort during use. The study also explored changes in electrical conductivity with repeated stretching to enhance the adaptability of carbon embedded silver plated electrodes for human body movements during electrotherapy sessions [4]. Additionally, these electrodes demonstrated good washing durability, resistance to cracking when stretched, and exhibited

* **Corresponding author:** Ali A., e-mail: azam.ali@tul.cz

qualities like drape, softness, and a comfortable feel. The electrodes were engineered by directly plating of very fine silver nanoparticles on them. These electrodes significantly reduced the risk of contact dermatitis and can be safely applied to wounded or injured skin due to the antibacterial and hygienic properties conferred by the silver nanoparticles in the developed carbon embedded rubber electrodes [5].

EXPERIMENTAL AND CHARACTERIZATIONS

Reagent grade chemicals were obtained from sigma Aldrich. Silver nitrate ($AgNO_3$), methanol (99.8%), and calcium carbonate (≥99%) were pur-chased from Sigma-Aldrich. Silicon based elastomers used as matrix in present study weresupplied by R & G Composite Materials (R&G Faserverbundwerkstoffe GmbH), Waldenbuch, Germany. The highly conductive carbonmicroparticles (100 µm) with trade name carbiso mil were obtained from Easy com-posites, UK. Firstly, 12 of carbon particles were added into methanol solution and then ultrasonicated for 30 min. After ultrasonics 100 mL of silicon elastomer solution was added slowly to the reaction mixture. Then the mixture further ultrasonicated for I hour to produce a conductive elastomer. The methanol was evaporated by placing the beaker in the oven at 55ºC. After the carbon filled elastomers were formed. Subsequently, silver electroplating was done at various time intervals over carbon embedded polymeric rubber. The utilization of SEM and XRD for surface morphology analysis, along with ASTM D257-07 for electrical volume resistivity measurement, indicates a comprehensive approach to characterizing the material properties. Additionally, the Zone of Inhibition test for qualitative measurements and quantitively assessments using AATCC 100-2004 standards, provide valuable insights into the material's antimicrobial properties. Behrens and Karber's technique were used to calculate the virus titer reduction from the basic viral titer of infectivity (107) titer. The plating time and sample codes are given in Table 1 below.

Table 1. Design of experiment of developed samples.

Sr #	Plating Time (min)	Sample code
1	10	S1
2	20	S2
3	30	S3
4	40	S4
5	50	S5
6	60	S6
7	70	S7
8	80	S8
9	90	S9
10	100	S10

RESULTS AND DISCUSSION

Electrical resistivity

Figure 1 is showing the effect of electroplating and weight gain percentage against the electrical resistivity. Increase in electroplating time tends to increase in silver plating and eventually decrease in electrical resistivity values. This trend indicates that optimal electroplating time is essential to achieve low resistivity, as it enhances conductivity by creating a more continuous conductive layer. The weight gain percentage serves as an indicator of the amount of silver coating applied to the electrode, with higher percentages corresponding to increased silver deposition and improved conductivity. The evaluation of the electrical resistivity of the silver-plated samples and the analysis of resistivity at different stretch percentages provide valuable insights into the behavior of the electrodes. The data from Figure 2 showing the resistivity value graphs for each sample is essential for understanding the variations among the samples. The observations regarding resistivity changes at different stretch levels, especially the significant increase in resistivity beyond 75% stretch up to approximately 51 K Ω.mm at 100% stretch, highlight the material's response to mechanical stress. This data suggests that, while silver-plated samples maintain low resistivity under moderate stretch, their conductive performance diminishes significantly under extreme stretching, emphasizing the importance of balancing stretchability and conductivity in electrode design. The durability testing of sample S10, with resistivity measurements at different stretch levels and the calculation of the mean resistivity during one complete cycle, offers a comprehensive assessment of the sample's performance under repeated stretching and release cycles. This detailed analysis is crucial for evaluating the reliability and stability of the electrodes in practical applications. The analysis is critical for applications where electrodes are subject to continuous movement, as it informs decisions about material selection and design parameters that can ensure long-term performance and consistency in electrotherapy applications.

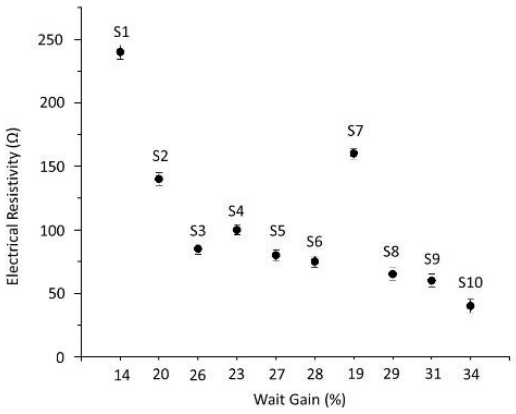

Figure 1. Electrical resistivity at normal stretch.

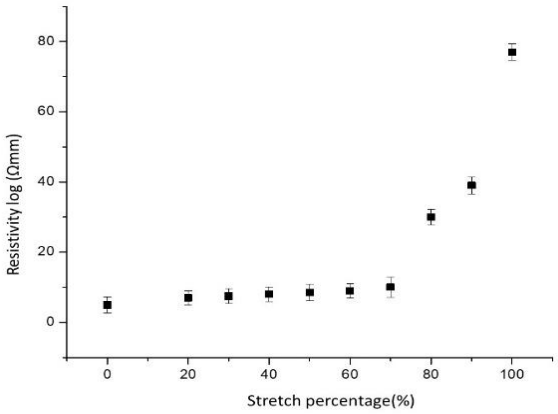

Figure 2. Electrical resistivity at different stretch percentage of Sample 10.

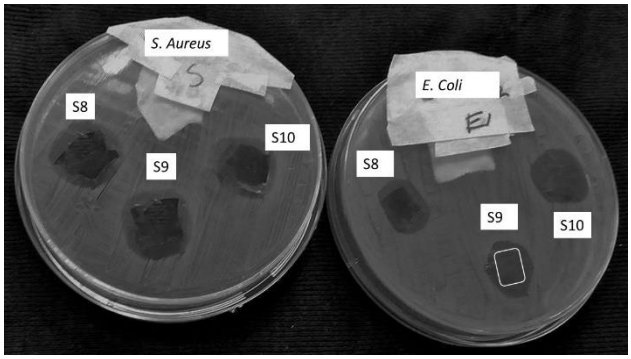

Figure 3. Antibacterial properties with Zone of inhibition.

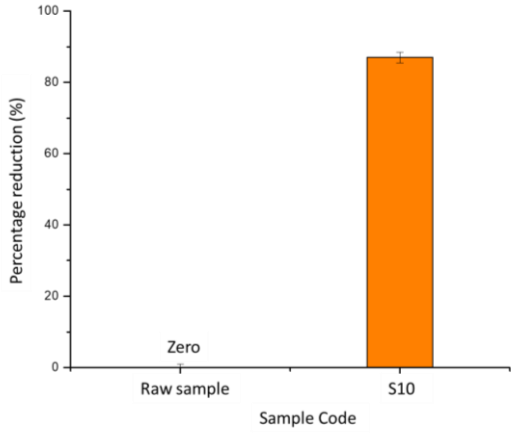

Figure 4. Antifungal activity of silver coated textile.

Antipathogenic properties of developed electrodes

Silver-plated electrodes for Transcutaneous Electrical Nerve Stimulation (TENS) applications are gaining attention not only for their excellent conductivity but also for their inherent antipathogenic properties. Silver is known for its strong antimicrobial effects, which are particularly beneficial in medical and therapeutic devices that come into direct contact with the skin. These properties help reduce the risk of bacterial and fungal contamination, enhancing the hygiene and safety of TENS electrodes used in repeated sessions or extended wear. By incorporating silver plating, TENS electrodes benefit from both improved conductivity and enhanced antipathogenic properties, offering a dual-functionality that aligns with the high standards needed for medical and therapeutic applications. This feature is particularly advantageous in clinical environments and for individuals who use TENS devices frequently, as it contributes to better skin health, reduces maintenance, and extends the electrode's usable life. The Gram-negative *E. coli* and Gram-positive *S. aureus* were used for testing the antibacterial activity of silver-plated elastomers. Figure 3 display the zones of inhibition around the samples after one day of incubation in dark at temperature 37 °C. The results clearly show that the silver coating on the elastomers was effective in creating zones of inhibition against both Staphylococcus aureus and Escherichia coli. The antimicrobial properties of the metal coating, with its unique features like microparticles and biomolecules such as polynuclear acids and proteins, contribute to its effectiveness. This action makes silver-plated electrodes a valuable option for TENS devices, as they can reduce the likelihood of infections and skin irritations often associated with prolonged electrode use. The antibacterial behavior of the silver coating may be due to chemical interactions, physical interactions, or a combination of both, making the prepared electrodes highly hygienic and ideal for hospital environments.

The antifungal activity assessment of silver-plated electrodes for electrotherapy, particularly against *Aspergillus fumigatus*, is an important aspect of ensuring the hygiene and safety of these devices. *Aspergillus fumigatus* is a common fungal pathogen associated with infections, especially on moist skin areas where electrotherapy electrodes are often applied. Silver, known for its broad-spectrum antimicrobial and antifungal properties, releases silver ions that interfere with fungal cell processes, disrupting membrane integrity and inhibiting growth. The antifungal activity assessment using *Aspergillus fumigatus* further underscores the benefits of the silver-plated elastomers in combating fungal growth. Figure 4 display the percentage reduction of fungi (*Aspergillus fumigatus*) with raw sample and samples loaded with silver (87% reduction). Testing silver-plated electrodes against *Aspergillus fumigatus* involves evaluating the fungal inhibition zone or measuring fungal colony counts in the presence of the electrode. Effective antifungal performance would manifest as significant inhibition of *Aspergillus fumigatus* growth around the silver-plated electrode, indicating that the silver ions released are actively preventing fungal proliferation. The silver-plated

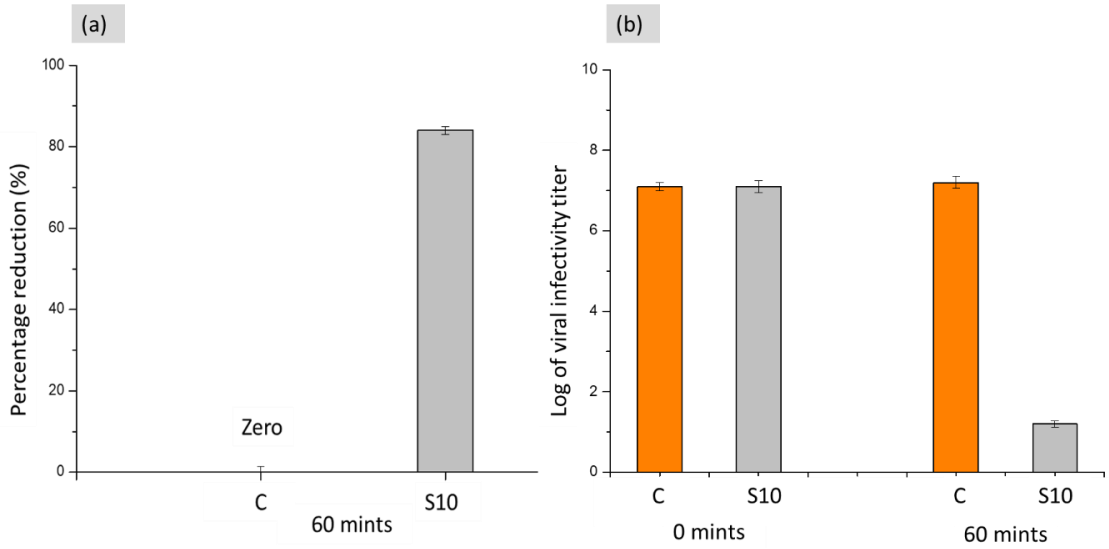

Figure 5. Reduction in viral infectivity titer (a) and percentage reduction (b) calculated from viral infectivity for untreated and treated fabrics at a contact time of 0 and 60 min.

sample exhibit maximum antifungal activity because the metal particles coated elastomer having suitable antibacterial properties. Hence, the percentage reduction of silver nanoparticles greater as compared to phytochemicals. Incorporating silver-plated electrodes with antifungal properties in electrotherapy devices enhances their clinical safety, particularly for patients with extended treatment sessions or sensitive skin.

Figure 5(a) display a graph which shows the virus infectivity titer log against contact time (0 h and 60 mins). Behrens and Karber's method was used for the calculation of virus titers reduction from the starting viral titter of infectivity (107) titer. The Figure 5(a) describes the infectivity titer change of corona virus (0 h and 60 mins) at 25^{o}C for uncoated elastomer and silver coated elastomer S10. It was examined that there is a major decrease in infectivity titer for fabrics coated sample after 60 mins instead of 0 hrs whereas no reduction in virus activity titer was calculated in vase of uncoated elastomer sample. While, Figure 5 (b) exhibit virus percent reduction for uncoated and coated S10 sample. The elastomer treated with silver reduces 84% in virus titer separately uncoated elastomer remained ineffective against virus [6]. The antiviral action exhibited through elastomer treated with silver could be due to the binding of metallic surface with glycoproteins at the viral surface working as an inhibitory action for viruses.

The effect of applied pressure on electrode resistivity during electrotherapy

The applied pressure on electrodes during electrotherapy significantly impacts electrode resistivity, which in turn affects the effectiveness of current delivery to the targeted tissue. When adequate pressure is applied, it improves the contact between the electrode and skin, reducing resistivity and allowing for better current flow. This optimized current distribution enhances the therapeutic benefits of electrotherapy. However, too much or too little pressure can alter resistivity unfavorably, either causing patient discomfort or reducing treatment efficacy. Therefore, controlling applied pressure is essential for achieving consistent and effective results in electrotherapy applications. The high potential signals from the skin are captured using wet and dry electrodes, even when the body is in motion. In our current research, we explored the effects of applying loads of 250g, 500g, and 750g on a 10cm × 10cm sample, which translates to pressures of 4 N/cm^2, 6 N/cm^2, and 8 N/cm^2.The trend line values of electrical resistivities with respective applied pressure are shown in Figure 6. The pressure applied had a significant impact on the electrical resistivity of the electrodes. An evident decrease in resistivity was noted with increasing pressure. Initially, the resistivities of samples S8, S9 and S10 were 62 Ω.mm, 55 Ω.mm, and 24 Ω.mm, respectively. When the pressure reached 6 N/cm^2, the values decreased to approximately 23 Ω.mm, 17 Ω.mm, 14 Ω.mm, and

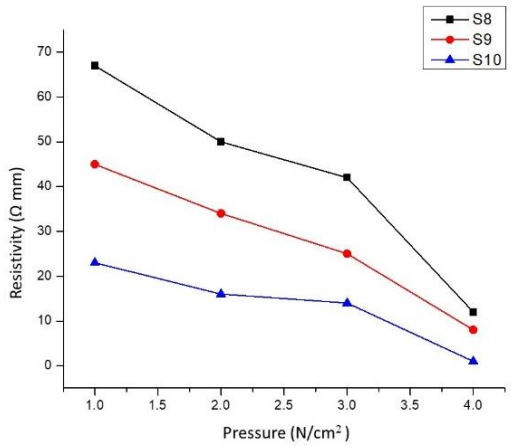

Figure 6. Trend line values of electrical resistivity with respective applied pressure.

1 Ω.mm. A similar approach was taken in a previous study that explored the effect of pressure on dry textile electrodes for obtaining ECG signals. They observed that increased pressure led to lower impedance. Specifically, the impedance decreased as the contact area between the conductive network and skin increased. Since polymers and textiles are soft materials, squeezing them improves the contact interface, resulting in better signal acquisition.

CONCLUSION

The development of those electrically conductive and highly stretchable electrodes for TENS machines sounds really impressive! Achieving a minimum resistivity of 1183 Ω.mm at 12% carbon particles and a volume resistivity of 23 Ω.mm in the conductive elastomer samples is quite remarkable. The fact that these electrodes also demonstrated significant effectiveness against various pathogens in antipathogenic testing is a great advantage. The silver electroplating over the carbon-embedded electrodes seems to have enhanced their properties further. The potential applications of these electrodes in electrostimulation and electrotherapy fields hold a lot of promise for future use. Silver-plated elastomers demonstrated robust antibacterial and antifungal effects, inhibiting bacterial growth (e.g., *E. coli* and *S. aureus*) and fungal pathogens like *Aspergillus fumigatus*. Antiviral tests showed an 84% reduction in viral infectivity after 60 minutes of contact time, making these materials ideal for applications in medical environments. Applying pressure to the electrodes during electrotherapy improved conductivity by reducing resistivity due to enhanced contact with the skin. Increased pressure (up to 8 N/cm²) led to significant resistivity reductions, indicating the importance of optimized contact pressure for effective electrotherapy. These silver-plated elastomers are particularly suited for Transcutaneous Electrical Nerve Stimulation (TENS) devices, offering dual benefits of low resistivity and antimicrobial protection. Their performance under mechanical stress and repeated usage cycles, coupled with their hygienic properties, make them valuable for clinical and home-based therapeutic applications. They are useful for clinical and home-based therapeutic applications because of their ability to withstand mechanical stress and numerous usage cycles as well as their hygienic properties.

Acknowledgement: *The work was supported by the project 'Advanced Structures for thermal insulation in extreme conditions (Reg. No. 21–32510M) granted by the Czech Science foundation (GACR).*

REFERENCES

1. Ali A., et al.: Silver-plated stretchable elastomeric electrodes for electrotherapy applications. Journal of Industrial Textiles, 54, 2024. https://doi.org/10.1177/15280837241287561
2. Kim S.H., Oh K.W., Bahk J.H.: Electrochemically synthesized polypyrrole and Cu-plated nylon/spandex for electrotherapeutic pad electrode. J Appl Polym Sci, 91(6), 2004, pp. 4064‑4071. https://doi.org/10.1002/app.13625
3. Johnson M.I.: Does transcutaneouselectrical nerve stimulation (TENS) work? Clin Eff Nurs, 2(3), 1998, pp. 111–120. https://doi.org/10.1016/S1361-9004(98)80002-2
4. Melzack R., Wall P.D.: Pain mechanisms: a new theory. In Psychosocial Processes and Health, Cambridge University Press, 1994, pp. 112–131. https://doi.org/10.1017/CBO9780511759048.009
5. Akgün D.E., Yesilpinar S., Senol Y., et al.: Design of a TENS Knee Pad with Integrated Textile Electrodes, 2018, online: https://www.researchgate.net/publication/328283140
6. Ali A., et al.: Flexible Electrically Conductive Elastomers. 2023, pp. 1–25. https://doi.org/10.1007/978-981-99-6002-6_1

ADSORPTION OF METHYLENE BLUE DYE FROM AQUEOUS SOLUTION USING BIO-WASTE POPLAR FIBER

USTA, CANAN*; SEYHAN, AYBENIZ AND GÜRARSLAN, ALPER

Istanbul Technical University, Textile Engineering Department, Istanbul, Turkey

ABSTRACT

Poplar fiber corresponds to the seed hairs of the Populus genus trees and is a naturally abundant lignocellulosic fiber with the features of thin-walled large lumen, lightweight and hydrophobic properties. Based on the structure and properties exhibited by poplar fiber nominate it as a highly favored adsorbent material for cationic dyes. This study aims to determine the adsorption efficiency for methylene blue (MB) dye with chemically enhanced poplar fibers and compare its capacity with milkweed fibers. Prior to adsorption experiments, the fibers were treated with NaOH solution to remove the wax coating attached on the fiber surface. Adsorption studies were performed in a batch system using dye solution with initial dye concentration of 50 mg L^{-1}. The adsorbent dosage was evaluated at 10 g L^{-1} amount, with contact time of 3 h and without pH adjustment. After the experiments, the remaining dye concentration in liquid was quantified in UV-Vis spectrophotometry. The results revealed that poplar fiber exhibited higher adsorption capacity compared with milkweed fiber. Poplar fibers were efficient to decolorize MB dye solution, reaching a higher color removal percentage than milkweed fibers. It can be concluded that poplar fibers were alternative adsorbents for removing cationic dyes due to their hollow structure.

KEYWORDS

Poplar fiber; Dyeing; Adsorption; Cationic dye; Methylene blue.

INTRODUCTION

Waste generation during industrial processes significantly contributes to various environmental pollution problems. Particularly, textile processes consume large amounts of water and synthetic dyes, leading to the generation of colored effluents. The presence of dye contaminants in wastewater is a major concern for both human health and the environment, as even trace amounts of dye are noticeable in water [1]. Among the common dyes, methylene blue (MB), the structure shown in Figure 1, is widely used in textile processing due to its water solubility. While not highly toxic to humans, MB can cause eye and skin irritation and has systemic effects. Hence, the removal of the dye from wastewater is critical in addressing water pollution.

Several methods are widely used for the removal of dye from wastewater, including membrane filtration, ion exchange, reverse osmosis, coagulation and adsorption [2] [3]. Among these, adsorption stands out as one of the simplest and most cost-effective physico-chemical treatment process for removing dye molecules from aqueous solutions. This study focuses on adsorption due to its practicality and efficiency.

There is an increasing demand for cost-effective alternative technologies or adsorbents for dye removal. Natural agricultural materials, which are readily available in large quantities, may serve as low-cost and effective adsorbents.

Poplar fibers are a type of trichome fiber and grow as seed hair fibers on the branches of poplar trees. The variation in poplar species over time can be attributed to factors such as human activities, biological processes and genetic pollution from hybrid poplars [4]. Each poplar tree is capable of generating approximately 25 kg of poplar seed fibers [5]. The length of these fibers depends on the specific tree and the region where they are harvested, and lengths ranging from 3 to 16 mm have been reported in the literature [6] [7]. Poplar fibers typically have a diameter between 5 and 10 μm. These fibers have large hollow lumen, allowing them to float in the air and facilitating their dispersal. The internal diameter of the fibers accounts for approximately 90% of the total fiber diameter, resulting in an extremely low density of around 0.3 g/cm³ [7]. Poplar fibers have similar properties to milkweed and kapok fibers due to their hollow structure. While extensive studies were conducted on these fibers, the potential of poplar fibers have not been thoroughly investigated about

* **Corresponding author:** Usta C., e-mail: cananusta@itu.edu.tr

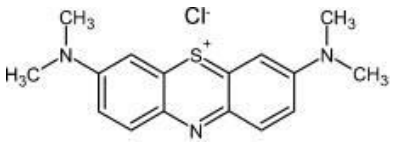

Figure 1. Chemical structure of Methylene Blue.

water treatment capacity. Therefore, this study aims to investigate the potential of poplar fiber as a viable solution for the adsorption of cationic dye from wastewater and provide an environmentally friendly and efficient approach to water purification.

EXPERIMENTAL

Materials

Poplar fibers were directly collected during the blooming period in mid-May in the Kırklareli region of Türkiye. Milkweed fibers were obtained in partnership with Pangai Materials Science, Italy. Both of the fibers were mechanically cleaned to remove contaminants such as seeds, leaves, dust etc. Sodium hydroxide, 99% (Merck) and methylene blue were used as received without further purification.

Methods

Pretreatment of poplar and milkweed fibers

Aqueous NaOH solution was prepared and cooled to room temperature in a glass bottle. Then, 1.0 g of fiber was added immediately into this solution. Subsequently, the generated fiber/solution mixture was placed into the Gyrowash vessels to be processed at 70 °C for 1 hour. Then, fiber sample was washed with distilled water at ambient room temperature until no residual chemicals could be detected on the fiber surface. The wet pretreated fibers were dried at 40 °C for 24 h.

Measurement of the adsorption capacity

The adsorption capacity was measured by calculation of methylene blue dye concentration in the aqueous solution after adsorption. The adsorption process was conducted in 50 mg L^{-1} of methylene blue solution. A glass flask containing 1 g of the modified fibers and 50 ml of the MB solution was shaken for 3 h at room temperature. Then, fibers were filtered and the residual solution was analyzed at λ_{max} of 660 nm using UV-Vis Spectrophotometer.

Scanning electron microscopy (SEM)

The morphology of milkweed and poplar fibers was examined by scanning electron microscopy using TESCAN VEGA3 instrument with 10 kV accelerated voltage and 2.08-6.92 mm working distance. Surface images were taken at 5 kX magnification. Before analysis, fiber samples were coated with Au/Pd under vacuum conditions for 3 min.

RESULTS AND DISCUSSION

Hollow fibers have become widely adopted across numerous industries, with wastewater treatment being one of the primary applications. Their unique structure, featuring a high surface area-to-volume ratio, enables efficient separation and filtration processes, making them ideal for removing contaminants from wastewater [8]. Characterizing the structural morphologies of hollow milkweed and poplar fibers is essential for advancing adsorption technologies.

Scanning electron microscope (SEM) analysis of the fibers revealed a smooth surface, free from rough structures. This smoothness is likely due to a natural wax coating adhered to the fiber surface, as previously reported [9]. Structurally, each fiber resembles a cylindrical microtube with nano-scale surface wrinkles, as seen in Figure 2. Poplar and milkweed fibers exhibit a hollow tubular shape, with diameters around 10 μm and 25 μm, respectively. The presence of a large air-filled lumen in both fibers makes them highly suitable for applications requiring lightweight materials with high absorbency [10].

Chemical treatment, particularly using NaOH, effectively removed the waxy surface of poplar and milkweed fibers. This treatment also facilitated deesterification, breaking down the ester bonds attached to the aromatic rings of lignin [11]. Delignification resulted in an increased proportion of amorphous cellulose, which reduced the hydrophobicity of the fiber (as evidenced by the decrease in the static water contact angle) as reported in the literature [12] [13]. NaOH treatment altered the naturally smooth surface of both fibers, causing the surface to become rougher and increasing the overall surface area [14]. Hence, the adsorption capacity of treated fibers is affected by their chemical reactivity and the porosity of the functional groups present on their surfaces. The structural changes after treatment improved the adhesion of the dye to the outer surface of the fiber and improved its penetration into the inner lumen, thus increasing the dye removal in the chemically treated fiber compared to the untreated fiber.

In this study, an oxidation pretreatment using sodium hydroxide (NaOH) was performed to remove wax, oil, pectin, lignin, and hemicellulose from poplar and milkweed fibers. Then, the increased hydrophilic properties of the treated fibers were used for organic pollutant removal application. Usage of natural milkweed and poplar fibers in removal of methylene blue from wastewater was studied and the decolorization effect was observed. Figure 3 shows the absorbance spectra of methylene blue (MB) at initial and post-adsorption concentrations. The maximum absorbance peak for all concentrations appears consistently at 660 nm in the visible light waveband, which is in agreement with other studies reporting that the absorbance peak of MB occurs at

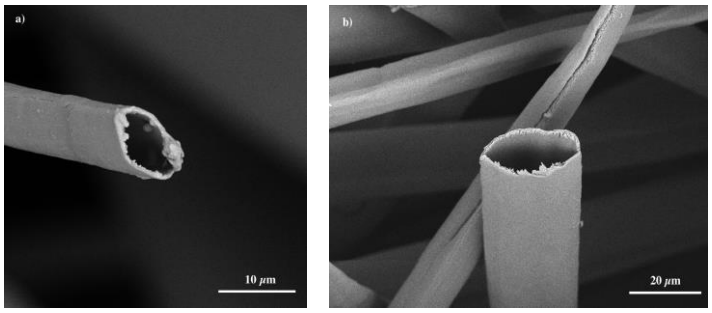

Figure 2. SEM images of raw (a) poplar and (b) milkweed fiber.

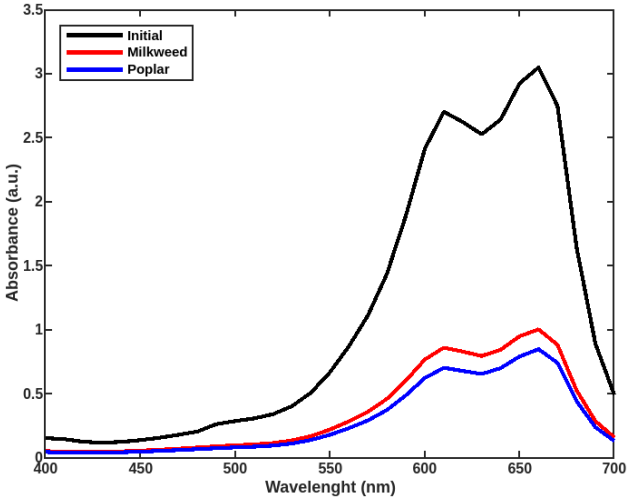

Figure 3. Absorbance curve of MB solution before and after the treatment with milkweed and poplar fibers.

Table 1. The percent value of MB concentration after the adsorption process.

	Milkweed Fiber	Poplar Fiber
MB Concentration (%)	~67%	~72%

660 nm in UV-Vis spectrophotometric analysis [15]. In our study, this peak was used to analyze the removal efficiency of methylene blue. As seen from Figure 3, it is clearly observed that the MB concentration decreases with adsorption by NaOH-treated milkweed and poplar fibers, leading to a corresponding decrease in the peak absorbance values. This behavior follows the Lambert-Beer law, which describes the quantitative analysis by UV-VIS spectrophotometry based on measuring the absorbance of MB solution at 660 nm due to equation (1) as follows [16]:

$$A = \varepsilon c l. \quad (1)$$

where A represents absorbance, ε is the molar absorption coefficient, c is the concentration, and l is the optical path length. Thus, the absorbance peak trend in the MB solutions can be effectively used to determine MB concentrations based on this relationship.

In Figure 3, the changes in the absorbance curve of MB around 660 nm wavelength before and after treatment with milkweed and poplar fibers were presented. It is seen that the absorbance peak decreases when treated with both fibers and reaches a minimum value with poplar fiber. According to the Lambert-Beer law in Equation (1), this indicates that the MB concentration in the solution will decrease when treated with poplar fiber.

Using the relationship between the absorbance value at 660 nm and the concentration of MB as given in Equation (1), the degree of decolorization (% decolorization) can be calculated using the formula:

$$\%Decolorization = \frac{C_{initial(MB)} - C_{treated(MB)}}{C_{initial(MB)}} \times 100 \quad (2)$$

where $C_{initial(MB)}$ is the initial absorbance value (before decolorization), and $C_{treated(MB)}$ is the absorbance value after treatment with poplar and milkweed fibers [17]. This calculation provides a quantitative measure of the effectiveness of the decolorization process with different fiber types.

The results for MB concentration percentages in this study are presented in Table 1, demonstrating that both treated fibers enhanced adsorption capacity effectively, showcasing the efficiency of these fibers for color removal. Particularly, poplar fiber presented slightly better performance compared to milkweed fiber. This improvement can be attributed to the structural differences between the fibers; specifically, poplar fiber's shorter length and smaller diameter increase its surface area, a critical factor since adsorption occurs on the fiber surface [18]. This increased surface area of poplar fiber facilitates greater adsorption capacity, emphasizing its suitability for efficient color removal.

CONCLUSIONS

This study investigated the potential of poplar fiber as an adsorbent for the decolorization of methylene blue (MB) dye in wastewater. The base modified milkweed and poplar fibers can be used as an effective alternative low-cost adsorbent for the removal of MB from its aqueous solutions. The amount of MB dye uptake on modified poplar fiber was found to be higher than milkweed fiber. Experimental results indicated that NaOH-treated poplar fiber facilitates a higher percentage of MB removal, showing its effectiveness as a decolorizing agent. It was found that the absorbance value of 0.8435 occurred for the initial dye concentration of 50 g L^{-1} by modified poplar

fiber, whereas for modified milkweed fiber it was 0.9985 for the same experiment conditions. When compared to milkweed fiber, poplar fiber demonstrates slightly better performance due to its structural characteristics, such as fine short length and fiber diameter which enhance its adsorption capabilities. The successful application of poplar fiber in this process suggests it as a promising, eco-friendly alternative for treating dye-contaminated wastewater, providing a sustainable solution for water purification.

Acknowledgement: *This work was supported by the Scientific and Technological Research Council of Türkiye (TÜBİTAK) under Grants No. 124N407. Besides, the authors gratefully acknowledge the financial support by ITU Scientific Research Projects (Grant no: MGA-2024-45727).*

REFERENCES

1. Yu Z., Qi T., Qu J., et al.: Removal of Ca(II) and Mg(II) from potassium chromate solution on Amberlite IRC 748 synthetic resin by ion exchange. J Hazard Mater, 167, 2009, pp. 406–412. https://doi.org/10.1016/j.jhazmat.2008.12.140
2. Dawood S., Sen T.K.: Removal of anionic dye congo red from aqueous solution by raw pine and acid-treated pine cone powder as adsorbent: equilibrium, thermodynamic, kinetics, mechanism and process design. Water Res., 46, 2012, pp.1933–1946. https://doi.org/10.1016/j.watres.2012.01.009
3. Mohammod M., Sen T.K., Maitra S., et al.: Removal of Zn^{2+} from aqueous solution using castor seed hull. Water Air Soil Pollut, 179, 2011, pp. 363–372. https://doi.org/10.1007/s11270-010-0503-0
4. Ciftci A., Kaya Z.: Genetic diversity and structure of Populus nigra populations in two highly fragmented river ecosystems from Turkey. Tree Genetics & Genomes, 15(4), 2019, 66 p. https://doi.org/10.1007/s11295-019-1370-5
5. Liu Y., Lyu L., Xiong X., et al.: Structural characteristics and sound absorption properties of poplar seed fibers. Textile Research Journal, 90(21–22), 2020, pp. 2467–2477. https://doi.org/10.1177/0040517520921396
6. Gurarslan A., Narinç M.E.: Investigating the rose oil and toluene absorption of populus fiber. Textile Research Journal, 89(10), 2019, pp. 1952–1963. https://doi.org/10.1177/0040517518783333
7. Chen H.L., Cluver B.: Assessment of Poplar Seed Hair Fibers as a Potential Bulk Textile Thermal Insulation Material. Clothing and Textiles Research Journal, 28(4), 2010, pp. 255–262. https://doi.org/10.1177/0887302X10375845
8. Huang J.H., Zhou C.F., Zeng, G.M., et al.: Micellar-enhanced ultrafiltration of methylene blue from dye wastewater via a polysulfone hollow fiber membrane, Journal of Membrane Science, 365 (1-2), 2010, pp. 138-144. https://doi.org/10.1016/j.memsci.2010.08.052
9. Sangalang R.H.: Kapok Fiber-Structure, Characteristics and Applications: (A Review), Oriental Journal Of Chemistry, 37(3), 2021, pp. 513-523. http://dx.doi.org/10.13005/ojc/370301
10. Usta C., Seyhan A., Gurarslan A.: Utilization of poplar fibers in needle punched nonwovens, Cellulose, 31, 2024, pp. 8351–8367. https://doi.org/10.1007/s10570-024-06062-w
11. Futalan C.M., Choi A.E.S., Soriano H.G.O., et al.: Modification Strategies of Kapok Fiber Composites and Its Application in the Adsorption of Heavy Metal Ions and Dyes from Aqueous Solutions: A Systematic Review. International Journal of Environmental Research and Public Health, 19(5), 2022, 2703 p. https://doi.org/10.3390/ijerph19052703
12. Wolok E., Lahay I.H., Machmoed B.R., et al.: Modification And Characterization Of Ceiba Pentandra (L.) Gaertn. (Kapok) Fiber: Physical Properties. International Journal of Research -GRANTHAALAYAH, 7(7), 2019, pp. 381-390. https://doi.org/10.5658/WOOD.2018.46.4.393
13. Liu Y., Wang J., Zheng Y., et al.: Adsorption of methylene blue by kapok fiber treated by sodium chlorite optimized with response surface methodology, Chemical Engineering Journal, 184, 2012, pp. 248–255. https://doi.org/10.1016/j.cej.2012.01.049
14. Mohamed M.A., W Salleh W.N., Jaafar J., et al.: Physicochemical characterization of cellulose nanocrystal and nanoporous self-assembled CNC membrane derived from Ceiba pentandra. Carbohydr Polym., 57, 2017, pp. 1892-1902. https://doi.org/10.1016/j.carbpol.2016.11.078
15. Shiffman D.: Chapter 7: Cellular automata. Nature of Code, 2012. 15. Tseng K.H., Chung M.Y., Chang C.Y., et al.: A Study of Photocatalysis of Methylene Blue of TiO_2 Fabricated by Electric Spark Discharge Method, Hindawi Journal of Nanomaterials, Volume 2017- 9346201. https://doi.org/10.1155/2017/9346201
16. Hołysz L., Rek P., Huber M., et al.: Evaluation and comparison of various methods used for aggregates investigations, Adsorption, 30, 2024, pp. 265–277. https://doi.org/10.1007/s10450-023-00393-z
17. Tiandho Y., Afriani F., Evi J., et al.: Kinetic evaluation of methylene blue decolorization by CuO as a Fenton-like catalyst. IOP Conf. Ser.: Earth Environ. Sci., 926, 2021, 012103 p. https://doi.org/10.1088/1755-1315/926/1/012103
18. Chatterjee S., Kumar A., Basu B., et al.: Application of Response Surface Methodology for Methylene Blue dye removal from aqueous solution using low cost adsorbent, Chemical Engineering Journal, 181–182, 2012, pp. 289-299. https://doi.org/10.1016/j.cej.2011.11.081

EVALUATING BIODEGRADATION RATES IN NEAT PCL- AND PCL/PLA-BASED BIOCOMPATIBLE TUBULAR SCAFFOLDS

OZTEMUR, JANSET[1*]; OZDEMIR, SUZAN[1]; TEZCAN-UNLU, HAVVA[2]; CECENER, GULSAH[2]; SEZGIN, HANDE[1] AND YALCIN-ENIS, IPEK[1]

[1] Textile Engineering Department, Istanbul Technical University, Istanbul, Turkey
[2] Department of Medical Biology, Faculty of Medicine, Bursa Uludag University, Bursa, Turkey

ABSTRACT

Vascular grafts are synthetic tubular structures that play an important role in replacing damaged vessels in the treatment of cardiovascular diseases. Existing grafts, especially in small-diameter vessels, face persistent issues such as thrombosis, immune rejection, and mechanical limitations. Vascular grafts designed with an innovative perspective to overcome these deficiencies are tubular scaffolds with a biodegradable structure and a layered design that mimics the native artery structure. This study focuses on the development of biodegradable and biocompatible tubular scaffolds with randomly distributed and radially oriented fibers in different layers to replicate the native structure of artery, utilizing neat polycaprolactone (PCL) and PCL/polylactic acid (PLA) blend with 4/1 polymer blend ratio. Electrospinning technique is employed to fabricate tubular fibrous structures. The biodegradation profiles of these scaffolds are assessed at 3, 6, and 9 months, with comparative analyses conducted to explore how polymer type and orientation level influence degradation rates and the structural integrity of the materials over time. The findings reveal that scaffolds with randomly distributed fibers exhibit higher biodegradation rates compared to those with oriented fibers, particularly in the PCL/PLA blends. Specifically, the study identifies PCL_R as having the highest degradation rate at 61% weight loss by the 9th month. Importantly, while PCL is known for its slow degradation, the high molecular weight of PLA leads to a slower degradation profile in the PCL/PLA samples. These insights underscore the critical role of scaffold morphology and composition in optimizing the performance and functionality of vascular grafts, highlighting the need for scaffolds that support cellular activities while effectively degrading to facilitate tissue regeneration without toxic effects.

KEYWORDS

Polycaprolactone; Polylactic acid; Tissue engineering; Electrospinning; Biodegradability.

INTRODUCTION

Tissue engineering aims to develop scaffolds that serve as effective substitutes for damaged tissues by facilitating biological activities and controlled biodegradation during tissue regeneration, while maintaining mechanical integrity [1]. The design of advanced biomaterials and the integration of implants with tissues are intricately linked to cell-scaffold interactions. Three-dimensional (3D) fibrous scaffolds that mimic the extracellular matrix (ECM) are essential, as they support critical cellular activities such as attachment, migration, proliferation, and differentiation necessary for tissue regeneration [2] [3]. On the other hand, cardiovascular diseases have become a major health problem, causing high rates of death and disability worldwide. The inadequacy of autologous vessels and the problems such as mismatch, thrombosis and occlusion in small-diameter replacements of existing commercial grafts have triggered the need for tissue-engineered vascular grafts [4-6].

Biodegradable polymers offer considerable advantages over non-biodegradable materials by minimizing the need for surgical removal and reducing the necessity for long-term immunosuppressive treatments [7]. The design of biodegradable vascular grafts focuses on fostering the development of an autologous vessel concurrently with scaffold degradation. In particular, the formation of a regenerated structure that will replace the damaged vessel and the realization of endothelialization require a long-term process, and at this point the importance of biodegradability in vascular graft structures emerges. The biodegradability period of the vascular graft should be slow enough to allow time for new tissue formation, but it should not cause a toxic effect during this process [8]. This approach aims to address issues related to immunogenicity and thrombus formation by

[*] **Corresponding author:** Oztemur J., e-mail: *oztemurj@itu.edu.tr*

ensuring that the scaffold's degradation rate is synchronized with the rate of neovascularization [9]. The degradation kinetics of the scaffold are influenced by several factors, including the choice of polymer, production techniques, and scaffold architecture. Thus, achieving a balance between degradation and tissue regeneration is critical for maintaining the scaffold's mechanical properties and functional performance throughout the regenerative process. In this context, the choice of material becomes pivotal. Although synthetic polymers such as polyurethane (PU), poly(ethylene glycol) (PEG), poly(glycolic acid) (PGA), poly(lactic acid-co-glycolic acid) (PLGA), poly(vinyl alcohol) (PVA), PLA, poly(L-lactic acid-co-ε-caprolactone) (PLCL), and PCL exhibit varying biodegradation times, they are frequently preferred in tissue engineering applications due to their high strength and comparatively slow degradation rates relative to natural polymers [10]. Among these materials, PCL and PLA are particularly noteworthy for their biocompatibility, adjustable degradation rates, and mechanical properties, making them highly cited in the literature as preferred polymers in various vascular graft applications [11-14].

On the other hand, using layered structures in vascular grafts and designing each layer to mimic the native artery structure is important in terms of obtaining the desired physical, mechanical and biological properties [15]. In this context, at least a two-layer graft design is envisaged and the inner layer is produced with random fiber distribution to mimic the *tunica intima*, the inner most layer of an artery that is in contact with blood, while the outer layer contains fibers with radial orientation to mimic the *tunica media*, the middle layer of an artery responsible for mechanical features [16]. This structural property, in addition to the material type, has an impact on the biodegradable values of the grafts [17].

This study investigates the biodegradation behavior of biocompatible scaffolds designed for vascular graft application. Utilizing electrospinning techniques, tubular scaffolds with randomly distributed and radially oriented fibers made from both neat PCL and PCL/PLA blend are developed. The biodegradation of these scaffolds is assessed over 3, 6, and 9 months. The biodegradability rates of the developed scaffolds are discussed comparatively, taking into account PLA addition and fiber orientation.

EXPERIMENTAL

Materials

PCL (Mn 80,000), PLA (Mn 230,000; Ingeo 2003 D with 4.3 mol% D-lactide content), and the components of solvent systems (chloroform (CHL), ethanol (ETH), and acetic acid (AA)) are supplied from Sigma Aldrich.

Methods

Scaffold fabrication

Neat PCL and PCL/PLA blend are dissolved in CHL/ETH/AA (8/1/1 wt.) solvent system, and polymer concentrations are kept constant at 8%. Blend ratio is selected as 4/1 by weight for PCL/PLA. Each polymer solution system is stirred for 2 hours at room temperature. Tubular structures with 6 mm diameter are fabricated using electrospinning set-up with a custom designed rotating feeding unit (Nanospinner, Basic System, Inovenso, Turkey). Scaffolds are produced at 200 rpm for randomly distributed fibers and 10,000 rpm for randomly oriented fibers. Randomly distributed fibers are indicated with the suffix _R, whereas surfaces with oriented fibers are denoted with the suffix _O.

Scaffold Sterilization

Samples are sterilized by washing once in 70% ethanol, followed by three rinses in sterile phosphate buffered saline (PBS). The fibrous webs are then exposed to UV light for 30 minutes on both sides. All UV sterilization processes are conducted in a laminar flow cabinet.

Biodegradation Analysis

Sterilized surfaces are cut into 1x1 cm pieces, with measurements taken at 3rd, 6th, and 9th months. Initial weights are recorded using a precision balance. The samples are placed in 24-well plates with 300 µl of PBS and incubated at 37°C in a 5% CO_2 humidified incubator (Panasonic, Osaka, Japan). Degradation rates are determined by measuring the mass loss of the samples over the 9-month period.

RESULTS

The biodegradation results of fibrous samples featuring randomly distributed and oriented fibers are presented in Figures 1 and 2. It is observed that scaffolds with randomly distributed fibers degrade more rapidly than samples with aligned fibers, owing to their loosely packed structure. The densely packed arrangement of the scaffolds, together with aligned fibers, establishes a barrier that impedes PBS penetration, thereby effectively decelerating the degradation process [18]. In the present study, it is noted that in both sample groups—PCL and PCL/PLA—the surfaces with randomly distributed fibers exhibited higher degradation rates, especially at the 6th and 9th months, compared to samples with radially orientated fibers. In a 12-month biodegradation assessment, Oztemur et al. (2024) observed that electrospun PCL surfaces with randomly distributed fibers displayed a relatively higher degree of degradation than their aligned fiber counterparts [16]. Similarly, Mirzaei et al. (2020), in a study utilizing blends of polyethylene oxide (PEO) and PCL, found that by the 7th day, surfaces with randomly distributed fibers demonstrated a slightly

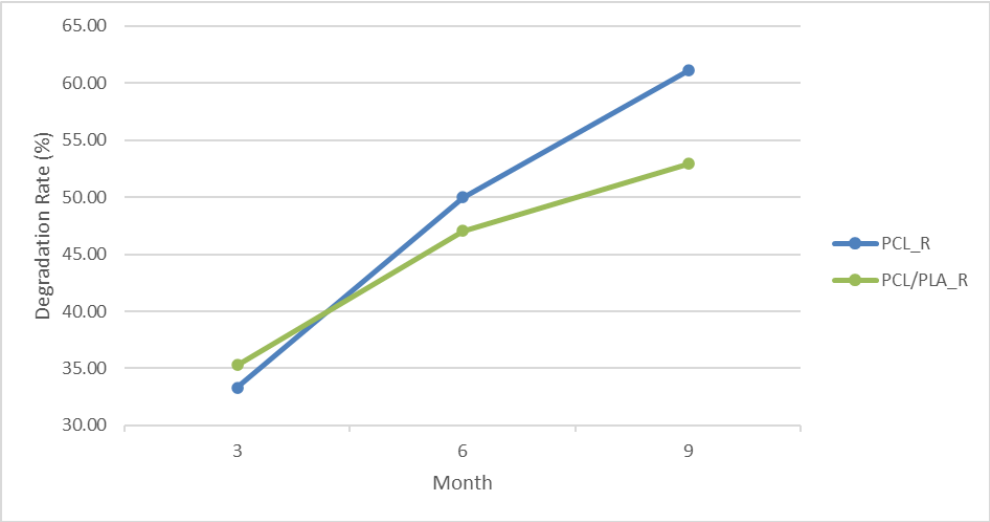

Figure 1. Biodegradation rates of PCL_R and PCL/PLA_R scaffolds.

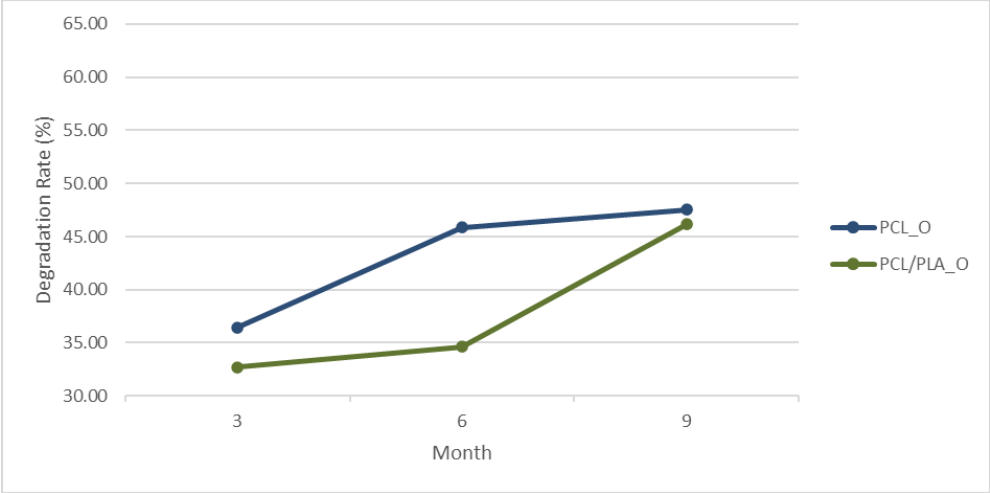

Figure 2. Biodegradation rates of PCL_O and PCL/PLA_O scaffolds.

higher degradation rate, independent of the blending ratio [19].

From a material-centered perspective, when the sample groups are compared, it is observed that both the scaffolds with randomly distributed fibers and those with radial orientation exhibit similar degradation rates within the initial 3 months. PCL degradation primarily occurs through the hydrolytic cleavage of ester bonds, which is generally a slow process taking approximately two to three years [20]; however, in the present study, PCL_R displays a more rapid degradation trend by the 6th and 9th months. This accelerated degradation rate in the PCL sample may be attributed to its substantially lower molecular weight in comparison to PLA. Molecular weight is a crucial factor in the hydrolytic degradation rate of polymers; higher molecular weights are known to correspond to a more stable degradation rate. Conversely, when molecular weight decreases below a specific threshold, degradation accelerates due to increased molecular mobility, a greater presence of hydrophilic groups, and enhanced water diffusion [19]. Additionally, among the radially oriented samples, while PCL_O exhibits a significant increase in degradation rate from the 3rd to the 6th month in comparison to PCL/PLA_O, by the end of the 9th month, both PCL_O and PCL/PLA_O have reached comparable values, with degradation rates of 47% and 46%, respectively.

CONCLUSION

In this study, the influence of fiber orientation and material type on the biodegradation profiles of electrospun scaffolds is evaluated to refine scaffold design for enhanced control over degradation kinetics in tissue engineering applications specifically, in vascular grafts. Through an analysis of fiber alignment and molecular weight variations, the study offers critical insights for optimizing scaffold composition to achieve precise biocompatibility and functional longevity in targeted biomedical applications. In this context, it is necessary to emphasize the following points as the key outcomes of the study:

- Fiber orientation significantly influences biodegradation behavior, with PCL_R and PCL/PLA_R, which possess randomly distributed fibers, exhibiting greater degradation compared to the oriented fiber counterparts, PCL_O and PCL/PLA_O, by the end of the 9-month period.
- Among all samples, PCL_R demonstrated the highest degradation rate at 61% weight loss by the end of the 9th month.
- Although PCL is generally recognized as a relatively slow-degrading biopolymer, the high molecular weight of PLA utilized in the PCL/PLA sample groups resulted in slower degradation rates in this study.

Acknowledgement: *This study is supported by the TUBITAK (The Scientific and Technological Research Council of Turkey) under grant no: 121M309.*

REFERENCES

1. Liu S., Qin S., He M., et al.: Current applications of poly (lactic acid) composites in tissue engineering and drug delivery. Composites Part B, 199, 2020, 108238 p. https://doi.org/10.1016/j.compositesb.2020.108238
2. Ermis M., Antmen E., Hasirci V.: Bioactive Materials Micro and Nanofabrication methods to control cell-substrate interactions and cell behavior : A review from the tissue engineering perspective. Bioactive Materials, 3(3), 2018, pp. 355–369. https://doi.org/10.1016/j.bioactmat.2018.05.005
3. Hao D., Lopez J., Chen J., et al.: Engineering Extracellular Microenvironment for Tissue Regeneration. Bioengineering, 9, 2022, pp. 1–17.
4. Daum R., Visser D., Wild C., et al.: Fibronectin Adsorption on Electrospun Synthetic Vascular Grafts Attracts Endothelial Progenitor Cells and Promotes Endothelialization in Dynamic In Vitro Culture. Cells, 9(3), 2020. https://doi.org/10.3390/cells9030778
5. Loh Q.L., Choong C.: Three-dimensional scaffolds for tissue engineering applications: Role of porosity and pore size. Tissue Engineering - Part B: Reviews, 19(6), 2013, pp. 485–502. https://doi.org/10.1089/ten.teb.2012.0437
6. Vaduganathan M., Mensah G.A., Turco J.V., et al.: The Global Burden of Cardiovascular Diseases and Risk: A Compass for Future Health. Journal of the American College of Cardiology, 80(25), 2022. https://doi.org/10.1016/j.jacc.2022.11.005
7. Hartley E.: Biodegradable Synthetic Polymers for Tissue Engineering : A Mini-Review. Reinvention, 15, 2022, pp. 48–70.
8. Fukunishi T., Best C.A., Sugiura T., et al.: Tissue-Engineered Small Diameter Arterial Vascular Grafts from Cell-Free Nanofiber PCL / Chitosan Scaffolds in a Sheep Model. PLoS ONE, 11(7), 2016, pp. 1–15. https://doi.org/10.1371/journal.pone.0158555
9. Wu J., Hu C., Tang Z., et al.: Tissue-engineered Vascular Grafts: Balance of the Four Major Requirements. Colloids and Interface Science Communications, 23, 2018, pp. 34–44. https://doi.org/10.1016/j.colcom.2018.01.005
10. Sankaran K.K., Krishnan U.M., Sethuraman S.: Axially aligned 3D nanofibrous grafts of PLA-PCL for small diameter cardiovascular applications. Journal of Biomaterials Science, Polymer Edition, 25(16), 2014, pp. 1791–1812. https://doi.org/10.1080/09205063.2014.950505
11. Li C., Wang F., Ge P., et al.: Anti-acute thrombogenic surface using coaxial electrospraying coating for vascular graft application. Materials Letters, 205, 2017, pp. 15–19. https://doi.org/10.1016/j.matlet.2017.06.050
12. Liu K., Wang N., Wang W., et al.: A bio-inspired high strength three-layer nanofiber vascular graft with structure guided cell growth. Journal of Materials Chemistry B, 5(20), 2017, pp. 3758–3764. https://doi.org/10.1039/c7tb00465f
13. Ozdemir S., Oztemur J., Sezgin H., et al.: Optimization of Electrospun Bilayer Vascular Grafts through Assessment of the Mechanical Properties of Monolayers. ACS Biomaterials Science and Engineering, 2023. https://doi.org/10.1021/acsbiomaterials.3c01161
14. Sankaran K.K., Krishnan U.M., Sethuraman S.: Axially aligned 3D nanofibrous grafts of PLA-PCL for small diameter cardiovascular applications. Journal of Biomaterials Science, Polymer Edition, 25(16), 2014, pp. 1791–1812. https://doi.org/10.1080/09205063.2014.950505
15. Enis I.Y., Sadikoglu T.G., Horakova J., et al.: The post-morphological analysis of electrospun vascular grafts following mechanical testing. Journal of Polymer Engineering, 38(6), 2018, pp. 525–535. https://doi.org/10.1515/polyeng-2017-0157
16. Ozdemir S., Yalcin-Enis I., Yalcinkaya B., et al.: An Investigation of the Constructional Design Components Affecting the Mechanical Response and Cellular Activity of Electrospun Vascular Grafts. Membranes, 12(10), 2022, 929 p. https://doi.org/10.3390/membranes12100929
17. Oztemur J., Ozdemir S., Tezcan-unlu H., et al.: Investigation of biodegradability and cellular activity of PCL / PLA and PCL / PLLA electrospun webs for tissue engineering applications. Biopolymers, 2023, pp. 1–10. https://doi.org/10.1002/bip.23564
18. Subramanian A., Krishnan U.M., Sethuraman S.: Axially aligned electrically conducting biodegradable nanofibers for neural regeneration. Journal of Materials Science: Materials in Medicine, 23(7), 2012, pp. 1797–1809. https://doi.org/10.1007/s10856-012-4654-y
19. Oztemur J., Ozdemir S., Tezcan-Unlu H., et al.: Static and Dynamic Cell Culture of Small Caliber Bilayer Vascular Grafts Electrospun from Polycaprolactone. International Journal of Polymeric Materials and Polymeric Biomaterials, 2024. https://doi.org/10.1080/00914037.2024.2421837
20. Mirzaei Z.S., Kordestani S., Kuth S., et al.: Preparation and Characterization of Electrospun Blend Fibrous Polyethylene Oxide:Polycaprolactone Scaffolds to Promote Cartilage Regeneration. Advanced Engineering Materials, 22(9), 2020, pp. 1–12. https://doi.org/10.1002/adem.202000131
21. Cipitria A., Skelton A., Dargaville T.R., et al.: Design, fabrication and characterization of PCL electrospun scaffolds - A review. Journal of Materials Chemistry, 21(26), 2011, pp. 9419–9453. https://doi.org/10.1039/c0jm04502k
22. Gorrasi G., Pantani R.: Hydrolysis and Biodegradation of Poly(lactic acid). In: Di Lorenzo, M., Androsch, R. (eds) Synthesis, Structure and Properties of Poly(lactic acid). Advances in Polymer Science, 279. Springer, Cham., 2017. https://doi.org/10.1007/12_2016_12

SUTURE RETENTION STRENGTH OF BILAYER VASCULAR GRAFTS MADE OF PCL, PLA AND THEIR COPOLYMER

OZDEMIR, SUZAN[1*]; OZTEMUR, JANSET[1]; YOLGOSTEREN, ATIF[2]; SEZGIN, HANDE[1] AND ENIS, IPEK YALCIN[1]

[1] Istanbul Technical University, Textile Engineering Department, Istanbul, Turkey
[2] Bursa Uludag University, Cardiovascular Surgery, Bursa, Turkey

ABSTRACT

The mechanical characteristics of small-diameter vascular grafts, including factors like modulus, elasticity, compliance, burst strength, and suture retention strength, need to be in line with those of native blood vessels. Even a slight mismatch in mechanical properties between the graft and the native vessel can lead to graft failure. Suture retention strength, a critical mechanical aspect, represents the force needed to remove a stitch from the graft or cause the graft wall to rupture. This property is vital for preventing leaks, maintaining proper blood flow, aiding tissue healing, ensuring long-term durability, and reducing complications in vascular grafts. In this study, bilayered vascular grafts are fabricated by electrospinning using polycaprolactone (PCL), poly (lactic acid) (PLA), and poly(l-lactide-co-caprolactone) (PLCL) polymers. The actual suturing conditions of vascular scaffolds are simulated and how the choice of polymer for the inner layer affects suture retention strength is assessed. At the post-mechanical stage, the morphologies of the scaffolds are investigated to gain a clearer understanding of how the material reacts to applied forces. The findings reveal that all the fabricated bilayer vascular scaffolds exhibit excellent suture performance, with strength values exceeding 10 N, and that polymer selection for the inner layer for the grafts significantly influences the results. Blending PCL and PLA in the inner layer is found to reduce suture retention strength, while using neat polymers results in better retention strength. This experiment offers a more precise assessment of suture retention strength for bilayer vascular grafts, facilitating further optimization of tissue-engineered grafts to meet specific mechanical requirements.

KEYWORDS

Suture retention strength; Vascular grafts; Blood vessels; Tissue engineering.

INTRODUCTION

Currently, due to global aging, cardiovascular disease (CVD) causes 17.3 million deaths each year, and this number is projected to rise to over 23.6 million by 2030 [1]. One of the most preferred treatments for cardiovascular diseases is graft bypass surgery using autologous blood vessels, allogenic blood vessels, or artificial blood vessels [2]. At present, various commercial artificial blood vessels made from synthetic materials like Dacron and e-PTFE are widely used for vascular replacement. However, these artificial grafts are nondegradable and often elicit long-term foreign-body responses [3]. In recent years, due to the collaborative efforts of researchers worldwide, tissue engineering vascular grafts (TEVGs) have made significant advancements. Large-diameter artificial blood vessels (greater than 6 mm) have shown considerable therapeutic success in clinical settings. However, it is unfortunate that small-diameter artificial vascular grafts (less than 6 mm), such as those used for inguinal and coronary artery transplants, have not yet achieved satisfactory outcomes [4]. Electrospinning is a well-established technique for creating customized vascular grafts. This process enables the fine-tuning of the mechanical properties of the final product. By using various materials, making micro- and macrostructural modifications, incorporating additives, and altering the electrospinning process, the mechanical properties can be adjusted and optimized [5]. Designing multi-layered electrospun vascular scaffolds is regarded as an effective method to replicate the structure and function of natural blood vessels [6].

Researchers have emphasized that the graft must be resilient and possess mechanical strength comparable to that of native vessels [7]. An ideal TEVG should have properties similar to those of the native artery and integrate seamlessly with it, as any disparity in mechanical properties between the TEVG and adjacent blood vessels can lead to graft rupture

[*] **Corresponding author:** Ozdemir S., e-mail: ozdemirsu@itu.edu.tr

or blood leakage. TEVGs must withstand distortion and compression, possess adequate tensile and shear strength to endure the forces exerted during suturing and implantation, and maintain circumferential strength to resist hemodynamic pressure. This ensures the prosthesis avoids rupture, scattering, edge wear, seam tearing, and retains structural integrity [8]. The mechanical properties of electrospun fibers are heavily influenced by the raw materials used [1]. Recently, researchers have shown significant interest in synthetic biomaterials like PCL, PLA, and their copolymers to address the mechanical limitations observed in natural biopolymers [9]. Because of its exceptional biocompatibility, moderate degradation rate, and demonstrated tensile strength and elongation capabilities, PCL is highly recommended as a biodegradable polymer for developing vascular grafts. Additionally, PLA is favored in biomedical applications for its excellent mechanical strength and modulus, biocompatibility, rapid biodegradation, lack of toxicity, and composition derived from aliphatic bio-based sources [10].

In clinical applications, the suture retention strength typically determines the reliability of the anastomosis [11]. The suture retention strength assessment measures the force needed to tear a suture from a scaffold or cause rupture of the scaffold wall. It is noted that the human saphenous vein has a suture retention strength of 1.81 ± 0.02 N [12]. Thus, there have been many research attempts to examine the suture retention strength of vascular grafts along with other mechanical features. The study by Kim et al. (2013) focused on fabricating a tubular double-layered scaffold using the PLCL gel spinning method and salt leaching. Suture retention strength tests were conducted on PLCL scaffolds with different thicknesses (ranging from 1 mm to 1.5 mm) and compared to ePTFE grafts. The results showed no significant difference in suture retention strength between the PLCL scaffolds and ePTFE grafts. Suture retention strength values for PLCL scaffolds with varying thicknesses ranged from 5.89 N to 10.28 N [13]. In another study, Meng et al. (2019) investigated the suture retention strength of P(LLA-CL) tissue-engineered vascular grafts. The results demonstrated that P(LLA-CL) tissue-engineered vascular scaffolds exhibited excellent suture performance. The study also emphasized the influence of fiber direction and number of stitches on suture retention strength. Specifically, the highest suture retention strength, ranging between 2 and 2.5 N, was observed when the suture was perpendicular to the fibers (in the circumferential direction) [8].

This study aims to create bilayered vascular grafts through electrospinning with different polymers (PCL, PLA, PLCL), simulate suturing conditions, and evaluate how the choice of inner layer polymer affects suture retention strength. Post-mechanical testing examines scaffold morphologies under stress. Results indicate that all grafts exhibit strong suture performance (>10 N), with significant variation depending on inner layer polymer. Blending PCL and PLA lowers retention strength compared to using neat PCL.

EXPERIMENTAL

Materials

PCL (Mw 80,000), PLA (Mw 230,000), and PLCL are utilized as the polymers. The solvent system includes chloroform (CH), acetic acid (AA), and ethanol (ETH). All polymers and solvents are procured from Sigma Aldrich.

Methods

Bilayer scaffold fabrication

To create bilayer tubular scaffolds with fibers that are either randomly distributed or radially oriented, PCL, PLA, and PLCL polymers are dissolved in a CHL/ETH/AA mixture (with a weight ratio of 8/1/1). The samples codes and blending ratios are provided in Table 1. PCL and PLA solutions are prepared in both pure and blended forms, while PLCL is used in its pure form. The blending ratio is adjusted in 10% increments, ranging from 80% to 100%. The polymer concentration for pure PCL, as well as PCL-PLA blends, is maintained at 8%, whereas PLCL solutions are at 10%. PLCL is utilized for the outer layers of all scaffolds, while the inner layer employs both neat and blended fibrous surfaces to examine their impact on suture retention strength.

A custom-built electrospinning unit, equipped with a vertical feeding direction and a closed chamber from Inovenso, Turkey (Nanospinner, Ne100+), is used to fabricate the tubular scaffolds from PCL, PLA, and PLCL polymers. The neat and blended polymer solutions are delivered using a 10 ml plastic syringe pump at a controlled flow rate of 3 ± 1 ml/h. They are subjected to an electric potential of 11 ± 1 kV over a distance from the needle tip, with an inner diameter of 0.6 mm, to a collector positioned 20 cm away. Tubular vascular grafts are produced using rotating rod collectors with a 5 mm diameter. The rotation speeds applied are 200 rpm for randomly distributed fibers (inner layer) and 10,000 rpm for radially oriented fibers (outer layer). The production time is set at 20 minutes for the inner layer and 55 minutes for the outer layer.

Table 1. Sample codes and blending ratios.

Samples	PCL/PLA blending ratio
PCL_R+PLCL_O	100/0
PCLPLA90_R+PLCL_O	90/10
PCLPLA80_R+PLCL_O	80/20

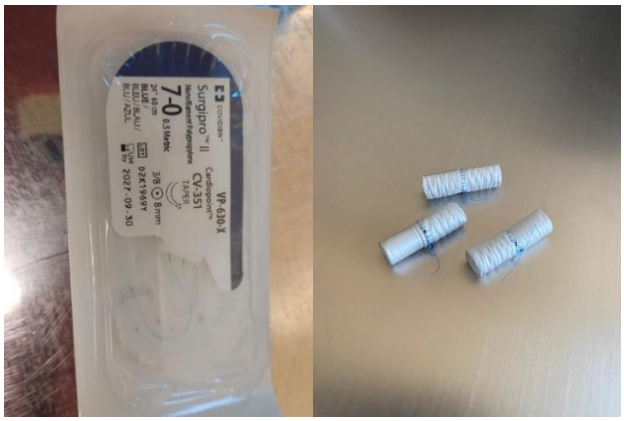

Figure 1. Images of the polypropylene thread used for stitching and the surfaces sewn with continuous stitching.

Table 2. Suture retention strength results of bilayer samples.

Samples	Suture retention strength (N)
PCL_R+PLCL_O	15.81 ± 4.06
PCLPLA90_R+PLCL_O	14.00 ± 3.47
PCLPLA80_R+PLCL_O	11.50 ± 0.63

Scanning Electron Microscope (SEM) Analysis

The morphology of the scaffolds is examined using FEI Quanta FEG 250 SEM after conducting suture retention tests. The samples are coated with a gold-palladium (Au-Pd) alloy in a sputter coating machine (Quorum SC7620) for observation.

Suture retention strength

To test the suture strength of the developed bilayer grafts, the grafts are cut into tubular pieces 1 cm in length, and two graft pieces are joined using continuous stitching, with 7/0 monofilament polypropylene thread applied to a standard vessel during surgery (Figure 1). The strength of the sutures in the scaffolds is evaluated by employing a Zwick-Roell Z005 universal testing machine fitted with a 200N load cell. The tubular segments, after being sewn, undergo testing in longitudinal direction. This examination is conducted at a cross-head speed of 10 mm/min and a gauge distance of 5 mm.

RESULTS AND DISCUSSION

SEM Analysis

SEM images of bilayer samples after suture retention strength can be seen in Fig. 2. When the suture areas are examined, it is seen that although the samples are damaged, they are not completely torn and are only opened from the seam areas.

Suture retention strength

Suture retention strength results are presented in Table 2. Upon examination, it is observed that the suture strength values of all samples fell within the range of approximately 11-16 N. This indicates superior results compared to the human saphenous vein, which typically exhibits suture retention strength between 2-3 N, known as the gold standard [14]. Furthermore, the highest suture retention strength is observed in the sample using neat PCL in the inner layer. In samples where PCL and PLA are blended, a decrease in results is noted with increasing PLA ratio. This decrease can be attributed to reduced mechanical integrity of the grafts, stemming from the immiscibility of PCL and PLA polymers, as well as increased incompatibility between the inner and outer layers due to blending polymers in the inner layer [10]. Phase separation results from the weak adhesion forces between the polymer chains in these scaffolds during the electrospinning process, which prevents the blending from being adequately achieved [15].

CONCLUSIONS

Based on the findings of this study, it is evident that the suture retention strength of bilayered vascular grafts is critically influenced by the choice of polymers used in the inner layer. The experiments demonstrated that grafts utilizing neat PCL in the inner layer exhibited superior suture retention strength compared to those incorporating PCL-PLA blends. The observed decrease in strength with increasing PLA content highlights the challenges posed by polymer immiscibility and phase separation during fabrication. SEM analysis further supported these findings, revealing structural integrity despite damage at suture sites. These insights underscore the importance of careful polymer selection and processing methods in optimizing the mechanical properties of vascular grafts for enhanced durability and clinical efficacy. Future research should focus on refining polymer blending and graft construction to better align with the demanding mechanical requirements of vascular applications.

Acknowledgement: *This study is funded by TUBITAK Project (Grant no: 121M309).*

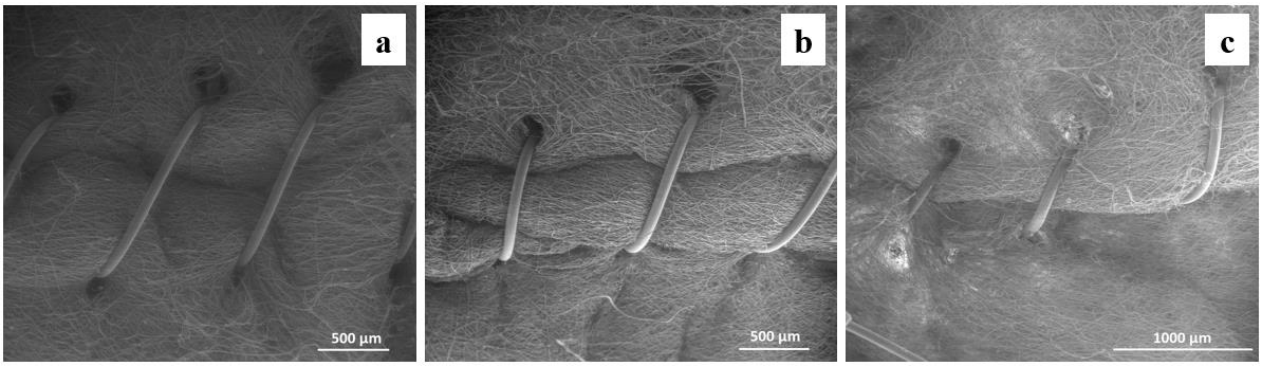

Figure 2. SEM images at 100x magnification of samples (a) PCL_R+PLCL_O, (b) PCLPLA90_R+PLCL_O, and (c) PCLPLA80_R+PLCL_O.

REFERENCES

1. Maleki S., Shamloo A., Kalantarnia F.: Tubular TPU/SF Nanofibers Covered with Chitosan-Based Hydrogels as Small-Diameter Vascular Grafts with Enhanced Mechanical Properties. Sci Rep, 2022, 12 (1). https://doi.org/10.1038/s41598-022-10264-2
2. Li M.X., Wei Q.Q., Mo H.L., et al.: Challenges and Advances in Materials and Fabrication Technologies of Small-Diameter Vascular Grafts. Biomaterials Research. BioMed Central Ltd., 2023. https://doi.org/10.1186/s40824-023-00399-2
3. Jia W., Li M., Weng H., et al.: Design and Comprehensive Assessment of a Biomimetic Tri-Layer Tubular Scaffold via Biodegradable Polymers for Vascular Tissue Engineering Applications. Materials Science and Engineering C, 110, 2020. https://doi.org/10.1016/j.msec.2020.110717
4. Yang L., Li X., Wu Y., et al.: Preparation of Pu/Fibrin Vascular Scaffold with Good Biomechanical Properties and Evaluation of Its Performance in Vitro and in Vivo. Int J Nanomedicine, 15, 2020, pp. 8697–8715. https://doi.org/10.2147/IJN.S274459
5. Stoiber M., Grasl C., Frieberger K., et al.: Impact of the Testing Protocol on the Mechanical Characterization of Small Diameter Electrospun Vascular Grafts: Dynamic Testing of Electrospun Small Diameter Vascular Grafts. J Mech Behav Biomed Mater, 104, 2020. https://doi.org/10.1016/j.jmbbm.2020.103652
6. Do T.M., Yang Y., Deng A.: Porous Bilayer Vascular Grafts Fabricated from Electrospinning of the Recombinant Human Collagen (Rhc) Peptide-Based Blend. Polymers (Basel), 13 (22), 2021. https://doi.org/10.3390/polym13224042
7. Liu D., Han J., Zhuang X., et al.: Evaluation of Mechanical Properties and Biocompatibility of Three-Layer PCL/PLLA Small-Diameter Vascular Graft with Pore Diameter Gradient. Eur Polym J, 186, 2023. https://doi.org/10.1016/j.eurpolymj.2023.111864
8. Meng X., Wang X., Jiang Y., et al.: Suture Retention Strength of P(LLA-CL) Tissue-Engineered Vascular Grafts. RSC Adv, 9 (37), 2019, pp. 21258–21264. https://doi.org/10.1039/c9ra04529e
9. Ozdemir S., Oztemur J., Sezgin H., et al.: Optimization of Electrospun Bilayer Vascular Grafts through Assessment of the Mechanical Properties of Monolayers. ACS Biomater Sci Eng, 2023. https://doi.org/10.1021/acsbiomaterials.3c01161
10. Ozdemir S., Oztemur J., Sezgin H., et al.: Structural Design and Mechanical Analysis of Small-Caliber Bilayer Vascular Prostheses. International Journal of Polymeric Materials and Polymeric Biomaterials, 2024. https://doi.org/10.1080/00914037.2024.2325968
11. Zhang F., Bambharoliya T., Xie Y., et al.: A Hybrid Vascular Graft Harnessing the Superior Mechanical Properties of Synthetic Fibers and the Biological Performance of Collagen Filaments. Materials Science and Engineering C, 118, 2021. https://doi.org/10.1016/j.msec.2020.111418
12. Montini-Ballarin F., Abraham G.A., Caracciolo P.C.: Mechanical Behavior of Polyurethane-Based Small-Diameter Vascular Grafts. In Advances in Polyurethane Biomaterials; Elsevier Inc., 2016, pp 451–477. https://doi.org/10.1016/B978-0-08-100614-6.00015-9
13. Kim S.H., Mun C.H., Jung Y., et al.: Mechanical Properties of Compliant Double Layered Poly(L-Lactide-Co-ε-Caprolactone) Vascular Graft. Macromol Res, 21 (8), 2013, pp. 886–891. https://doi.org/10.1007/s13233-013-1095-5
14. Rodriguez M., Kluge J.A., Smoot D., et al.: Fabricating Mechanically Improved Silk-Based Vascular Grafts by Solution Control of the Gel-Spinning Process. Biomaterials, 230, 2020. https://doi.org/10.1016/j.biomaterials.2019.119567
15. Carvalho J.R.G., Conde G., Antonioli M.L., et al.: Biocompatibility and Biodegradation of Poly(Lactic Acid) (PLA) and an Immiscible PLA/Poly(ε-Caprolactone) (PCL) Blend Compatibilized by Poly(ε-Caprolactone-b-Tetrahydrofuran) Implanted in Horses. Polym J, 52 (6), 2020, pp. 629–643. https://doi.org/10.1038/s41428-020-0308-y

INVESTIGATION OF THE PRODUCTION OF TRICLOSAN/CHITOSAN NANOCAPSULES FOR FUNCTIONAL SURFACE APPLICATIONS

DASDEMIR, MEHMET[1,2]; SERDAR, SERAP GAMZE[2*] AND IBILI, HATICE[2]

[1] The Nonwovens Institute, North Carolina State University, Raleigh, NC 27606, USA
[2] Gaziantep University, Textile Engineering Department, Gaziantep, 27310, Turkey

ABSTRACT

This study focuses on producing monodisperse nanocapsules with a triclosan/chitosan core-shell structure using the coaxial electrospray method. The coaxial electrospraying method enables the production of core/shell structured nanocapsules in a single step. The effects of flow rate, core-to-shell flow rate ratio, and needle size on the coaxial electrospray process were systematically analyzed. The resulting nanocapsule structures were characterized using scanning electron microscope (SEM), transmission electron microscope (TEM) and size measurements. The experiments demonstrated that fibrillation more likely occurred when the chitosan content was highest.

KEYWORDS

Coaxial electrospray; Encapsulation; Chitosan; Triclosan.

INTRODUCTION

Chitosan (CS), a natural polysaccharide-based biopolymer derived from chitin deacetylation. It has diverse applications in drug delivery, tissue engineering, encapsulation, nano- and microparticle formation, plant protection thanks to its biocompatibility, biodegradability, low toxicity, and antibacterial properties [1–4]. Triclosan (Irgasan), another widely used antibacterial agent, is often applied on synthetic fibers like polyester, polypropylene, nylon, cellulose acetate, and acrylic, and is valued for its durability during washing [5] [6]. It can be applied on textile material by several application methods, exhaustion during or after dyeing, pad-dry-cure and melt mixing [7]. Electrospraying is increasingly recognized as an advanced method for encapsulating sensitive bioactives with minimal damage or structural loss [1] [8]. Coaxial electrospraying is also a one-stage process given in multiple studies to capsulate varied materials [9–11]. Nano- and microparticles provide larger surface area and consequently allows greater bioavailability of the encapsulated substances. Several studies reported that both solution parameters as well as process parameters directly affect particle size and formation [1].

Because of chitosan's cost-effectiveness, non-toxicity, antibacterial properties, and compatibility with biological systems, it is viewed as an ideal encapsulating agent for textile applications [12]. Several methods can be used for the formation of chitosan micro- and nanospheres, including solvent evaporation, coacervation/precipitation, ionic gelation and spray drying [13]. For microencapsulation process, techniques such as emulsification, spray drying, coaxial electrospray systems, freeze-drying, coacervation, in situ polymerization, extrusion, fluidized-bed coating, and supercritical fluid technology can be utilized [12]. Cotton fabric was treated with antimicrobial peptides encapsulated in alginate-chitosan microcapsules, for potential textile applications [14]. O. sanctum leaf extract was encapsulated in chitosan and applied to cotton garments, showed exceptional antibacterial activity and wash durability [15]. Hui et al. [16] microencapsulated Traditional Chinese Herbs in chitosan–sodium alginate blend matrix and grafted onto the cotton fabric's surface for the clinical treatment of atopic dermatitis. Another study reported excellent antimicrobial efficacy of electrosprayed chitosan onto wool surface [17].

Triclosan loaded chitosan and alginate-based microcapsules have been used for coating applications in surfaces such as textiles or plastics [18]. Santos Alves de Lima [5] investigated these microcapsules using 2.5 wt% to 3 wt% of triclosan in both shell and core structures produced through

* **Corresponding author:** Dasdemir M., e-mail: sgserdar@gantep.edu.tr

emulsification method. These microcapsules were aimed for future applications in antibacterial textiles and other materials such as medical device materials and plastics [18–21]. For antibacterial purposes, triclosan, silver and chitosan were used via pad-dry-cure method and showed significant performance against Gram-positive and Gram-negative bacteria [22]. Ouerghemmi et al. [23] focused on the manufacture of core-sheath nanofibers (NFs) based on chitosan (CHT) as sheath and cyclodextrin polymer (PCD)/triclosan as core triclosan using coaxial electrospinning method. They investigated the nanofibrous structure. This study, differing from previous researches, aims to produce monodisperse distributed nanocapsules with a triclosan/chitosan core/shell structure using the coaxial electrospray method. The influences of flow rate, core/shell flow rate ratio, and needle size on the coaxial electrospray process, which facilitates single-step production, were systematically investigated. The resulting nanocapsule structures were characterized through SEM images, TEM images and size measurements.

EXPERIMENTAL

Materials

Chitosan polymer was purchased from Sigma Aldrich (448869, low molecular weight; DDA ≤75.0%). Acetic acid (Merck & Co., Inc.) was used as solvent for chitosan. Chitosan solutions were prepared according to weight/volume percent (wt/v%) which was the ratio of solute quantity as volume in 100 unit of solution. Chitosan solutions were prepared by dissolving chitosan polymer (2 wt/v%) in acetic acid, 90/10 v/v% acetic acid/distilled water. Triclosan was purchased from Sigma Aldrich (72779, ≥ 97.0%). Ethanol (Merck & Co., Inc.) was used as solvent for triclosan. Triclosan solutions were prepared by (1 wt/v%) in 50/50 v/v% ethanol/distilled water.

Methods

The coaxial electrospraying process was carried out using a vertically arranged electrospraying setup which consists of a high voltage power supply (Gamma High Voltage Series ES100P), a syringe pump (New Era NE-1000X), a nozzle, and a grounded collector. Chitosan solution is fed from the outer needle tip while the triclosan solution is fed from inner needle tip through dual syringe pumps via micro pumps. The resulting samples were collected on aluminum foil (200x200 mm) placed over the grounded plate. The coaxial electrospraying application is carried out at 2.5 kV.cm^{-1} electrical field, 8 cm distance between the needle and collector for 5 min. Different co-fluids flow rates are studied throughout the study. First, total flow rates are arranged as 5 µl.min^{-1}, 10 µl.min^{-1}, 20 µl.min^{-1}, and 40 µl.min^{-1}. Different coaxial needle sizes were also investigated. Moreover, varied core/shell flow rates are studied as 25/75%, 50/50% and 75/25% for 10 µl.min^{-1} total flow rate.

Co-axial electrosprayed nanocapsules were examined with SEM (JEOL JSM 6390) for determining morphology. Before SEM investigation, samples were coated with Au/Pd in SC 7620 Sputter Coater. SEM pictures were taken at 5-20 kV accelerating voltage and 12-15 mm working distance with magnifications between 100 and 5000. MALVERN Zetasizer Nano ZS was also used to determine the dimension of nanocapsules. Transmission electron microscopy (TEM, FEI Tecnai G2 F30) was used to reach a high-level resolution for identification of nanocapsules' formation. Electrosprayed nanocapsules were collected onto Cu grids during co-electrospraying.

RESULTS AND DISCUSSION

Effects of Total Flow Rates on Chitosan Nanocapsule Formation

To investigate the effect of total flow rate on the formation of chitosan/triclosan nanocapsules, four different total flow rates were determined; 5 µl.min^{-1} (2.75/2.25), 10 µl.min^{-1} (5.5/4.5), 20 µl.min^{-1} (11/9) and 40 µl.min^{-1} (22/18). Core/shell flow rate ratios were calculated as 55/45%. In Figure 1, it is seen clearly flow rate of the solution has a major impact on the particle formation. At higher flow rates (20 µl.min^{-1} and 40 µl.min^{-1}), the nanocapsules began to lose their spherical morphology and exhibited a tendency to aggregate. Higher flow rates lead to the formation of larger particles as the increased supply of polymer solution causes the droplets from the needle to exceed the rate of solvent evaporation, resulting in the production of these larger particles [1,24]. Particles generated at higher flow rates exhibited a tendency to agglomerate or adhere to one another, leading to the absence of distinct independent particles [9,25]. Irregular morphology may observe due to insufficient drying time. Conversely, reducing the flow rate leads to smaller droplet formation at the needle and enhances solvent evaporation, resulting in the production of smaller particles [1]. At 5 µl.min^{-1} total flow rate, even though the smaller particles were seen, fibrillation was also observed which may occur at low total flow rates due to the rapid drying of nanocapsules, without sufficient time to separate from each other. At 10 µl.min^{-1} total flow rate, no fibrillation was observed, and the particle size was smaller compared to those at higher flow rates.

In the size distribution graph, all flow rate conditions, with the exception of 10 µl.min^{-1}, exhibit a measurable percentage of larger particles within the distribution. At a flow rate of 10 µl.min^{-1}, monodisperse distribution is observed (Figure 1). Both the SEM analysis and the particle size distributions indicated that the 10 µl.min^{-1} flow rate was optimal.

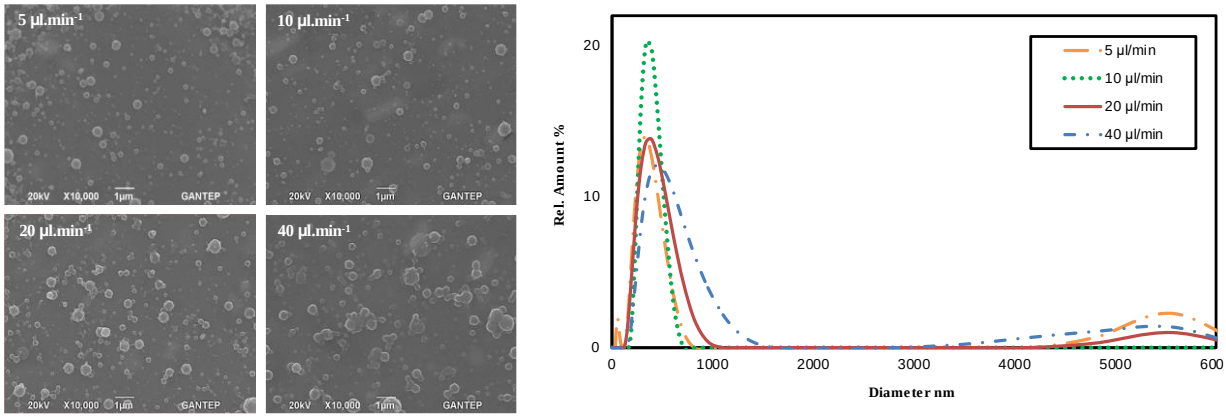

Figure 1. SEM images and size distributions (intensity) of nanocapsules at various total flow rates.

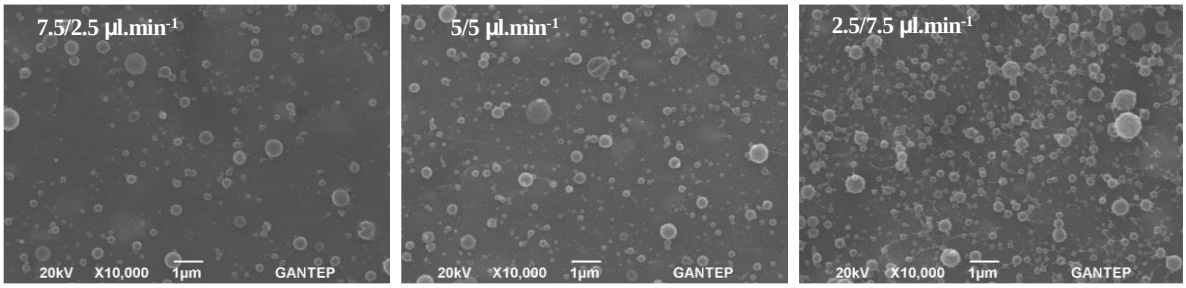

Figure 2. SEM images of nanocapsules at various core/shell flow rate ratios.

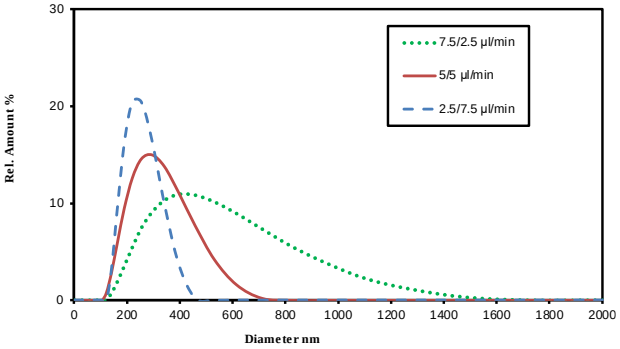

Figure 3. Size distributions (intensity) of nanocapsules at various core/shell flow rate ratios.

Effects of Core/Shell Flow Rate Ratios on Chitosan Nanosphere Formation

A specific flow ratio between the core and shell solutions must be maintained to achieve a stable cone-jet mode during electrospraying [26]. To investigate the effects of core/shell flow rate ratios on nanocapsule formation, three different ratios were selected; 75/25%, 50/50%, 25/75%, respectively. Total flow rate was kept constant at 10 µl.min^{-1}. SEM images and size distributions of electrosprayed nanocapsules at various core/shell flow rate ratios are presented in Figure 2 and Figure 3, respectively. Since the core solution, triclosan, is water-based and has a low concentration, a higher core flow rate promoted film formation. Conversely, reducing the core flow rate while increasing the shell flow rate—and thus the chitosan concentration—enhanced nanocapsule formation. As concentration rises, interactions between chains lead to intermolecular entanglement, which limits the mobility of individual chains [27]. The lowest shell flow rate resulted in fewer particles being formed, as a low shell flow rate may lead to inadequate encapsulation of the core [28]. As the shell flow rate increased, particle formation correspondingly increased. However, at higher shell flow rate ratios, particles tended to agglomerate and fibrillate. Higher flow rates hindered complete solvent evaporation, leading to adhesion and clumping, which reduced the formation of individual particles [25].

Even though the sizes of the nanocapsules were similar at different ratios, higher chitosan content led to fibril formation between the nanocapsules. Although the 2.5/7.5 µl.min^{-1} core/shell flow rate ratio yielded the most uniform size distribution (Figure 3), because of the fibrillation, the 5/5 µl.min^{-1} core/shell flow rate ratio represented the most optimal configuration. Wang et al. [29] was reported smaller particle sizes at higher shell flow rate too.

Effects of Needle Size on Chitosan Nanosphere Formation

Modifying the needle characteristics in electrospray processing directly affects the operating conditions and the outcomes of the process [30]. Different needles with varied gauge were employed to assess the impact of needle size on nanocapsule formation and size. Nanocapsule formation was examined using 26/22 gauge, 26/21 gauge, and 24/21 gauge needles for core/shell solutions, respectively. SEM

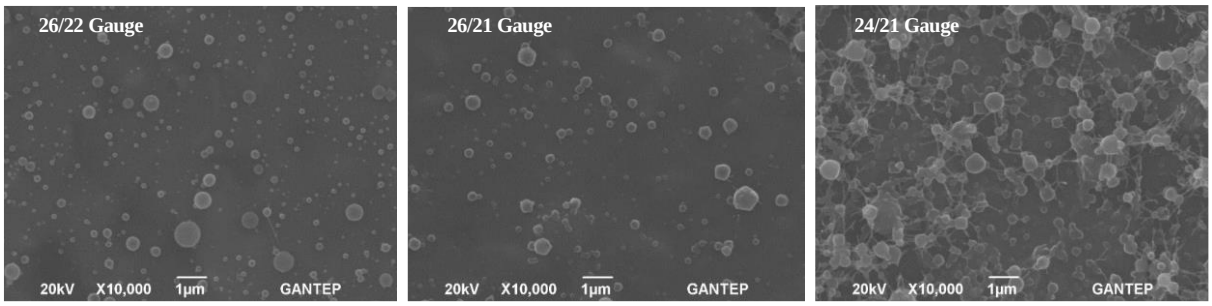

Figure 4. SEM images of nanocapsules at various needle size.

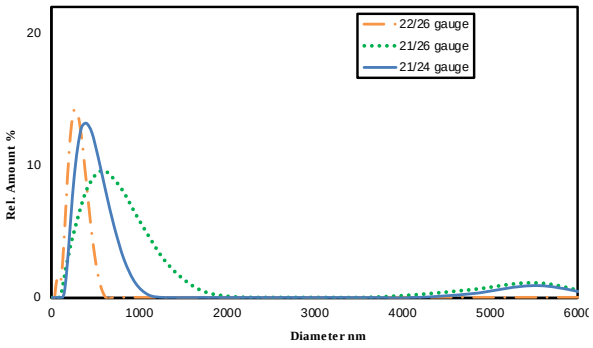

Figure 5. Size distributions of nanocapsules at various needle size (intensity).

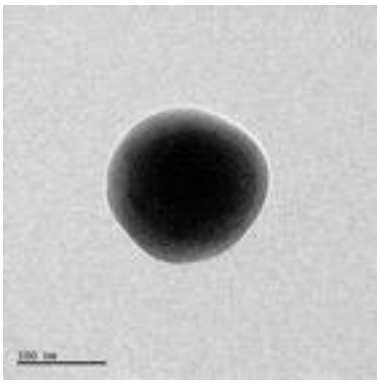

Figure 6. TEM image of nanocapsules at 5/5 μl.min-1 flow rate ratio and 26/22 G needle.

images of nanocapsules produced with different needles are presented in Figure 4. Nanocapsules were successfully formed with all needle configurations. However, significant fibrillation was observed with 24/21 gauge needles. Larger needle diameter leads unseparated particles. A smaller needle diameter results in reduced droplet size at the nozzle tip due to a smaller meniscus and increased surface tension. This requires a greater Coulombic force to initiate the jet, which slows down jet acceleration and extends flight time, providing more opportunity for Rayleigh disintegration and further breakdown into smaller droplets [9]. The use of 26-gauge needle for the core solution yielded more uniform spherical structures.

The size distribution of the nanocapsules is illustrated in Figure 5. Among the configurations with comparable SEM image appearances, the 26/22 gauge needle combination demonstrated a more monodisperse distribution than 26/21 gauge. Consequently, the 26/22 gauge needle configuration was selected to achieve better distribution.

The TEM image of the nanocapsule at a 5/5 μl.min^{-1} flow rate ratio and a 26/22 G needle, shown in Figure 6, clearly displays both the core and the shell in spherical structure, indicating successful encapsulation.

CONCLUSIONS

The objective of this study is to produce chitosan-based nanocapsules with a spherical structure and monodisperse distribution. To achieve this, experiments were conducted with various process parameters, including total flow rates, flow rate ratios for core/shell solutions, and core/shell needle sizes. When the total flow rate was reduced, fibrillation was observed between the capsules, while at higher rates, the capsules tended to aggregate, leading to deformation of their shapes. In the experiments focused on core/shell flow rate ratios, fibrillation was noted when the chitosan content as shell material was at its highest. In comparison with other flow rate ratios, the study with an equal core/shell ratio demonstrated the most promising size distribution. Smaller needle diameters produced smaller particles, while larger needles resulted in poorly separated capsules. The optimal results were achieved using the smallest needle gauge.

Acknowledgement: *The authors are grateful to The Scientific and Technological Research Council of Turkey (TÜBİTAK) for funding this work (Project No: MAG-113M517).*

REFERENCES

1. Kurakula M., Raghavendra Naveen N.: Electrospraying: A facile technology unfolding the chitosan based drug delivery and biomedical applications. Eur Polym J., 147, 2021,110326 p. https://doi.org/10.1016/j.eurpolymj.2021.110326
2. Massella D., Giraud S., Guan J., et al.: Textiles for health: a review of textile fabrics treated with chitosan microcapsules. Environ Chem Lett., 17(4), 2019, pp. 1787–1800. https://doi.org/10.1007/s10311-019-00913-w
3. Muñoz-Bonilla A., Echeverria C., Sonseca Á., et al.: Bio-Based Polymers with Antimicrobial Properties towards Sustainable Development. Materials, 12(4), 2019, 641p. https://doi.org/10.3390/ma12040641
4. Ibili H., Dasdemir M.: Formation, Characterization and Multifunctional Activity of Chitosan Nanoparticle Coating. Fibers Polym, 23, 2022, pp. 1856–1869. https://doi.org/10.1007/s12221-022-4116-1

5. Lima C.S.A.D., Varca G.H.C., Costa S.M.D., et al.: Development of natural polymeric microcapsules for antimicrobial drug delivery: triclosan loaded chitosan and alginate-based microcapsules. Drug Dev Ind Pharm, 46(9), 2020, pp. 1477–1486. https://doi.org/10.1080/03639045.2020.1809445
6. Tania I.S., Ali M., Arafat M.T.: Processing techniques of antimicrobial textiles. In: Antimicrobial Textiles from Natural Resources, 2021, pp. 189–215. https://doi.org/10.1016/B978-0-12-821485-5.00002-0
7. Liyanage S., Parajuli P., Hossain M.T., et al.: Antimicrobials for protective clothing. In: Antimicrobial Textiles from Natural Resources, 2021, pp. 349 – 376. https://doi.org/10.1016/B978-0-08-100576-7.00016-X
8. Wang J., Jansen J.A., Yang F.: Electrospraying: Possibilities and Challenges of Engineering Carriers for Biomedical Applications—A Mini Review. Front Chem., 25(7), 2019, 258 p. https://doi.org/10.3389/fchem.2019.00258
9. Alfatama M., Shahzad Y., Choukaife H.: Recent advances of electrospray technique for multiparticulate preparation: Drug delivery applications. Adv Colloid Interface Sci., 325, 2024, 103098 p. https://doi.org/10.1016/j.cis.2024.103098
10. Park J.E., Kim Y.K., Kim S.Y., et al.: Biocompatibility and Antibacterial Effect of Ginger Fraction Loaded PLGA Microspheres Fabricated by Coaxial Electrospray. Materials, 16(5), 2023, 1885 p. https://doi.org/10.3390/ma16051885
11. Zhang Y., Tremblay P.L., Zhang T.: Electrosprayed trilayer poly (d,l-lactide-co-glycolide) nanoparticles for the controlled co-delivery of a SGLT2 inhibitor and a thiazide-like diuretic. J Drug Deliv Sci Technol, 81, 2023, 104311 p. https://doi.org/10.1016/j.jddst.2023.104311
12. Valle J.A.B., Valle R.D.C.S.C., Bierhalz A.C.K., et al.: Chitosan microcapsules: Methods of the production and use in the textile finishing. J Appl Polym Sci., 138(21), 2021, 50482 p. https://doi.org/10.1002/app.50482
13. Arya N., Chakraborty S., Dube N., et al.: Electrospraying: A facile technique for synthesis of chitosan-based micro/nanospheres for drug delivery applications. J Biomed Mater Res B Appl Biomater, 88B(1), 2009, pp. 17‑31. https://doi.org/10.1002/jbm.b.31085
14. Antunes L., Faustino G., Mouro C., et al.: Bioactive microsphere-based coating for biomedical-textiles with encapsulated antimicrobial peptides (AMPs). Ciênc Tecnol Mater, 26(2), 2014, pp. 118–125. https://doi.org/10.1016/j.ctmat.2015.03.006
15. Rajendran R., Radhai R., Kotresh T.M., et al.: Development of antimicrobial cotton fabrics using herb loaded nanoparticles. Carbohydr Polym., 91(2), 2013, pp. 613–617. https://doi.org/10.1016/j.carbpol.2012.08.064
16. Hui P.C.L., Wang W.Y., Kan C.W., et al.: Microencapsulation of Traditional Chinese Herbs—PentaHerbs extracts and potential application in healthcare textiles. Colloids Surf B Biointerfaces, 111, 2013, pp. 156–161. https://doi.org/10.1016/j.colsurfb.2013.05.036
17. Islam S., Jadhav A., Fang J., et al.: Surface Deposition of Chitosan on Wool Substrate by Electrospraying. Adv Mater Res., 331, 2011, pp. 165–170. https://doi.org/10.4028/www.scientific.net/AMR.331.165
18. Silva A.C.Q., Silvestre A.J.D., Freire C.S.R., et al.: Modification of textiles for functional applications. In: Fundamentals of Natural Fibres and Textiles, 2011, pp. 303–365. https://doi.org/10.1016/B978-0-12-821483-1.00010-3
19. Abbaszad Rafi A., Mahkam M.: Preparation of magnetic pH-sensitive microcapsules with an alginate base as colon specific drug delivery systems through an entirely green route. RSC Adv., 5(6), 2015, pp. 4628–4638. https://doi.org/10.1039/C4RA15170D
20. Elisseeff J.: Structure starts to gel. Nat Mater, 7(4), 2008, pp. 271–273. https://doi.org/10.1038/nmat2147
21. Karzar Jeddi M., Mahkam M.: Magnetic nano carboxymethyl cellulose-alginate/chitosan hydrogel beads as biodegradable devices for controlled drug delivery. Int J Biol Macromol, 135, 2019, pp. 829–838. https://doi.org/10.1016/j.ijbiomac.2019.05.210
22. Dhiman G., Chakraborty J.N.: Antimicrobial performance of cotton finished with triclosan, silver and chitosan. Fash Text, 2(1), 2015, 13 p. https://doi.org/10.1186/s40691-015-0040-y
23. Ouerghemmi S., Degoutin S., Maton M., et al.: Core-Sheath Electrospun Nanofibers Based on Chitosan and Cyclodextrin Polymer for the Prolonged Release of Triclosan. Polymers, 14(10), 2022, 1955 p. https://doi.org/10.3390/polym14101955
24. Chang M.W., Stride E., Edirisinghe M.: Controlling the thickness of hollow polymeric microspheres prepared by electrohydrodynamic atomization. J R Soc Interface, 2010. https://doi.org/10.1098/rsif.2010.0092.focus
25. Liu Y., Li S., Li H., et al.: Synthesis and properties of core-shell thymol-loaded zein/shellac nanoparticles by coaxial electrospray as edible coatings. Mater Des., 212, 2021, 110214 p. https://doi.org/10.1016/j.matdes.2021.110214
26. Tsai S., Ting Y.: Synthesize of alginate/chitosan bilayer nanocarrier by CCD-RSM guided co-axial electrospray: A novel and versatile approach. Food Res Int., 116, 2019, pp. 1163–1172. https://doi.org/10.1016/j.foodres.2018.11.047
27. Dasdemir M., Ibili H.: Formation and characterization of superhydrophobic and alcohol-repellent nonwovens via electrohydrodynamic atomization (electrospraying). J Ind Text, 47(1), 2017, pp. 125–146. https://doi.org/10.1177/1528083716639061
28. Rathore P., Schiffman J.D.: Beyond the Single-Nozzle: Coaxial Electrospinning Enables Innovative Nanofiber Chemistries, Geometries, and Applications. ACS Appl Mater Interfaces, 13(1), 2021, pp. 48–66. https://doi.org/10.1021/acsami.0c17706
29. Wang Y., Yu D.G., Liu Y., et al.: Progress of Electrospun Nanofibrous Carriers for Modifications to Drug Release Profiles. J Funct Biomater, 13(4), 2022, 289 p. https://doi.org/10.3390/jfb13040289
30. Ahmad Z., Zhang H.B., Farook U., et al.: Generation of multilayered structures for biomedical applications using a novel tri-needle coaxial device and electrohydrodynamic flow. J R Soc Interface, 5(27), 2008, pp. 1255–1261. https://doi.org/10.1098/rsif.2008.0247

IMPROVE THE ANTIBACTERIAL PROPERTIES OF COTTON BANDAGES COATED WITH SILVER PARTICLES AND FINISHED WITH A NATURALLY EXTRACTED DYE

RASHID, SABA[1*] AND FATIMA, MAHVISH[2]

[1] Department of chemistry, Riphah International University Faisalabad, Pakistan
[2] Department of Physics, College of Science, Qassim University, Buraydah 51452, Qassim, Saudi Arabia

ABSTRACT

We created antibacterial stretchable medicated textiles. Initially, we used a versatile one-pot green synthesis method to produce a concentrated and stable colloidal solution of silver nanoparticles (Ag-NPs) by self-assembling tannic acid, avoiding any harmful chemicals. The silver particles were later deposited on the cotton fabrics. The surface morphologies were analyzed by SEM and the presence of metals was inspected by dynamic light scattering and XRD. In second step, the natural antibacterial dye from the pomegranate peel was prepared and the fabrics of silver coated cotton were treated by the exhaust dyeing method. We assessed the CILAB (L*, a*, b*, C, h, and K/S) and color fastness properties of the dyed fabric samples. Additionally, we evaluated the antipathogenic properties (antibacterial, antiviral, and antifungal) of all coated fabrics.

KEYWORDS

Silver nanoparticles; Antibacterial bandages; Natural dyes; Green synthesis; Aesthetic properties; *S. Aureous*; *E. Coli*.

INTRODUCTION

Silver nanoparticles (AgNPs) are identified as nanomaterials with sizes ranging from 1 to 100 nm. They have a higher surface area (area-to-volume ratio) and a greater volume capacity than bulk silver. Due to the distinct electrical, optical, and catalytic characteristics of AgNPs at the nanoscale, research and development has been directed toward uses in targeted drug delivery, imaging, diagnosis and detection [1] [2]. The impressive antibacterial properties of AgNPs have garnered significant attention from both researchers and industries. They have demonstrated effectiveness against multidrug-resistant bacterial populations and various infectious and pathogenic microorganisms, showcasing their antimicrobial activity. The enhanced antibacterial action of silver at the nanoscale is beneficial in the medical and healthcare fields. AgNPs have been integrated into numerous products, including food contact materials, cosmetics, surgical instruments, wound dressings, catheters, textiles and dental products [3]. Research has shown that AgNPs can function as antibiotics through multiple mechanisms of action that impact various microbial structures simultaneously, allowing them to effectively target different bacterial strains [4]. Because of their potent antibacterial qualities, AgNPs are frequently utilized in a variety of commercial products, especially in the textile industry, to avoid microbial contamination. Many researchers have identified AgNPs as ideal antibacterials, ensuring that fabrics remain free from microorganisms such as viruses, bacteria and fungi. The incorporation of AgNPs significantly enhances the antimicrobial effectiveness of wound dressings when sprayed onto fabrics. Most antimicrobial composites containing AgNPs have shown high efficacy against nearly 650 different bacterial strains. The methods used to prepare these nanoparticles can lead to variations in their physical and chemical properties [5]. Traditional synthesis methods often involve toxic substances, which can endanger both the environment and human health. Currently, fabrics are coated with nanoparticles using various techniques such as screen spraying, painting, padding, dip coating, and sonochemical methods. These coating techniques aim to improve the nanoparticles' stability and adsorption on the fabric. It is crucial that the resulting nanoparticles maintain a stable structure, whether in colloidal or metallic form. These factors are important considerations for the coating process to ensure optimal performance [6]. Researchers have concentrated on producing stable Ag NPs while controlling their size and minimizing the

* **Corresponding author:** Rashid S., e-mail: *sabarasheed345@gmail.com*

use of harmful chemicals. In this context, green-synthesized nanoparticles were employed, which eliminates the need for cryogenically synthesized nanoparticles and their associated adverse effects. The green synthesis method ensures that the nanoparticles do not contain toxic substances, leading to formation of colloidal Ag NPs [7]. In this study, the synthesis of Ag NPs used *Peltophorum pterocarpum* flower extract as a non-toxic reducing and binding agent. Additionally, the dip and sonication methods did not require any adhesive, as the green-synthesized Ag NPs were directly applied directly to cotton textiles. Medical products that contain silver compounds are utilized for treating burns, wounds, and various infectious diseases. The growing issue of antibiotic resistance poses a significant challenge in treating certain infections, which raises concerns in the fight against contagious diseases. If not properly regulated, the excessive use of antibiotics could diminish the effectiveness of many bacterial pathogens. As a response to this, antimicrobial dressings have been increasingly developed using biological polymers that are integrated with antimicrobial components [8]. Each type of wound dressing aids in the healing process, but scientists are striving to deepen their understanding to create wound dressings that are free from toxins, have longer durability, offer stronger resistance, and gain clinical acceptance. Among the available materials, cotton is often considered a suitable candidate for modified dressings. Traditionally, cotton has been used in many countries for dressing wound sites to prevent contamination. Wounds such as cuts or grazes tend to heal faster when treated with cotton, and it is generally non-irritating to sensitive skin. However, using cotton pads for wound treatment presents several challenges. When immersed in wound fluids, cotton fibers can adhere strongly, similar to glue. As a result, when the cotton is pulled away, it can unintentionally remove healing cells from the wound site, leading to side effects such as prolonged healing times and pain during dressing changes, especially since the wound area is often sensitive [9]. This issue can be effectively addressed by using chitosan, a structural biopolymer known for its ability to form hydrogels and its anti-pathogenic properties, which facilitate easier wound management. Additionally, glycogen, a safe and nontoxic animal polysaccharide, can help mitigate these problems. It not only aids in healing but also prevents tissue scarring when the injury areas form albumin and are dressed, thereby promoting a more effective healing process [10]. Clinical textiles, often referred to as 'hospital textiles,' must meet specific standards, including being non-toxic, anti-allergic, antimicrobial, and anti-inflammatory. Various agents, such as metal particles and specific treatments, are applied to textile materials to impart antibacterial properties. Recently, the use of metallic compounds as nanoparticles has gained traction for integrating beneficial properties into fabrics, thereby reducing the spread of diseases and microbial growth. Commonly used compounds include Ag (silver), TiO_2 (titanium dioxide), Cu (copper), CuO (copper (II) oxide), Cu_2O (copper(I) oxide), ZnO (zinc oxide), and MgO (magnesium oxide) polycrystalline. Among these, silver and its compounds stand out due to their exceptional surface disinfectant properties, which include antiviral, antibacterial, and antifungal effects against various pathogens. Research by Ali et al. demonstrated that cotton fabric coated with silver nanoparticles exhibits significant effectiveness against harmful microbes, leading to the designation of this material as a multifunctional textile. In light of these findings, the article proposes a novel approach to producing antimicrobial cotton fabrics coated with silver, aiming to enhance both aesthetic and functional properties. The objective is to explore how these fabrics can benefit commercial and medical applications, particularly as they are expected to exhibit improved antibacterial activity post-dyeing. Beyond medical uses, these antimicrobial fabrics could find applications in pillow covers, bedsheets, and even clothing for patients, as well as in compression bandages [11]. The cotton fabric is indeed a remarkable achievement in textile engineering, known for its comfort, absorbance, and breathability. While it may not always match the strength of some synthetic materials, its unique characteristics keep it in high demand globally. Nowadays, consumers are increasingly focused on aesthetics, leading to a growing need for cotton fabrics that are not only stylish but also convenient and comfortable [12]. Nanotechnology has opened up exciting possibilities for modifying cotton textiles to fulfill these modern requirements. In textile manufacturing, there is now a greater emphasis on achieving multifunctional properties through specific finishes. These finishes, which have become standard, include antistatic, durability, antimicrobial, dirt repellent, flame resistance, water repellent, easy crease recovery, self-cleaning, and UV protection [13]. Enhancing the surface of textiles is a key method for augmenting these functional characteristics. The use of noble metal nanoparticles has emerged as an effective strategy for creating fabrics with multiple useful functions. Different types of nanoparticles offer distinct advantages for textile surfaces. For instance, zinc oxide nanoparticles are known for providing UV protection in garments, silver nanoparticles are recognized for their antibacterial properties, and titanium dioxide is utilized in self-cleaning fabrics. This innovative approach allows for the development of cotton fabrics that not only meet but exceed modern consumer expectations [14]. These nanoparticles are indeed applied to the surfaces of cotton fabrics, making them suitable for various applications, including casual clothing, sportswear, and medical settings such as bandages, absorbent pads, gowns, gauzes, and padding

materials. The moisture-rich nature of cellulose-containing cotton fibers does make them vulnerable to microbial invasion, creating a conducive environment for bacterial and fungal growth [15]. Silver nanoparticles are particularly noteworthy due to their excellent antimicrobial properties when applied to textile materials. The effectiveness of these antibacterial characteristics increases as the particle size decreases. Anisotropic silver nanoparticles can also be used to dye cotton fabrics in a variety of colors while imparting those antibacterial properties [16]. Most research efforts have focused on assessing the antimicrobial properties of these nanoparticles, but there has been limited investigation into their wash durability. Factors such as shape, particle size, concentration, and surface treatment both before and after application can significantly influence the levels of antimicrobial activity observed. Interestingly, this research indicates that wash durability can be improved. However, to date, there has been no study specifically evaluating color uniformity in cotton materials coated with silver nanoparticles [17].

EXPERIMENTAL

Materials and Methodes

In this Method, silver nanoparticles are synthesized and deposited onto cotton stretch fabric. The chemicals used for this process were of 99.99% purity and sourced from Sigma-Aldrich. The pretreated fibers were first treated with a 12 wt% aqueous sodium hydroxide solution at room temperature for 10 minutes, followed by rinsing with distilled water. This treatment likely aimed to enhance the surface properties of the fibers for better nanoparticle adhesion. Three different concentrations of silver nitrate ($AgNO_3$) solution were prepared: 1M, 0.5M, and 0.25M. Aqua ammonia (28 wt%) was gradually added to these solutions and stirred continuously until a clear $[Ag\ (NH_3)_2]^+$ solution formed. The alkali-treated textiles were then immersed in each solution for 10 minutes and dried at 90°C for another 10 minutes. This immersion and drying process was repeated for a total of 10 cycles to maximize the deposition of $[Ag\ (NH_3)_2]^+$ and Ag+ ions onto the textiles. Finally, the treated fabrics were immersed in a 0.3M glucose stock solution, along with any remaining $[Ag\ (NH_3)_2]^+$ solution [18].

Application of dye on fabric

The fabric was dyed using a material-to-liquid (M: L) ratio of 1:40. This means that for every1 part of fabric, there are 40 parts of the dyeing liquid. The dyeing process began with the addition of alkali sodium hydroxide (NaOH) at a concentration of 1 g/L. This helps to increase the pH of dye bath, which can improve the dye uptake by the fabric. Next, 40 g/L of sodium sulfate (Na_2SO_4) was added to the dye bath. Sodium sulfate acts as an electrolyte, helping to maintain the ionic strength of the dye bath and improving the leveling of the dye on the fabric. After that, the fabric was soaked in the dye bath to allow it to absorb the color. The exhaust dyeing method typically involves heating the dye bath to help the dye penetrate the fabric more effectively. After the desired dyeing time, the stained fabric was taken out of the dye bath and washed with tap water. This washing step is crucial to remove any excess dye that did not bond to the fabric, ensuring that the final product has a clean and even color.

RESULTS AND DISCUSSION

Colorimetric data measurement

The CIELAB values of silver coated dyed and undyed fabrics differs considerably. The K/S values for dyed sample was relatively high (11.31) than for undyed fabric (7.47), indicating that dyeing has altered the light-colored silver coated fabric to a relatively dark-colored fabric. The variation in L* values among both fabrics confirmed the dark shade of the colored fabric. The L* value of the dyed fabric was relatively low (37.15) than the differences in color characteristics between silver-coated dyed and undyed fabrics, using CIELAB color space values. The K/S (absorbance/scattering) values indicate how much light is absorbed and scattered by the fabric. The dyed sample has a K/S value of 11.31, which is significantly higher than the undyed fabric's K/S value of 7.47. This suggests that dyeing has resulted in a darker appearance for the silver-coated fabrics. The L* value measures lightness, where lower values indicate darker shades. The dyed fabric has an L* value of 37.15, compared to 55.35 for the undyed fabric. This confirms that the dyed fabric is indeed darker than the undyed fabric. Chroma represents the intensity or saturation of the color. The dyed fabric has a C* value of 34.98, which is lower than the undyed fabric's C* value of 37.79. This indicates that the undyed fabric has a more vibrant and sharper shade, while the dyed fabric appears darker and duller. Both dyed and undyed fabrics have positive a* and b* values, indicating the presence of yellowish and reddish hues. This suggests that both fabrics share some color characteristics, but the differences in K/S, L*, and C* values highlight the impact of dyeing on the overall color perception. In summary, the dyeing process significantly alters the color properties of the silver-coated fabric, resulting in a darker, less vibrant appearance compared to the undyed fabric the L* value of the undyed fabric (55.35), indicating that the dyed sample is darker in color than the undyed sample. The chroma (C*) for the dyed fabric was relatively low (34.98) than for the undyed sample (37.79), indicating that the undyed samples had a sharper shade and the dyed sample had a darkened and duller shade. The a* and b* values were positive for both undyed and dyed fabric, representing a yellowish and reddish color.

Levelness of silver treated dyed and undyed fabric

The dye levelness provides valuable insights into the uniformity of dye application on silver-coated fabrics. Spectrophotometer Measurements: The use of a spectrophotometer to measure the reflectance at 12 different points on both dyed and undyed fabrics allowed for a comprehensive evaluation of dye levelness. K/S Values and Standard Error: The K/S values were accompanied by standard error measurements, which indicate the consistency of the dye application. The standard error was 0.12 which is quite low for dyed silver-coated fabric. This suggests that the dye is distributed evenly across the fabric, leading to excellent levelness. Comparison with Undyed Fabric: In contrast, the standard error for the silver-coated undyed fabric was significantly higher at 2.21. This indicates a highly uneven appearance, suggesting that the undyed fabric does not have a consistent look. Visual Assessment Ratings: The visual assessment further supports these findings, with dyed fabrics rated as grade 5 (excellent levelness) and undyed fabrics rated as grade 2 (poor levelness). This visual confirmation aligns with the quantitative measurements, reinforcing the conclusion that dyeing silver-treated fabrics results in a smoother and more even appearance.In summary, the dyed silver-coated fabrics demonstrate superior levelness and uniformity compared to their undyed counterparts, both in terms of statistical analysis and visual assessment [19].

Morphology of silver coated knitted dyed cotton fabrics

Visuals in Figure 1 (a) displayed nanometer-scale images of silver particles pre-application on fabric, showing spherical features without aggregations. The claim was supported by Zeta potential and polydispersity index (PDI) values of -51.63 ± 5.19 mV and approximately 0.292, respectively. These values indicated even particle distribution and high polydispersity. Scanning electron microscopy (SEM) revealed structural morphologies of silver particles on fabrics pre and post dyeing in Figures 1 (b,), showing a more consistent and denser silver coating. Moreover, Figures 1 (c) and Table 2 are showing the elemental composition of silver gained. Figures 1 (d) The average particle size distribution for silver nanoparticles was found to be approximately 13.23 ±1.6 nm. The phase composition of silver nanoparticles was determined by XRD. Figure 1 (e) presented XRD spectra in the range of 20 to 80 ° with a 0.02-degree step, showing ideal indexing to the silver structure, confirming the phase purity of the synthesized silver nanoparticles.

Antibacterial activity, antifungal and antiviral activity

The antibacterial efficacy of both undyed and dyed silver treated textile substrates was assessed through qualitative and quantitative standard testing protocols.

The qualitative evaluation of all treated samples was conducted using the AATCC-147 (disc-diffusion method) protocol, which tested the samples for antibacterial efficacy against both Gram-positive (*S. aureus*) and Gram-negative (*E. coli*) pathogens. The antibacterial efficacy of both undyed and dyed silver-treated textile substrates was assessed using the AATCC-147 (disc-diffusion method) protocol (Figure 3). The Zone of Inhibition (ZOI) for the dyed fabrics was found to be higher than that for the undyed fabrics. The higher ZOI values for the dyed fabrics indicate that the antibacterial qualities of the silver nanoparticles were unaffected by the antibacterial dye. Antibacterial dye did not negate the antibacterial properties of silver nanoparticles, as seen by the higher ZOI values for textiles colored with silver coatings. The antifungal activity of all treated fabric samples (both dyed and undyed) was evaluated using the AATCC-100 method against A. *niger* fungal species. In Figure 2(a), the results show the percentage reduction in fungal spore germination for all samples. All of the fabric samples that were treated showed strong antifungal activity against the A. *niger* fungus. The antifungal activity of the dyed samples was enhanced, indicating that the dye used has excellent antifungal properties. Among the undyed

Table 1. Reflectance measurement data for the dyed and undyed silver coated fabrics.

Number of Scans	K/S Values dyed sample	Standard deviation (S.D)	K/S Values undyed sample	Standard deviation (S.D)
Reading 1	11.32	0.12	13.75	2.21
Reading 2	11.56		16.56	
Reading 3	11.21		7.34	
Reading 4	11.98		12.56	
Reading 5	11.65		6.45	
Reading 6	11.45		11.35	
Reading 7	11.99		14.67	
Reading 8	11.56		7.65	
Reading 9	11.25		12.34	
Reading 10	11.42		8.45	

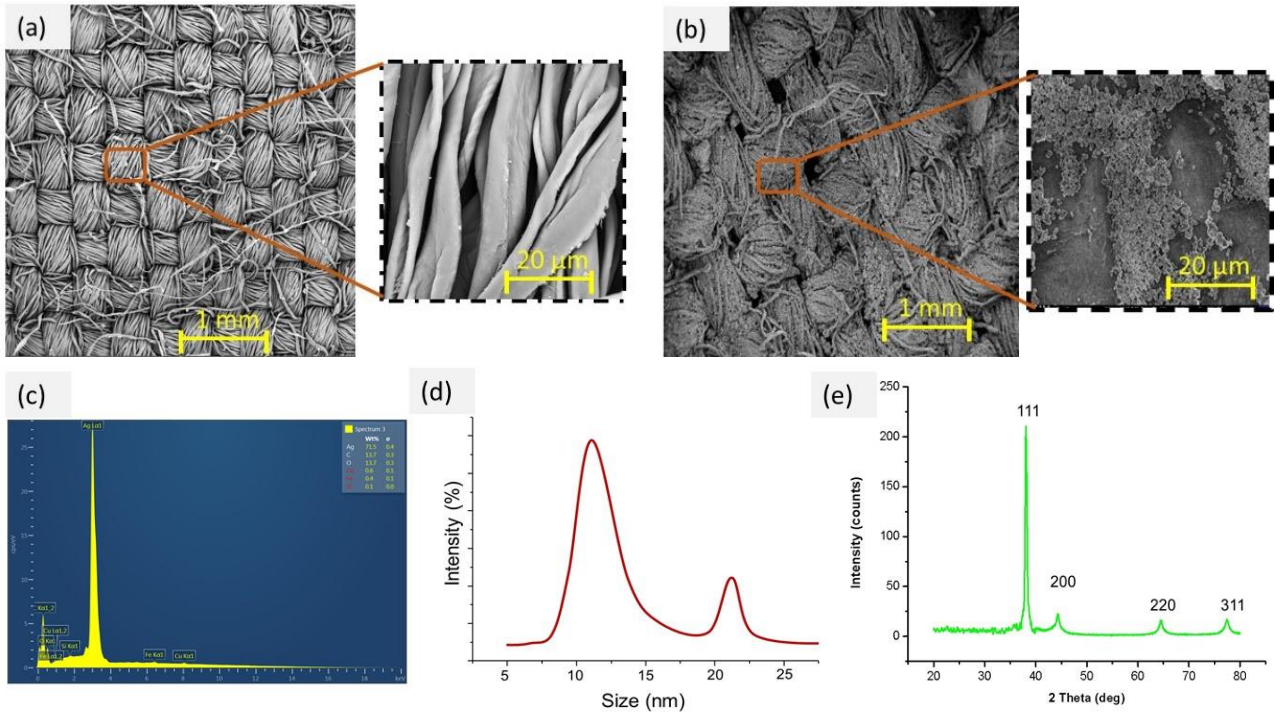

Figure 1. SEM images of (a) silver particles, (b) silver particles coated cotton fibers, (c) silver particles coated and dyed cotton fibers, (d) EDX analysis, (e) Size analysis and (f) XRD of silver particles.

Table 2. Elemental percentage of Silver.

Element	Line Type	Wt%	Wt% Sigma	Atomic %
C	K series	13.73	0.26	42.61
O	K series	13.71	0.31	31.94
Si	K series	0.12	0.03	0.15
Fe	K series	0.37	0.07	0.25
Cu	K series	0.60	0.10	0.35
Ag	L series	71.48	0.35	24.70
Total:		100.00		100.00

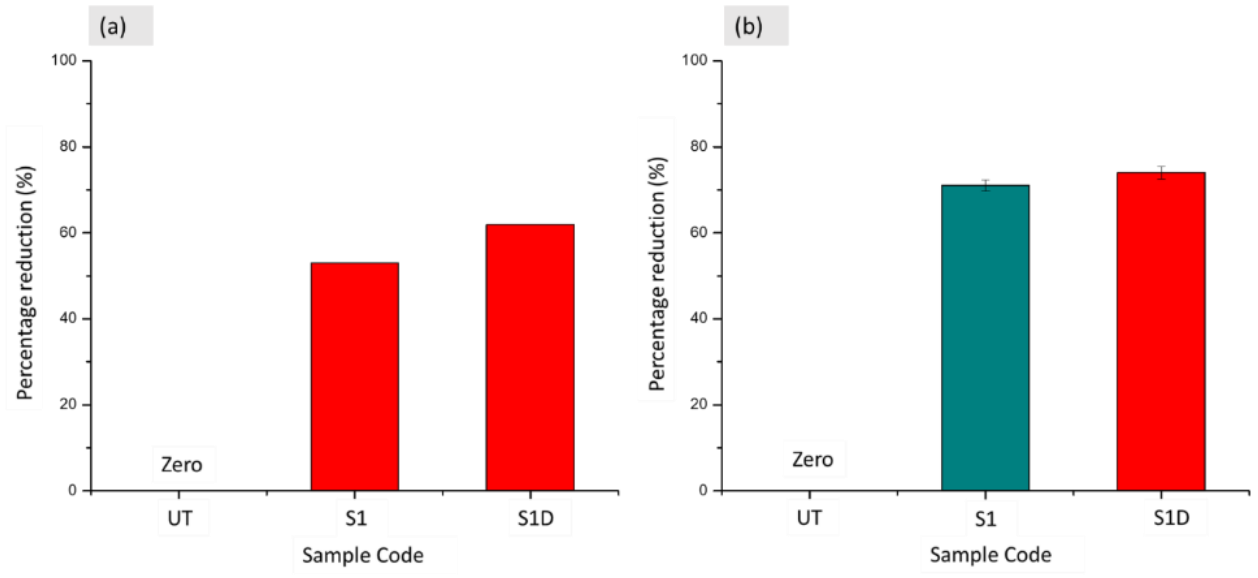

Figure 2. (a) antifungal activity (b) Antiviral reduction in percentage.

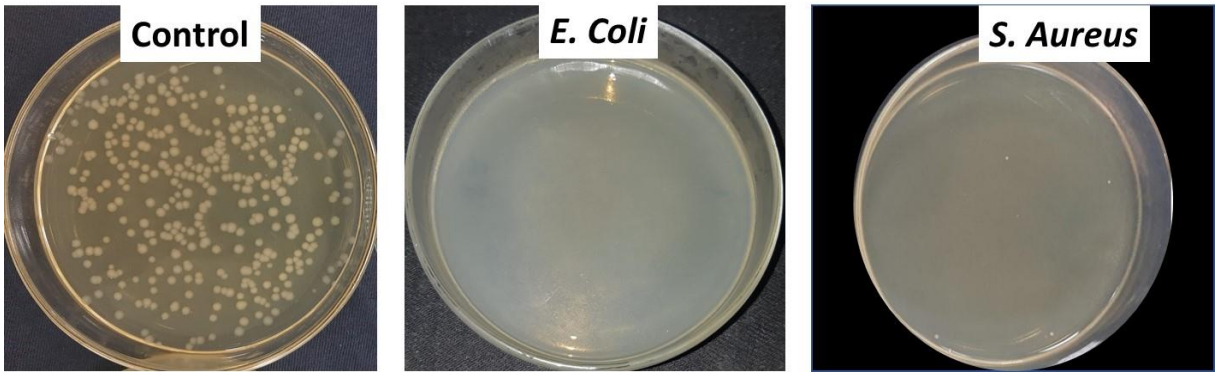

Figure 3. Antibacterial activity against gram positive and gram negative bacteria.

samples, with antifungal actions and 91%. The untreated fabric did not exhibit any inhibitory effect on the test microbe, confirming that the antifungal properties in all treated samples (dyed and undyed) were attributed to the presence of antimicrobial dye and silver nanoparticles. Overall, the study demonstrated superior antifungal properties of silver-coated dyed fabric. The reduction in the percentage of fungus seen in green-synthesized silver particles is consistent with this result and a previous study [20]. The present study showed better antifungal properties of silver-coated dyed fabric is justified by the results and comparison with related studies. The sample S3 (among all undyed fabrics) and S3D (among all dyed fabrics) showed the highest reduction in antiviral activity, with 80% and 84% effectiveness, respectively. The antiviral effect of silver-treated undyed and dyed fabrics can be explained by the binding of metallic nanoparticles and the phenolic part of the polyphenols to glycoproteins on the viral surface, which inhibits the viruses. In a recent study, fabric coated with silver particles using the photo deposition method exhibited a 97% reduction in the specific viral load of SARS-CoV-2. The antiviral activity of silver-treated undyed and dyed fabrics is due to the presence of silver nanoparticles and natural antimicrobial dye, which inhibit viruses by binding to glycoproteins on the viral surface [21].

CONCLUSION

Antibacterial properties of silver-coated fabrics are quite interesting and highlight the effectiveness of dyeing in enhancing antibacterial activity. A hygienic samples were created, consisting dyed and undyed fabrics, all treated with silver nanoparticles. This setup allows for a direct comparison of the antibacterial effects between dyed and undyed sample. X-Ray diffraction (XRD) and scanning electron microscopy (SEM) are used to determine the presence of silver nanoparticles on the fabric as well as their surface shape. These techniques are essential for understanding how the silver interacts with the fabric and how it might contribute to antibacterial properties The antibacterial efficacy against dyed silver-coated samples is higher than that of undyed samples, which indicates that the dyed materials are more effective at preventing the development of bacteria. This suggests that the dyeing process may enhance the antibacterial properties of the silver coating. Dyed fabric sample exhibited the strongest antibacterial effect, which is significant for applications where hygiene is critical. Overall, the findings suggest that dyeing silver-coated fabrics not only enhances their aesthetic appeal but also significantly improves their antibacterial properties, making them suitable for hygienic applications.

REFERENCES

1. Ali A., Baheti V., Militky J., et al.: Utility of silver-coated fabrics as electrodes in electrotherapy applications. J Appl Polym Sci, 135(23), 2018. https://doi.org/10.1002/app.46357
2. Yaqoob A.A., Ahmad H., Parveen T., et al.: Recent Advances in Metal Decorated Nanomaterials and Their Various Biological Applications: A Review. Front. Chem., 8(341), 2020. https://doi.org/10.3389/fchem
3. Marambio-Jones C., Hoek E.M.V.: A Review of the Antibacterial Effects of Silver Nanomaterials and Potential Implications for Human Health and the Environment. J. Nanopart. Res., 12(5), 2010, pp. 1531– 1551. https://doi.org/10.1007/s11051-010-9900-y
4. Cheng G., Dai M., Ahmed S., et al.: Antimicrobial drugs in fighting against antimicrobial resistance. Front. Microbiol., 7, 2016, 470 p. https://doi.org/10.3389/fmicb.2016.00470
5. Babapour A., Akhavan O., Moshfegh A.Z., et al.: Size Variation and Optical Absorption of Sol–Gel Ag Nanoparticles Doped SiO_2 Thin Film. Thin Solid Films, 515 (2), 2006, pp. 771–774. https://doi.org/10.1016/j.tsf.2005.12.191
6. Ulacha A.B., Rybicki E., Zgondek E.M., et al.: A New Method of Finishing of Cotton Fabric by in Situ Synthesis of Silver Nanoparticles. Ind. Eng. Chem. Res., 53 (11), 2014, pp. 4147–4155. https://doi.org/10.1021/ie4011113
7. Goodsell D.S., Bionanotechnology: Lessons from Nature. Wiley, Hoboken, 2004.
8. Kaushik M., et al.: Investigations on the antimicrobial activity and wound healing potential of ZnO nanoparticles. Applied Surface Science, 479, 2019, pp. 1169–1177. https://doi.org/10.1016/j.apsusc.2019.02.189
9. Božanić D.K., Dimitrijević-Branković S., Bibić N., et al.: Silver nanoparticles encapsulated in glycogen biopolymer: Morphology, optical and antimicrobial properties. Carbohydrate Polymers, 83(2), 2011, pp. 883–890. https://doi.org/10.1016/j.carbpol.2010.08.070

10. Dahl M.V.: Suppression of immunity and inflammation by products produced by dermatophytes. Journal of the American Academy of Dermatology, 28(5), 1993, pp. S19–S23. https://doi.org/10.1016/S0190-9622(09)80303-4
11. Ali A., Baheti V., Militky J., et al.: Comparative Performance of Copper and Silver Coated Stretchable Fabrics. Fibers and Polymers, 19(3), 2018, pp. 607–619. https://doi.org/10.1007/s12221-018-7917-5
12. Gorenšek M., Recelj P.: Nanosilver Functionalized Cotton Fabric. Text. Res. J., 77, 2007, pp. 138–141. https://doi.org/10.1177/0040517507076329
13. Islam S.U., Mohammad F.: High-Energy Radiation Induced Sustainable Coloration and Functional Finishing of Textile Materials. Ind. Eng. Chem. Res., 54, 2015, pp. 3727–3745. https://doi.org/10.1021/acs.iecr.5b00524
14. Becheri A., Dürr M., Nostro P.L., et al.: Synthesis and characterization of zinc oxide nanoparticles: Application to textiles as UV-absorbers. J. Nanopart. Res., 10, 2008, pp. 679–689. https://doi.org/10.1007/s11051-007-9318-3
15. Czajka R.: Development of medical textile market. Fibres Text. East. Eur., 13, 2005, pp. 13–15.
16. Tang B., Zhang M., Hou X., et al.: Coloration of Cotton Fibers with Anisotropic Silver Nanoparticles. Ind. Eng. Chem. Res., 51, 2012, pp. 12807–12813. https://doi.org/10.1021/ie3015704
17. Ilic V., Šaponjić Z., Vodnik V., et al.: The influence of silver content on antimicrobial activity and color of cotton fabrics functionalized with Ag nanoparticles. Carbohydr. Polym., 78, 2009, pp. 564–569. https://doi.org/10.1016/j.carbpol.2009.05.015
18. Neely A.N., Orloff M.M.: Survival of Some Medically Important Fungi on Hospital Fabrics and Plastics. J. Clin. Microbiol., 39, 2001, pp. 3360–3361. https://doi.org/10.1128/JCM.39.9.3360-3361.2001
19. Li B., Li D., Wang J.: Copper deposition on textiles via an automated dispensing process for flexible microstrip antennas. Text Res J., 84, 2014, pp. 2026–2035. https://doi.org/10.1177/0040517514534753
20. Ali A., Baheti V., Vik M., et al.: Copper electroless plating of cotton fabrics after surface activation with deposition of silver and copper nanoparticles. Journal of Physics and Chemistry of Solids, 137(October 2018), 2020, 109181 p. https://doi.org/10.1016/j.jpcs.2019.109181
21. Kumar A., Nath K., Parekh Y., et al.: Antimicrobial silver nanoparticle-photodeposited fabrics for SARS-CoV-2 destruction. Colloids and Interface Science Communications, 45, 2021. https://doi.org/10.1016/j.colcom.2021.100542

CUTTING ROOM SOFTWARE: ENHANCING EFFICIENCY IN GARMENT PRODUCTION

ARSOY, RAŞIT*

Kafkas University, Fine Art Faculty, Department of Textile and Fashion Design, 36000, Kars, Turkey

ABSTRACT

The rapid growth of the ready-to-wear industry has created a need for continuous improvement, along with the necessity to shorten production times and increase quality. The processes in this industry comprise a series of sequential activities carried out by machines and workers in a specific order. Particularly before cutting, checking model information is critically important. However, the various document formats used in the industry and the software employed to manage this data can complicate the work for personnel. In this context, there is a need for user-friendly software to enhance operational efficiency and minimize errors. This research aims to develop software focused on cutting processes. The developed software allows users to quickly and effectively access model and fabric information, measurement charts, and warehouse data, while simplifying complex processes. Additionally, its simple interface enables use without the need for special training and allows for the remote management of processes. As a result, the software aims to increase operational efficiency while reducing errors and workload.

KEYWORDS

Software; Cut Order Plan; Wastage; Depot.

INTRODUCTION

The rapid growth in the apparel industry has created a need for manufacturers to increase production speed, ensure product quality [4] [10], and reduce material waste [7] [17], particularly in the cutting process, leading to a demand for advanced approaches aimed at operational efficiency [20]. In this context, cutting, as a fundamental phase of the clothing production process, has a decisive impact on direct material usage, labor costs, and the quality of finished products [6] [24] [25].

Efficient cutting operations require the accurate and integrated management of technical drawings, model specifications, fabric details, measurement charts, and cut order plans (COP). However, this data is often stored in disconnected formats such as Excel sheets, PDFs, and JPEGs, and is delivered to the cutting room as physical files, which complicates efficient data sharing among departments.

These traditional methods can lead to inefficiencies, fabric waste, increased labor demands, and cost-increasing delays that jeopardize product standards, often relying on manual measurements, basic planning tools, and isolated data storage [18]. To overcome these issues, automation has emerged as a key solution for enhancing accuracy and efficiency [5] [12].

In particular, the use of computer-aided software in garment production allows for the optimization of sewing room operations, machinists, cycle times, and the order of processes. These software solutions have the capacity to identify potential problems and test various scenarios to enhance production efficiency [2]. Moreover, cutting optimization systems supported by advanced algorithms create automatic cutting plans that reduce costs, minimize errors, and increase overall management efficiency [22].

However, while some manufacturers prefer to use comprehensive production management software [3] [16], these systems often contain dense data and require extensive training for operators [1]. This complexity limits the ability to access and modify task-specific data quickly, particularly considering the needs of the cutting room. The lack of software specifically tailored for cutting rooms has further highlighted the need for automation solutions that cater to the unique requirements of this department.

Software designed exclusively for cutting room operations resolves these issues by enabling operators to quickly access technical data, fabric information, measurement and layout details, inventory updates, and order changes. Such a system not only reduces the likelihood of human error but also allows the cutting department to rapidly adapt to changing production demands. The software

* **Corresponding author:** Arsoy R., e-mail: *rasit.arsoy@kafkas.edu.tr*

contributes to an integrated structure of business processes by facilitating information connections among different departments. This enables rapid and effective communication of data across departments, allowing them to work in coordination rather than in isolation. This structural integrity enhances communication efficiency while simplifying access for all employees in every department.

This user-friendly, centrally managed data interface, accessible from any internet-connected device, reduces workforce requirements, increases productivity, and helps operators make timely, informed, and effective decisions. The use of software systems in cutting rooms not only provides better control over the production process but also contributes to significant improvements in quality and efficiency in the apparel industry by ensuring consistency and coherence in production.

MATERIAL AND METHOD

In this study, a system has been developed to model the use of software before and after the cutting process in the ready-to-wear industry. Through this system, technical information about models and fabrics, measurement charts, and COP can be viewed, warehouse data can be entered, and calculations for fabric waste can be made. The information conveyed to the cutting room is organized by the production planning department, and access to this data is provided through a touch monitor located in the cutting room via the developed software. This integrated data/information system supports cutting room management processes by strengthening interdepartmental coordination and contributes to the effective management of resource utilization in production processes. The necessary operations in the study were performed using the Microsoft Visual Studio C# programming language. The reason for selecting this language is its widespread use and compatibility with Windows.

Main Interface

The program named Ready- to-Wear Cutting Room Plan (RWCOPlan), shown in Figure 1, consists of three main sections: New, Open Folder, and Quit. The program provides access to product model and fabric information, measurement charts, and COP, allowing for the entry and tracking of warehouse data. Additionally, the program has the capability to perform calculations for fabric waste.

When the "New" section in the interface is clicked, a window opens for adding and calculating new product data, consisting of six stages: general model, fabric sample, COP, measurement chart, waste, and warehouse. In this section, product data entered by the user is calculated by the software. The "Open Folder" section is for loading previous data, while "Quit" is used to close the software.

Model Interface Section

In the Model section of the program, model information is entered into the system in the first step. At this stage, technical drawing information is also included in the system. The technical drawing of the garment is typically defined as a projection reflecting the correct proportions, lines, and silhouette details, often presented in a frontal or isometric view. These critical drawings convey the silhouette, structure, and design elements of the garment with clear and precise lines [15]. The cutting room staff can access the technical report of the model to be sewn, accurately understanding the product's proportions, stitching layout, finishing lines, and model details. A schematic of a new product model is shown in Figure 2.

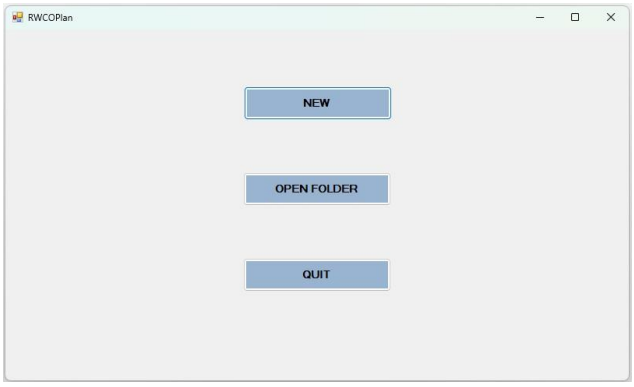

Figure 1. RWCOPlan programme's splash screen.

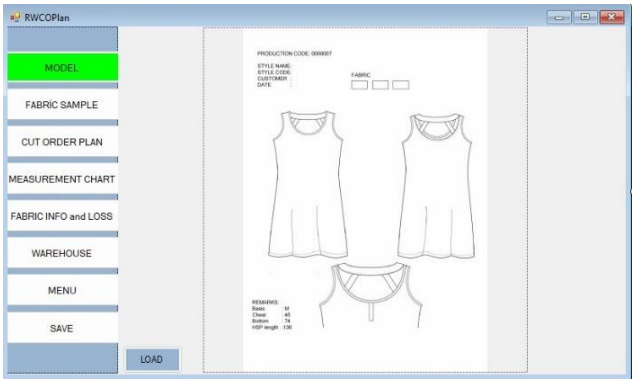

Figure 2. Technical drawing information interface page.

Figure 3. Fabric sample section of the interface.

Figure 4. Cut Order Plan section of the interface.

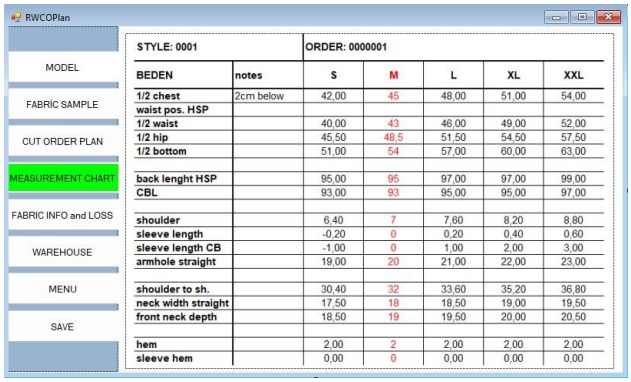

Figure 5. Measurement Chart section.

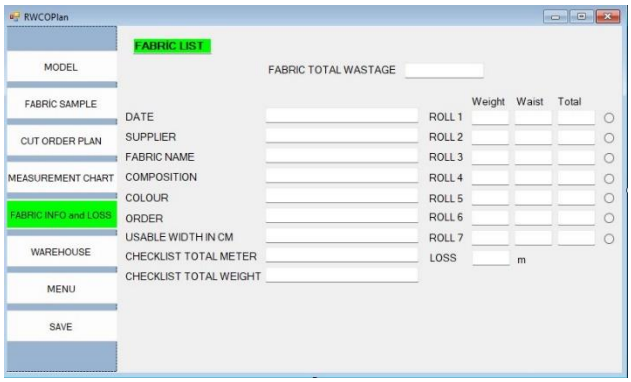

Figure 6. Fabric Info and Loss section.

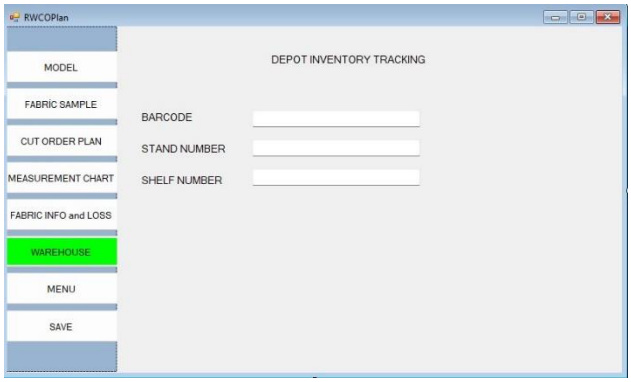

Figure 7. Warehouse section.

Fabric Sample Interface Section

At this stage, information regarding fabric visuals related to the product is entered into the system. The pattern information page is shown in Figure 3.

Cut Order Plan Interface Section

The spreading length, ply and layer counts, and size distribution for each layer can be tracked from the COP created in the software. This report includes information such as the amount of fabric in the warehouse, total usage needs, and consumption values. This allows the operator to make the correct fabric selection, check the cutting quantities for ply, and conduct pre-cut pattern checks. COP is one of the challenging aspects of garment production and can be significantly improved through automation. The primary goal of COP is to optimize fabric usage, which generally constitutes 50% of production costs [23]. COP involves the layout design of garment parts and is carried out considering variables such as fabric properties and production volume. The intuitive algorithms used in this process provide optimized cutting plans that reduce material waste, cutting time, and cost [14] [19]. Traditional COP methods are labor-intensive and prone to errors, potentially leading to unnecessary fabric waste. It is vital for the cutting room operator to verify COP data and compare it with the patterns on the fabric to minimize waste.

Measurement Chart Interface Section

In the next stage, measurement data is entered into the system. The measurement information from the technical file is shown in Figure 5. The creation of ready-to-wear products requires the formation of patterns according to standard sizing, measurement charts, and grading guidelines based on body measurements of the model [21]. The cutting room operator needs this data to verify pattern measurements on the fabric when necessary.

Fabric Info and Loss Interface Section

At this stage, fabric information is entered, and the weight information obtained from the rested fabric rolls is recorded in the system. The difference in meterage indicated on the technical documents of fabric rolls and the meterage after resting is identified by the cutting room staff [8]. After the data is entered, the system automatically calculates the actual meterage. The values of waste such as fabric errors during spreading and cutting, excess fabric pieces, roll ends, and scraps are entered by the operator, allowing the total fabric loss to be calculated [9] [11] [13].

Warehouse Interface Section

In the final stage, warehouse codes and numbers are entered to easily locate the fabric's position in the warehouse. Efficient use of the workspace is

essential for successful production. Organizing the shelves allows for easy access to fabric rolls and other materials, providing quick access during production. Software systems regulate inventory management by tracking the usage of fabric rolls in cutting rooms and ensure a workflow compatible with all production stages.

CONCLUSION

In this study, it is aimed to create a software that enables the management of the information of the ready-to-wear enterprise with the support of an integrated data / information system within the scope of cutting room management and at the same time provides inter-departmental control.

The cutting room management software developed in the study stands out as a powerful tool that enables the effective fulfilment of critical functions such as planning, raw material selection, waste management and monitoring of production activities in garment production. Unlike complex general-purpose production software, this software responds to the specific needs of cutting departments by offering a user-friendly and comprehensive interface. In particular, it allows operators to make quick adjustments by providing easy access to basic data such as cutting orders, fabric specifications and warehouse management. The simplicity and clarity of the interface is expected to not only increase productivity but also contribute to the operators to be more agile and responsive in the production process by minimising errors.

REFERENCES

1. Chaudhary S., Pardeep K., Johri P.: Maximizing Performance of Apparel Manufacturing Industry through CAD Adoption. International Journal of Engineering Business Management, 12, 2020, pp. 1-4. https://doi.org/10.1177/1847979020975528
2. Cocks T., Harlock S.: Computer-aided Simulation of Production in the Sewing Room of a Clothing Factory. Journal of The Textile Institute, 80, 1989, pp. 455-463. https://doi.org/10.1080/00405008908658298
3. Cosma Technology. Digital Cutting Room Software, 2024, online: https://cosmatechnology.com/software/digital-cutting-room-software-5 [cit. 16.06.2024]
4. Eroglu D., Orbak Â.: Simulated Annealing Algorithm and Implementation Software for Fabric Cutting Problem. Textile and Apparel, 30(1), 2019, pp. 10-19. https://doi.org/10.32710/tekstilvekonfeksiyon.521944
5. Fernandes S., Vidhya D.S.: Designing a Prototype of Automated Fabric Cutter. 2021 IEEE Bombay Section Signature Conference (IBSSC), 2021, pp. 1-4. https://doi.org/10.1109/IBSSC53889.2021.9673395
6. Guo-ning Q.: Two Stage Optimization Method of Cut Order Planning for Apparel Mass Customization. Computer Integrated Manufacturing Systems, 18(3), 2012, pp. 479-485.
7. Indrie L., Ilieva J., Zlatev Z., et al.: Development of an Algorithm for Textile Waste Arrangement. Sustainability, 15, 2023, 11399 p. https://doi.org/10.3390/su151411399
8. Kalkancı M., Kurumer G.: An Investigation About the Effects of Knitted Fabrics Dimensional Change on the Pattern Size in Garment Production. Pamukkale University Journal of Engineering Sciences, 23(7), 2017, pp. 833-840.
9. Magowan J.: Optimising Material Utilisation. Readywear, 11, 1982, pp. 28-31.
10. Michelini R., Razzoli R.: Robotics in Clothes Manufacture. International Journal of Mechanical Engineering and Applications, 1, 2013, 17 p. https://doi.org/10.11648/J.IJMEA.20130101.13
11. Milokhina V.A., Burlakin A.I., Skututa M.A.: Use of a Regression Model to Calculate Fabric Loss along the Length of the Overlays. Tekhnologiya Legkoi Promyshlennosti, 29, 1(169), 1986, pp. 90-91.
12. Nayak R., Padhye R.: Introduction to Automation in Garment Manufacturing. (Nayak, R., Padhye, R. eds). In The Textile Institute Book Series, Woodhead Publishing, 2018, pp. 1-27. https://doi.org/10.1016/B978-0-08-101211-6.00001-X
13. Ng S.F., Hui C.L., Leaf G.A.V.: Fabric Loss During Spreading: A Theoretical Analysis and its Implications. The Journal of The Textile Institute, 89(4), 1998, pp. 686-695. https://doi.org/10.1080/00405000.1998.11090907
14. Ranaweera R., Rathnayaka R., Chathuranga L.: Optimal Cut Order Planning Solutions Using Heuristic and Meta-Heuristic Algorithms: A Systematic Literature Review. KDU Journal of Multidisciplinary Studies, 2023. https://doi.org/10.4038/kjms.v5i1.66
15. Rukavishnikova A.S.: Technical Drawıng in the System of Training of Bachelors Designers of Clothes. Modern Problems of Science and Education, 3, 2016.
16. Sentez Business Solutions. Cutting Card, 2024, online: https://www.sentez.com/upload/Books/SenVogue/content/kesim.htm [cit. 15.06.2024]
17. Silva E., Viães C., Oliveira J., et al.: Integrated Cutting and Production Planning: A Case Study in a Home Textile Manufacturing Company. (Póvoa, A., Miranda, J. eds). In: Operations Research and Big Data. Studies in Big Data, 15. Springer, Cham, 2015, pp. 213-220. https://doi.org/10.1007/978-3-319-24154-8_25
18. Silva P., Lanel G., Perera M.: Integer Quadratic Programming (IQP) Model for Cut Order Plan. IOSR Journal of Mathematics, 13, 2017, pp. 76-80. https://doi.org/10.9790/5728-1302027680
19. Tsao Y., Linh V., Liao L.: Hybrid Heuristics for the Cut Ordering Planning Problem in Apparel Industry. Computers and Industrial Engineering, 144, 2020, 106478 p. https://doi.org/10.1016/j.cie.2020.106478
20. Ünal C., Yüksel A.: Cut Order Planning Optimisation in the Apparel Industry. Fibres & Textiles in Eastern Europe, 28, 2020, pp. 8-13. https://doi.org/10.5604/01.3001.0013.5851
21. Vinué G., León T., Alemany S., et al.: Looking for Representative Fit Models for Apparel Sizing. Decision Support Systems, 57, 2014, pp. 22-33. https://doi.org/10.1016/j.dss.2013.07.007
22. Wang X., Huang Z., Qiu M., et al.: Research in Garment Cutting Plan Optimization System. In: Soft Computing in Information Communication Technology. Springer Berlin Heidelberg, 2012, pp. 403-409. https://doi.org/10.1007/978-3-642-29148-7_56
23. Wong W., Leung S.: Genetic optimization of fabric utilization in apparel manufacturing. International Journal of Production Economics, 114, 2008, pp. 376-387. https://doi.org/10.1016/J.IJPE.2008.02.012
24. Wong W., Leung S.: Optimizing Cut Order Planning in Apparel Production Using Evolutionary Strategies. Optimizing Decision Making in the Apparel Supply Chain Using Artificial Intelligence (AI): From Production to Retail, Woodhead Publishing, 2013, pp. 81-105. https://doi.org/10.1533/9780857097842.81
25. Yan-mei L., Shao-cong Y., Shu-ting Z.: Research on Cut Order Planning for Apparel Mass Customization. In: Deng, H., Miao, D., Wang, F.L., Lei, J. (eds) Emerging Research in Artificial Intelligence and Computational Intelligence. AICI 2011. Communications in Computer and Information Science, 237. Springer, Berlin, Heidelberg, 2011, pp. 267-271. https://doi.org/10.1007/978-3-642-24282-3_36

THE TYPES OF TEXTILES USED IN THE FACADE AND ROOFING SYSTEMS OF STADIUM FACILITIES IN TURKEY

ŞAHIN, YELDA DURGUN[1*] AND OKUR, MEHMET[2]

[1] Adana Alparslan Türkeş Science and Technology University, Faculty of Design and Architecture, Architecture Department, Adana, Turkey
[2] Adana Alparslan Türkeş Science and Technology University, Institute of Graduate School, Adana, Turkey

ABSTRACT

Technical textiles are functional fabrics that have applications across including both construction (BuildTech) and architecture (ArchiTech). This technical textile is developed for high-tech and high-performance applications. In modern architecture, high-performance textile materials are highly valued and widely used in various applications, including self-cleaning, low-maintenance structures, fabric canopies, and energy-efficient buildings. They are also utilized for high-performance façades, energy-harvesting curtains, flexible mega-structures, responsive phase-change materials, air-supported fabric constructions, thermal regulation, green roofs, smart living spaces, acoustic solutions, advanced building materials, and creating habitable spaces in extreme weather conditions.

In this study, the types of textiles used in the facade and roofing systems of stadium facilities in Türkiye have been examined. The advantageous properties of textiles employed in stadium structures characterized by substantial roof and facade openings at the structural scale have been critically analyzed in relation to other conventional building materials. The technical textile material summary demonstrates the tremendous diversity of today's membrane materials using stadium facilities in Turkey.

KEYWORDS

Technical textiles; Stadium facilities; Facade and roofing system.

INTRODUCTION

Technology-driven materials, designs, and construction techniques play a major role in façades and roofing systems, becoming essential elements of modern architecture (Göppert and Paech,2015).

Technical textile provide limitless opportunities for architectural expression, allowing for free-form and complex geometries that are both structurally viable and economically appealing in stadium building.

In Architextile composite structures, the use of glass, ceramic, carbon fibers, aramids, liquid crystal polymers, and high-modulus polyethylenes provides textile materials with high performance and quality (Gezer, 2008).

In a building, façade cladding materials serve different functions based on their various applications. When assessing the potential demands for each cladding material, the following can be highlighted as the most important.

That are protection from external environmental conditions (wind, rain, temperature, sun, etc.), creation of private interiors, cladding to withstand outer loads (wind, temperature,maintenance loads, etc.), thermal performance, solar/light performance, fire behaviour, durability, acoustic performance, aesthetic surface appearance (translucency, colour, etc.), possible complex architectural geometries, material weight for substructure design, material cost, installation cost/time and modularity, maintenance requirements, and/or replacement methods, recyclability, sustainability (Göppert and Paech,2015., Hernández, 2006).

According to the literature, it can be observed that studies on the performance of textile materials used in the façades and roof coverings of stadium structures have focused on topics a, b, and c.

The relationship between early textile architecture in history and in modern period textile façade and roofing systems differs from a period where materials were applied in layer by layer to a more technologically advanced approach that integrates these layers together.

A wide variety of fabric materials are used in architecture. These are evaluated as PVC Fabric (PVC-Coated Polyester), PVDF, PVF, PTFE Fabric (PTFE Coated Fiberglass), Fabric options – PVC and

[*] **Corresponding author:** Şahin Y.D., e-mail: *ydurgunsahin@atu.edu.tr*

PTFE, PVC / Polyester fabric, and PTFE / Fiberglass fabric (Gandi, 2020., Kamal, 2020).

In stadium structures, a wide variety of textile membrane composite materials are used in façade systems. Based on the expected demand requirements from these materials, combinations of various materials are utilized for textile membrane composites. Architectural fabrics are commonly woven from polyester (PES) yarns coated with polyvinyl chloride (PVC) or from glass fiber yarns coated with either polytetrafluoroethylene (PTFE) or silicone. The purpose of the coating is to shield the yarn fibers from environmental factors while also enabling individual membrane segments to be welded together. Uncoated fabrics are typically composed of PTFE or polyvinylidene fluoride (PVDF).

Uncoated fabrics are typically made from PTFE or polyvinylidene fluoride (PVDF). Textile membranes can either be fully coated to create a water- and wind-proof fabric with translucencies of approximately 0–40%, or woven with gaps between the yarns to form an open mesh membrane with localized yarn coatings. These mesh membranes are commonly used for sunscreens and architectural envelopes that provide views in two directions. Various mesh patterns are available, differing in size and arrangement of open areas. Both glass/PTFE and PES/PVC membranes come in multiple colors, with some being printable for a customized appearance. Depending on structural requirements, different strength classes are offered. Recently, laminated open mesh membranes have been developed, featuring a continuous lamination of transparent fluoropolymers, offering high transparency (>50%) and material strengths up to 60 kN/m (Göppert and Paech,2015).

Different fibrous materials shaped by knitting and weaving techniques in textile technology are also used in architectural façades (Gezer, 2007/a; Garcia, 2006). Woven and knitted fabrics made from metal fibers, as well as steel wire meshes, are examples of materials used in stadium façades.

The performance of fabric structures is significantly influenced by the environment in which they are located. Key factors affecting fabric performance include geographic latitude and temperature, UV radiation, humidity, pollution levels, dust accumulation, cleaning frequency, deposition of plant matter, staining from rainwater runoff, and exposure to rainfall that helps remove dirt and dust (Tolani, 2016., Kamal, 2020). The characteristics of textile materials used in stadium structures built in Türkiye have been grouped according to these factors. The grouping has been evaluated based on regions, taking into account the differing seasonal characteristics.

THE ROOFING MATERIALS USED IN STADIUM STRUCTURES

Factors determining the selection of roofing materials include climate, architectural and structural design, and cost estimation. The roof surface is a layer exposed to external elements. The roofing material must be resistant to atmospheric conditions. Therefore, the covering material should have water and thermal insulation properties, a long service life, and be lightweight while also conforming to the shape of the roof (Durgut, 2019).

MATERIAL PROPERTIES

Materials should be selected and designed according to the function of the structure. The materials used for the façade and covering systems of stadium structures directly affect user comfort. Therefore, the compatibility between structure and covering materials in stadium buildings is a crucial issue that must be addressed (Durgut, 2019). Materials have a direct impact on visual, acoustic, and climatic comfort. Technological advancements and innovations in façade and covering materials have brought criteria such as long-term durability, fire resistance, ease of replacement and repair, material permeability, sustainability, and user comfort to the forefront. With a material selected for its permeability feature, daylight can easily enter the field, ensuring the healthy growth of the field grass (Seçgin, 2023).

With advancing technology, newly developed materials are frequently preferred due to characteristics such as their lightness, strength, flexibility, and load-bearing capacity. Today, a wide variety of materials are predominantly used in stadium structures, including steel, concrete, new-generation plastics (ETFE, PTFE, PVC, etc.), aluminum, galvanized sheet metal, and smart materials.

PVC (Polyvinyl Chloride) and PVDF (Polyvinylidene Fluoride) Membrane Covering

While the lifespan of PVC is between 10 and 15 years, it can extend up to 25 years with a PVDF (Polyvinylidene Fluoride) coating. It offers a variety of colors and is more cost-effective than other building materials. PVC is waterproof and, with its light-transmitting property, allows natural light to enter the space, reducing the need for artificial lighting. It has strong UV resistance, high fire resistance, and is a lightweight, recyclable material (Alioğlu, 2018; Uğurlu, 2021).

PTFE (Polytetrafluoroethylene) Textile Membrane

PTFE is a textile material used in façade and covering systems, consisting of fiberglass fabric coated with Teflon resin. Commercially known as Teflon, it has a

lifespan of approximately 30-50 years and starts to degrade above 250 degrees Celsius. It offers strong UV resistance, high fire resistance, and reflects about 60% of light. It does not mold or yellow under atmospheric conditions and is waterproof. PTFE withstands temperatures ranging from -73°C to +232°C. Single-layer membrane structures made with PTFE reflect 75% of sunlight and absorb 10% of it (Krüger, 2009; Durgut, 2019).

ETFE (Ethylene Tetrafluoroethylene) Membrane Covering

ETFE is a fluorine-based plastic material used in air-supported covering systems, with a thickness between 0.05 and 0.20 mm. It has high light and UV transmittance, an approximate lifespan of 100 years, and is recyclable (Compagno et al., 2004; Durgut, 2019). ETFE allows 90-97% of light to pass through. Thanks to the air between the foil layers in ETFE cushions, it provides better insulation than glass panels. ETFE foils are flame-resistant and can withstand temperatures up to 270°C (Durgut, 2019). ETFE material can also be integrated with textile materials in façade and covering systems.

Carbon Fiber (CF)

Carbon fiber is a technologically advanced material with a fibrous structure composed of tar, nylon, and orlon, known for being rigid, lightweight, and durable. It offers high strength, is resistant to corrosion and fire, and is non-flammable. Although it is costly, its application requires specialized experience and equipment (Bajpai, 2013).

REVIEW OF STADIUMS IN TÜRKIYE ACCORDING TO ROOF AND FACADE MATERIAL SELECTIONS

In the literature, due to the direct impact of materials on comfort, Türkiye's 7 climate zones have been examined, and façade and roof covering material selections for stadium structures have been analyzed according to these regions. Table 1 provides an overview of technical textiles used in stadium architecture applications in Türkiye.

The use of textiles as façade and roofing materials is achieved through one of the textile types: plain PVC, perforated (mesh), PTFE (Teflon), and ETFE materials. When grouping these textile types according to regions, eight stadium structures built in the Marmara Region were examined. Of these, one stadium uses only PVC membrane covering, while three use a combination of PVC membrane covering and other cladding materials. One stadium uses both PVC membrane and PTFE textile covering along with other cladding materials. Another uses PTFE textile covering, one employs aluminum roofing, and another combines PVC membrane and PTFE textile coverings. Overall, a mixed covering system has been applied in five of the stadiums.

In the Aegean Region, four stadium structures were examined. Of these, two use only PVC membrane covering, one uses a combination of PVC membrane and other (composite cladding) covering systems, and one utilizes an alternative (polycarbonate cladding) system. In the Central Anatolia Region, five stadiums were studied; two of these use a mixed system of PVC membrane and other covering materials, while another two use a combination of PVC membrane and PTFE textile covering. Lastly, one uses an aluminum roof covering. In the Black Sea Region, three stadiums were analyzed, all of which share PVC membrane covering as a common feature. Among these, one employs a combination of PVC membrane and PTFE textile covering, one combines PVC membrane and other covering materials (PVC mesh), and one uses PVC membrane alone. In the Mediterranean Region, of the five stadiums constructed, two use PVC membrane alone, two combine PVC membrane with other covering systems (PVC mesh and standing seam roof), and one uses a combination of PVC membrane, ETFE membrane, and other (standing seam roof) systems. In Southeastern Anatolia, three stadiums were examined: one uses a mixed system of PVC membrane, PTFE textile, and other (GFRC, GRC precast) covering systems, one uses ETFE membrane, and one employs other (composite cladding). In Eastern Anatolia, two stadium coverings were analyzed: one uses PVC membrane, while the other combines polycarbonate and standing seam roofing systems.

In Figure 1, the distribution of materials used in stadiums by region can be seen. In Figure 2, the usage rates of materials used in stadiums across Türkiye are shown.

In Türkiye, regarding the roofing material usage in stadiums, a single roof material using is utilized in 43,3% of cases, while 56.7% prefer composite material usage. A stadium roof design plays a critical role in determining the amount of light that penetrates the field, thereby affecting the growth of the turf. If the roof design is not covered with an appropriate light-transmitting material, artificial lighting has to be used to sustain grass growth. This practice contradicts the principle of sustainability and results in significant energy costs. In line with the UN (United Nations)'s SDG 7 and SDG 11 principles, it is recommended that the design of the southern facade and roof sections of stadium structures incorporate a light-transmitting textile material to promote low-energy, sustainable living environments

RESULT

Technological advancements playing a role in architectural textile interactions are influencing the shaping of architectural structures. As a sustainable material, the high-performance textile group stands out and diversifies into new composite forms through technological advancements. This diversity not only

Table 1. Material Selections and Stadium Facilities in Türkiye.

Region	Photo	Stadium Name	City	Construction Year	Construction Site	Capacity (Spectators)	Classification According to Cover System	Classification According to Stadium Tribune Covering System	Facade and Covering System	Materials
Marmara Region		Atatürk Olympic Stadium (1,2)	İstanbul	2002	240.929 m² (Land Area)	77563	Semi-Covered	Semi-Covered	Steel, Concrete	1. PVC Membrane Covering
		Ali Sami Yen Sports Complex Rams Park (1,3,4,31)	İstanbul	2011	82.000 m²	52600	Semi-Covered	Covered	Steel, Membrane	1. PVC Membrane Covering, 4.Other(Compact Laminate Panel)
		Fenerbahçe Şükrü Saraçoğlu Stadium (1,5,6)	İstanbul	Renewal: 2006	55.000 m²	50530	Semi-Covered	Covered	Steel, Membrane ve Aluminum	1. PVC Membrane Covering, 4.Other(Composite)
		Beşiktaş Park Stadium (1,7,8,9)	İstanbul	2016	50.000 m²	42590	Semi-Covered	Covered	Steel, Concrete, Membrane	2. PTFE Textile Membrane Covering
		Yüzüncüyıl Atatürk Stadium (Bursa Timsah Arena) (1,7,10,11,64)	Bursa	2015	179.611 m²	43361	Semi-Covered	Covered	Steel, Membrane	1.PVC Membrane Covering ,2.PTFE Textile Membrane Covering
		Kocaeli Stadium (7,12)	Kocaeli	2018	90.700 m²	34829	Semi-Covered	Covered	Steel, Aluminum	4.Other (Aluminum Roof Covering)
		Sakarya Stadium (7,14,15,16,69)	Sakarya	2017	128.000 m²	28154	Semi-Covered	Covered	Steel, Membrane	1. PVC Membrane Covering,2.PTFE Textile Membrane Covering ,4.Other (PVC Mesh)
		Başakşehir Fatih Terim Stadium (34,35,36,37)	İstanbul	2014	160.000 m²	17300	Semi-Covered	Covered	Steel, Aluminum	1. PVC Membrane Covering, 4.Other (Glass, Composite)
Aegean Region		İzmir Atatürk Stadium (17)	İzmir	Renewal:2005	216.330 m² (Land Area)	51337	Uncovered	Semi-Covered	Steel, Concrete, Membrane	1. PVC Membrane Covering
		Gürsel Aksel Stadium (38,39,40)	İzmir	2020	94.541 m²	25000	Semi-Covered	Covered	Steel, Aluminum	4.Other (Precast, Polycarbonate)
		İzmir Alsancak Stadium (18,61)	İzmir	2021	22.500 m²	15000	Semi-Covered	Semi-Covered	Steel, Membrane	1. PVC Membrane Covering
		Akhisar Stadium (67)	Manisa	2018	52.137 m² (Land Area)	12139	Semi-Covered	Covered	Steel, Membrane	1. PVC Membrane Covering, 4.Other (Composite)
Central Anatolia Region		Konya Metropolitan Municipality Stadium (1,7,19,65)	Konya	2014	90.000 m²	42000	Semi-Covered	Covered	Steel, Membrane	1. PVC Membrane Covering, 4. Other (Transparent Membrane)
		Yeni Eskişehir Stadium (41,42)	Eskişehir	2016	86.783 m²	34930	Semi-Covered	Covered	Steel, Aluminum	1. PVC Membrane Covering, 4.Other (Aluminum Panel)
		Kayseri Kadir Has City Stadium (32,33)	Kayseri	2009	80.000 m²	32864	Semi-Covered	Covered	Steel, Aluminum	4. Other (Aluminum Roof Covering)
		Sivas 4 Eylül Stadium (43,44,45)	Sivas	2016	58.700 m²	27532	Semi-Covered	Covered	Steel, Aluminum	1- PVC Membrane Covering ,2.PTFE Textile Membrane Covering
		Eryaman Stadium (46,47)	Ankara	2016	37.462 m²	20672	Semi-Covered	Covered	Steel, Aluminum	1. PVC Membrane Covering,2. PTFE Textile Membrane Covering
Black Sea Region		Şenol Güneş Sports Complex (Akyazı Stadium) (7,20,21,63)	Trabzon	2016	170.000 m²	41131	Semi-Covered	Covered	Steel, Membrane	1. PVC Membrane Covering,2.PTFE Textile Membrane Covering
		Samsun 19 Mayıs Stadium (22,23,66)	Samsun	2017	140.000 m²	33919	Semi-Covered	Covered	Steel, Membrane	1. PVC Membrane Covering, 4.Other (PVC Mesh)
		Giresun Çotanak Sports Complex (24,62)	Giresun	2022	89.673 m²	21500	Semi-Covered	Covered	Steel, Membrane	1. PVC Membrane Covering
Mediterranean Region		Yeni Adana Stadium (28,29,30)	Adana	2021	78.012 m²	33543	Semi-Covered	Covered	Steel, Membrane	1. PVC Membrane Covering, 4.Other (PVC Mesh)
		Antalya Stadium (48,49,50)	Antalya	2015	87.331 m²	29307	Semi-Covered	Covered	Steel, Aluminum	1. PVC Membrane Covering, 4.Other (Standing Seam Roof)
		Mersin Stadium (1,7,25,68,70)	Mersin	2013	55.000 m²	25534	Semi-Covered	Covered	Steel, Membrane	1. PVC Membrane Covering
		Yeni Hatay Stadium (58,59)	Hatay	2021	55.395 m²	25000	Semi-Covered	Covered	Steel, Aluminum, Standing Seam	1. PVC Membrane Covering
		Alanya Oba Stadium (57)	Alanya	2011	23.000 m²	9789	Semi-Covered	Covered	Steel, Composite	1. PVC Membrane Covering, 3.ETFE Membrane Covering, 4.Other (Standing Seam Roof)
Southeastern Anatolia Region		Gaziantep Stadium (7,13,26)	Gaziantep	2017	61.215 m²	33502	Semi-Covered	Covered	Steel , Aluminum	1. PVC Membrane Covering,2. PTFE Textile Membrane Covering, 4.Other (PTFE Mesh, GFRC, GRC Precast)
		Diyarbakır Stadium (27)	Diyarbakır	2018	50.000 m²	33000	Semi-Covered	Covered	Steel,Membrane	4. Other (Composite)
		11 Nisan Stadium (55,56)	Şanlıurfa	2009	36.400 m²	28965	Semi-Covered	Covered	Steel, Aluminum	3.ETFE Membrane Covering
Eastern Anatolia Region		Yeni Malatya Stadium (52,53,54)	Malatya	2017	93.000 m²	25745	Semi-Covered	Covered	Steel, Aluminum	1. PVC Membrane Covering
		Elazığ Atatürk Stadium (51,60)	Elazığ	Renewal: 2023	55.395 m²	17600	Semi-Covered	Covered	Concrete, Steel, Standing Seam	4. Other (Polycarbonate, Standing Seam Roof)

(1): Arslan,2016. , **(2)**: Url-1, **(3)**: Url-2, **(4)**: Url-3, **(5)**: Url-4, **(6)**: Url-5, **(7)**: Bülbül,2017, **(8)**: Uğurlu,2021, **(9)**: Url-6, **(10)**: Kara,2020, **(11)**: Url-7, **(12)**: Url-8, **(13)**: Url-9, **(14)**: Url-10, **(15)**: Url-11, **(16)**: Url-12, **(17)**: Url-13, **(18)**: Url-14, **(19)**: Kurumak,2019, **(20)**: Url-15, **(21)**: Url-16, **(22)**: Url-17, **(23)**: Url-18, **(24)**: Url-19, **(25)**: Url-20, **(26)**: Url-21, **(27)**: Url-22, **(28)**: Url-23, **(29)**: Sürgülü, 2023, **(30)**: Url-24, **(31)**: Gözütok, 2019, **(32)**: Url-25, **(33)**: Url-26, **(34)**: Url-27, **(35)**: Url-28, **(36)**: Url-29, **(37)**: Ceylan,2020, **(38)**: Url-30, **(39)**: Url-31, **(40)**: Url-32, **(41)**: Url-33, **(42)**: Url-34, **(43)**: Url-35, **(44)**: Url-36, **(45)**: Url-37, **(46)**: Url-38, **(47)**: Url-39, **(48)**: Url-40, **(49)**: Url-41, **(50)**: Url-42, **(51)**: Url-43, **(52)**: Url-44, **(53)**: Url-45, **(54)**:Url-46, **(55)**: Url-47, **(56)**: Url-48, **(57)**: Url-49, **(58)**: Url-50, **(59)**: Url-51, **(60)**:Url-52, **(61)**: Url-53, **(62)**: Url-54, **(63)**: Url-55, **(64)**: Url-56, **(65)**: Url-57, **(66)**: Url-58, **(67)**: Url-59, **(68)**: Url-60, **(69)**:Url-61, **(70)**: Url-62

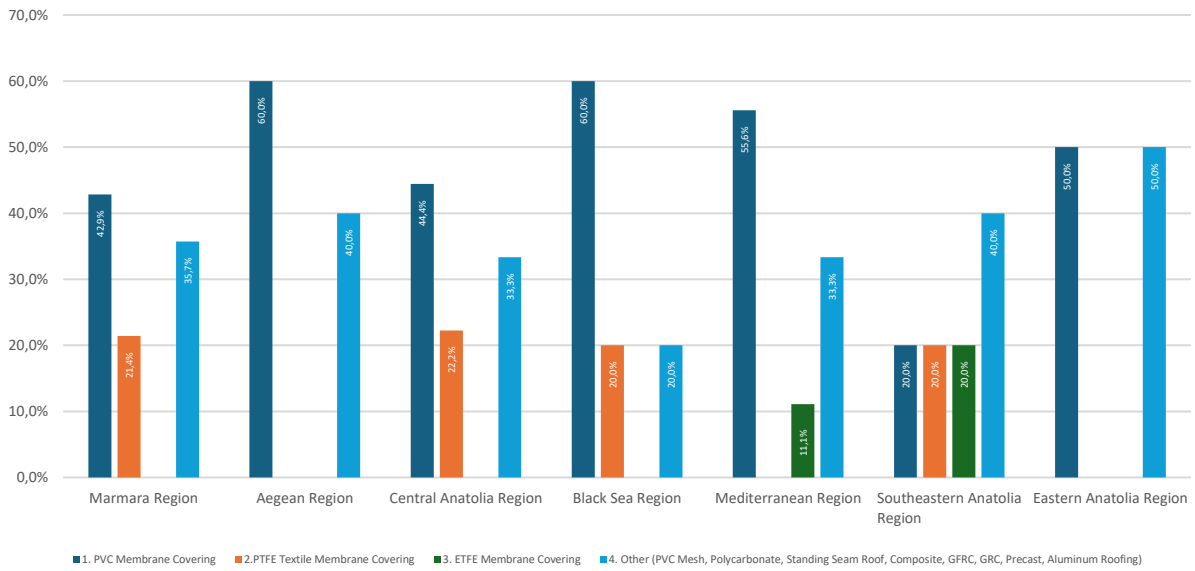

Figure 1. Materials Used in Stadiums by Region.

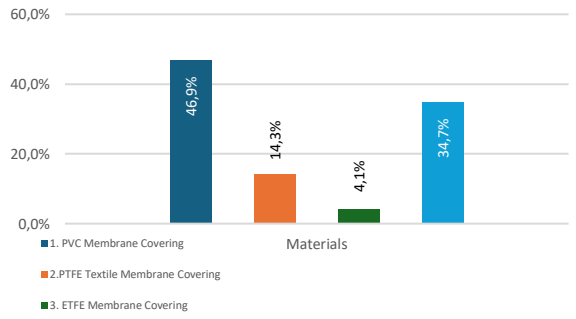

Figure 2. The Use of Materials in Stadiums in Türkiye.

makes significant contributions to stadium architectural design but also alters the symbolic values of the structure on an urban scale. Among the examined examples, regional differences have been observed in the textile materials used for stadium facades and roofing. Facade and roofing materials selected in harmony with the covering system and structural characteristics play a key role in the formal shaping of stadium structures, enhancing their visibility within the city. Material choices become the focal point of stadium designs, and the way the selected material is used gives the structure an iconic quality. This study has presented that PVC membrane coverings are the most commonly used in stadiums in Türkiye. The study has shown that the use of composite materials is also prevalent as a secondary choice in facade and covering systems.

The findings of the study have shown that in Türkiye, covering materials used in stadiums were not selected in accordance with the climate characteristics of the regions, nor was light permeability taken into consideration. This lack of alignment could lead to issues in the development of grass in stadiums, supporting the hypothesis that this relational mismatch may contribute to such problems. In this context, the study serves as a foundation for further research.

REFERENCES

1. Alioğlu T.: Tekstil Esaslı Malzemelerin Mimaride Kabuk Tasarımında Kullanımı ve Sürdürülebilirlik Açısından Değerlendirilmesi. Doktora Tezi, İstanbul Aydın Üniversitesi, Fen Bilimler Enstitüsü, İstanbul, Türkiye, 2018.
2. Arslan N.: Stadyum Yapılarının Tasarım Kriterlerinin Uluslararası Yönetmelikler Doğrultusunda İncelenmesi, Yüksek Lisans Tezi, Yıldız Teknik Üniversitesi Fen Bilimleri Enstitüsü, İstanbul, Türkiye, 2016.
3. Bülbül E.: Stadyum Yapılarındaki Strüktür Sisteminin Biçim Oluşumuna Etkisi, Yüksek Lisans Tezi, Gazi Üniversitesi, Fen Bilimleri Enstitüsü, Ankara, Türkiye, 2017.
4. Ceylan E.E.: Enerji Etkin Stadyum Tasarım Kriterleri Önerisi, Yüksek Lisans Tezi, Konya Teknik Üniversitesi Lisansüstü Eğitim Enstitüsü, Konya, Türkiye, 2020.
5. Durgut S.: Stadyum Yapılarında Çekmeye Çalışan Çatı Strüktürleri Kullanımının Kronolojik Değerlendirilmesi, Yüksek Lisans Tezi, Dokuz Eylül Üniversitesi Fen Bilimleri Enstitüsü, İzmir, Türkiye, 2019.
6. Göppert K., Paech C.: High-performance materials in façade design Structural membranes used in the building envelope. Steel Construction 8 (4), 2015, pp. 237-243. https://doi.org/10.1002/stco.201510033
7. Garcia G.: November- December “Prologue For A History and Theory of Architextiles”, Architectural Design-Architextiles, 2006, pp. 13-20.
8. Gandhi U.: Design and Construction of Tension Membrane Structures, 2020, online: http://homepages.cae.wisc.edu/~ukgandhi/documents/tensile%20structures_paper.pdf [cit. 25.07.2020]
9. Gezer H.: Titanyum’un Konut Mimarisinde ve İç Mekan Düzenlemelerinde Kullanılması. TMMOB Mimarlar Odası Yayını, ISBN 9944-89-196-7, İstanbul, 2006, pp. 480-487.
10. Gezer H.: Üretim Alanında Tekstil ve Mimari Arasındaki Etkileşim. İstanbul Ticaret Üniversitesi Fen Bilimleri Dergisi Yıl:7 Sayı:13 Bahar, 2008, pp. 21-49.
11. Gözütok M.M.: Stadyumlarda Uygun Akustik Ortamın Oluşturulması Bağlamında Genel İlkelerin Belirlenmesi, Yüksek Lisans Tezi, Yıldız Teknik Üniversitesi, Fen Bilimleri Enstitüsü, İstanbul, Türkiye, 2019.
12. Hernández M.J.J.: Fabric Membranes As Daylighting Control Systems In Buildings. Doctor of Philosophy, The University of Nottingham, 2006.
13. Kamal A.M.: An investigation into tensile structure system: construction morphology and architectural interventions.

Journal of Building Materials and Structures, 7, 2020, pp. 236-254. https://doi.org/10.34118/jbms.v7i2.776
14. Kurumak M.: Stadyum Tasarımında Ulusal/Uluslararası Standartlara Göre Seyirci Mekanlarının Analizi, Konya Büyükşehir Stadyumu Örneği, Yüksek Lisans Tezi, Necmettin Erbakan Üniversitesi, Fen Bilimleri Enstitüsü, Konya, Türkiye, 2019.
15. Seçgin M.: Stadyumların Örtü Sistemlerinin Örneklerle İncelenmesi, Yüksek Lisans Tezi, İstanbul Aydın Üniversitesi Lisansüstü Eğitim Enstitüsü, İstanbul, Türkiye, 2023.
16. Sürgülü U.: Stadyum Yapılarında Çatı Strüktürlerinin İncelenmesi, Yüksek Lisans Tezi, Yıldız Teknik Üniversitesi, Fen Bilimleri Enstitüsü, İstanbul, Türkiye, 2023.
17. Uğurlu İ.: Stadyum Yapılarında Hareketli Cephe ve Örtü Malzemelerinin Mimari Biçim Oluşumu Üzerindeki Etkileri, Yüksek Lisans Tezi, Fatih Sultan Mehmet Vakıf Üniversitesi Lisansüstü Eğitim Enstitüsü, İstanbul, Türkiye, 2021.
18. https://yuzuncuyilgalerisi.eba.gov.tr/tema/ataturk-olimpiyat-stadyumu 18#:~:text=Atat%C3%BCrk%20Olimpiyat%20Stad%C4%B1%2C%20Uluslararas%C4%B1%20Atletizm,antrenman%20ve%20%C4%B1s%C4%B1nma%20alan%C4%B1%20mevcuttur.
19. https://erkel.com.tr/referanslarimiz/turk-telekom-arena/
20. http://www.mtfproje.com.tr/portfolios/turk-telekom-arena/
21. https://tr.wikipedia.org/wiki/Fenerbah%C3%A7e_%C5%9E%C3%BCkr%C3%BC_Saraco%C4%9Flu_Stadyumu#:~:text=Mimarisi%20dikd%C3%B6rtgen%20%C5%9Feklinde%20olan%20bu,100%20tane%20VIP%20locas%C4%B1%20bulunmaktad%C4%B1r.
22. https://www.ozaymuhendislik.com.tr/pg_212_sukru-saracoglu-fenerbahce-stadyumu
23. https://www.dbarchitects.com.tr/tr/bjk-vodafone-arena/
24. https://tr.wikipedia.org/wiki/Y%C3%BCz%C3%BCnc%C3%BC_Y%C4%B1l_Atat%C3%BCrk_Stadyumu
25. https://alperaksoy.com.tr/proje/kocaeli-arena-stadyumu-35000-kapasite-146
26. https://www.tensaform.com/tr-TR/catalogue/tamamlanmis-projeler/39?searchText=stadyum
27. https://www.asma-germe.com/tr/projeler
28. https://alperaksoy.com.tr/proje/sakarya-arena-stadyumu-105#
29. https://www.erduman.com.tr/project/sakarya-stadyumu/
30. https://en.wikipedia.org/wiki/%C4%B0zmir_Atat%C3%BCrk_Stadium
31. https://alperaksoy.com.tr/proje/izmir-alsancak-stadyumu-159
32. https://www.erduman.com.tr/project/trabzonspor-senol-gunes-stadyumu/
33. https://www.trthaber.com/haber/spor/ktuden-medical-park-stadyumu-aciklamasi-655114.html
34. https://tr.wikipedia.org/wiki/Samsun_19_May%C4%B1s_Stadyumu
35. https://www.passo.com.tr/tr/mekan/25715/25715
36. https://www.tucsa.org/tr/celik_yapilar_yazi.aspx?yazi=1013
37. https://tr.wikipedia.org/wiki/Mersin_Stadyumu
38. https://www.tucsa.org/images/celik_yapilar/54/53_celik_yapilar.pdf
39. https://tr.wikipedia.org/wiki/Diyarbak%C4%B1r_Stadyumu
40. https://www.stendustri.com.tr/adana-stadi-projesinde-serge-ferrari-farki
41. https://www.dbarchitects.com.tr/tr/adana-stadyumu/
42. https://tr.wikipedia.org/wiki/Kayseri_Kadir_Has_%C5%9Eehir_Stadyumu
43. https://bkaarchitecture.com/projects-item/kayseri-kadir-has-stadium/
44. https://tr.wikipedia.org/wiki/Ba%C5%9Fak%C5%9Fehir_Fatih_Terim_Stadyumu
45. http://www.suldem.com/basaksehir_fatih_terim_stadyumu.html
46. https://erketasarim.com/projelerimiz/sosyal-kullanim-amacli-projeler/basaksehir-fatih-terim-stadyumu
47. https://www.dbarchitects.com.tr/tr/goztepe-gursel-aksel-stadyumu/
48. https://www.polikarbonat.com/goztepe-gursel-aksel-stadyumu-10-mm-solid-polikarbonat-cati-kaplamasi/
49. https://www.raf.com.tr/goztepe-gursel-aksel-stadyumu/
50. https://www.eskisehirspor.org.tr/stadyum
51. https://stadiumdb.com/stadiums/tur/eskisehir_stadyumu
52. https://tr.wikipedia.org/wiki/Yeni_4_Eyl%C3%BCl_Stadyumu
53. https://bkaarchitecture.com/projects-item/sivas-stadium/
54. https://www.passo.com.tr/en/venue/45216/45216
55. https://www.dbarchitects.com.tr/tr/ankara-eryaman-stadyumu/
56. https://tr.wikipedia.org/wiki/Eryaman_Stadyumu
57. https://tr.wikipedia.org/wiki/Antalya_Stadyumu
58. https://www.antalyaspor.com.tr/tr/tesislerimiz/antalyaspor-stadyumu.html
59. https://eskametal.com/tr/uygulama-birimi/
60. https://alperaksoy.com.tr/proje/elazig-ataturk-stadyumu-ve-spor-salonu-17600-kapasite-200#
61. https://atakeng.com.tr/portfolio-items/malatya-stadyumu/
62. https://bkaarchitecture.com/projects-item/malatya-stadium/
63. https://ilci.com.tr/proje/25-000-ki%CC%87s%CC%A7i%CC%87-kapasi%CC%87teli%CC%87-malatya-s%CC%A7ehi%CC%87r/
64. https://tr.wikipedia.org/wiki/11_Nisan_Stadyumu
65. https://azaksu.com/tr/spor/urfa-stadyumu
66. https://tr.wikipedia.org/wiki/Alanya_Oba_Stadyumu
67. https://alperaksoy.com.tr/proje/hatay-arena-stadyumu-30000-kapasite-136#
68. https://www.baselyapi.com.tr/projects/proje-adi-03/
69. https://tucsa.org/tr/celik_yapilar_yazi.aspx?yazi=1443#:~:text=Projede%20çim%20sahanın%20gün%20ışığından,çatıda%20ve%20cephede%20yırtıklar%20açılmıştır

NUMERICAL SIMULATIONS OF 3D-DISTANCE FABRICS

VOTRUBEC, VLASTIMIL*

VÚTS, a.s., Department of Virtual and Applied Mechanics, Svárovská 619, Liberec XI – Růžodol I, 460 01 Liberec, Czech Republic

ABSTRACT

This paper presents the results of numerical simulations conducted on inflated panels made from 3D distance fabrics. 3D distance fabrics constitute a subset of 3D woven fabrics. If coated, the structure of the fabric permits the formation of a panel with parallel layers through the process of air inflation. The pressurised air creates a stiff, lightweight and fail-safe structure that can be utilised in a multitude of applications. The mechanical behaviour of these panels can be described analytically by appropriate mathematical theory; however, this approach remains limited to common loading cases. This paper presents computational method for numerical simulations of inflated panels, including determination of the deflections of skins and the distribution of stress. The simulations are based on the results of material property tests and a nonlinear geometric model. The results are then compared with the mathematical theory and experimental data. The results demonstrate the efficacy of this approach and illustrate its advantages. Furthermore, an illustrative example of a specific loading case is presented to demonstrate the versatility of this approach for predicting the behaviour and conducting structural analysis of loaded 3D fabric panels.

KEYWORDS

Simulations; FEM; Distance fabric; 3D fabric.

INTRODUCTION

3D distance fabric is composed of two distinct skins, the upper and lower fabrics, which are simultaneously woven and connected by pile (drop) yarns (Figure 1). The pile yarns serve to lock the two skins together, thereby creating a robust connection. The base fabrics are separated from one another by a distance equal to the length of the pile yarns. This length constitutes a fundamental parameter of the fabric, as it defines its shape and stiffness, and is contingent upon the properties of the weaving machine. This is typically maintained at a constant length, ensuring that the inflated panel exhibits parallel and uniform surfaces. It is likewise feasible to weave distance fabrics with varying lengths of pile yarns; however, the primary advantage of this structure lies in its parallelism of skins. The skins are rendered impermeable through the application of an additional coating material (e.g. PVC, polychloroprene, etc.). The stability and load capacity of inflatable panels depend on their material properties, air pressure, fabric parameters, and shape. During inflation, the air pressure causes biaxial pretensioning of fabric layers and elongation of pile yarns, thereby enabling the panel to achieve the requisite shape and stiffness. 3D distance fabrics, also known as drop-stitched fabrics or space fabrics, offer numerous advantages, including a lightweight structure, portability in a non-inflated state, and a fail-safe mechanism during overload conditions.

The research of 3D fabrics is primarily concerned with woven and knitted fabrics in general where yarns in the third axis are present and the thickness of the fabric is negligible. A survey of 3D woven fabrics can be found in references [1-3]. Earlier research on the mechanics of inflatable fabric structures was limited, with only a few studies conducted on distance fabric panels [4]. Cavallaro [5] described the mechanics of a panel subjected to a four-point bending load, utilising experimental data from material tests to inform his analytical model. Additionally, he conducted an experiment on a bent panel for comparison. Hou [6] employed the finite element method to model knitted spacer fabric. A notable area of development has been the utilisation of these fabrics as reinforced composites [7].

The paper outlines the creation of an appropriate material model and the requisite tests for it (section Material model). It then describes the general rules for building FEM model of the panels and presents the building of a specific FEM model of a panel based on real-world testing (section FEM model). It then presents the results of the simulations and discusses the comparison with the theoretical and experimental results (section Simulation results). Finally, it presents the simulation of an overloaded panel as an

* **Corresponding author:** Votrubec V., e-mail: *vlastimil.votrubec@vuts.cz*

illustrative example of the indispensable role of numerical simulations in the design and analysis of distance fabric panels (section A comparison between the experimental and theoretical results).

MATERIAL MODEL

A comprehensive understanding of the material data is essential for the successful development of a model. In order to serve as a point of reference, real coated 3D distance fabric was selected for the purposes of experimental and simulation validation. The fabric is composed of a primary fabric woven on a weaving machine DIFA produced by VÚTS, a.s. All yarns (warp, weft and pile) are made of polyester (PES) with a fineness of 55 tex. The outer surfaces of the fabric skins were coated with polychloroprene on a nylon fabric substrate. The coating does not typically impact the mechanical properties of the material; however, it does ensure airtightness. Figure 2 illustrates the structure of the fabric and its basic textile properties, as produced by the Taiwan Textile Research Institute.

Textile materials, including yarns and fabrics, typically exhibit nonlinear tensile properties. However, the deviation from linearity is typically minor, with a constant young modulus. Fabrics are composed of two types of yarns: warp and weft. These are woven with varying densities, and warp and weft yarns may also differ in material and fineness. Consequently, fabrics are orthotropic materials, exhibiting nonlinear properties in both the warp and weft directions.

The tensile curves of the fabric were measured on a universal testing machine (Instron) in accordance with the standard ISO 13934-1, which outlines a procedure for determining the maximum force and elongation at maximum force using a strip method. Furthermore, the specimens were modified to a dog-bone shape, thereby ensuring that rupture occurred in the centre of the specimen, rather than in the jaws (Figure 3 on the left). The specimens were marked with white dots on the coated surface in order to facilitate the measurement of strain with an optical extensometer. The pile yarns were measured in accordance with the standard ISO 2062 on the same testing machine with pneumatic textile jaws (Figure 3 on the right). For the purpose of measuring strain, small balls with a through hole were placed and glued on the yarns. A tensile test was conducted on fabric skins and pile yarns using a universal testing machine.

The tensile curves are presented in Figure 4. It is evident that there is a notable distinction between the warp and weft tensile properties, as well as a nonlinear character. However, the divergence from the linear course is not substantial, and for the purposes of simulations, it can be approximated by a line. Notably, in the initial portion of the tensile curve, the variance is minimal. In the textile industry, it is customary to relate the tensile properties, strength of the fabric, and young modulus to the unit width of a fabric. Similarly, this approach is also employed in this case.

It should be noted, however, that FEM software requires the input of a material model in stress/strain quantities. Therefore, both tensile curves of fabric and pile yarns are recalculated in order to obtain the stress-strain dependence, despite the fact that the absolute values lack practical significance.

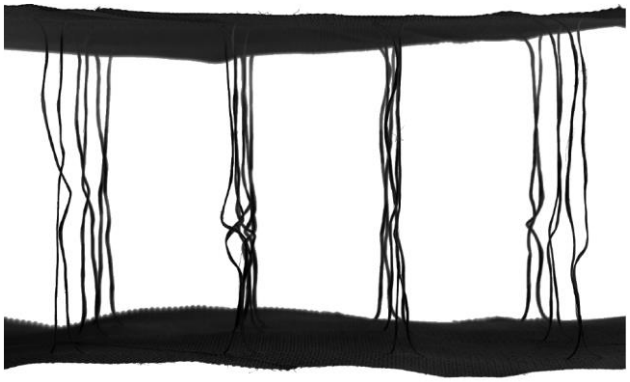

Figure 1. An example of 3D distance fabric.

Figure 2. The 3D distance fabric made by Taiwan Textile Research Institute. Total warp pile is 64 650 with different density after warp (150 ends/10 cm) and weft (4.31 ends/ 10 cm). The length of pile yarns is 180 mm.

Figure 3. Tensile test of fabric skin and pile yarns using a universal testing machine.

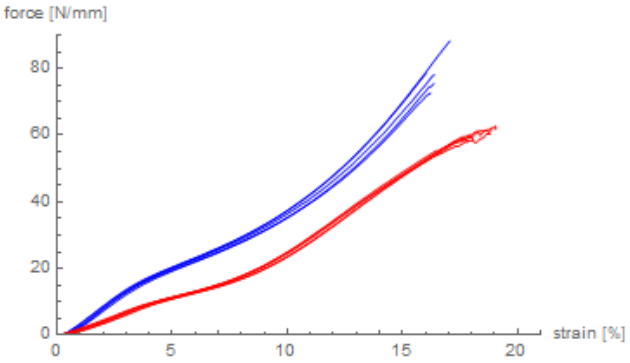

Figure 4. The tensile curves of the fabric skin for both the warp and weft directions. The units are related to the 1 mm width of the fabric.

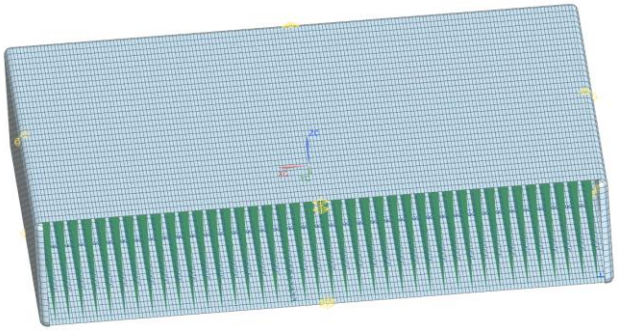

Figure 5. A section of the simulation model of the 3D distance panel. The mesh on the skins is created in such a way that four elements are placed after warp, which ensures an accurate representation of skin deflection. The green lines represent pile yarns, while the blue crosses represent suppressed displacements.

The combination of a nonlinear tensile curves and an orthotropic material presents a significant challenge for modelling. The nonlinear solver in the Siemens NX software is designed to work with isotropic nonlinear materials or orthotropic linear materials. However, it has been observed that using linear and orthotropic materials results in a smaller error. The calculated Young modulus of fabric is 428 MPa for the warp and 299 MPa for the weft.

FEM MODEL

The FEM model was built in a manner analogous to that of the tested panel. The dimensions of the panel used for experiments are identical to those of the modelled panel, namely 94 x 94 mm in area, 180 mm in thickness and subjected to a loading pressure of 100 kPa. The tested panel differs in that the edges were affixed by adhering the ends of the fabric and clamping them together with steel bars. The common application of a glued belt necessitates the replication of this panel in the same manner.

It is essential to prepare the geometry of the fabric panel in an inflated state. There is no relevant reason for simulating the panel in its undeveloped state, as this would entail significant difficulties. The model's geometry corresponds to the state, wherein the pile yarns are extended but the axial force is still zero, and the fabric skin between the binding points is not deflected. The side belt of the panel is affixed to the upper and lower skins, and thus is modelled and simulated. However, the model lacks a glue layer, the fabrics (and meshes) are connected directly. This is a reasonable simplification, as the stress distribution is analysed with precision and the computation is considerably more straightforward. Furthermore, potential sources of computational errors in corners are eliminated.

A further significant issue pertains to the question of bending stiffness. The actual bending stiffness of a fabric can be considered to fall between the values of a membrane, which exhibits no bending stiffness, and a solid sheet, which demonstrates full bending stiffness and is dependent on the thickness of the fabric. The modelling of fabric as an aerial body can be achieved through the use of shell elements. These elements permit the setting of arbitrary bending stiffness, although this is limited to a linear solver. Consequently, the bending stiffness cannot be adjusted. The behaviour of coated fabric is further complicated by the fact that the coating is situated on only one side of the fabric. This results in a dependence of the bending stiffness on the direction of bending loading, as the coated side of the fabric exhibits a greater bending stiffness than the uncoated side.

Pile yarns are represented as one-dimensional continuous rod (CROD) elements. The aforementioned elements are responsible for connecting the upper and lower skins, which have been prepared in accordance with the specified nodes, in a regular pattern. Non-linear material is assigned to these elements, thereby allowing for compression without stiffness. The young modulus of the tensile part of the curve is calculated from the measured tensile curve, while the young modulus of the compression part of the curve is set to be almost zero (zero is not a viable option). The inflation of the panel results in significant displacement of the side belt, causing the edgings of the skins to move towards the centre plane of symmetry. Here, the pile yarns undergo a reduction in length with no resistance, while in the middle of the panel, the pile yarns experience an increase in length.

The boundary conditions include the pressure loading on the inner walls and the suppressed displacements at specific nodes. The pressure value was set to 100 kPa, which is typical for common applications. All lower binding points (nodes for pile yarns) were disabled to enable vertical movement, thereby simulating the free inflation of the panel. To suppress displacement of the panel in both horizontal axes, one line of lower nodes in each direction was disabled to move.

SIMULATION RESULTS

The simulation results, namely the fabric deflections (Figures 6 and 7), are in accordance with the observed experimental outcomes. The greatest

deflection is observed in the panel sides, which lack the fixation provided by pile yarns in the upper and lower skins. However, from the perspective of mechanics and real-world applications, the displacement of the fabric in the vertical direction (z-axis) is of greater significance. It is expected that the elongation of the pile yarns (measured in distance) will correspond to the results obtained from the experimental and analytical studies. A closer examination of the fabric surface reveals a series of undulations, indicative of a pronounced deflection of the fabric between pile yarns following the warp direction. Conversely, the deflection of the fabric between pile yarns after weft is nearly negligible. The discrepancy can be attributed to the notable disparity in the density of the pile yarns following the warp and weft processes. The height of the "wave" (the distance between the binding point and the peak value) is another crucial parameter in panel mechanics. It is also employed for the validation of simulations, with a value of 0.8 mm for a 100 kPa pressure within the panel.

The values of strain and displacement demonstrate that the stresses are minimal, falling below the ultimate strength of the fabric and pile yarns. The concentration of stress is observed to be located around the mesh connections in corners where the simulation consistently produces slight distortions in the results. Another location of concentration of stress is in binding points, where the material exhibits non-standard behaviour. Nevertheless, the stress is consistently below the ultimate strength.

A COMPARISON BETWEEN THE EXPERIMENTAL AND THEORETICAL RESULTS

The deflection of skin u between binding points after warp is described by the following relation:

$$u(x) = \frac{D}{H}\frac{1}{k}\left(\frac{e^{k(D-x)}+e^{k\,x}}{e^{k\,D}-1} - \frac{e^{k\,D}+1}{e^{k\,D}-1}\right) - \frac{(D-x)^2}{H} + \frac{D}{H}(D-x)$$

where *D* represents the distance between the binding points after warp, *H* denotes the length of the pile yarns, and *k* incorporates the bending stiffness. This equation integrates the theories of thin plates and membrane theory. If the bending stiffness is disregarded (first bracket), the deflection shape transforms into a parabolic function. The maximum deflection occurs at the midpoint of the arc, where *x* = *D/2*.

The objective of the experiment was to measure the height of the profile (deflection of the skin) by means of a laser scanner and to compare the experimental data with theoretical predictions and then the simulation results (Figure 8). The vertical distance from the scanner was recorded for an increasing level of pressure. The test was concluded at the level of 120 kPa of air pressure inside the panel. Both the experimental and theoretical aspects were described in detail in paper [8], and thus no further details are provided here.

The data presented in Figure 9 comprises measured data, calculated data derived from aforementioned equation, and data obtained from the simulation. The data demonstrate a high degree of correlation. The displacements calculated from the FEM simulations exhibit discrepancies from the experimental data, particularly in the mid-arc region where the curve intersects with the theoretical curve, which does not account for bending stiffness. Closer to the margins

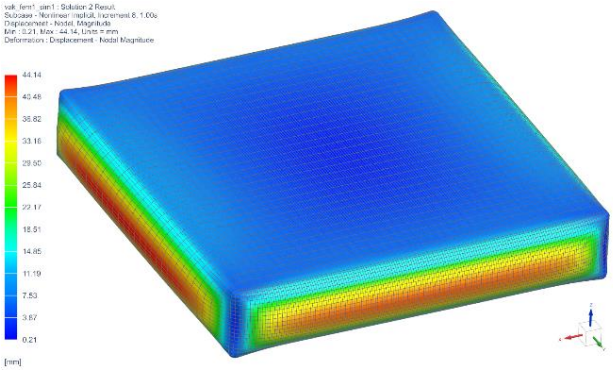

Figure 6. Displacements of pressure loaded fabric panel.

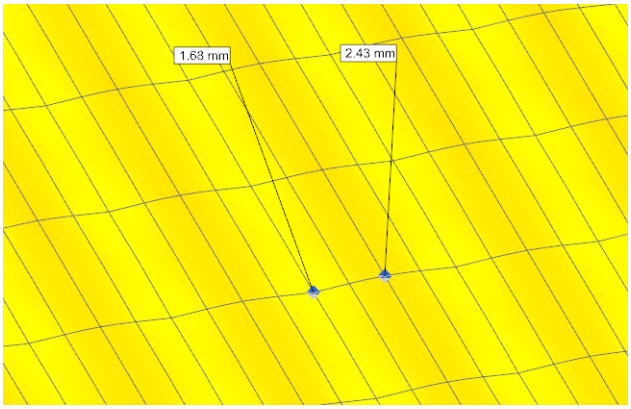

Figure 7. A detail of the displacements of the vertical axis of the bent fabric skin between the pile yarns.

Figure 8. The 3D distance fabric panel during the safety test. In the center there are visible deflections of the skin between binding points that were measured by a laser scanner.

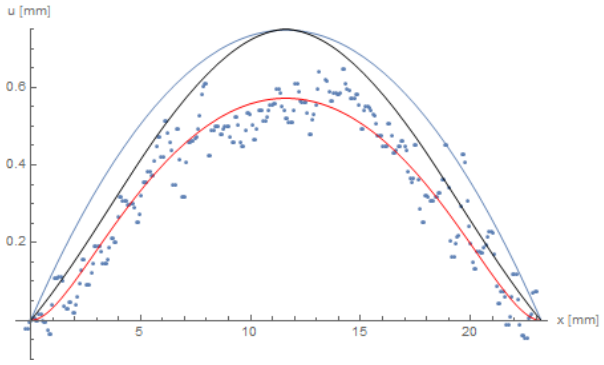

Figure 9. A comparison of the measured deflection of the fabric skin, loaded by 100 kPa (blue dots). The theoretical curve, derived from the equation, is shown in red. The interpolated simulation data is represented in black and a theoretical curve, which neglects the bending stiffness, is illustrated in blue.

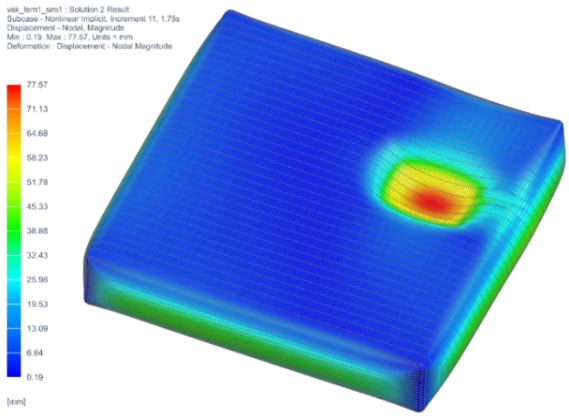

Figure 10. A case study of an overloaded fabric panel. Large displacements occur in the place of loading.

of the arc the simulation curve is getting nearer to the experimental data. However, due to the inherent limitations of the FEM model, as previously discussed, the agreement between the simulation and experimental data is still fine. When considering the absolute values of displacement along the arc, it is evident that the exact value is not a crucial parameter for practical applications. Instead, it serves primarily to validate the mathematical theory and ensure the accuracy of the simulations.

A CASE STUDY OF AN OVERLOADED PANEL

The advantages of this methodology are readily apparent when considering the example of the overloaded fabric panel. The panel is typically loaded by its working pressure, as illustrated in the preceding example. Additionally, it is subjected to a force 15 kN acting on an area of approximately 120 x 150 mm. This force causes significant deflection of the upper skin, with a maximum value of 78 mm. The depression almost reaches approximately half of the panel thickness, which is clearly unacceptable in practical terms. The maximum values of stress and strain are considerably higher than the typical range, yet they remain within the third of the tensile curve, indicating that the structure remains safe. Nevertheless, a discernible decline in stability is evident, attributable to the considerable displacements. The fabric between the depression and the panel edge exhibits slight warping, which presents numerical challenge. A larger load would result in computational collapse, which is not viable state for the panel. While the expansion of the panel can be well described analytically using the elongation of pile yarns, the external compression of the panel must be computed numerically. As with loading of panel sides, combined loading or complicated boundary conditions require the use of a numerical simulation via the finite element method is irreplaceable.

CONCLUSIONS

In many cases, numerical simulations are an invaluable tool for the analysis and design of air inflated 3D distance fabric structures. These simulations are based on precise material testing and the nonlinear computation of appropriate FEM software. The correlation between the outcomes of these simulations and the mathematical theory, as well as the results of physical experimentation, is highly satisfactory, thereby substantiating the efficacy of this approach. The benefits of simulation are most evident in the context of structures subjected to challenging boundary conditions, as illustrated by the example of an overloaded panel.

Acknowledgement: *This publication was supported by the Ministry of Industry and Trade (MPO) within the framework of institutional support for long-term strategic development of the research organization - provider MPO, recipient VÚTS, a. s.*

REFERENCES

1. Badawi S.S.: Development of weaving machine and 3D woven spacer fabric structures for light-weight composite materials. Ph.D. Thesis, Technical university in Dresden, Dresden, Germany, 2007.
2. Chen X.: Advances in 3D Textiles. Woodhead Publishing, 2015.
3. Gokarneshan N., Alagirusamy R.: Weaving of 3D fabrics: A critical appreciation of developments. Textile Progress, 41(1), 2009, pp. 1-58. https://doi.org/10.1080/00405160902804239
4. Falls J., Waters J.K.: Bending test of inflatable dropstitch panel. Proceedings of the 11th International Conference on Fast Sea Transportation, Hawai, USA, 2011.
5. Cavallaro P.V., Hart C.J., Sadegh A.M.: Mechanics of air-inflated drop-stitched fabric panels subject to bending loads. Proceedings of ASME International Mechanical Engineering Congress and Exposition, ASME, 2013. https://doi.org/10.1115/IMECE2013-63839
6. Hou X., Hu H., Silberschmidt V.V.: A study of computational mechanics of 3D spacer fabric: Factors affecting its copmression deformation. Journal of Material Science, 47, 2012, pp. 3989-3999. https://doi.org/10.1007/s10853-012-6252-2
7. Chen X., Taylor L.W., Tsai L.J.: An overview on fabrication of three-dimensional woven textile preforms for composites. Textile Research Journal, 81, 2011, pp. 932-944. https://doi.org/10.1177/0040517510392471
8. Votrubec V., Žák J.: Mechanics of air-inflated 3D distance fabric. Applied and Computational Mechanics, 15(1), 2021, pp. 85 – 96. https://doi.org/10.24132/acm.2021.650

AIMS AND SCOPES

“Vlakna a Textil” is a peer-reviewed scientific journal serving the fields of fibers, textile structures and fiber-based products including research, production, processing, and applications.

The birth of this journal is connected with three institutions, Research Institute for Man-Made Fibers, Svit (VÚCHV), Research Institute of Chemistry of Textiles (VÚTCH) in Žilina and Department of Fibers and Textiles at the Faculty of Chemical Technology, Slovak Technical University in Bratislava, having a joint intention to provide, utilize and deposit results obtained through the research, development and production activities dealing with the aforementioned scopes. „Vlákna a Textil“ journal has been launched as a consequence of a joing of existing magazines „Chemické vládkna“ (VÚCHV) and „Textil a chémia“ (VÚTCH). Their tradition should provide a good framework for the new journal with the main aim to create a closer link between the basic element of the product - fibre and its fabric - textile.

Since its founding in 1994, the journal introduces new concepts, innovative technologies and better understanding of textile materials (physics and chemistry of fiber forming polymers), processes (technological, chemical and finishing), garment technology and its evaluation (analysis, testing and quality control) including non-traditional applications, such as technical textiles, composites, smart textiles or garment, and nano applications among others. The journal publishes original research papers and reviews. Original papers should present a significant advance in the understanding or application of materials and/or textile structures made of them.

VLÁKNA A TEXTIL
Volume 32, Issue 1, March 2025

CONTENT